NASA-CR-165838
19820012350

NASA Contractor Report 165838

Integral Throat Entrance Development, Qualification and Production for the Antares III Nozzle

F.I. Clayton, R.B. Dirling, D.A. Eitman and W.C. Loomis
Material Sciences Operation
Science Applications Incorporated
Irvine, California

Prepared for
Langley Research Center
under Contract NAS1-15650
January 1982

National Aeronautics and
Space Administration

Langley Research Center
Hampton, Virginia 23665

All Blank Pages

Intentionally Left Blank

To Keep Document Continuity

TABLE OF CONTENTS

LIST OF FIGURES

LIST OF FIGURES (cont'd)

LIST OF FIGURES (cont'd)

LIST OF TABLES

INTEGRAL THROAT ENTRANCE DEVELOPMENT, QUALIFICATION AND PRODUCTION FOR THE ANTARES III NOZZLE

F.I. Clayton, R.B. Dirling Jr., D.A. Eitman and W.C. Loomis

Science Applications, Incorporated
Material Sciences Operation
Irvine, California

SUMMARY

This report documents the work performed to develop, qualify and produce an integral throat entrance for the Antares III solid rocket motor nozzle. The initial work consisted of design analyses of a G-90 graphite design that had evolved from past experience. While the analyses indicated acceptable margins of safety, the nozzle throat insert suffered a thermo-structural failure during the first development firing. Subsequent re-analysis using properties measured on material from the same billet as the nozzle throat insert showed negative margins. Several design modifications were investigated showing only limited improvement. Carbon-carbon was investigated and found to result in large positive margins of safety.

The SAI Fast Processed 4-D material was selected to replace the G-90 graphite. This material uses Hercules HM 10000 fiber as the reinforcement. Its unique construction allows powder filling of the interstices after preform fabrication which accelerates the densification process. Allied 15V coal tar pitch is then used to complete densification. The properties were extensively characterized on this material and six nozzles were subjected to demonstration, development, and qualification firings.

INTRODUCTION

Under contract to NASA Langley Research Center, the Vought Corporation has, in the last two decades, developed the Scout vehicle for the economical launch of scientific and reentry experiment payloads. This highly successful small-payload capability vehicle has been used in many space exploration programs, both in the United States and abroad. To increase the payload capability of Scout vehicles for use in the 1980's, the NASA Scout Project Office developed through a team of contractors, a new third stage motor. The result of this effort is the Antares III rocket motor developed by Thiokol/Elkton Division under contract to Vought. SAI was initially contracted to assess the adequacy of the Antares III nozzle design specified by Vought/Thiokol and to participate in the selection of a higher confidence nozzle throat material should that be necessary. Subsequently, SAI was selected to supply the insert material and participated in the development, qualification and production of the nozzle throat inserts.

The Antares III rocket motor is depicted in Figure 1. There overall dimensions are shown and specifications for the nozzle and propellant system are delineated. The TP-H-3340 propellant develops a maximum thrust of 92,500 N (20,800 lb) for a firing duration of 42.5 seconds with a chamber pressure of 5.52×10^6 Pa (800 psia) and a flame temperature of 3282°C (5940°F).

Figure 2 shows the nozzle throat insert for several different designs which evolved during engineering development of the Antares III nozzle. The G-90 insert design shown in Configuration 1 evolved from Thiokol's past experience on nozzles of similar configuration and type. Because of eventual failures associated with substandard G-90 graphite for this design, the insert was replaced in Configuration 2 with ATJ-S graphite. A split insert design was configured to relieve high strains in the interior of

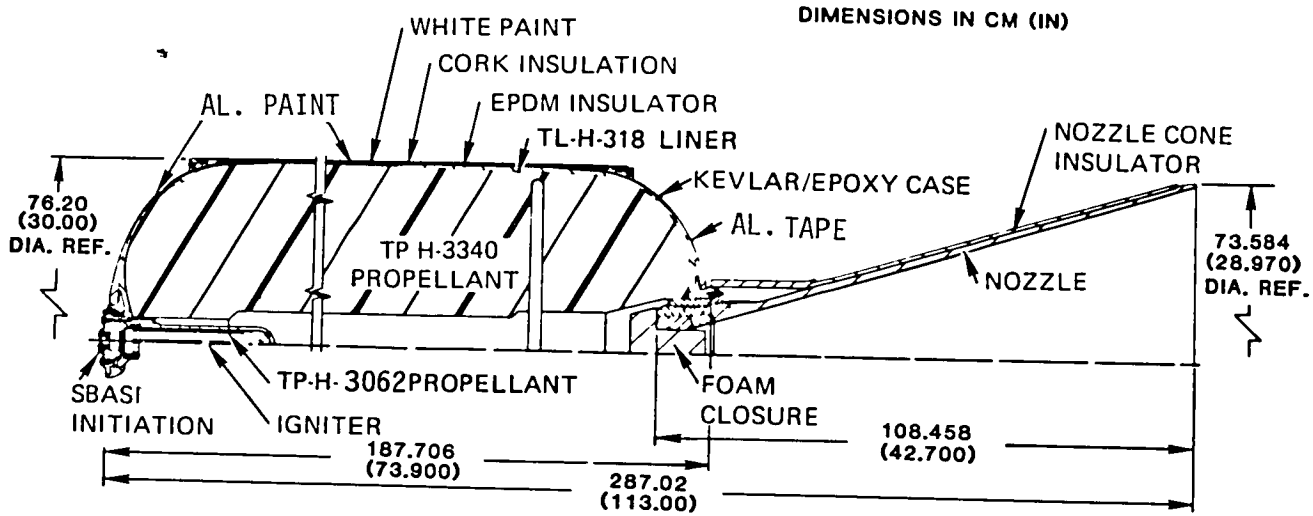

Figure 1. Antares III Rocket Motor

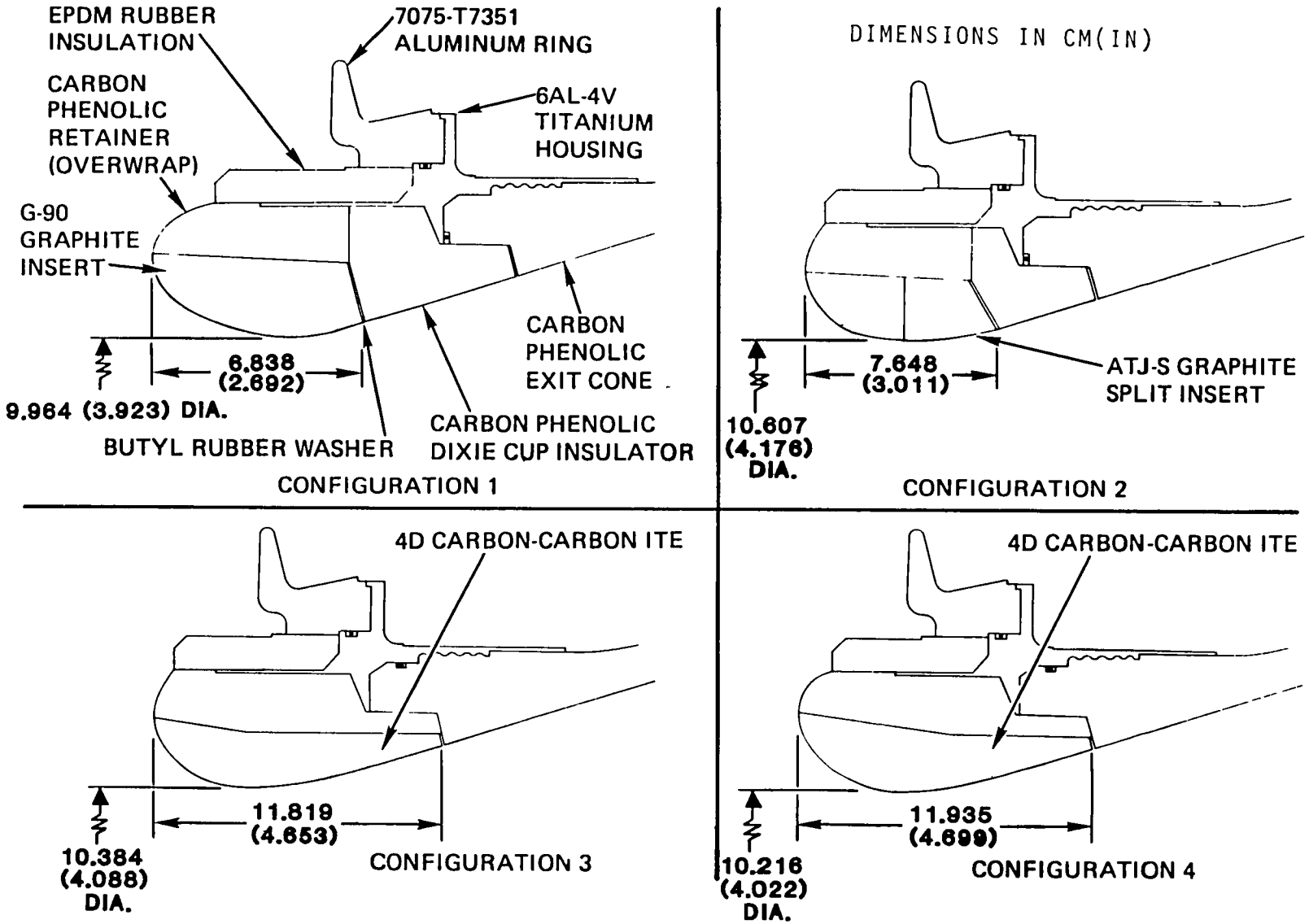

Figure 2. Sequence of Antares III Configurations Analyzed

the graphite insert observed in the analysis results of Configuration 1. Due to deficiencies of ATJ-S meeting minimum properties billet acceptance criteria specified by Vought and potential design problems with the split insert, ATJ-S was dropped from consideration during engineering development. A carbon-carbon integral throat entrance cap was then selected (Configuration 3) and developed specifically for application to the Antares III. The final configuration, Configuration 4, was selected for full scale development testing and shows slight modifications in comparison to the insert shown in Configuration 3, modified primarily to increase resistance to blowout loads. This final configuration utilizing carbon-carbon is the present Antares III rocket nozzle throat design.

Advanced multidirectional carbon reinforced carbon composites have the potential for applications in rocket nozzles, ram jets, nose tips, turbines, and other elevated temperature areas. The primary limitations to their application is that both their cost and schedule, due to iterative, labor-intensive fabrication methods, are prohibitive for all but the most critical applications. A technique has been devised at SAI which significantly reduces both fabrication costs and time required for fabrication through the use of a combination of pre-rigidized reinforcements and particulate additives to the composite matrix region. In addition, the technique greatly expands the potential for composite tailorability since direct, and relatively massive particulate additions to matrix areas is effected.

The initially developed carbon-carbon composite utilizing this fabrication procedure was adopted for use on the Antares III for the NASA Scout vehicle. The acceptance of this material for Antares III followed a successful demonstration firing in an Altair motor on January 27, 1978. This was followed by an intensive effort to develop an approved quality assurance system including

a complete set of materials and fabrication specifications which paralleled the fabrication of material for both development and and qualification testing.

Two logs of the SAI material were submitted to Southern Research Institute (SoRI) in Birmingham, Alabama for characterization testing. Mechanical testing included tension, compression, flexure, torsion and shear testing at temperatures up to 2650°C (4800°F). Thermophysical properties evaluated were thermal expansion and thermal conductivity up to 2760°C (5000°F). In all cases the test specimens were excised from three material directions i.e. axial, transverse aligned in a reinforcement direction and transverse aligned 30° between the reinforcement directions.

Ground test firings were conducted during both the development and qualification phases of the program. Two nozzles were fired with two different throat diameters at Thiokol/Elkton during development. The object was to obtain a data base on the erosion/chamber pressure response of the carbon-carbon insert in order to select a final design throat diameter. Based on the data from these firings a design throat diameter was selected, utilized for the three qualification firings at AEDC, and subsequently in the flight motor production.

The authors would like to acknowledge the contributions of those who worked on the present program. Among these are Messrs. D. Guthrie and D. Dearing of the Scout Program Office at NASA/Langley, S. Song of Vought Corporation, and C. Canada of Southern Research Institute. At Science Applications, the following made significant contributions: M. White and C. Heightland in thermostructural analysis, J. Brunet and J. Glatz in quality control, and W. Mixon in material processing.

NOZZLE ANALYSES

Initial Antares III Design

Analyses of the Antares III nozzle as originally designed (Configuration 1, Figure 1) were conducted in order to predict both thermal and structural performance during motor firing. The analyses consisted of prediction of the following: a) nozzle flowfield; b) boundary layer development and heat transfer rates; c) nozzle materials' erosion, charring, and surface temperatures; d) internal temperature distributions; and e) material mechanical response and thermostructural margins of safety. The analyses indicated above were performed sequentially with each item providing the input data required for the succeeding item in essentially an uncoupled manner. Although it would be desirable to predict rocket motor performance via an analysis which coupled flowfield, heat transfer, surface erosion, and internal heat conduction this capability does not presently exist. For most applications, however, an uncoupled procedure is adequate except in regions where large differential erosion rates between adjacent materials occur leading to the formation of steps or gaps which may significantly influence the nozzle flowfield. The methodology employed for each of the items listed above is described in the following sections.

Flowfield. - The nozzle flowfield was computed for three different chamber pressures which spanned the expected pressure history. A two-dimensional, two-phase computer code was used for the transonic and supersonic region from the throat to the nozzle exit plane; forward of the throat, a one-dimensional, constant specific heat analysis was performed for the gas phase. Figure 3 presents typical results at one chamber pressure for the boundary layer edge gas pressure, temperature, and Mach number as a function of wetted surface length from the first

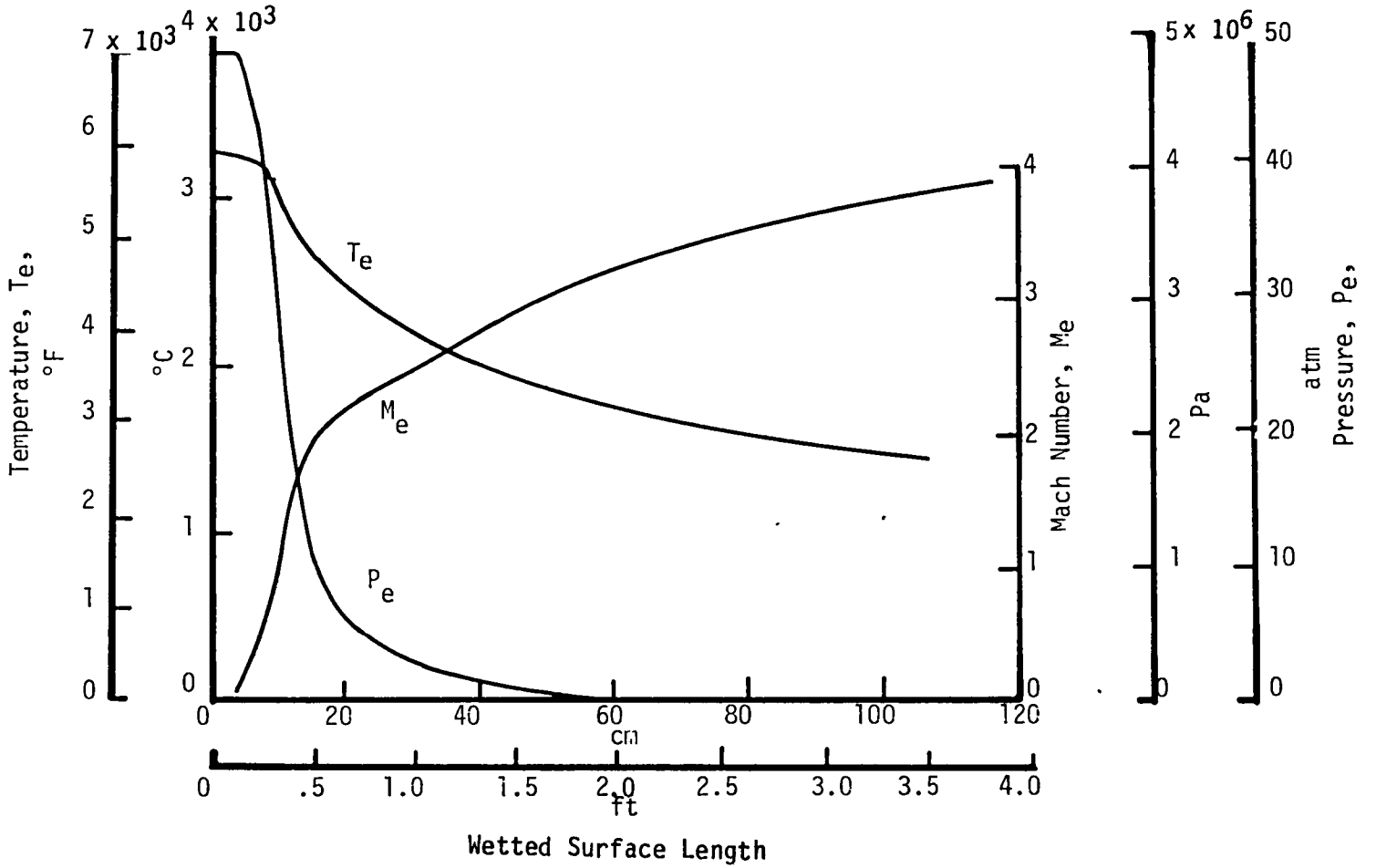

Figure 3. Antares III Nozzle Environment

analysis station located at the junction of the EPDM insulation and the carbon phenolic overwrap. These results were used to compute the boundary layer development and convective heat transfer rate discussed in the next section.

Heat Transfer Rates. - The convective heat transfer rate to the nozzle wall was computed using the momentum integral equation and a heat transfer similarity law for compressible, roughwall flow, Reference 1. This method accounts for the increase in convective heating due to surface roughness using the roughwall skin friction data of Nikuradse, Reference 2 and the heat transfer similarity law of Dipprey and Sabersky, Reference 3.

The radiative heat transfer rate to the nozzle surface was calculated using the parallel plate model and an effective gas emissivity calculated from Beers' Law.

Figure 4 presents the calculated heat transfer coefficient and radiative rate to the nozzle surface for a chamber pressure 4.83 x 10^6 Pa (700 psia). Radiative heating is noted to be of consequence only upstream of the throat where both gas density and temperature are high. The effects of surface roughness are included in the convective heating rate and result in approximately a 35 percent increase in peak heating rate which occurs just forward of the nozzle throat. For G-90 graphite an equivalent sand roughness of .0086 cm (.0034 in) based on optical measurements made on ablated specimens of this material was used. For the carbon phenolic materials the sand roughness was determined based on an analysis of carbon phenolic ablation rate data as a function of fabric angle, Reference 4, and varied from .0152 cm (.006 in) for most of the aft exit cone to 1.52 cm (.06 in) in the dixie cup region aft of the G-90 throat insert. As noted in Figure 4, the boundary layer was assumed to be turbulent downstream of the forward stagnation point of the submerged

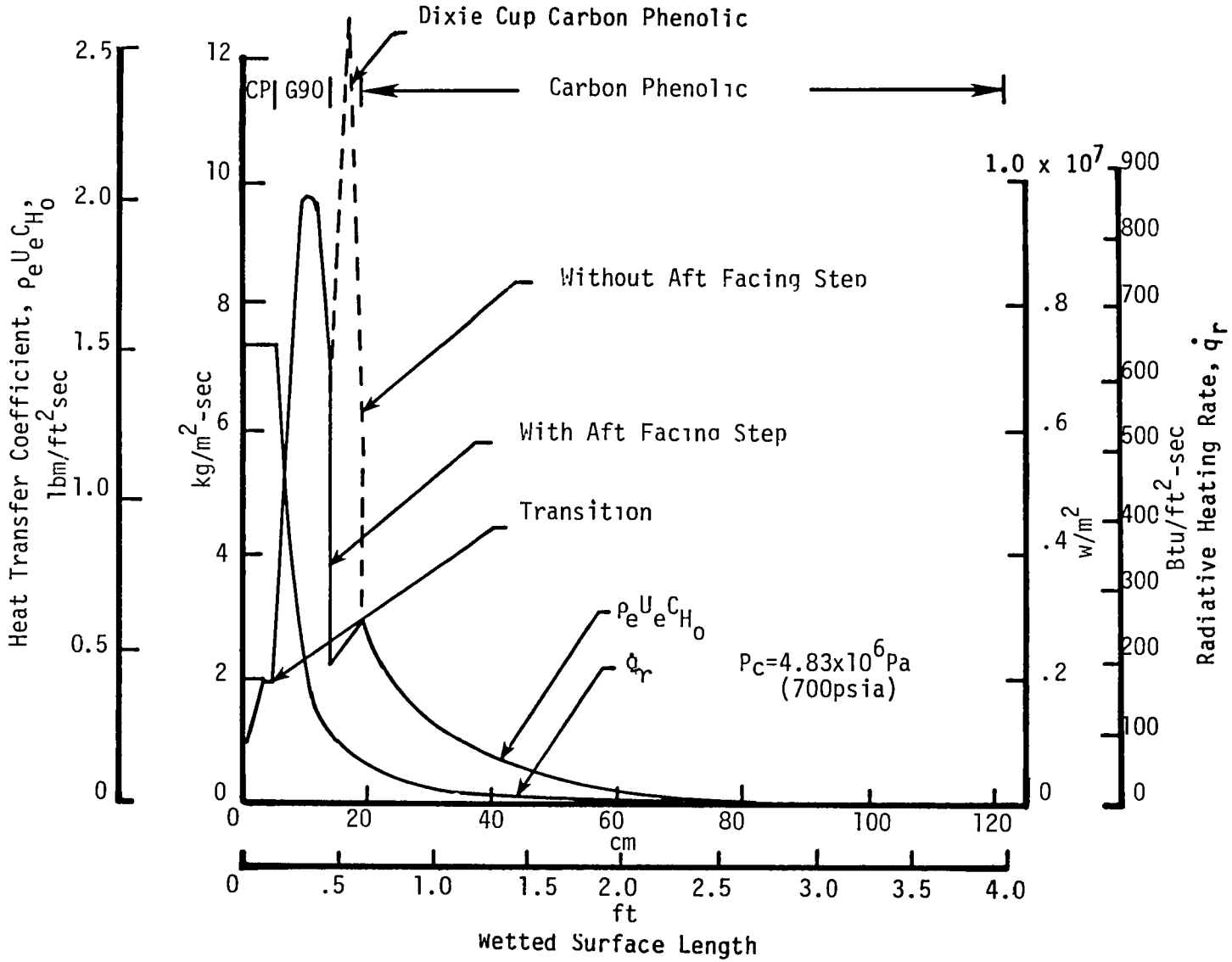

Figure 4. Antares III Nozzle Heating

nozzle. For the aft insulator (dixie cup region) the high sand roughness results in the prediction of the large increase in heat transfer coefficient shown by the dashed line. Because of the increased recession expected due to this large increase in heating, an aft-facing step was expected to develop which would reduce the heat transfer coefficient due to boundary layer separation. Modification of the heat transfer coefficient which would result in an equilibrium condition was made based on heat transfer data for aft-facing steps, Reference 5, as seen by the solid line in Figure 4.

Ablation. - Nozzle material ablation rates were predicted using both the CMA, Reference 6 and GASKET2, Reference 7, computer codes. Both codes analyze the ablation process using a transient one-dimensional heat conduction model. Due to the unavailability of kinetic reaction rate coefficient data for carbon-phenolic, all carbon-phenolic materials were analyzed using CMA assuming chemical equilibrium. This approach, of course, overpredicted the surface recession rate especially for the exit cone; however, the total heat affected zone (recession plus partially pyrolyzed resin) subsequently appeared to be well predicted. For the G-90 throat insert the GASKET2 code was employed with the built-in kinetic data. Typical results for the ablation rate of G-90 at the throat are presented in Figure 5 in terms of the mass transfer rate parameter, B', as a function of wall temperature. The kinetics of the G-90 reaction with the propellant gases are such as to suppress the hydrogen reaction at low temperatures and shift the sublimation reaction to higher temperatures. As a point of interest, the kinetic reaction rate of ATJ graphite is seen to be faster than that of G-90.

Figure 6 shows the results of the ablation analysis in terms of the final eroded nozzle contour and the heat affected zone. Predicted nozzle throat recession was 0.612 cm (.241 in) with

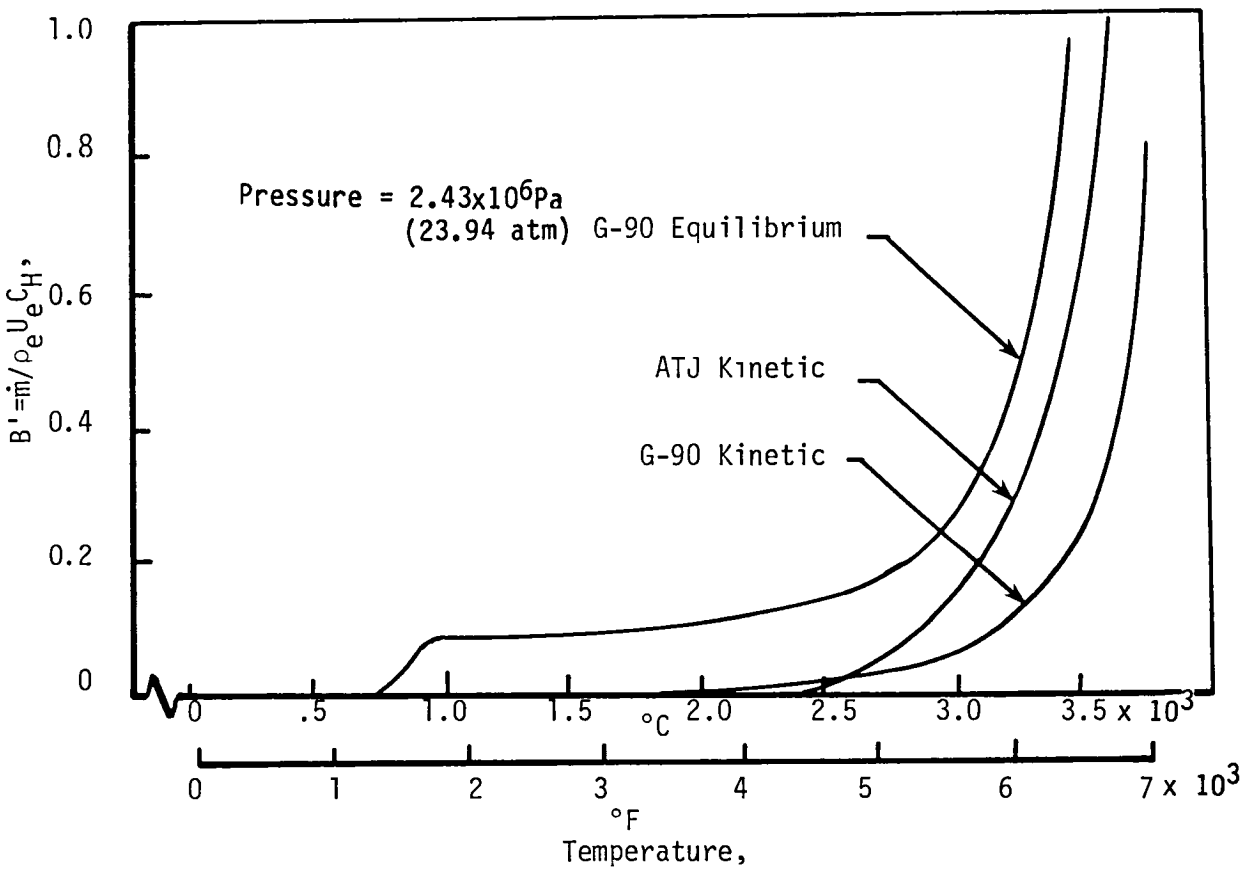

Figure 5. Graphite Ablation Rate at Throat

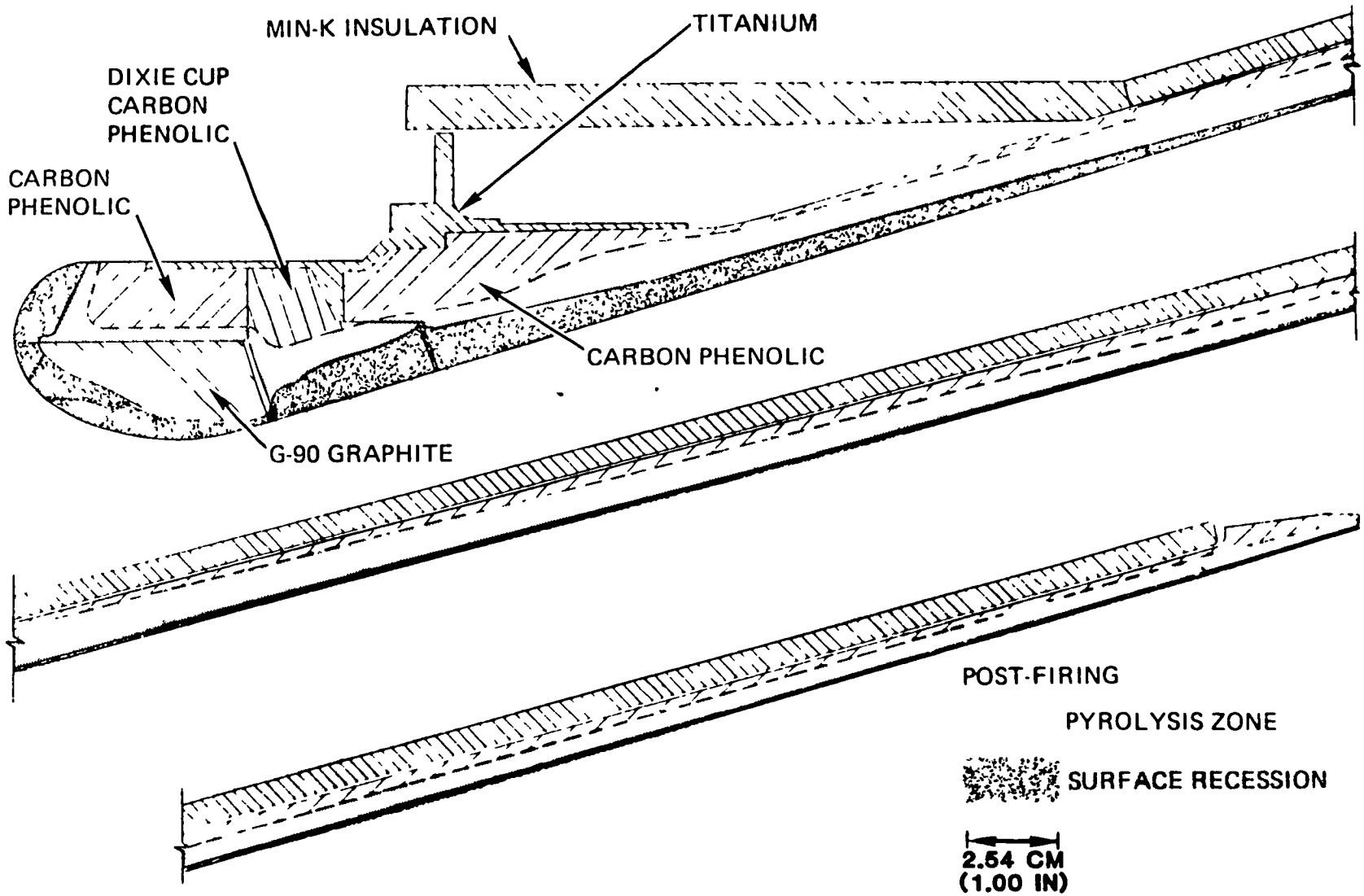

Figure 6. Antares III Nozzle Recession

higher recession occuring forward of the throat where the heat transfer coefficient was predicted to be a maximum.

The formation of an aft-facing step in the dixie cup carbon phenolic insulator should be noted. Fairly large recession was also predicted for the nose region of the carbon phenolic overwrap, and substantial pyrolysis zone depth is evident for the overwrap adjacent to the graphite insert and the carbon phenolic exit cone material.

Internal Heat Conduction. - Internal temperatures for use in the structural analysis were generated using an SAI axisymmetric heat conduction code, FIELDC (FInite ELement Diffusion and Conduction). Figure 7 shows a computer plot of the thermal finite element mesh geometry for Configuration 1 at ignition (time = 0). Materials considered in the 2-D analysis were the 6 Al-4V titanium housing, the carbon phenolic overwrap, dixie cup, and exit cone, the G-90 graphite throat insert, and the rubber washer, assumed to have the properties of EPDM. The graphite and carbon phenolic materials were considered to be orthotropic.

The heat conduction solution is based on imposed surface temperatures at the ablating nozzle surface. Both the surface temperature and the surface geometry were made continuous in the model by utilizing a cubic fit of the temperature and recession data obtained from the one-dimensional CMA and GASKET2 analyses already described. The method used to handle the change in geometry due to surface recession was to allow the finite elements near the surface to diminish in size while preserving the original number of elements.

Boundary conditions used for the analysis, in addition to the time varying surface temperatures previously discussed, were as follows. Adiabatic boundary conditions were used

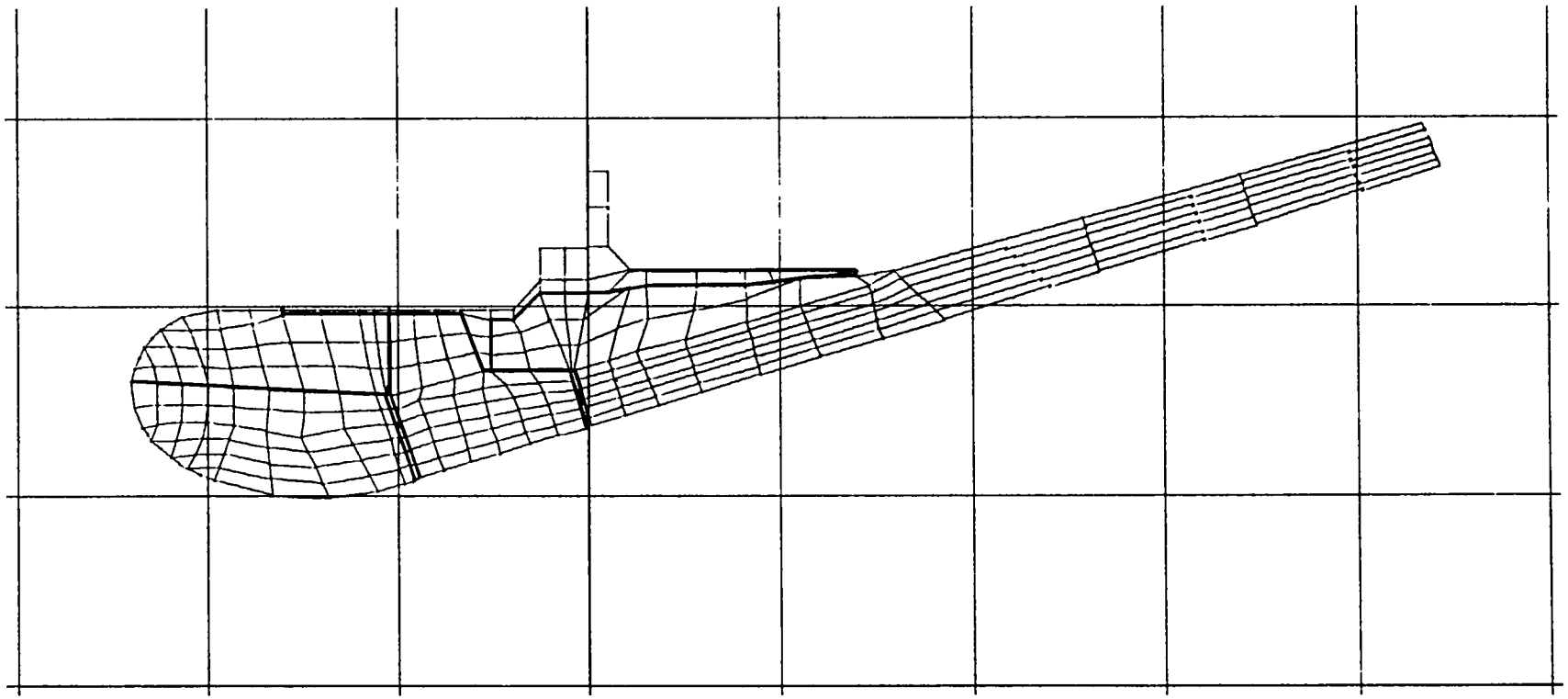

Figure 7. Antares III Thermal Finite Element Mesh at Time = 0.

for the submerged region of the nozzle protected by EPDM and for the outer boundary aft of this region. At the aft boundary of the finite element model, in-depth temperatures obtained from the appropriate one-dimensional analysis were input as a function of time.

A sequence of isotherm plots for four times during the firing (2, 10, 25, and 42.5 seconds) are presented in Figure 8. These plots provide a good qualitative picture of the heat penetration in the nozzle and of the relationships which exist between surface recession and the movement of the isotherms. The protective effect of the adiabatic boundary below the EPDM and the influence of the orthotropic thermal properties in the carbon phenolic overwrap are also worth noting.

Thermostructural Analyses. - The thermostructural analysis of the Antares III nozzle was conducted using the SAAS III finite element code, Reference 8. SAAS III determines the displacements, mechanical and thermal stresses and strains in axisymmetric and plane solids with different orthotropic temperature dependent material properties in tension and compression. The SAI version of this code will also simultaneously compute margins of safety based on both stress and strain allowables (which may vary as a function of temperature). Figure 9 shows the initial structural mesh used for the nozzle analysis of Configuration 1. The figure is broken into two regions for convenience, but the entire structure including the exit cone and the 7075-T7351 aluminum casing ring were analyzed.

The nozzle was restrained in the axial direction by stipulating zero axial movement at one node on the aft face of the aluminum casing ring (see Figure 9). Except for the internal restraints from the stiffness of the components, the nozzle was allowed to move freely in the radial direction. Nozzle response was driven

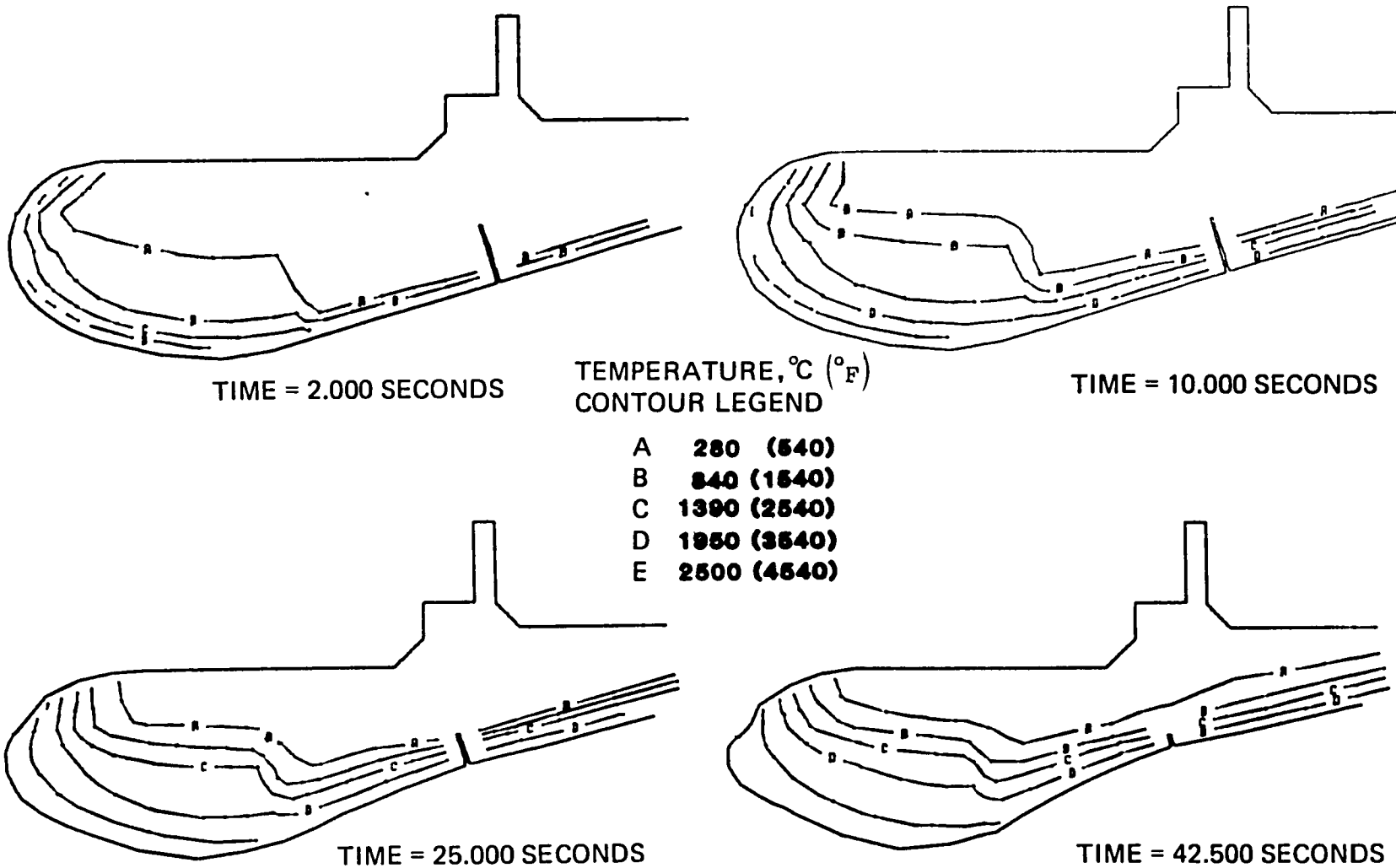

Figure 8. Nozzle Isotherm Plots at Various Times

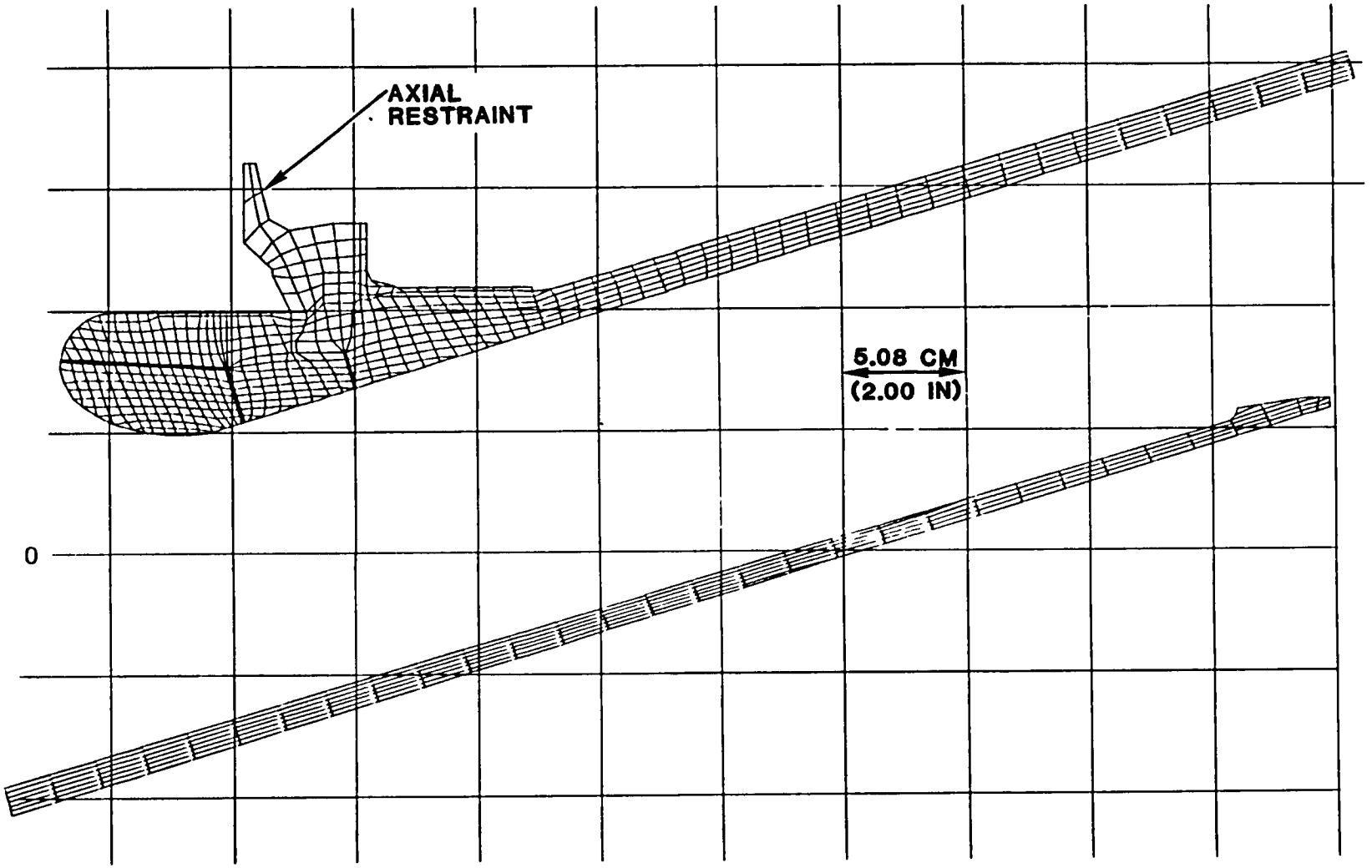

Figure 9. Structural Analysis Mesh (Configuration 1)

by both mechanical and thermal loads, the mechanical loads resulting from the difference in pressure between the inner nozzle surface due to the nozzle flowfield (Figure 3) and a constant 1.67×10^5 Pa (14.7 psi) external pressure on the exit cone to stimulate a ground test condition. Temperatures used for the SAAS III analysis were interpolated spatially and temporally from the FIELDC analyses for the exit cone region. A preprocessor program was used to automatically generate all of the SAAS III input data (including geometry, temperatures, and pressures) for desired analysis times.

Material properties for the G-90 material were based primarily on data from Reference 9; however, data from References 10 through 14 were also used. Properties for the analysis were selected for billets similar in size to those used for the Antares III throat insert. For the carbon phenolic materials, the principal data source was Reference 15, although References 16 through 18 were also used. Selection of carbon phenolic properties for the analysis was based on material configuration (ring vs. flat panel) and the principal reinforcement directions for each part. Actual properties used for the nonmetallic materials are contained in Reference 19. Properties used for the metallic materials were obtained from Reference 20.

The thermostructural analyses which were performed for Configuration 1 consist of linear elastic baseline analyses at 1.5, 3, 4.5, 6, 10, 25, and 42.5 seconds, and supplementary analyses which investigate the effects of (1) variations in material properties for the G-90 and carbon phenolic materials, (2) degradation of the bondline between the G-90 and carbon phenolic overwrap materials, and (3) bilinear elastic material properties. The baseline analysis results will be presented first.

Figure 10 shows the overall deformation of the forward region of the nozzle (greatly magnified), together with the surface reces-

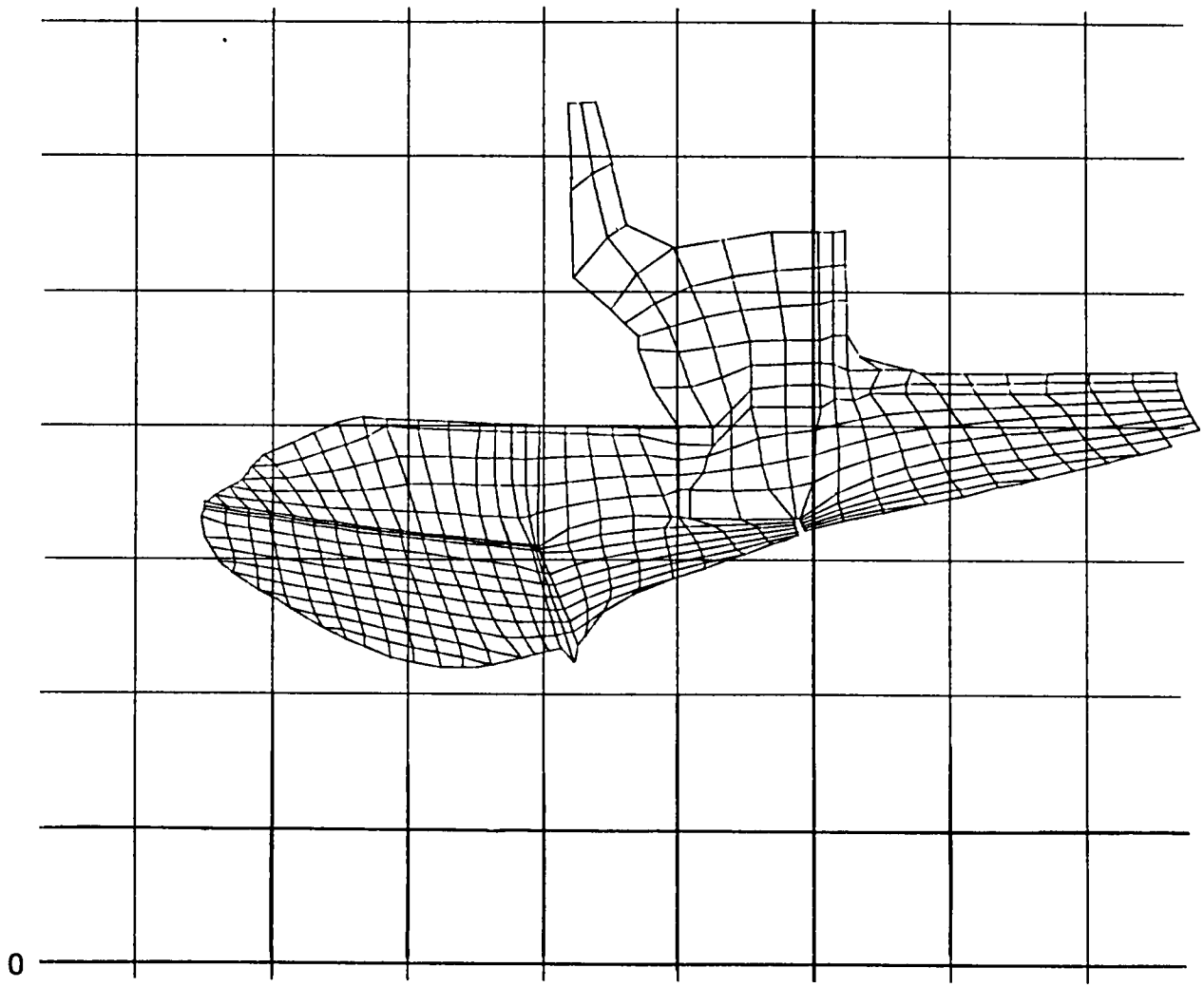

Figure 10. Predicted Recession and Exaggerated Deformation (Configuration 1)

sion. The upward rotation of the carbon phenolic-overwrap/G-90 bondline is to be noted, but the inward radial expansion of the rubber washer should be regarded as a gross exaggeration of actual response.

Strain margin of safety histories for selected elements in the carbon phenolic overwrap material are presented in Figure 11. These margins are calculated in the standard way, so that a negative margin is an indication of failure. Indicated failure for carbon phenolic materials is usually of no great concern as long as the failure locations are near the material surface, which is indeed occurring here. What happens in this event is local delamination or crossply tensile failure. This is rarely a serious matter, because the "failed" material is usually above 260°C (500°F), where the material stiffness is drastically reduced, (thereby reducing the internal loads), and the locally failed material can still remain attached to the structurally sound material. Thus it is normal to expect degraded carbon phenolic material to develop near the heated surface. It is apparent in this figure that the carbon phenolic material exhibits both an early- and late-time critical response. This is implied by the presence of the two lobes in the curves for certain elements, which is due to a change in sign in the shear stress, τ_{MN}, during the firing. The direction of shear deformation changes after sufficient bulk heating has occurred to cause the upward rotation of the forward portion of the nozzle.

For the G-90 insert material, the strain margin of safety history is shown in Figure 12. Again the early- and late-time response is seen to occur, but the former is clearly more critical. No negative strain margins were observed for the G-90, but negative shear strength margins were predicted for the aft OD corner of the insert early in the firing (-0.42 at 3 seconds). This finding could not be corroborated by strain margin calculations because shear strain allowables were unavailable. On the basis

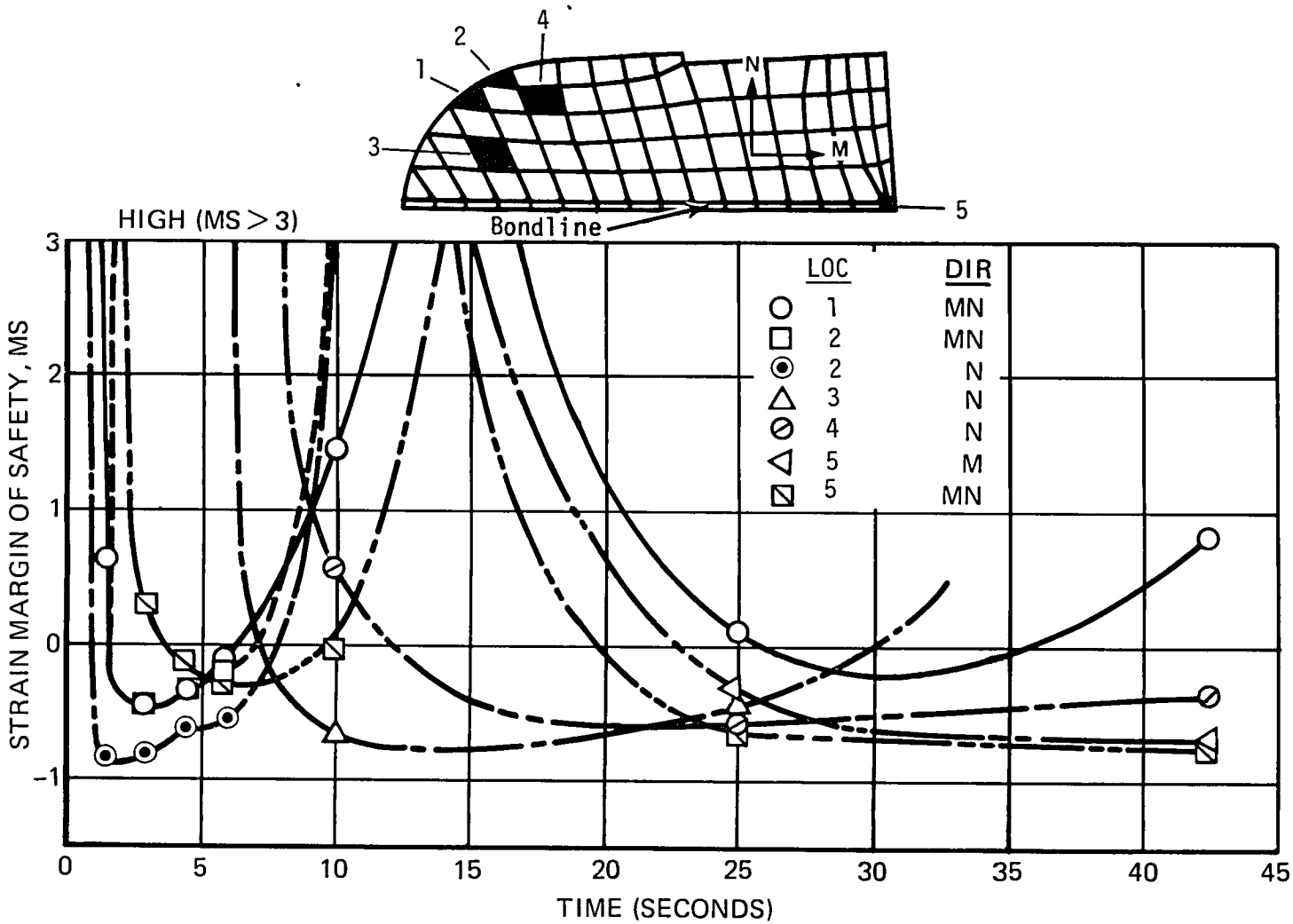

Figure 11. Strain Margins for Carbon Phenolic Overwrap Material (Configuration 1)

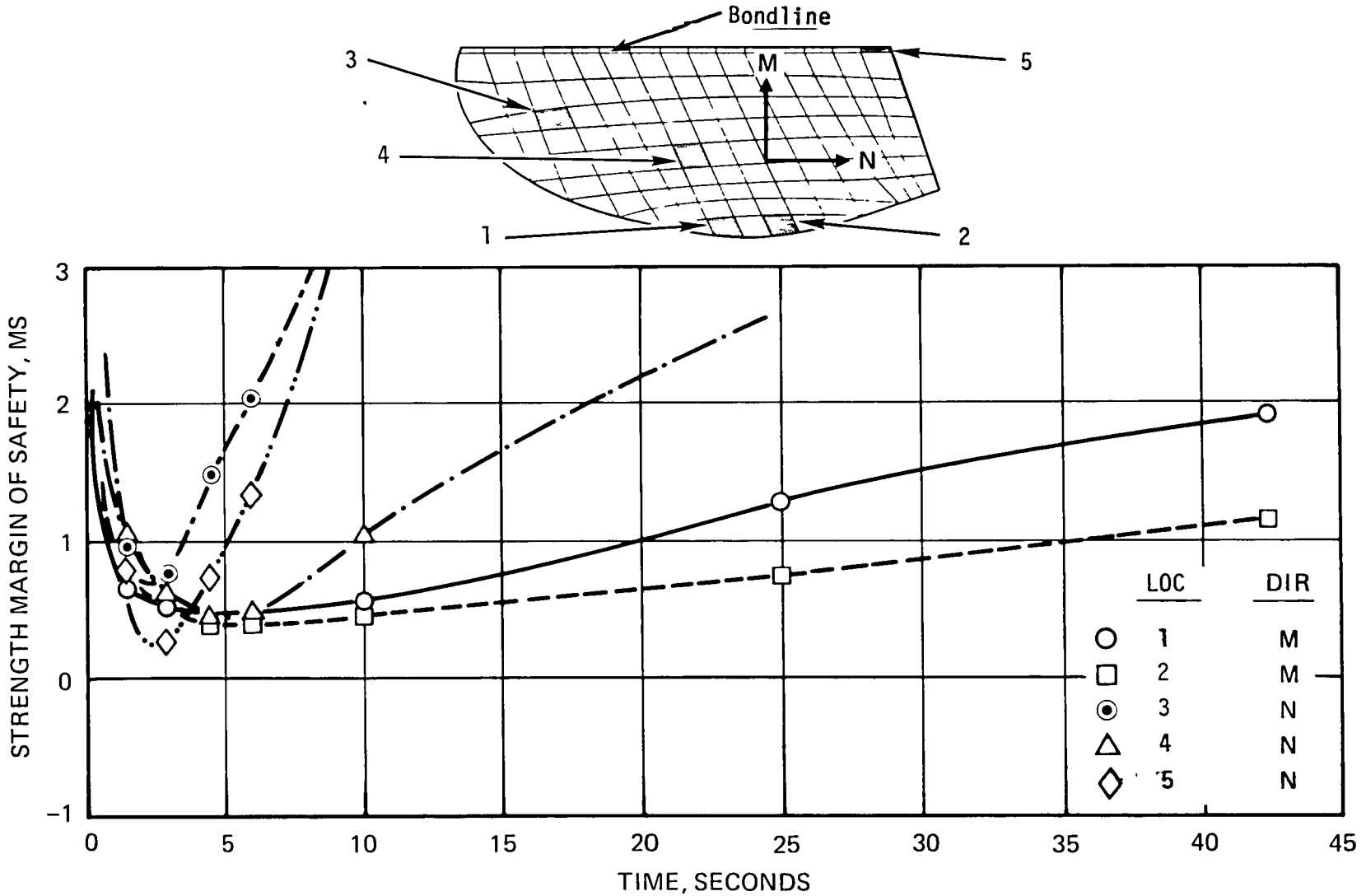

Figure 12. Strain Margins for G-90 Material
(Configuration 1)

of the strength calculations it was concluded that a very local chipping of the corner might be observed upon post-test inspection; however, this was not considered a significant compromise of the overall structural integrity of the insert.

A second local shear problem of the G-90 was predicted to possibly occur at the throat early in the firing due to shear stresses acting in the radial-circumferential plane. The shear stresses are due to the large unbalance between the high circumferential compressive stresses and the small radial compressive stresses. Post-test observations were suggested to investigate the problem, which would be evidenced by flaking off of trough-like chips, elongated in the axial direction. However, it was believed possible that subsequent erosion could obscure most of the actual damage which might occur.

Aside from the two potential local shear problems in the G-90 insert, no serious thermostructural problems were detected by the baseline analysis. Using nominal allowables, the minimum margin in the interior of the insert was 0.46 in the axial (N) direction at 4.5 seconds (see location 4, Figure 12). Also, no problems were indicated in the interior of the forward carbon phenolic materials, or anywhere in the exit cone, although the usual local delamination of exit cone surface material was predicted.

The procedure used in the material property sensitivity study was to run several cases to bound the response of the nozzle when off-nominal thermomechanical constitutive properties were input for the G-90 and carbon phenolic materials. Variations in allowables did not require running additional cases because the linear analyses contemplated permitted modifying the margins calculated from baseline allowables using the simple formula

$$MS_o = \frac{A}{A_o} \quad (MS + 1) - 1$$

where MS_o and MS are the original and revised margins of safety, and A_o and A are the original and revised allowables, respectively. Thus the effects of altering the allowables can be readily and accurately determined after performing the analyses.

Table 1 briefly defines the bounds selected for modulus and thermal expansion of the G-90 and carbon phenolic materials. In establishing cases to be run, the adopted rationale, based on observation of a variety of similar materials, was that properties of carbon phenolic materials tend to vary independently, while those of graphite usually do not. With graphite it was believed, for instance, that a particular billet having an upper bound strain-to-failure will also usually show higher than normal thermal expansion. (This assumption, as will later be seen, is not always true.) The three cases selected for analysis focus primarily on three different heating rate effects on thermal expansion for the carbon phenolic material. Figure 13 displays the differences between the coefficient of thermal expansion curves for the three cases.

Before discussing the results obtained, it is to be noted that two additional supplementary analyses, the bilinear analysis and the degraded bondline analysis, were also conducted. The former is self-explanatory and was accomplished using an existing option of the SAAS III code; the latter was performed by introducing degraded material characteristics (incapable of transmitting shear and normal tension) into the finite elements located at the forward and aft regions of the G-90/carbon phenolic overwrap interface. Degradation of the type considered could result from excessive shear stress along the bond, tensile stress normal to the bond, or temperatures in excess of approximately 540°C (1000°F). All of the supplementary analyses were conducted for a time of 4.5 seconds.

A comparison of results from all supplementary analyses with those of the baseline analysis is presented for selected critical

Table 1. Material Property Sensitivity Study
Material Variations Considered

Property	G-90	Carbon Phenolic
Modulus	E $\pm$ 13.1%	E $\pm$ 10%
Coefficient of Thermal Expansion	$\alpha \pm$ 10%	High Heating Rate (Baseline) Low Heating Rate Altered High Heating Rate

Cases Chosen

Case	G-90	Carbon Phenolic	Comments
1	E - 13.1% α + 10%	E + 10% α Baseline	High thermal expansion, large G-90 deformation
2	E + 13.1% α - 10%	E Baseline α Low Heating Rate	Low thermal expansion, small G-90 deformation
3	E - 13.1% α + 10%	E + 10% α Altered High Heating Rate	Same as Case 1 except for some high temperature expansion in carbon phenolic

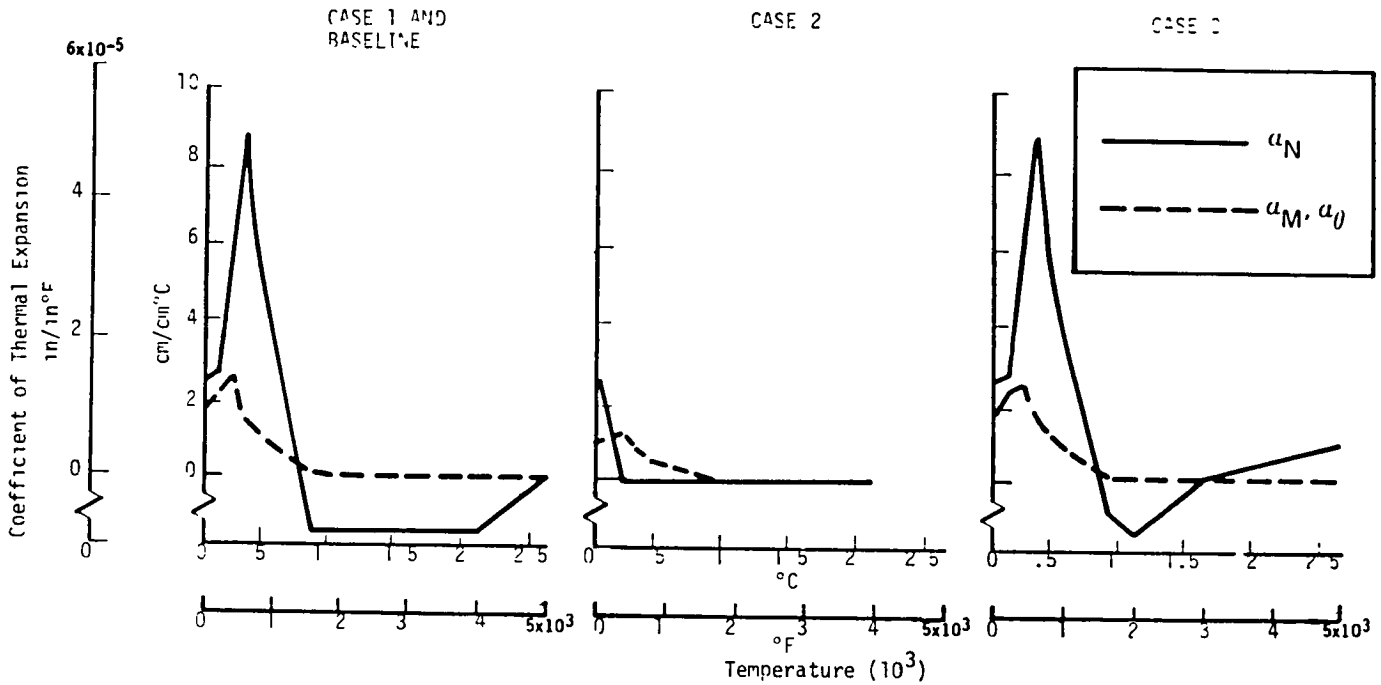

Figure 13. Carbon Phenolic Thermal Expansion (Material Property Sensitivity Study)

G-90 elements in the bar chart of Figure 14. The key for understanding the chart is given above the first critical element and direction listed (92-M). The surface elements, 92 and 124 (Figure 12), are both critical in the M (radial) direction, and are linked to the potential throat shear problem mentioned earlier. These elements are unusual in that, due to a Poisson coupling effect, they experience radial tensile strain under radial compressive stress. Results for the interior elements indicate that the margins for the N (axial) direction are always critical, and that for the adjacent elements 88 and 104, the Case 1 properties produce the lowest margin (0.31 using nominal allowables). For element 153, the bilinear elastic analysis provides the lowest margin. Additional data will be presented later for comparison of results for various cases run.

Static Firing. - The first development (D-1) firing of the Antares III motor was conducted on 27 April 1978. During the firing all test objectives were met and the motor's chamber pressure and thrust time traces were close to those predicted. On removal of the nozzle assembly from the motor, however, it was evident that the G-90 graphite throat insert had failed to survive the test intact. Subsequent detailed examination revealed that two cracks had developed in the plane normal to the motor axis just forward of the throat. Each crack encompassed approximately 180-deg. circumferentially, overlapping slightly at the ends, and extended from the insert ID to OD. Microscopic examination of the fracture surface indicated a tensile failure in the axial direction and that the failure had occurred relatively early in the firing. Figure 15 shows a cross-section of the nozzle prior to complete disassembly and a view of the crack overlap region. The wide separation of the crack surfaces and the rounding of the edges also indicates that failure occurred early in the firing.

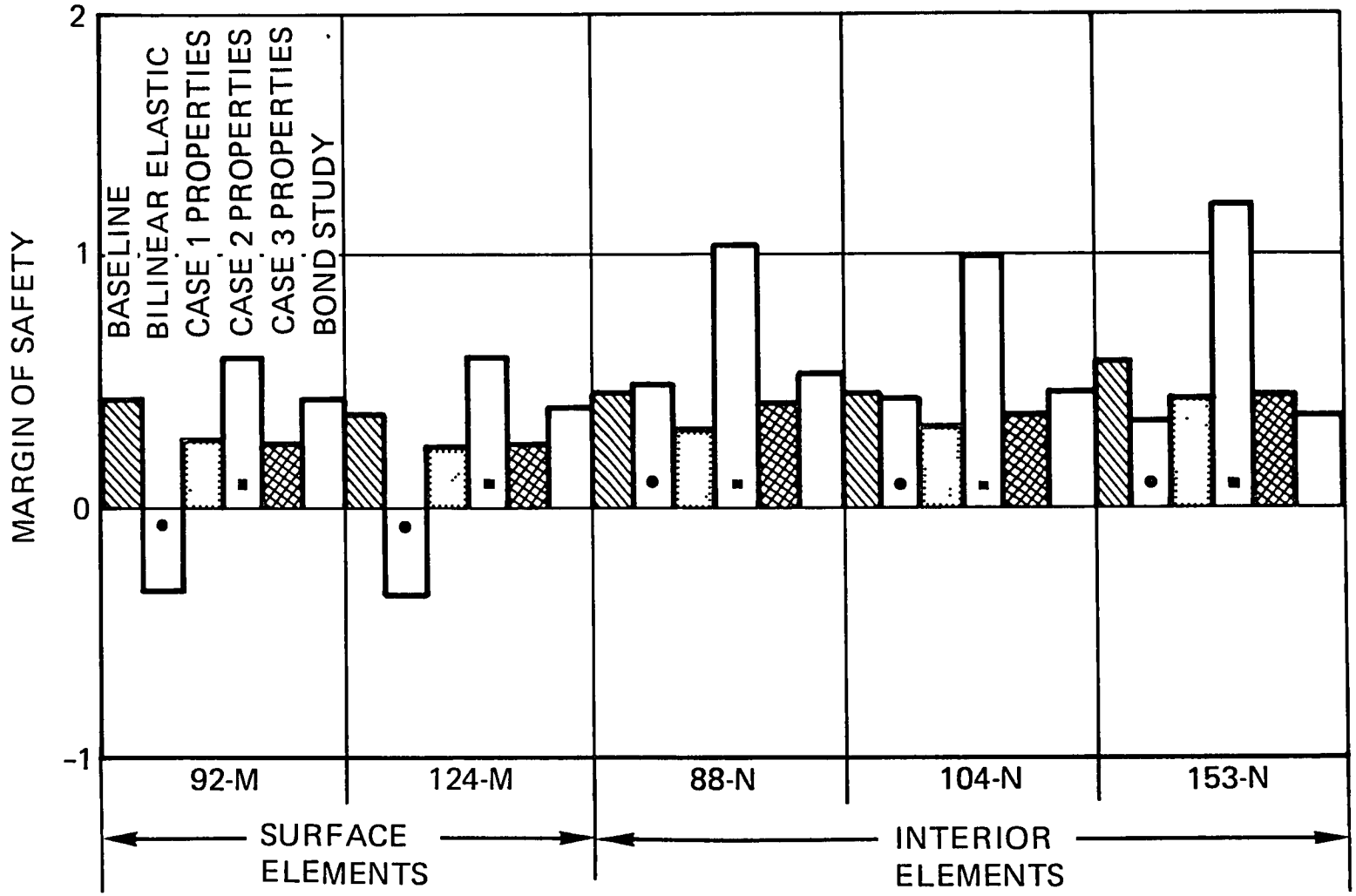

Figure 14. Strain Margin Summary for Various Cases at 4.5 Seconds (G-90 Graphite)

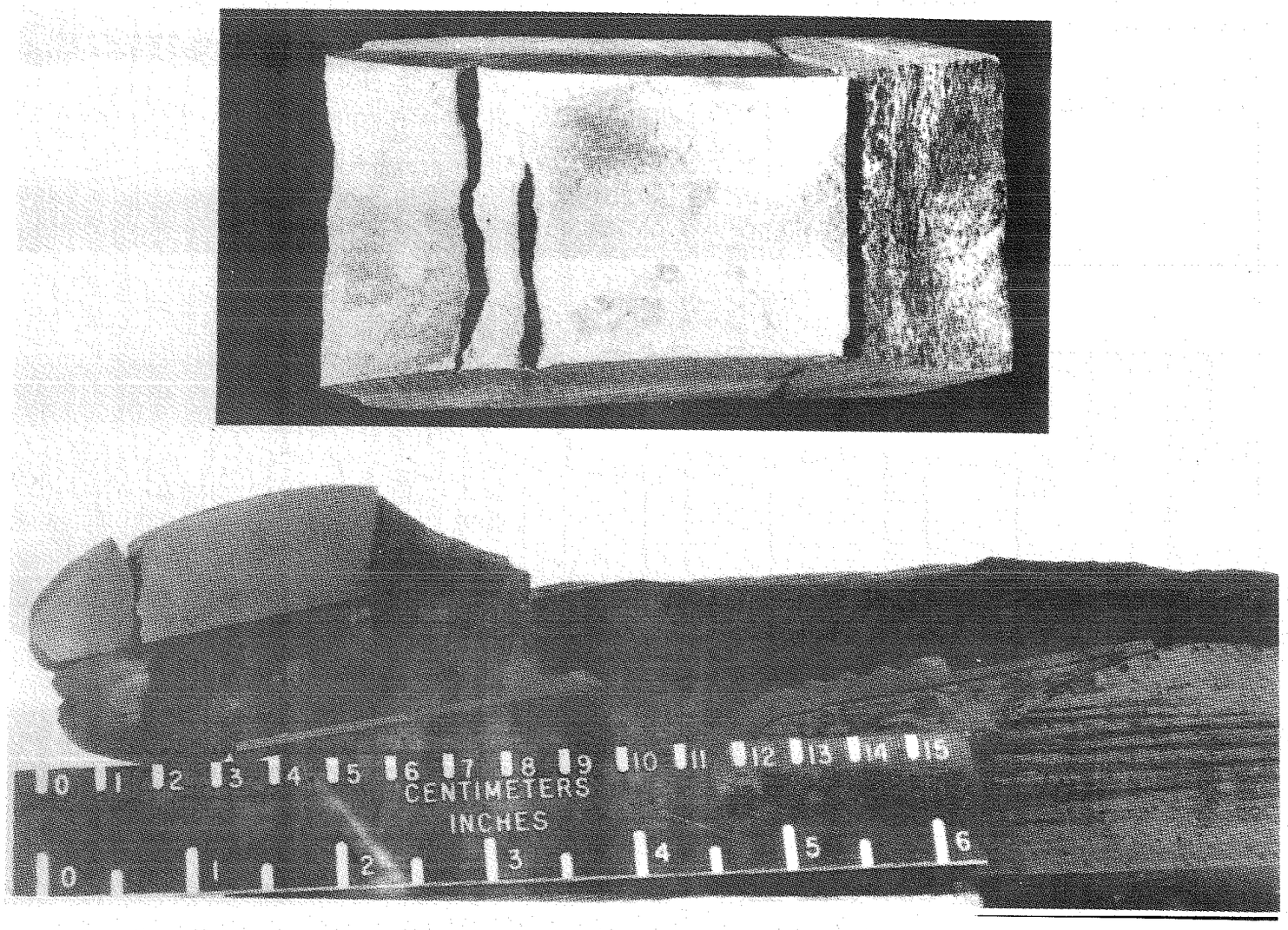

Figure 15. Post-Firing Views of D-1 Nozzle

The eroded surface profile was quite similar to that predicted; measured throat recession was 0.597 cm (0.235 in) compared to 0.612 cm (0.241 in) predicted. Also, the increased recession predicted forward of the throat was evident. Both the exposed carbon phenolic overwrap and dixie cup insulator regions evidenced large erosion depths. In particular, the large aft-facing step developed as predicted. Exit cone erosion was overpredicted, as expected, due to the assumption of chemical equilibrium.

Post-Test Design Modification Studies

After the failure of the G-90 throat insert, it became necessary to explore whether certain configuration changes might alleviate the axial strain. At the same time, it was decided to investigate whether the current lots of G-90 graphite were providing material properties consistent with those used in the analyses. Thus a two-pronged effort was initiated.

To examine the effects of possible design changes various cases, shown in Table 2, were identified. Basically, the analyses were to determine the effect of the titanium housing length (Cases A and B), the G-90 thickness (Cases E1 and E2), and the G-90 length (Cases C and D). A case was also added (Case F) to determine whether massive degradation of the forward portion of the carbon phenolic overwrap material might be the cause of the cracking of the insert. (The results for this case proved negative). By making alterations in the basic finite element model, all of the above analyses - including thermal analyses where required - were accomplished. Design changes which yielded positive results were to shorten the titanium housing, thicken the G-90 insert, and use a split G-90 insert (Cases A, E2 and C). Shortening the G-90 insert (Case D) improved the strain margins in some areas but worsened them in others. By far the biggest single improvement in axial margin of safety (52% in-

Table 2. Antares Redesign Studies
Matrix of Cases Analyzed

Case	Times Analyzed (sec) 4.5	10.0	25.0	New Thermal Analysis
A - Shorter Ti	x	x	x	
E1 - Thinner G-90	x			
B - Longer Ti	x	x	x	
E2 - Thicker G-90	x			x
C - Split G-90	x			
F - Degraded Carbon Phenolic		x	x	
D - Shorter G-90	x			x

crease) occurred with the split insert, Case C. This result is not only interesting, but an intuitively obvious solution, i.e. pre-split the insert to preclude cracking under thermal stress.

The material property investigation proved enlightening also. Results from a variety of tests, Reference 21, conducted at Vought and SoRI indicated that current lots of G-90 were yielding free thermal expansion data approximately 30% higher than that used in the analysis, while the strain-to-failure data were approximately 30% lower. This combination of results, as noted earlier, was contrary to what had been expected. The changes in properties for the most recent material appear to be due to processing modifications which eliminate the coarse-grained, highly cracked microstructure typical of early 1970 vintage G-90. Figures 16 and 17 show the comparison of thermal expansion and strain-to-failure data used in the baseline analysis versus that from the recent tests. Log 1072 noted in both figures is the material used for the particular G-90 insert which cracked in the D-1 firing. In Figure 17 the solid line defines the nominal allowable strain curve (drawn through the data from Reference 9) which was used for the Configuration 1 baseline analysis. The parallel dashed line represents the revised allowable curve which is based on room temperature tests conducted on log 1072 material at Vought and SoRI.

To examine the impact of the newly acquired data on the original analytical predictions, the linear analysis was repeated for Configuration 1 at the 4.5 second time point. Results for this case indicated a strain margin of safety of -16.1% in the N (axial) direction for interior element 88. The trajectory of axial mechanical strain for element 88 is shown in Figure 17, and failure is predicted for all points on the trajectory which exceed the revised allowable strain. Hence, given realistic property data, the analysis indeed predicted failure at the correct

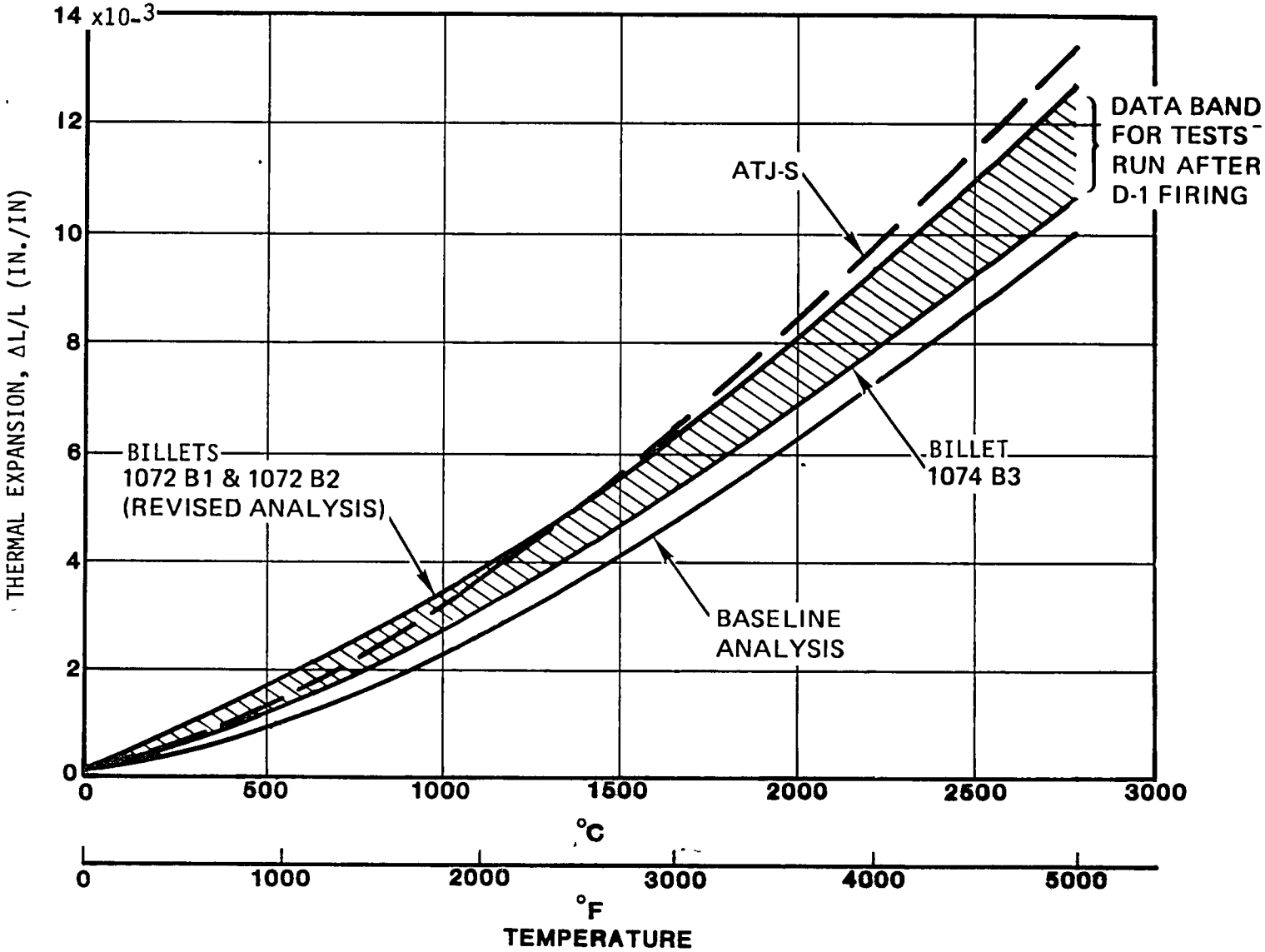

Figure 16. G-90 With-Grain (Axial) Thermal Expansion

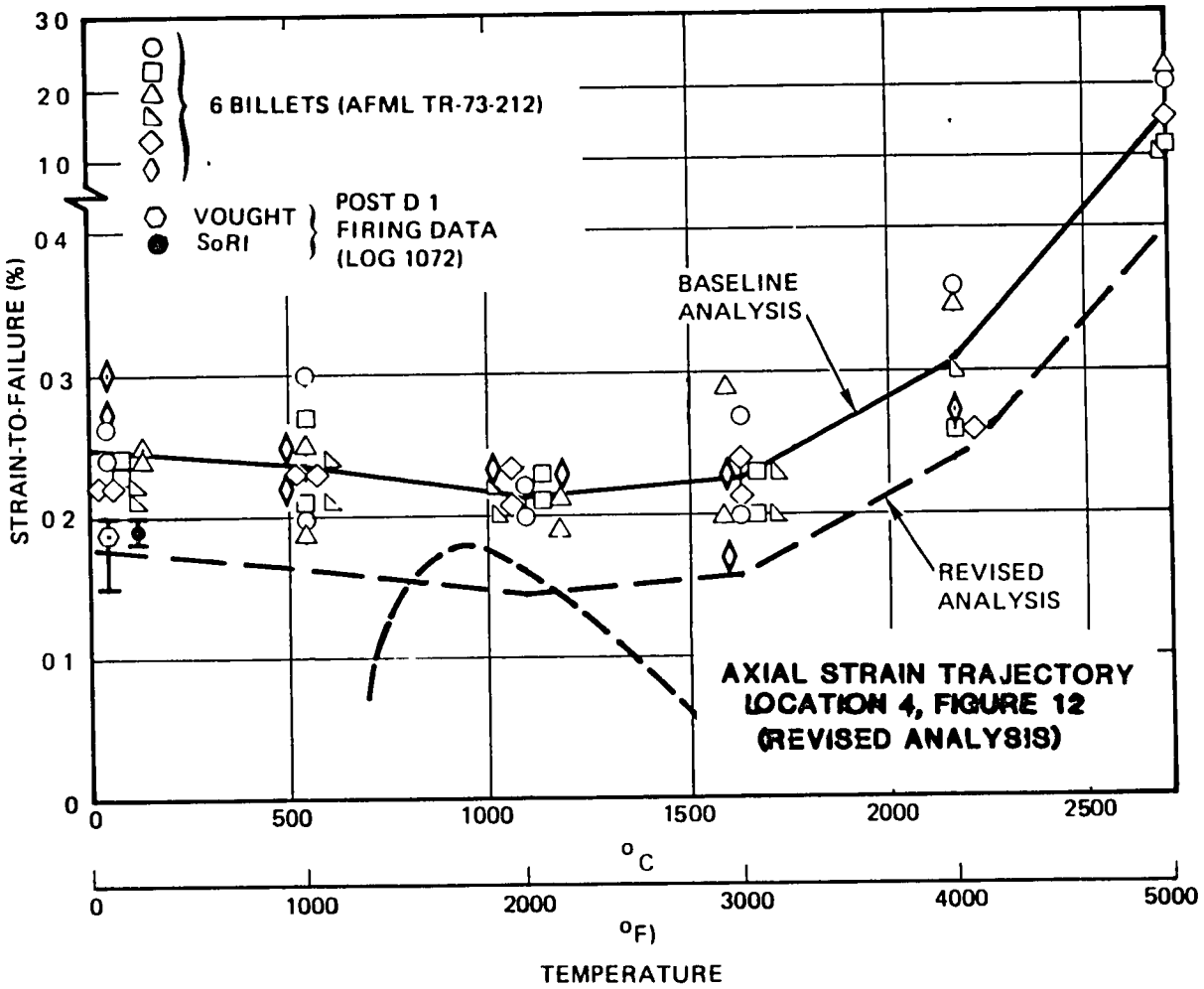

Figure 17. G-90 With-Grain (Axial) Strain-to-Failure Data

location and direction. A comparison of results predicted for all analyses conducted at 4.5 seconds is made in Table 3.

Given the disappointing property data for the available G-90 material, and the limited benefits derivable from configuration changes, the decision was made to seek an improved graphite which could overcome the deficiencies of G-90 for the Antares III nozzle. Graphites which were immediately considered were 994 and ATJ-S. Issues which surfaced for these replacement graphites were availability in the size required, 7.75 cm long x 16.3 cm diam. (3.05 in x 6.4 in), and quality assurance in terms of minimum properties acceptable for use in the Antares III nozzle. For protection against a large schedule slippage which might occur in the event the search for an improved graphite was unsuccessful, it was decided that a backup alternate design would also be examined on a low-level effort. The carbon-carbon generic class of materials was chosen for the backup design. It was felt that the somewhat higher cost of carbon-carbon could be justified by eliminating both the graphite insert and the carbon phenolic dixie cup, i.e., employing the concept of a carbon-carbon integral throat entrance (ITE). Still, however, this concept required the carbon-carbon selected to be low-cost in order to be competitive with the improved graphite design concept.

Improved Graphite Design

During the search for an improved graphite it became clear that many of the special high-strain graphites developed several years ago for aerospace applications, particularly 994 and some of the advanced Navy graphites, were no longer commercially available. Even ATJ-S graphite was no longer in production. However, Union Carbide Corporation believed they could locate a sufficient stock of ATJ-S for the Antares III program and if this were not the case, they were willing to resume production

Table 3. Strain Margin Summary for Various Cases at 4.5 Seconds

Matl	El.	Dir.	Location	Strain Margin						
				Linear (Baseline)	Bilinear Elastic	Case 1 Props.	Case 2 Props.	Case 3 Props.	Bond Study	Revised G-90 Props.
Carbon Phenolic Overwrap	2	M	Surface and Subsurface	0.302	0.283	0.208	0.504	0.185	**	+0.005
	61	M		0.987	0.102	1.018	High	2.862	0.742	+1.169
	20	N		-0.732	-0.771	-0.732	High	-0.728	-0.782	-0.715
	1			0.338	0.334	0.264	0.588	0.265	0.283	+0.044
	2			0.179	0.172	0.121	0.489	0.205	**	-0.060
	2	MN		0.132	-0.009	0.119	0.166	-0.172	**	-0.105
	31	MN		-0.334	-0.367	-0.313	High	0.344	-0.500	-0.276
	45	MN		-0.339	-0.395	-0.325	High	0.209	0.211	-0.302
	219	MN	Aft Corner, Interior	-0.213	-0.640	-0.234	0.391	-0.246	**	0.000
Carbon Phenolic Dixie Cup	253	M	Surface and Subsurface	High	-0.002	High	High	High	0.778	High
	269	M		-0.351	0.313	0.348	High	1.901	0.175	+0.337
	326	N		-0.828	-0.856	-0.828	2.747	-0.788	-0.852	-0.829
	327	N		-0.865	-0.880	-0.865	2.225	-0.203	-0.875	-0.866
	254	MN		0.156	-0.261	0.160	High	0.515	-0.417	+0.155
	269	MN		-0.373	-0.292	-0.368	High	High	-0.398	-0.374
G-90 Graphite	92	M	Surface	0.431	-0.327	0.289	0.611	0.279	0.437	+0.045
	124	M		0.397	-0.348	0.261	0.611	0.259	0.419	+0.019
	88	N	Interior	0.463	0.502	0.313	1.071	0.415	0.534	-0.161
	104	N		0.473	0.440	0.323	1.051	0.388	0.468	-0.154
	153	N		0.591	0.362	0.440	1.234	0.474	0.376	-0.130

** Margin not calculated for this element in bondline study

for a special order. Therefore ATJ-S graphite was selected as a replacement material for the G-90 throat insert. In order to gauge the quality of material subject to purchase, the Vought Corporation laid down certain material requirements which could be readily checked by simple room temperature tests. Vought established that subsequent analyses of the ATJ-S material would be based on lower bound allowables, and therefore, the material purchased for the insert should also be expected to meet reasonably conservative standards. Among the criteria used to determine whether the quality of material was acceptable were: (1) the room temperature minimum batch or sample average tensile strengths in the across-grain (AG) and with-grain (WG) directions must be at least 2.85×10^6 Pa (4100 psi) and 3.27×10^6 Pa (4700 psi), respectively, and (2) the minimum AG and WG tensile strengths from any given sample or batch must be at least 2.78×10^6 Pa (4000 psi) and 3.2×10^6 Pa (4600 psi), respectively. For all analyses which were to be conducted, it was established that the thermal conductivities, elastic moduli, and Poisson's ratios would be based on nominal data, while thermal expansion would be based on $+1\sigma$ data, and all allowables would be based on -2σ data. The major sources of data were Reference 22 for constitutive properties, and Reference 23 and 24 for allowables.

In addition to making a change in the throat insert, the original design configuration was modified slightly to accommodate the split throat insert which was predicted to perform well in the finite element design modification study. Configuration 2 (see Figure 2) defines the revised geometry.

The thermostructural analysis of the ATJ-S nozzle design required special treatment because of the split insert. At the split interface, it was necessary to enforce the requirements that no axial tension could occur, and that a nonzero shear stress could only occur in regions where the axial stress was compressive.

These requirements made it necessary to perform iterative analyses at each time point, although a linear analysis was used for each iteration.

Figure 18 shows the strain margin of safety histories obtained for several critical elements of the ATJ-S insert. The partially darkened symbols represent the critical axial strain elements for the interior of each portion of the insert, and the minimum margin is 0.98, obtained for element 80 at 6 seconds. This is marked improvement compared to the axial strain margin for the G-90. The forward portion of the insert is also seen to experience a low radial strain margin for the surface material near the throat. Local shear problems are also evident along the forward portion of the horizontal bondline (element 17), and at the aft boundary near the outer diameter (element 270), where the margins of safety are negative (-0.19 and -0.05, respectively). The shear strength margins were not negative at these locations, but only slightly positive (0.01 and 0.11, respectively). It was concluded from the analysis that the ATJ-S design substantially alleviated the interior axial strain problem, but had little effect on the surface and corner problems evidenced by the G-90 insert design.

Carbon-Carbon Design

The selection of the carbon-carbon class of materials for the backup design left considerable latitude for the choice of constituent materials, weave geometry, and fabrication process to be employed. For the Antares III application, however, it was evident that virtually any reasonable carbon-carbon material design would dramatically outperform the graphite materials thermostructurally. This has been demonstrated on a wide variety of government programs. To the authors' knowledge, no carbon-carbon ITE has ever failed in a nozzle firing. The concern at

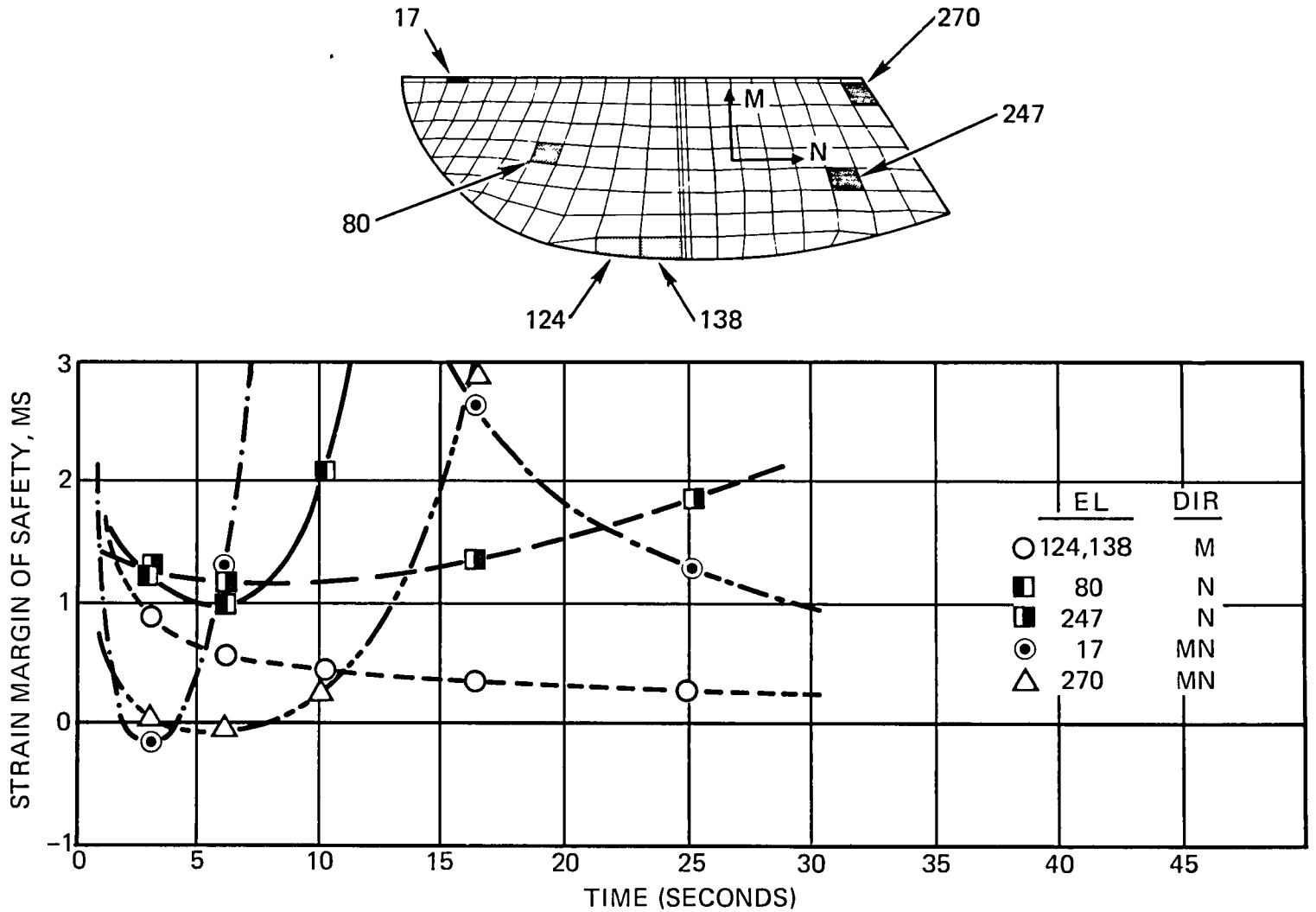

Figure 18. Strain Margins for ATJ-S Insert

this point in the program, therefore, was not whether the carbon-carbon selected was optimized structurally, but whether it could be produced cheaply and reliably with properties which could be replicated, and whether the materials could be delivered within the requirements of the Antares III schedule.

A particular material design developed under IR&D funding by the Material Sciences Operation of SAI was ideally suited to meet these constraints. The material has a 4D construction, with axial (Z) yarns which are orthogonal to three transverse (U,V,W) yarns oriented at equal angles (120°) with respect to each other. The construction is demonstrated in the plastic model shown in Figure 19. The material is made from pultruded carbon yarns (Hercules HM grade) which are woven into a 4D preform and then put through a low pressure pitch process.

Demonstration of this material in a nozzle firing was considered a necessary prerequisite for its possible use in the Antares III program. At that time a partially processed billet was available in the size required for a firing in the Altair III motor. Testing the material in the Altair III motor was felt to be an ideal demonstration because many G-90 throat inserts have been tested in that motor and a new material's relative performance could be quickly evaluated. Thus it was decided that the SAI billet would be tested after it was fully processed, and that a thermostructural analysis of the 4D carbon-carbon ITE in the Antares III nozzle should be initiated.

In order to conduct the thermostructural analysis it was first necessary to develop a satisfactory data base for the thermal and mechanical properties. To accomplish this end, half of the processed billet was sent to the Southern Research Institute (SoRI) for testing, and thermal and mechanical minimechanics models were developed for prediction of properties analytically.

The analytical models were based on the idealization of the unit cell shown in Figure 20. In both the thermal and mechanical models, the yarn bundles are considered to be transversely isotropic, while the matrix material is isotropic.

The prediction of properties took place before any test results were obtained, and were transmitted to NASA in Reference 25. Subsequent data from SoRI were then used to complement the original predictions and to provide a real basis for all properties to be used in the design analysis. Figure 21 shows the predicted thermal conductivity in the direction normal to the nozzle centerline as a function of temperature, together with the actual data. The analysis predicted isotropic behavior in the transverse plane, but the data showed slightly higher conductivity in directions 30 degrees off-axis from the yarns. In general, however, the predictions were very good, and were not modified in the temperature region where data were available. The same held true for the axial thermal conductivity. As shown in Figure 21, in the higher temperature range, two curves were used - one which would be conservative for thermal response (the analytically predicted curve), and one which would be conservative for structural response (extrapolation of the test data).

For the thermomechanical properties the correlation was reasonably good, but in most cases the available data required that some adjustment be made from the original predictions. In general, however, the relative shapes of the curves (the temperature-dependence effects) were based on the original predictions. Properties actually used in the analysis are presented in Reference 26, and examples are shown for tensile strain-to-failure and strength in Figure 22.

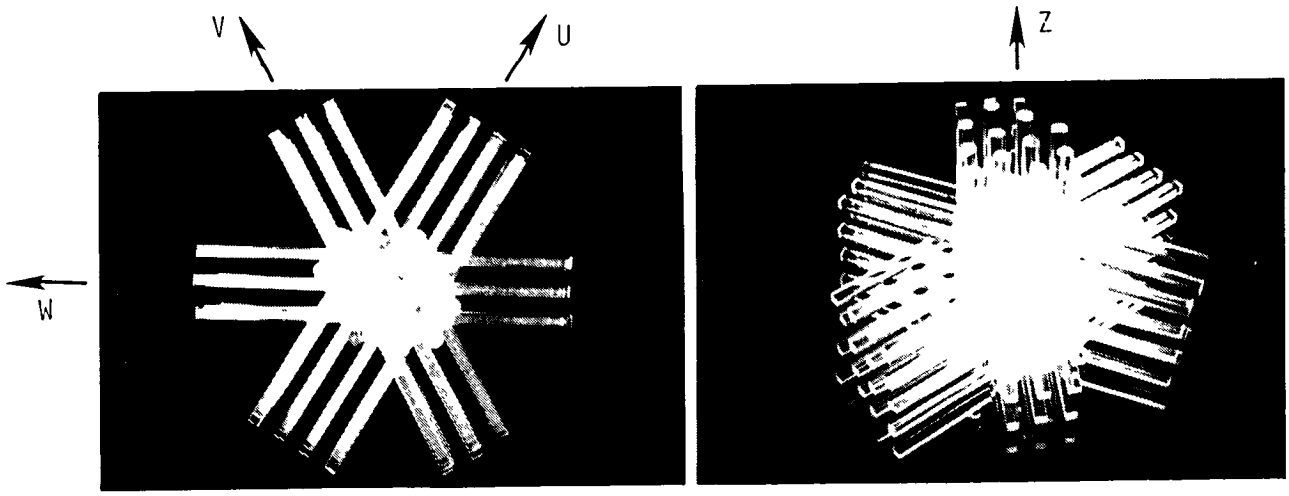

Figure 19. Plastic Model of 4D Construction

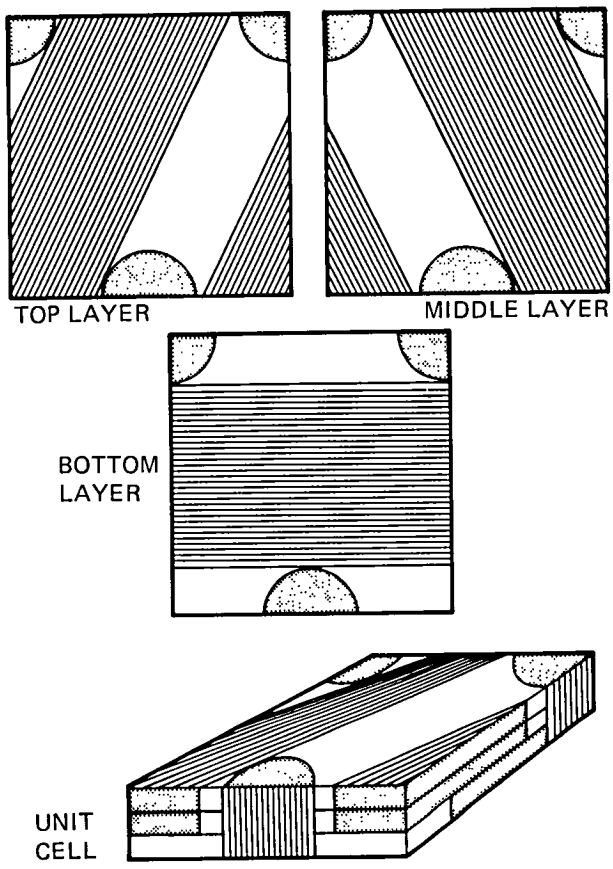

Figure 20. Idealization of 4D Unit Cell

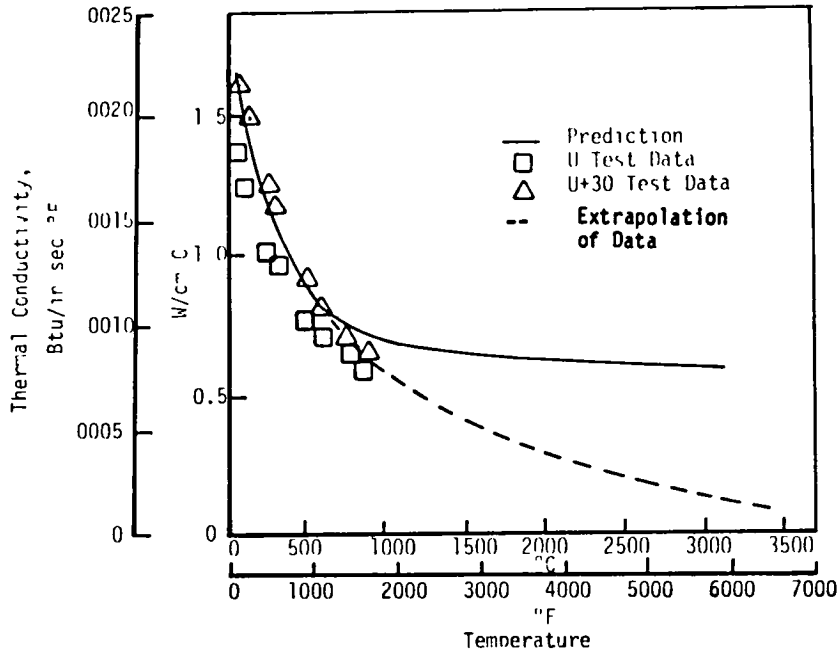

Figure 21. Transverse Thermal Conductivity for 4-D Carbon-Carbon

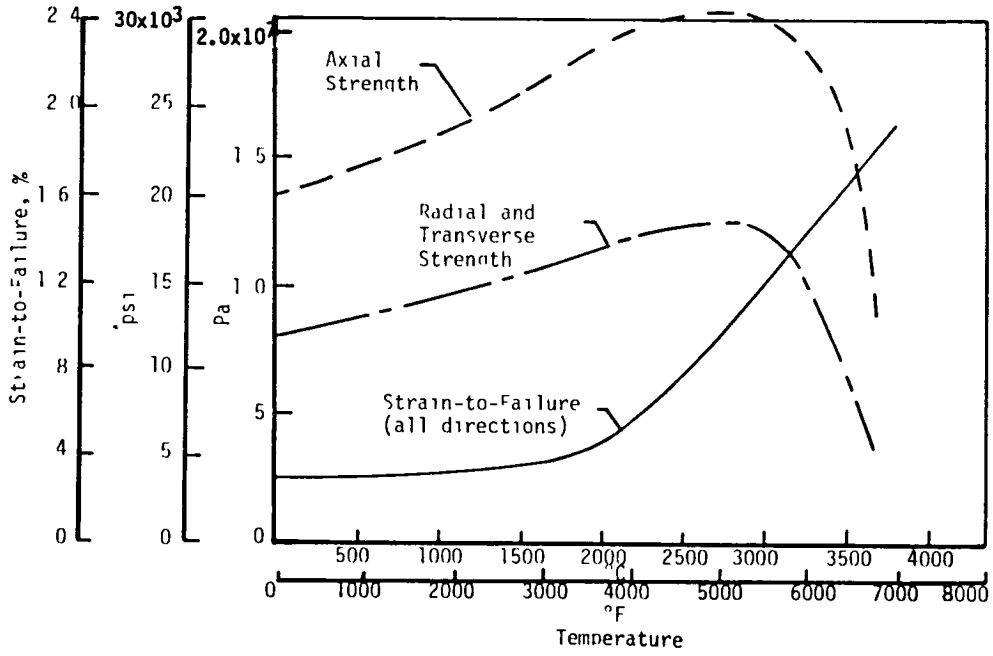

Figure 22. Allowables Used for 4-D Carbon Carbon

The thermostructural analysis was conducted for the Configuration 3 design (Figure 2). Margins obtained for this material were high (greater than 3.0) in most areas, except for two local regions on the carbon-carbon/carbon phenolic overwrap bondline. Figure 23 shows the critical margins calculated from both strain and strength allowables.

The minimum strain margin (2.08 at 6 seconds) occurred at the midlength of the tapered bondline, in the circumferential direction. No axial or radial strain margins were found to be less than 3.0. The strength margin calculations showed a minimum of 0.53 for the same conditions (time, location, direction) given above for the minimum strain margin. The strength margin calculations also predicted a critical axial value of 2.64 at the midlength of the horizontal bondline at 3 seconds. The 0.53 strength margin was not believed to be a reason for concern because it was felt that the 4D material has an intrinsic capability for modulus degradation in the circumferential direction.

A question which did subsequently arise was whether or not the length of tapered interface at the OD surface was sufficient to resist the blowout load caused by nozzle surface pressure. A secondary but related question was whether the bond might sufficiently degrade to allow ITE slippage in the aft direction and allow the aft interface to bear against the charred CP exit cone material. To provide added confidence that these events would not occur, the ITE was reconfigured to Configuration 4 (Figure 2) and the thermostructural analysis was repeated for a degraded bondline at 4, 6, 10 and 42.5 seconds. In this analysis, sufficient iterations were performed to guarantee that the blowout load was resisted only by stresses normal to the OD interface, and not by boundary shear, or by reactions at the aft boundary of the ITE. Results of this extreme analysis case showed that the 2.08 strain margin for the fully bonded ITE had reduced to

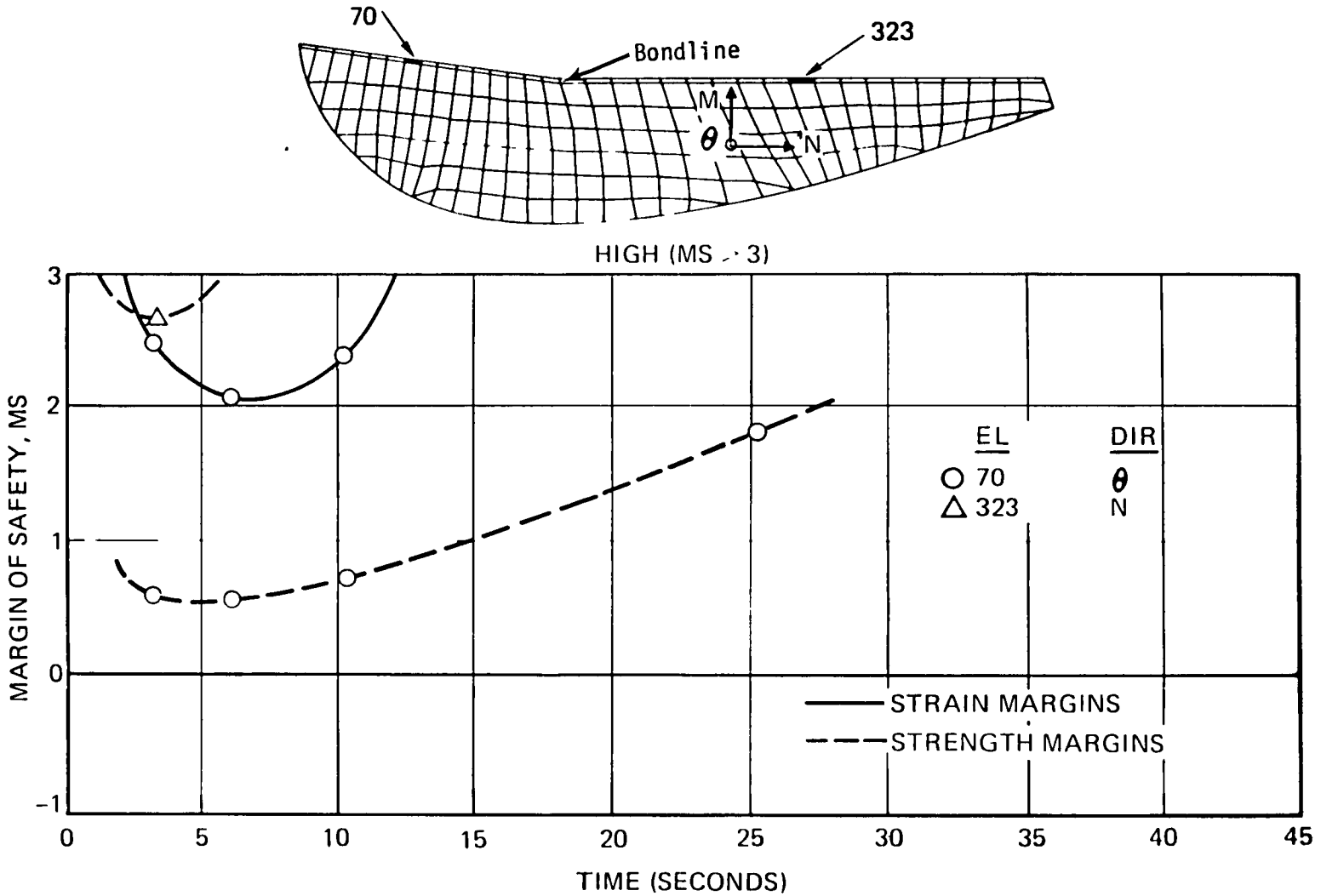

Figure 23. Critical Margins of Safety for 4D Carbon-Carbon Material

1.97. Also, the 0.53 and 2.64 strength margins for the fully bonded ITE changed to 0.52 and 1.20, respectively. The 1.20 margin, which pertained to the axial (Z) direction occurred slightly aft of the corresponding location for the undegraded bond, and at a later time (10 seconds instead of 3 seconds). With regard to the question of the ITE bearing against the charred carbon phenolic material, no problem was indicated; the maximum gap closure was 0.038 cm (0.015 in) at 6 seconds, which still left a gap of 0.089 cm (0.035 in) before contact could occur. On balance, the ITE analysis provided satisfactory results even for the extreme case of a fully degraded bondline.

The predicted response of the carbon-carbon material was also very encouraging from an ablation and erosion standpoint. Figure 24 displays the predicted shape of the nozzle at the end of the ground test firing. The use of a single material to replace the G-90 and dixie cup components is seen to virtually eliminate the aft-facing step which was shown to develop for the original design.

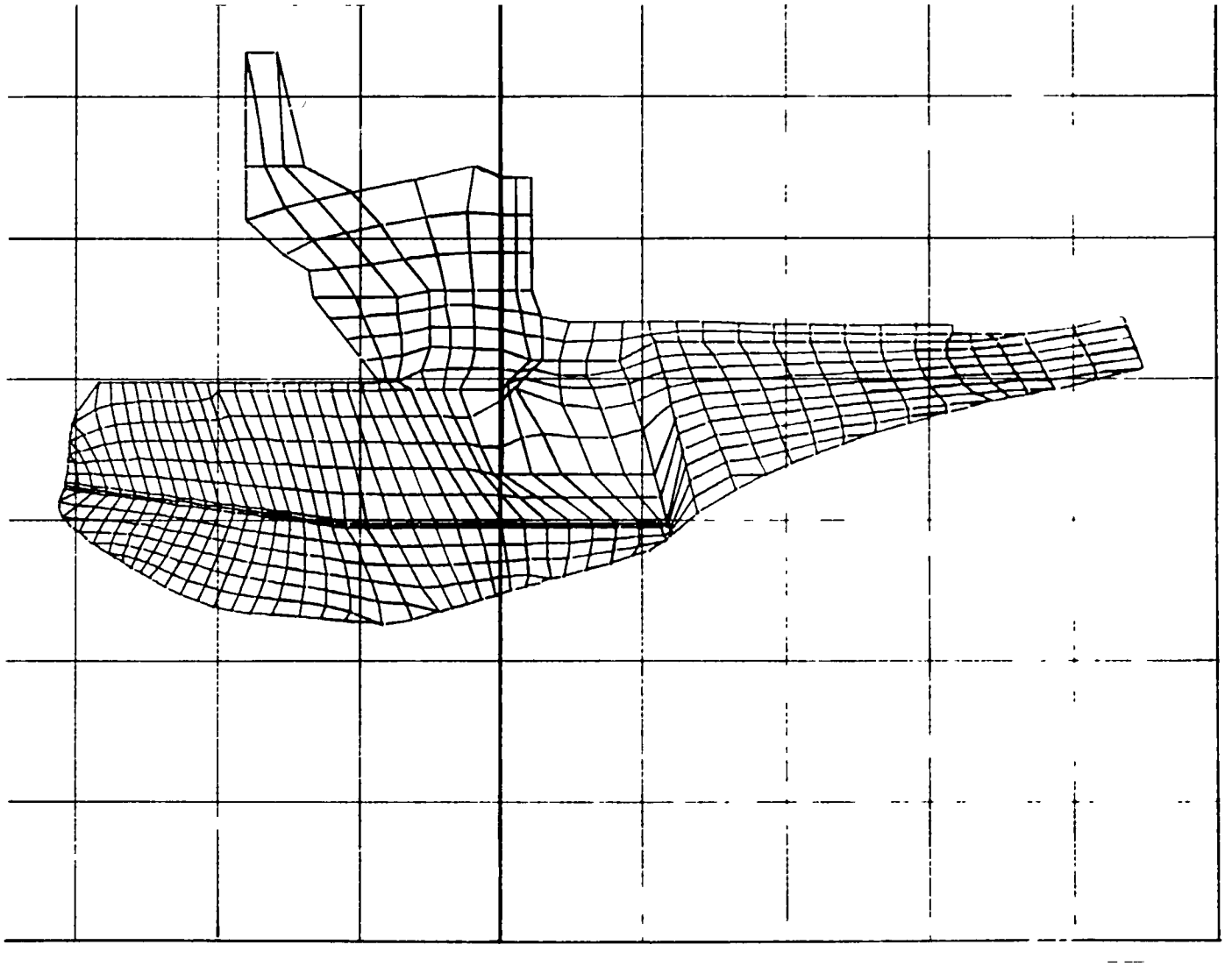

Figure 24. Predicted Recession 42.5 Seconds (Configuration 4)

MATERIAL DEVELOPMENT AND PRODUCTION

Material Description

Conventional multidimensional carbon-carbon composites start with the initial fabrication of an array of reinforcement yarns to form a preform. For carbon-carbon ITE's, the most common technique results in a preform which has rotational symmetry and a polar geometry. There are, however, some preform designs in which the ITE may be machined from a solid block after densification. The common construction feature of all of these preforms is that they contain reinforcement bundles, which are approximately 60% filled with filaments, and empty spaces between these reinforcement bundles. The objective of the densification procedure is to fill the spaces between the filaments in the yarn bundles and the empty "matrix pockets" with a low porosity binder. This is generally accomplished by infiltrating the preform with an organic material, and then decomposing the organic material to leave a carbon residue. The carbon residue is then heated to approximately 2700°C (5000°F) so that a maximum amount of solid state ordering can occur. The carbon residue becomes a high density graphitic material (depending on the impregnant) which fills approximately 30 - 40% of the available void spaces. The exact amount of filling is dependent on the type of impregnant used, the pressure during carbonization, the amount of available surface area, and the achievable density of the solid carbon residue during graphitization. This cycle of filling is repeated until the total void volume in the composite reaches 6 to 10%. A simple calculation quickly shows that the yarn bundles achieve a low porosity much more rapidly than the empty spaces (matrix pockets), Table 4. Therefore, the final 1/3 of the densification process is directed toward filling the still significant void volume outside of the yarn bundle reinforcements.

Table 4. Porosity of a Carbon-Carbon Composite During Densification*

Densification Cycle	Reinforcement Bundles, %	Matrix Pockets, %	Composite %
0	40	100	58
1	28	70	41
2	20	49	29
3	14	34	20
4	10	24	14
5	7	17	10
6	5	12	7

* 30% void filling assumed. Cracking due to differential thermal expansion effects is ignored

A novel technique has been developed at SAI for placing large volumes of fully dense material in the matrix pockets prior to the liquid densification process. In this way, there can be a decrease in the number of densification cycles required to complete the composite fabrication, thus resulting in a decrease in both elasped time and densification costs. In addition, since the later cycles of densification for carbon-carbon composites, due to the highly anisotropic thermal expansion of high performance graphite reinforcements, induces a substantial amount of microstructural damage, this damage may be minimized. The addition of solid materials to the matrix pockets is accomplished by utilizing a preform construction array in which the matrix pockets have congruent sides. The particular geometry utilized for the Antares III material has reinforcements in an axial direction with three reinforcement directions perpendicular and lying in the X, Y plane, Figure 25. Thus the void spaces around each axial yarn form a spiral ladder geometry through which particulate material can flow. In order to enhance the conditions for particulate flow through the preform, the reinforcement material is made of smooth, pultruded rods which contain a sacrificial binder material. Flow and packing in the preform is enhanced by the use of graphitic material which does not contain either needlelike or flakelike particles. The flow is also aided by the use of vibration techniques typically used for powder metallurgy. In this way all the matrix pockets are filled with solid material to the same degree as the reinforcement yarn bundles are with filaments. After driving the sacrificial binder from the pultruded reinforcement rods, the preform contains nearly uniform porosity throughout its entire structure and is ready for conventional densification processing.

A photograph of the first 4-D preform assembled at SAI is shown in Figure 26. It was found that the rigid reinforcement rods

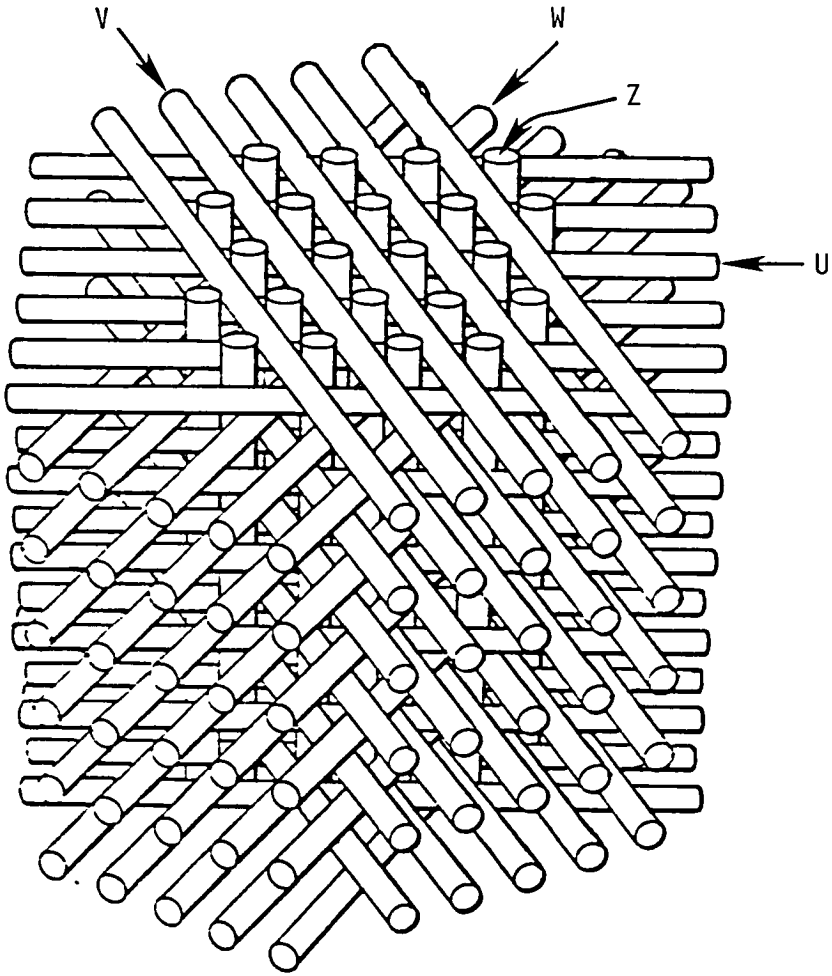

Figure 25. Schematic of the 4-D Reinforcement Geometry

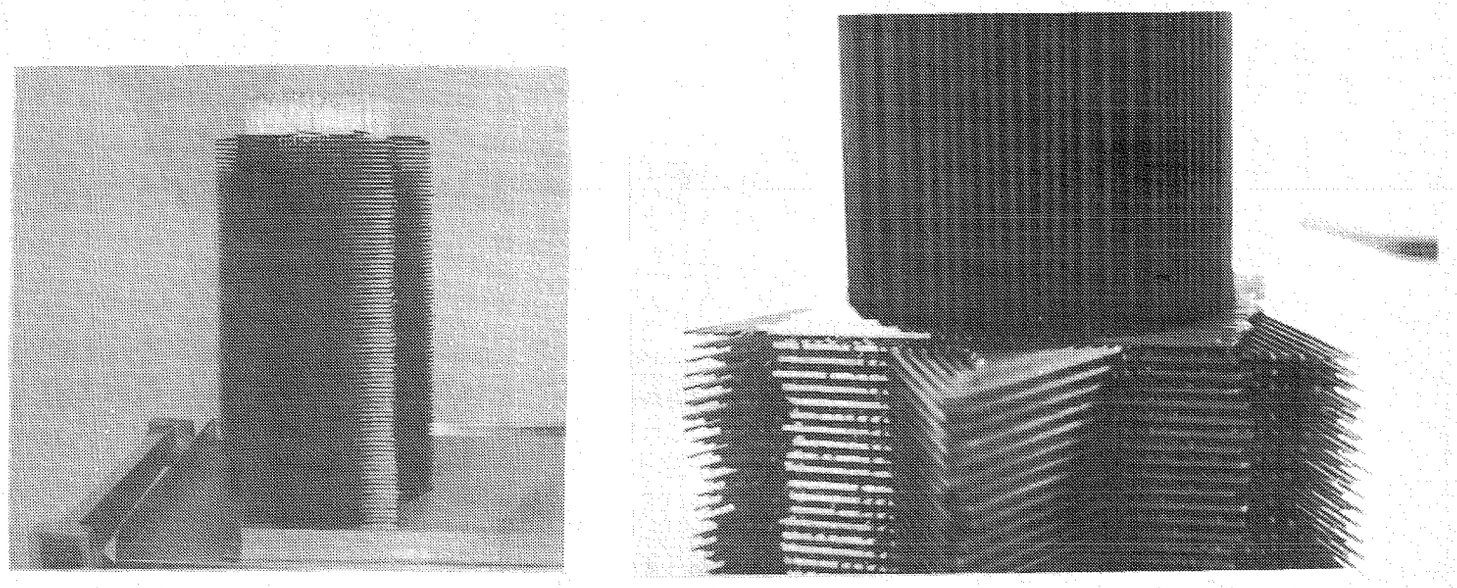

Figure 26. 4-D Carbon-Carbon Preform

were readily handled and therefore could be rapidly assembled. The sacrificial binder also provided protection from damage to the reinforcement bundles since they could not be kinked, bent or frayed to degrade their integrity. Another added benefit found with this straight line construction was that it enabled both easy inspection and rework to be accomplished on the preform. The inspection technique developed for the Antares III program utilizes visible light for preform inspection by examining the preform in a darkened room with a strong light behind it. Any area with missing or misplaced reinforcement rods is clearly shown. The area can then be reworked to eliminate the defect in the reinforcement assembly structure. A photograph of the first preform just prior to installation in its cage, and just prior to powder filling, is shown in Figure 27. Details of the more conventional densification will be discussed in the next section.

Manufacturing Process

Figure 28 presents the manufacturing flow diagram for the Antares III carbon-carbon insert material. The designations below each box specify the relevant documentation controlling the activities/ materials for that box. The Hercules HM yarn, 15V coal tar pitch, and Union Carbide's BB4 powder are received and inspected for specification compliance. The yarn goes to pultrusion, where it is formed into stiffened rods by pulling it through an appropriate sized die after wetting with the sacrificial binder. These rods are subjected to on-line inspection and are cut to the desired length for the weaving operation. The preform is then manually assembled and inspected. After inspection, the preform is placed in a graphite cage preparatory to powder filling (Figure 27). The BB4 powder is screened to the size range of -80 to +325 mesh to provide a proper size distribution for infiltrating the preform. The preform, in its

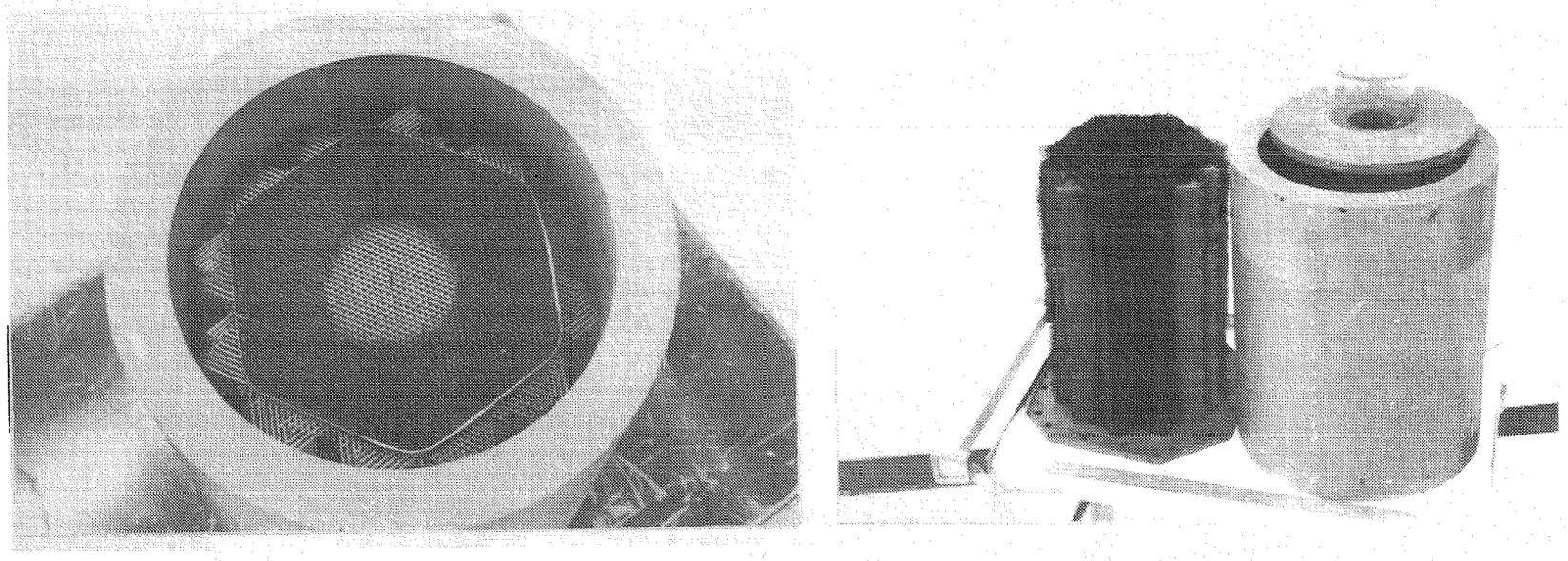

Figure 27. Preform Prepared for Powder Filling

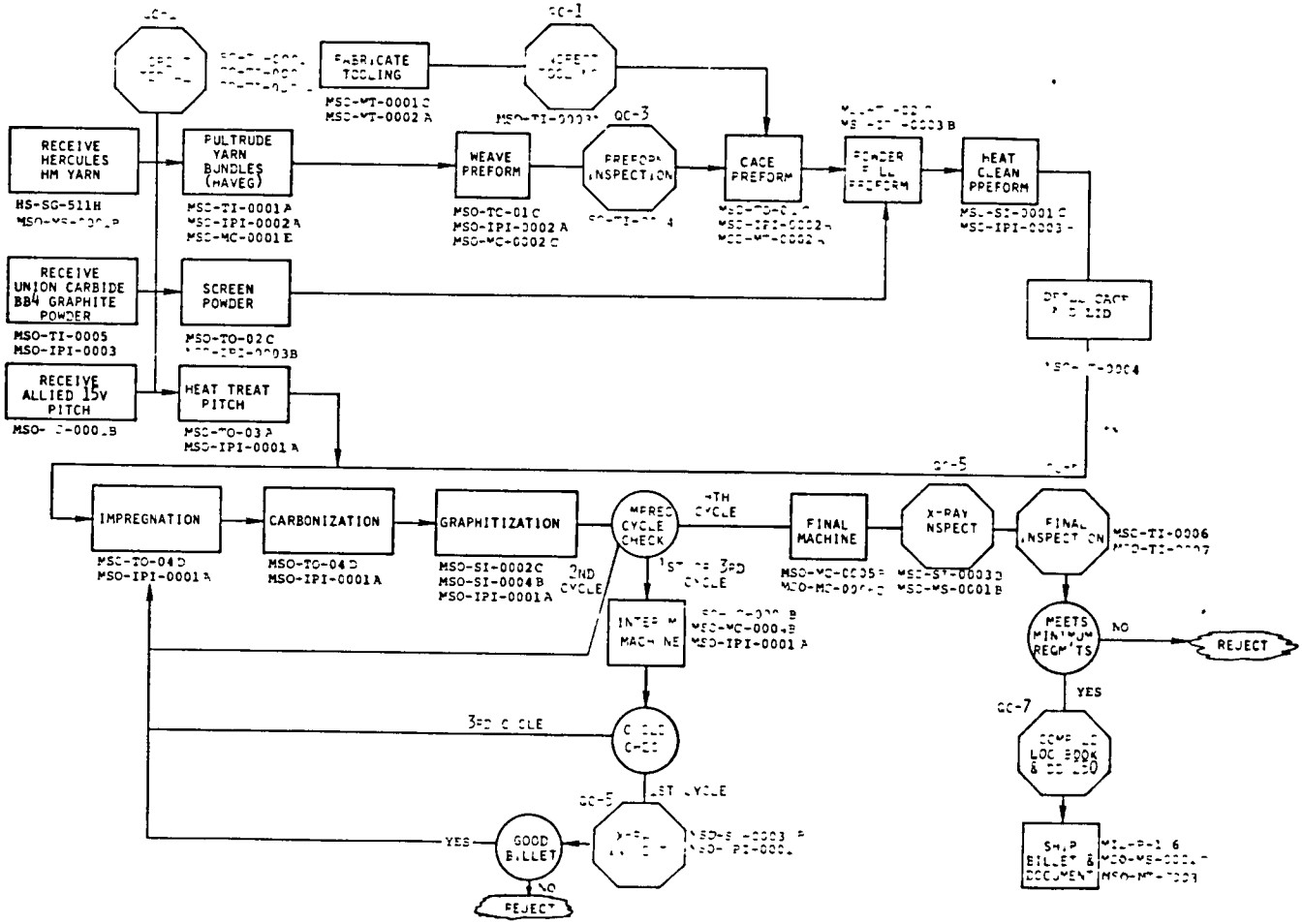

Figure 28. Manufacturing Flow Diagram for Antares III Material

cage, is placed on a vibrating table and filled with this powder. After filling, the assembly is heat cleaned at 900°C in an inert atmosphere to remove the binder from the reinforcement elements.

At this time the caged assembly is placed in an impregnator which is shown schematically in Figure 29. Prior to impregnation, the 15V coal tar pitch is heat treated for about 12 hours at 400°C to polymerize low molecular weight compounds. The purpose of this step is to obtain a uniform char yield material so that barrel-to-barrel and lot-to-lot variability is eliminated. Once impregnated, the assembly is carbonized at 3000 psi in argon to a temperature of 650°C. The next step in the densification cycle is graphitization at 2750°C.

Four cycles of the impregnation, carbonization, and graphitization sequence are used to obtain a density of about 1.83 g/cc. After the first and third cycles, the billet is rough machined to remove any low permeability "skin" on the surface. After the fourth cycle, machining to final dimensions is performed. The final x-ray inspection is then performed in the radial, tangential, and axial directions. Samples are then excised from the end of the billet for either flexure or ring tensile testing. Processing, testing and inspection documentation is assembled and shipped along with the finished part.

Production Results

A total of thirteen logs of material were produced following the above manufacturing plan; one log was rejected after first cycle. These logs were sized to obtain three billets from each, two for nozzle inserts and one for tag end quality assurance testing. Table 5 presents a summary of the logs produced and the intended use for each. Since individual log books were

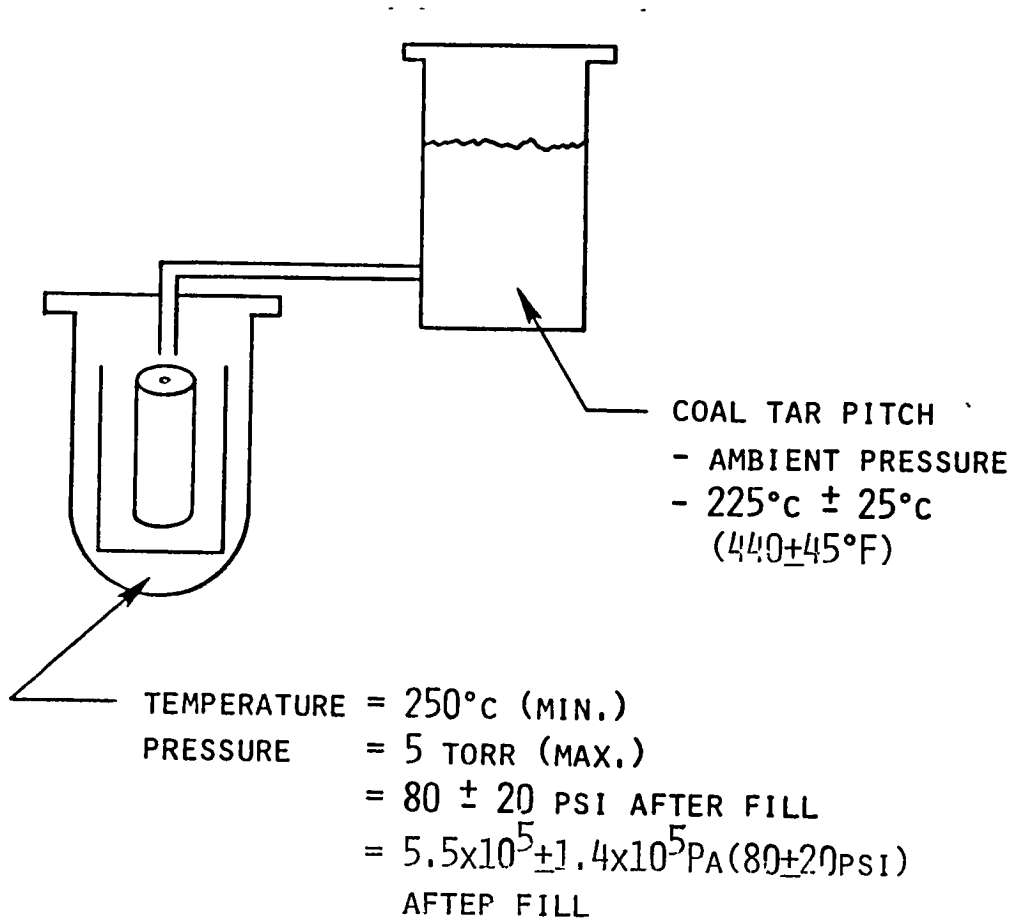

Figure 29. Schematic of Impregnation Setup

Table 5. Logs Produced

Log S/N	Use
103	Development Motors
104	Qualification Motor & Flight Motor
105	Qualification Motors
108	Characterization Testing
109	Flight Motors
119	Rejected After First Cycle
120	Flight Motors
121	Flight Motors
122	Flight Motors
123	Flight Motors
124	Flight Motors
125	Flight Motors
126	Flight Motors
127	Flight Motors

supplied with each billet, the intent here is to supply a summary of and typical results from the production effort.

Raw Materials. - Table 6 presents the raw yarn certification data as supplied by Hercules, Incorporated for the two lots of HM-10000 used in these logs. The two lots are quite comparable. The graphite powder used was Union Carbide, grade BB4. A sample of the powder was heated to 900°C (1650°F) and found to contain 0.356% ash. A second sample was used to measure vibration compaction and achieved a density of 0.96 g/cm^3 (60 lb/ft^3). Both of these values were within the acceptance limits.

Of somewhat more concern was the control on the liquid impregnant, 15V coal tar pitch from Allied Chemical. Material from lot 501 was used for log S/N's 104, 105, 108 and the initial impregnation of S/N 109. Lot 901 was used for all the remaining impregnations for all the logs except a small amount of lot 701 was used for the first impregnation of S/N 122. Table 7 presents the standard control values for these lots in their as-received condition. Data from various sources are presented and, as can be seen, there is a fairly wide scatter in the results.

The benzene and quinolene insolubles are usually taken to be minute carbon particles similar to lamp black. Their significance is that they form nucleation sites for spherule formation during the mesophase transition of the pitch during carbonization. This leads to a finer crystalline microstructure where these particles are present than where they are absent. It turns out that during impregnation, these particles tend to be filtered out by the yarn bundles and are thus concentrated near the free surfaces of the part. Thus, it is not unusual to see a finer matrix phase microstructure near a free surface than in the interior of a part. To date, no one has determined whether this phenomenon has a significant impact upon material properties or

Table 6. Summary of HM-10000 Yarn Certification Data

Lot No.	Tensile Strength, Pax10^9 (psix10^5)	Tensile Modulus, Pax10^{11} (psix10^6)	Denier, kg/mx10^{-4}(lb/inx10^{-6})	Density, g/cm^3 (lb/in^3)	PVA Sizing, (%)	Used in Log S/N
56-7	2.482 (3.60)	3.571 (51.8)	8.044 (45.04)	1.822 (.0658)	.68	104,105,108
133-5	2.254 (3.27)	3.344 (48.5)	8.121 (45.47)	1.830 (.0661)	1.27	109,119,120 121,122,123 124,125,126 127

Table 7. Comparison of Allied 15V Coal Tar Pitch As-Received Data

Lot No.	Specific Gravity, g/cm^3 (lb/ft^3)	Conradson Coke Value, %	Softening Point, °C (°F)	Benzene Insoluble, %	Quinolene Insoluble, %	Ash, %	Data Source
501	___	41.2	92.4 (198.3)	10.6	2.5	___	Allied
501*	___	___	87.5 (189.5)	14.5	2.5	.15	SAI
501**	___	44.0	91.0 (195.8)	22.0	6.8	.14	Y-12
701	1.29 (80.5)	49.5	95.0 (203.0)	15.8	4.5	.13	Allied
701*	___	___	91.1 (196.0)	17.7	4.1	.10	SAI
901	1.30 (81.1)	46.0	94.4 (201.9)	___	5.1	.10	Allied
901***	___	___	___	9.3	4.0	___	SAI

* Average of 3 barrels
** Average of 4 barrels
*** Average of 2 barrels

performance. In fact, because the finer matrix microstructure is confined to near the free surfaces, it is usually removed during machining.

As can be seen in Table 7, there is a fair degree of variability in the as-received 15V pitch. In an attempt to reduce this variability, it was decided to heat treat the pitch at a given temperature for a given time. The idea behind heat treatment is to drive off the lower temperature volatiles. In addition to reducing lot-to-lot and barrel-to-barrel variability, removing these volatiles gives a higher char yield and should increase densification efficiency. Finally, driving these volatiles off initially means less are given off during carbonization in the autoclave which reduces clean-up and turn around time between high pressure runs.

Figure 30 presents thermogravimetric analysis (TGA) data showing the influence of heat treatment time at a temperature of 405 $\pm$ 5°C (760 $\pm$ 10°F). This temperature was selected based upon earlier work. It should be noted that the pitch is stirred continuously after reaching temperature. The cross-hatched region is the condition selected for this program, namely

$$\begin{aligned} T &= 405 \pm 5°C\ (760 \pm 10°F) \\ \text{Time} &= 12 \pm 1\ \text{hr} \\ \text{Char} &= 43 \pm 3\% \end{aligned}$$

Tables 8 and 9 present the influence of heat treatment upon benzene and quinolene insolubles and TGA data, respectively. The fraction of insolubles increases as would be expected; however, the variability does not seem to be markedly reduced. This may be a reflection of data accuracy.

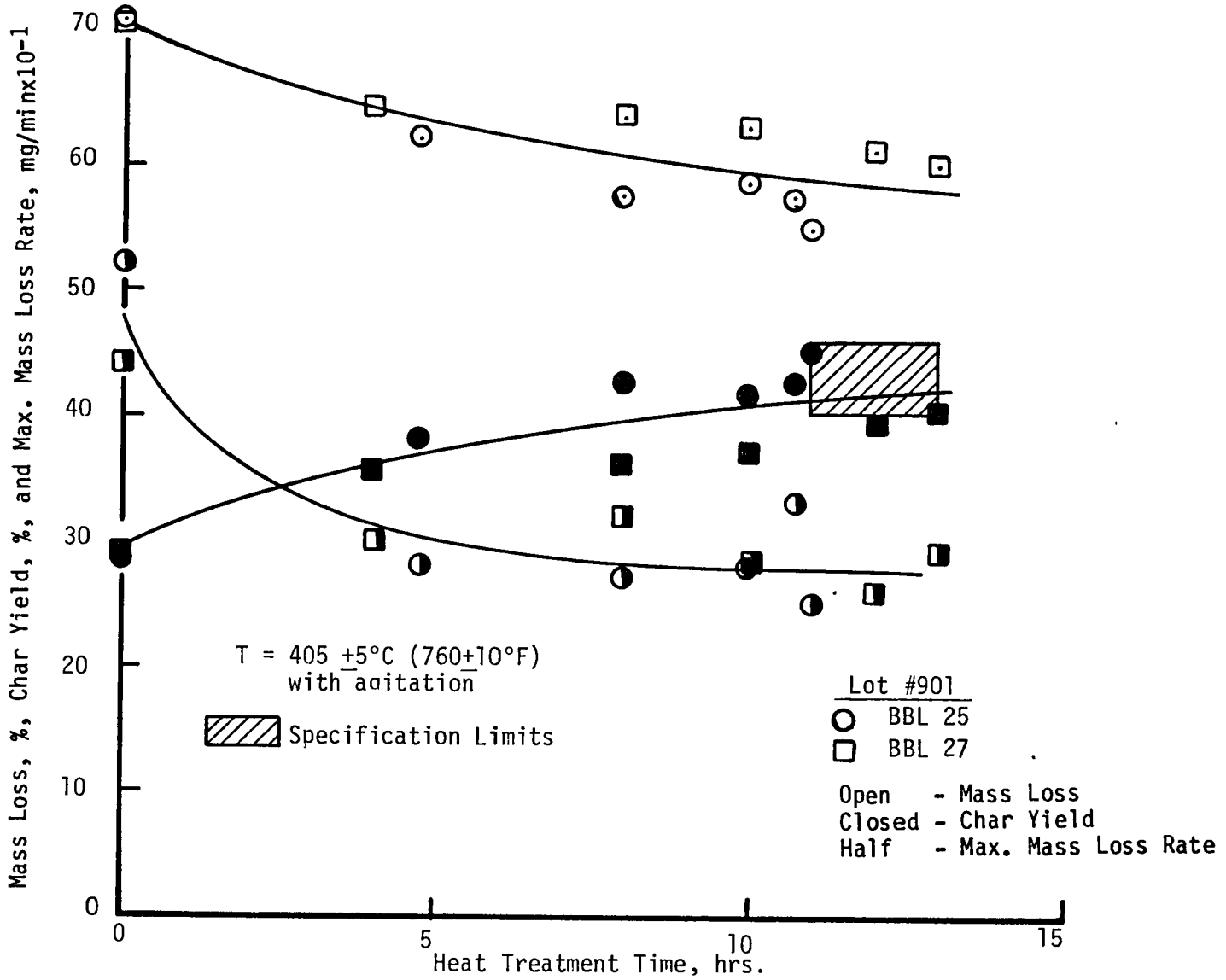

Figure 30. Effect of Heat Treatment Time

Table 8. Effect of Heat Treatment* on Benzene and Quinolene Insolubles for Allied 15V Coal Tar Pitch

Lot No.	Heat Treat Batch No.	Benzene Insolubles, %		Quinolene Insolubles, %	
501	As-Received	14.5		2.5	
	2	21.6		6.4	
	3	32.1	Average =	3.1	Average =
	4	23.7	25.8	2.0	4.7
	5	24.4		3.4	
	7	27.4		8.5	
901	As-Received	9.3		4.0	
	10	33.6		25.8	
	14	29.2		12.0	
	17	24.0	Average =	11.6	Average =
	19	21.3	32.1	7.3	12.3
	22	28.6		8.3	
	23	45.6		12.1	
	24	31.8		10.6	
	26	42.8		10.5	

* Nominally 12 ± 1 hours @ 405 ± 5°C (760 ± 10°F) with agitation

Table 9. Summary of TGA Data for As-Received and Heat Treated Allied 15V Coal Tar Pitch

Lot No.	Heat Treat Batch No.	Mass Loss, %	Char, %	Maximum Mass Loss Rate, mg/min @ °C
501	As-Received*	72.9	27.1	4.3 @ 400
	3	57.3	42.7	3.0 @ 400
	4	58.1	41.9	3.2 @ 380
	5	58.6	41.4	2.8 @ 380
	7	54.8	45.2	3.0 @ 380
901	As-Received**	71.7	28.3	4.4 @ 440
	13	58.1	41.9	2.6 @ 370
	21	58.0	42.0	3.0 @ 385
	22	59.7	40.3	3.3 @ 400
	23	56.0	44.0	2.5 @ 380
	26	56.8	43.2	2.4 @ 400
	29	54.9	45.1	2.5 @ 380
	30	57.5	42.5	2.4 @ 400
	31	60.0	40.0	2.9 @ 400
	34	54.9	45.1	3.7 @ 390

* Average of 2 barrels
** Average of 5 barrels

Tooling. - The tooling for each log consists of a base plate, cage and top plate assembly. The base plate is used to hold the axial rods upright and in place during weaving. The cage is placed around the preform after weaving for protection during handling while powder filling and to contain the powder. The top plate assembly is used to restrain the preform during handling and powder fill to prevent tilting and/or twisting. ATJ or an equivalent fine grain graphite was used for all tooling.

Figure 31 presents the base plate showing the hole pattern into which the outer rows of the axial rods are inserted and the hole pattern for mounting to the cage presented in Figures 32, 33 and 34. Just prior to powder fill, the holes were drilled in the cage wall to assist liquid impregnation. This operation was inserted after the rejection of S/N 119. Figure 35 shows the top plate while Figures 36 through 39 show the retainers to restrict the preform movement and the top plate hole drilling pattern.

Preform Fabrication. - Preform fabrication begins with pultrusion of the round axial and square transverse rods. This was carried out in two steps at Haveg Industries, Santa Fe Springs, CA. First, the rod stock lengths are fabricated. This is performed by combining 10000 filament yarns with a sacrificial binder and pulling them through an appropriate sized die. Three yarns were used for the round axial rods and two for the square transverse rods. Figure 40 presents the rod designs and specifications. The stock lengths are approximately nine feet in length. The second step is to cut these into the appropriate lengths for weaving the preform, 33 cm (13 in) for the axials and 16.5 cm (6.5 in) and 20.3 cm (8 in) for the transverse.

Rod identification as to lots and batches were as defined in Figure 40. Inspection of the rods consisted of verifying vendor supplied certification of material properties, metallographic

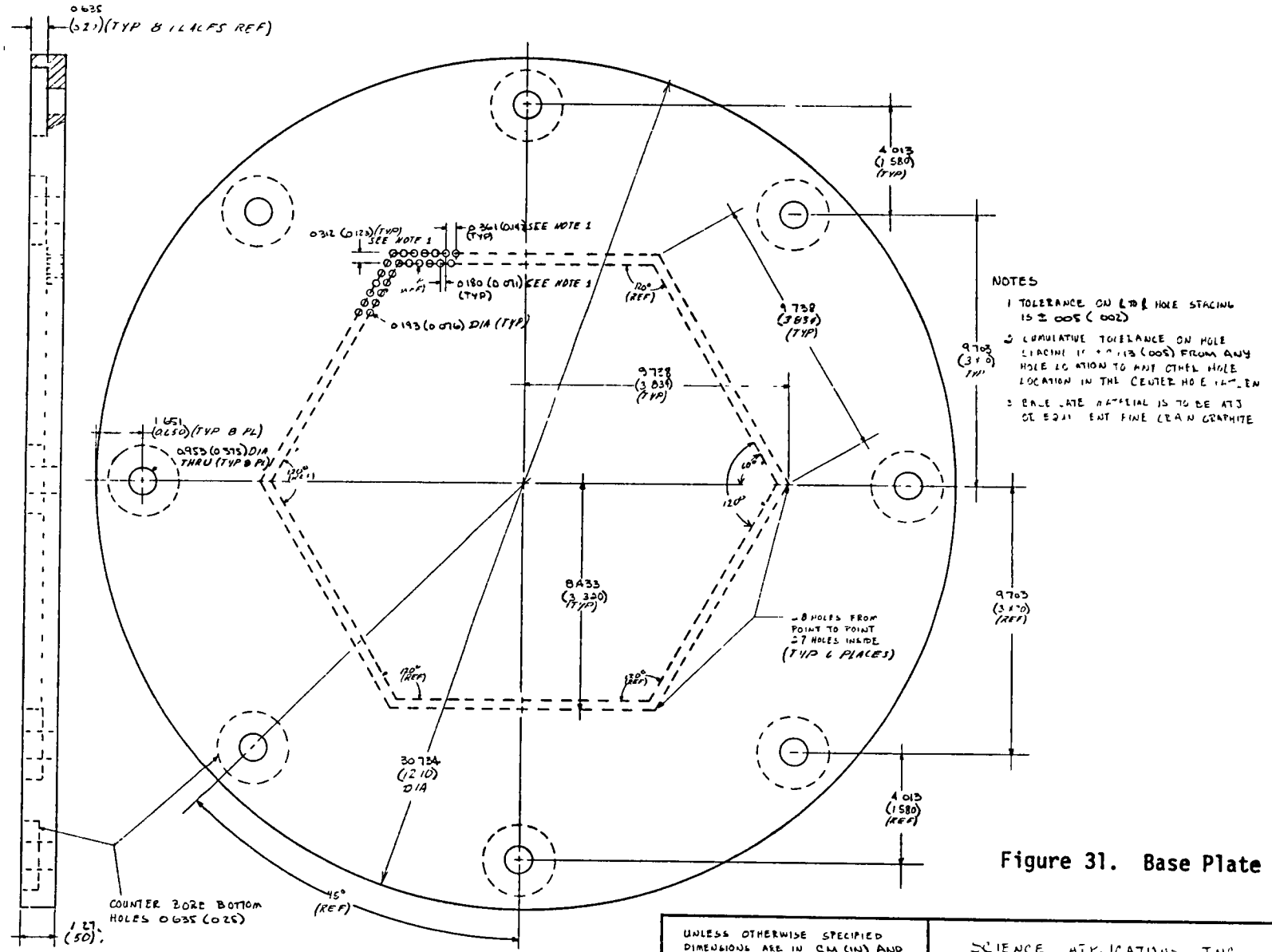

-7 BOTTOM PLATE

Figure 31. Base Plate

UNLESS OTHERWISE SPECIFIED DIMENSIONS ARE IN CM (IN) AND TOLERANCES ON	SCIENCE APPLICATIONS INC
FRACTIONS = ± 1/16 ANGLES = ± 0.5 DEG X = ± .25 (.10) XX = ± .076 (.030) XXX = ± .025 (.010)	SCALE FULL · APPROVED BY D A Gilman · DRAWN BY · DATE 1-21-78 · REVISED 11/18/80
	PREFORM TOOLING ASSEMBLY
CONTRACT NO DAAG46 73 A-0127 · NEXT ASSEMBLY	SIZE · SHEET 5 OF 5 · REV C · DRAWING NUMBER

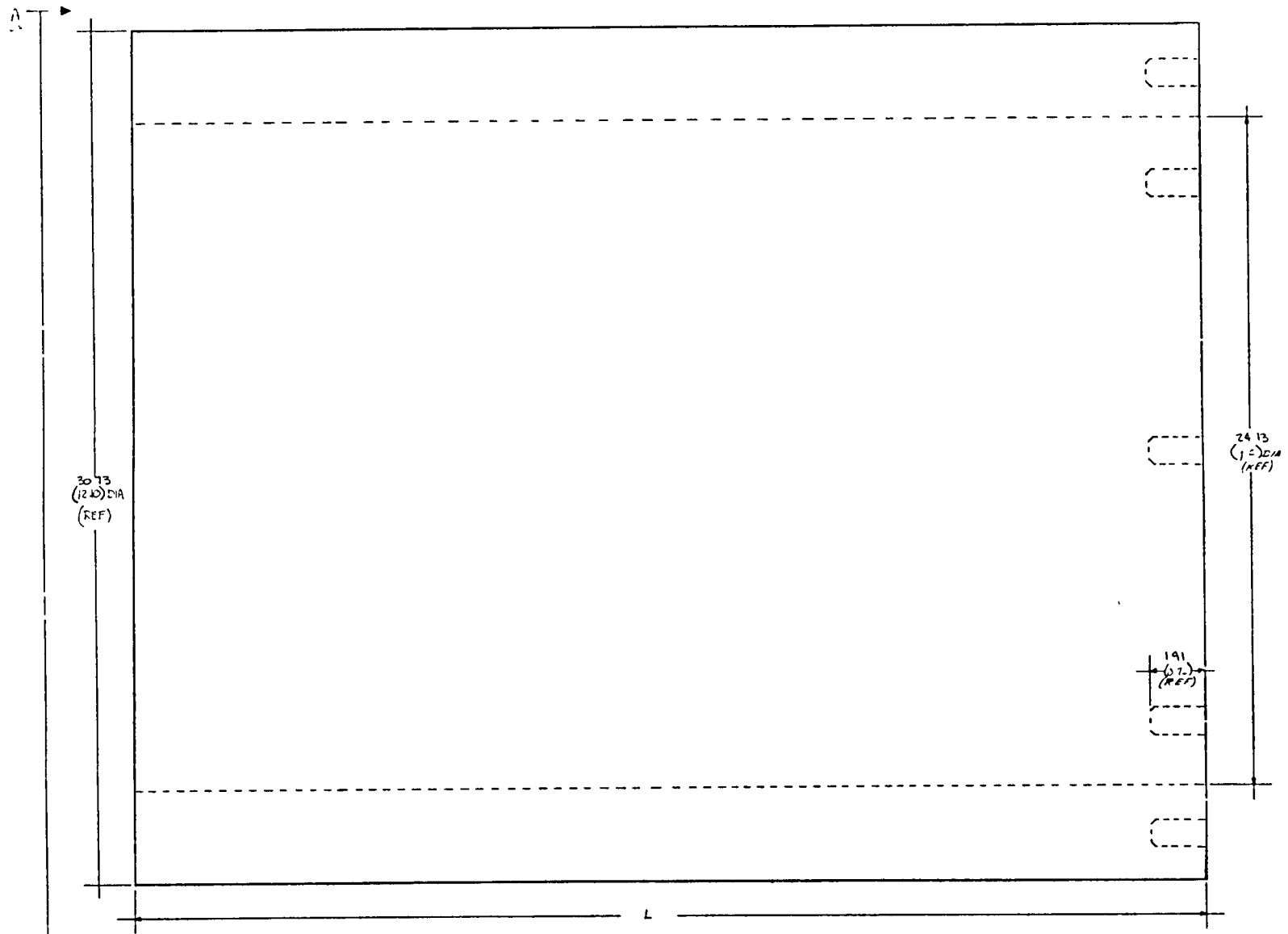

NOTES

1 MAKE FROM COMERICAL GRADE GRAPHITE, CYLINDRICAL STOCK

-3 CAGE

Configuration	L
-A	36.83 (14.50)
-B	34.29 (13.50)

UNLESS OTHERWISE SPECIFIED DIMESIONS ARE IN CM (IN) AND TOLERANCES ON

FRACTIONS = ± 1/16
ANGLES = ± 0.5 DEG
X = ± .25 (.10)
XX = ± .076 (.030)
XXX = ± .025 (.010)

SCIENCE APPLICATIONS INC

SCALE FULL | APPROVED BY: | DRAWN BY
DATE 11/1 | REVISED 11/18/83

PREFORM TOOLING ASSEMBLY

CONTRACT NO DAEA18-83-A 0127 | NEXT ASSEMBLY | SIZE | SHEET 2 OF 5 | REV C | DRAWING NUMBER MSO NT 2001

Figure 32. Cage

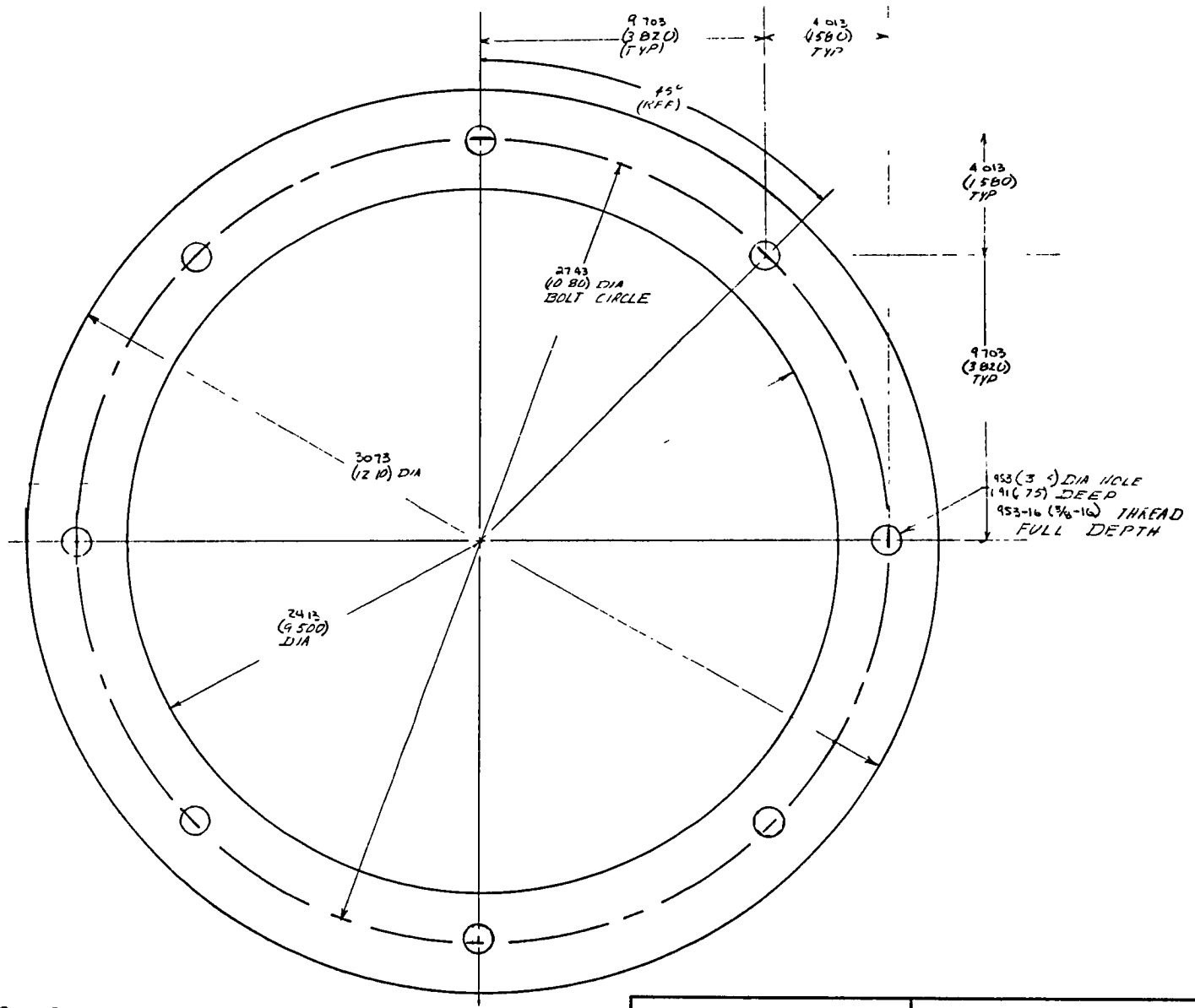

VIEW A-A From page 1
FULL SCALE
-3 CAGE (REF)

Figure 33. Cage

UNLESS OTHERWISE SPECIFIED DIMENSIONS ARE IN CM (IN) AND TOLERANCES ON FRACTIONS ± 1/16 ANGLES ± 0.5 DEG X ± .25 (.10) XX ± .076 (.030) XXX ± .025 (.010)	SCIENCE APPLICATIONS INC	
	SCALE FULL / DATE: / /	APPROVED BY: D A Eftman / DRAWN BY / REVISED 1/15/83
	PREFORM TOOLING ASSEMBLY	
CONTRACT NO DAEA18-73-A 0127 / NEXT ASY EMPLY	SIZE / SHEET 3 OF 5	REV C / DRAWING NUMBER

NOTES FOR CAGE AND LID DRILLING

1 Holes to be drilled in cage and lid after heat cleaning but prior to impregnation

2 Location of base plate attachment bolts to be identified on the side of cage

3 All holes to be drilled thru the cage wall with minimum amount of powder disturbance in a radial direction + 5° from 60° orientation to avoid drilling into base plate attachment bolts

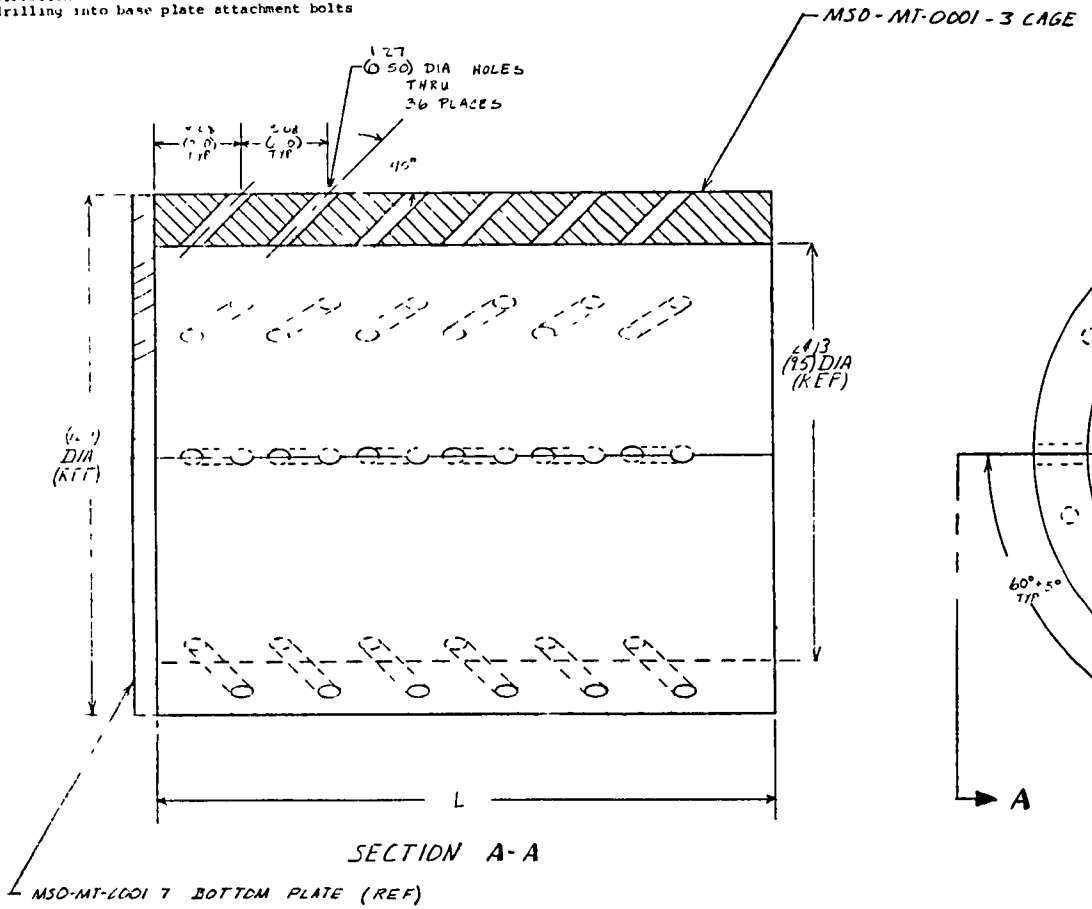

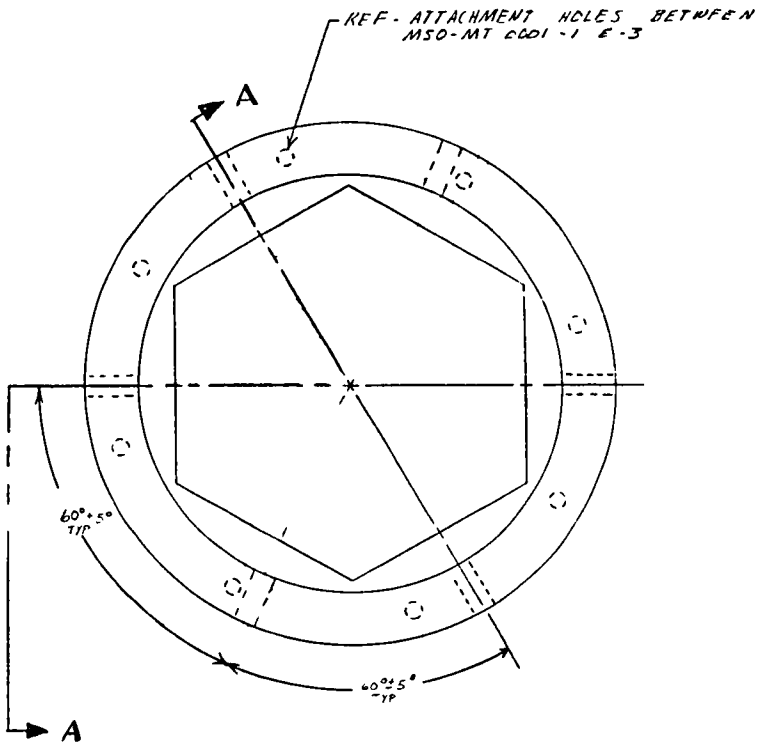

CAGE NO	L (REF)
A	36.83 (14.50)
B	34.29 (13.50)

Figure 34. Cage

UNLESS OTHERWISE SPECIFIED DIMENSIONS ARE IN CM (IN) AND TOLERANCES ON FRACTIONS ± 1/16 ANGLES ± 0.5 DEG X ± .25(.10) XX ± .076(.03) XXX ± .025(.01)	SCIENCE APPLICATIONS INC
SCALE 1/ 1 APPROVED BY: DRAWN BY	
DATE 10 10 77 REVISED 1 4/6	
	CAGE AND LID DRILLING
CONTRACT NO EAE AIR 72-A-077	USED ON NEXT ASSEMBLY NONE
E SIZE	SHEET 1 OF 1 REV NEW DRAWING NUMBER

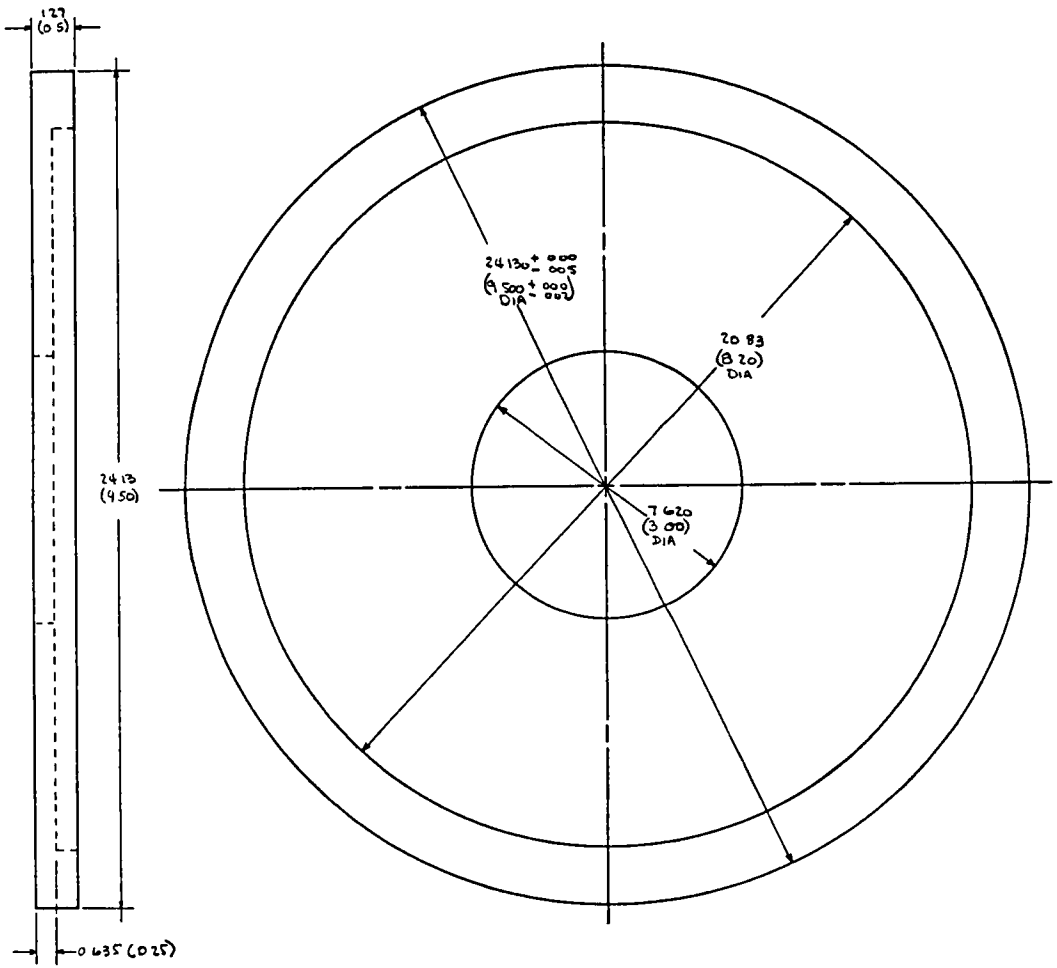

NOTES

1 MAKE FROM FINE GRAIN COMERICAL GRADE GRAPHITE

-5 TOP PLATE

UNLESS OTHERWISE SPECIFIED DIMENSIONS ARE IN mm (IN) AND TOLERANCES ON FRACTIONS ± 1/16 ANGLES ± 0 5 DEG; X ± 25 (10), XX ± 076 (020), XXX ± 025 (010)	SCIENCE APPLICATIONS INC	
	SCALE FULL; APPROVED BY; DRAWN BY; DATE 9-20-78; REVISED 11/16/53	
	TITLE: PREFORM TOOLING ASSEMBLY	
CONTRACT NO DAEA18-73-A-0127; NEXT ASSEMBLY	SIZE; SHEET 1 OF 5; EV C; DRAWING NUMBER	

Figure 35. Top Plate

Rev	Description	Date
A	INCORPORATE METRIC EQUIVALENT UNITS AND NEXT ASSEMBLY	11/15/80

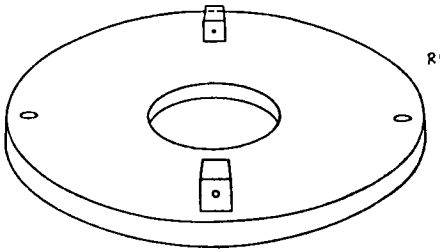

REF M50-MT-0001-5 AND M50-MT-0002 13

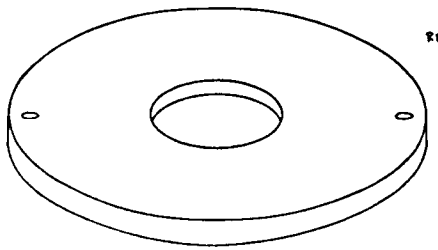

REF M60-MT-0002-7

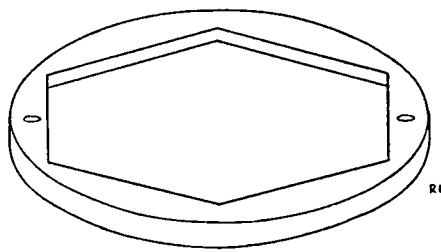

REF M50 MT-0002-5

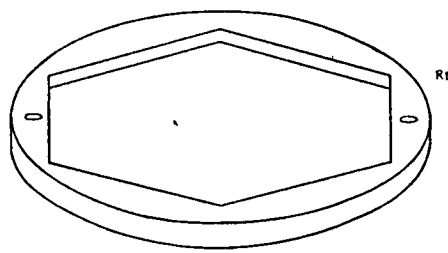

REF M50-MT-0002-3

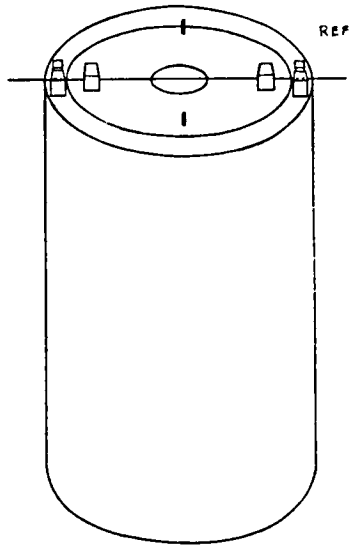

REF M60 MT-0002

	1	-17	RETAINER BAR		[illegible]	
	1	-15	RETAINER CAGE	M 3 MT 0001-7	[illegible] GRADE GRAPHITE	
	1	-13	RETAINER LID	M50 MT 000 -5	[illegible] GRADE GRAPHITE	
	2	-11	LID BLOCK		[illegible] GRADE GRAPHITE	
	4	-9	CAGE BLOCK		[illegible] GRADE GRAPHITE	
	1	-7	UPPER SPACER		FOAM RUBBER	
	1	-5	LOWER SPACER		FOAM RUBBER	
	1	-3	PREFORM RETAINER		PLASTIC	
		PART NO	NOMENCLATURE	[illegible]	[illegible]	MATERIAL [illegible]

UNLESS OTHERWISE SPECIFIED DIMENSIONS ARE IN CM (IN) AND TOLERANCES ON
FRACTIONS ± 1/16
ANGLES ± 0.5 DEG
X ± 25 (.10)
XX ± 076 (.030)
XXX ± 0254 (.010)

SCIENCE APPLICATIONS, INC - LSO

SCALE [illegible] APPROVED BY [illegible] DRAWN BY [illegible]
DATE 5 79 REVISED 11/15 FJ

INTEGRATED CAGE ASSEMBLY

CONTRACT NO DABA18 73 A-0127 | NEXT ASSEMBLY M50-MT-0004 | SIZE | SHEET 1 OF 3 | REV A | DRAWING NUMBER [illegible]

Figure 36. Top Plate Assembly

NOTES

1. Use 1-17 to Transfer Bar into 11 Lid Blocks and locate 11 & 17 in 13 & 3 of new Lid is pressed. Bond the two 11 blocks in 13 with adhesive. Install 13 into 15 Retainer Cage. Locate 9 Cage Blocks to allow easy insertion of 17 and 11 blocks in place. Blocks are graphite.

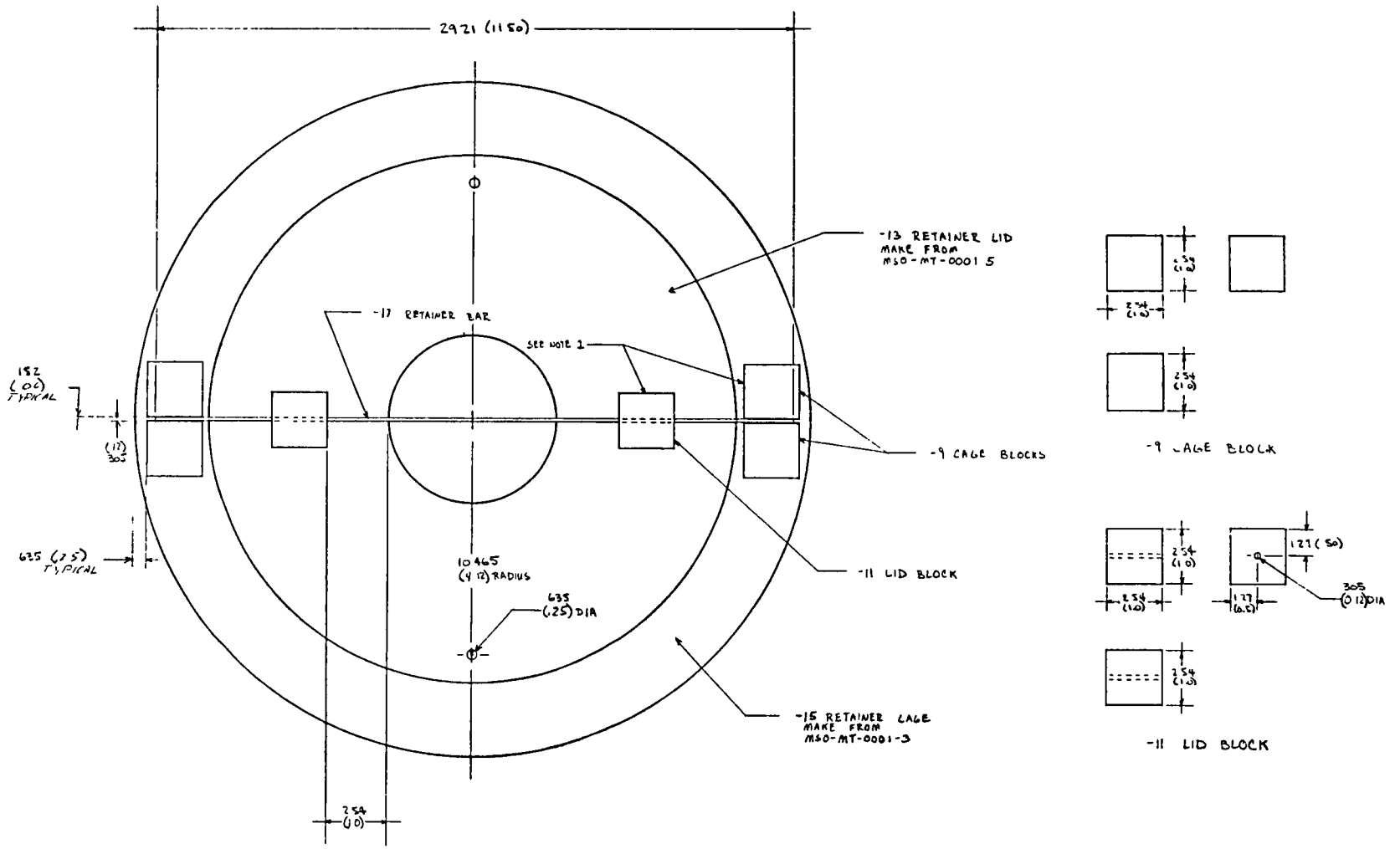

Figure 37. Top Plate

UNLESS OTHERWISE SPECIFIED DIMENSIONS ARE IN CM (IN) AND TOLERANCES ON FRACTIONS ±1/16 ANGLES ±0.5 DEG X ±.25 (.10) XX ±.076 (.030) XXX ±.025 (.010)	SCIENCE APPLICATIONS, INC - MSO		
	SCALE 1/1 1 A/V	APPROVED BY D G Ehman	DRAWN BY [illegible]
	DATE 3-15 79		REVISED 11/17/80
	TITLE INTEGRATED AGE ASSEMBLY		
CONTRACT NO DAEA18 73 A-0127	NEXT ASSEMBLY MSO-MT-0006	E	SHEET 2 OF 2
		REV A	DRAWING NUMBER [illegible]

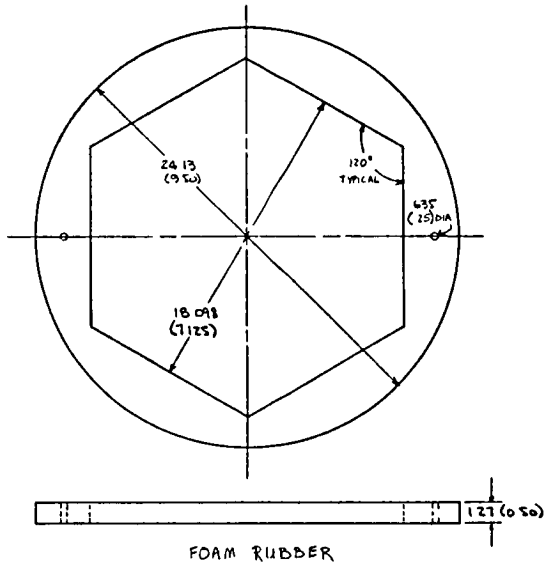

FOAM RUBBER

-5 LOWER SPACER

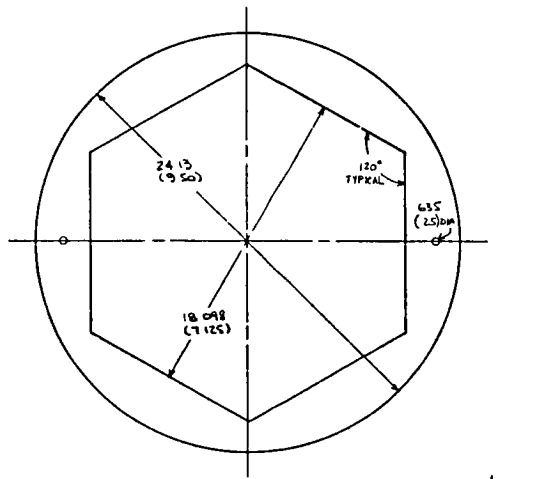

PLASTIC

-3 PREFORM RETAINER

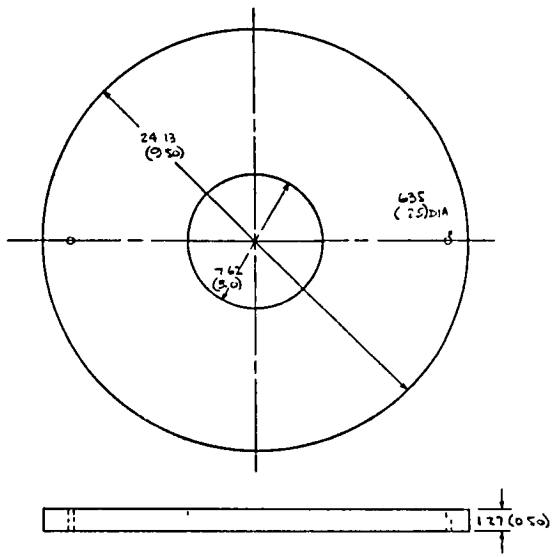

FOAM RUBBER

-7 UPPER SPACER

UNLESS OTHERWISE SPECIFIED DIMENSIONS ARE IN CM (IN) AND TOLERANCES ON FRACTIONS = ± 1/16 ANGLES = ± 0.5 DEG X = ± .25 (.10) XX = ± .076 (.030) XXX = ± .025 (.010)	SCIENCE APPLICATIONS, INC - MSO				
	SCALE 1/1 1"	APPROVED BY		DRAWN BY [illegible] A	
	DATE 11-1-79			REVISED 11/16/83	
	TITLE INTEGRATED CASE ASSEMBLY				
CONTRACT NO DAEA18 79 A 0127	NEXT ASSEMBLY MSO-MIT-CX-XX	LE	SHEET 2 OF 3	REV A	DRAWING NUMBER MSO [illegible]

Figure 38. Retainer Components

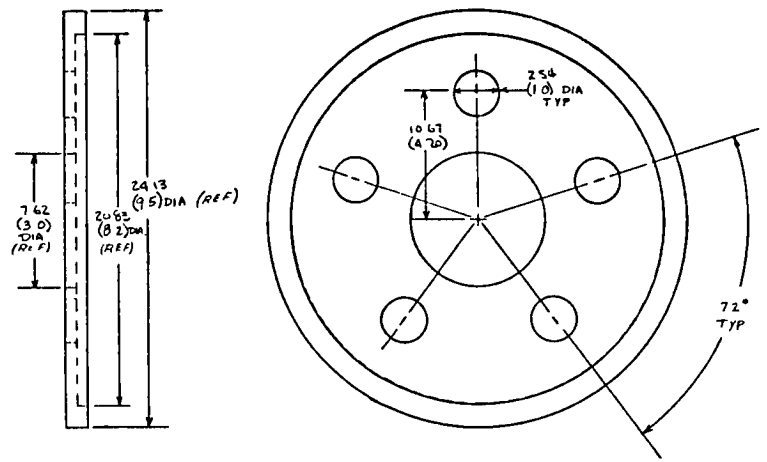

MAKE FROM MSFC-MIT-C001-5 TOP PLATE

Figure 39. Top Plate

UNLESS OTHERWISE SPECIFIED DIMENSIONS ARE IN CM (IN) AND TOLERANCES ON FRACTIONS ± 1/16 ANGLES = ± 0.5 DEG X = ± 2 (1) XX = ± 0.76 (.03) XXX = ± .025 (.01)	SCIENCE APPLICATIONS INC		
	SCALE - 1	APPROVED BY:	DRAWN BY R. W. JA.
	DATE 10-15-74		REVISED 1-10-75
	GAGE AND LID DRILLING		
CONTRACT NO DAE A18-73 A-0127	NEXT ASSEMBLY NONE	SIZE	SHEET 2 OF 2 REV 1 (No.) DRAWING NUMBER MSFC-MIT-C001-4

REV	DESCRIPTION	DATE
E	INCORPORATE METRIC EQUIVALENT UNITS	11/18/80
A	[illegible] TYPE 2 + TYPE U, V, W	[illegible]
B	HANDLE [illegible] TO 45-55-[illegible]	[illegible]
C	LOT = BATCH [illegible] BINDER INSPECTION	6/8/79
D	REQUIREMENTS BINDER, SOLVENT	11/6/79

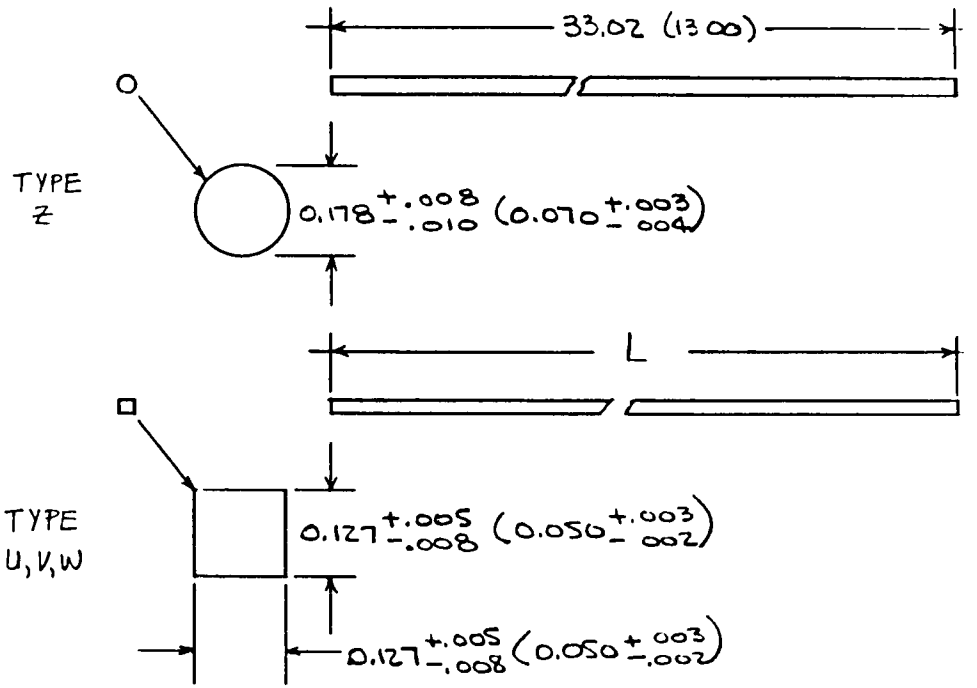

	L_1	L_2
TYPE U, V, W	16.51 (6.50)	20.32 (8.00)

Figure 40. Reinforcement Rods

UNLESS OTHERWISE SPECIFIED DIMENSIONS ARE IN CM (IN) AND TOLERANCES ON
FRACTIONS = ± 1/16 .X = ±.25 (.10)
ANGLES = ± 0.5 DEG. .XX = ±.076 (.030)
.XXX = ±.025 (.010)

SCIENCE APPLICATIONS, INC - MSO

SCALE	APPROVED BY:	DRAWN BY
FULL	[signature]	[illegible]
DATE 6/8/79		REVISED 11/18/80

TITLE
REINFORCEMENT RODS

CONTRACT NO.	NEXT ASSEMBLY	SIZE		REV	DRAWING NUMBER
DAEA18-73-A-0127	MSO-MC-0002		SHEET 1 OF 2	E	MSO-MC-0002

NOTES:

1. MATERIAL TO BE HM-10000 PER HERCULES CHEMICAL CORPORATION HS-SG-511H (NON-GLASS FILAMENT FIBER) CARBON AND GRAPHITE, CONTINUOUS FILAMENT TOW.

2. TYPE UVW RODS SHALL BE MADE OF 2 PLIES OF HM 10000 TOW. TYPE Z RODS SHALL BE MADE OF 3 PLIES OF HM 10000 TOW.

3. THE BINDER SHALL BE POLYMETHYL-METHACRYLATE.

4. THE SOLVENT SHALL BE METALENE CHLORIDE.

5. A "LOT" OF RODS IS DESIGNATED BY THE HAVEG JOB NUMBER WHICH IN TURN IS DEFINED BY THE SAI PURCHASE OR ITEM NUMBER.

6. A "BATCH" IS WHAT IS PRODUCED IN CONTINUOUS OR SEMI-CONTINUOUS OPERATION OVER A 24 HOUR PERIOD FOR A GIVEN CONFIGURATION i.e. U, V OR W VS. Z, USING A SINGLE FIBER LOT AND BINDER INGREDIENTS LOT.

7. EACH "LOT" OF BINDER AND SOLVENT SHALL BE ACCEPTED PRIOR TO IT'S USE BY THE FOLLOWING METHODS. TGA FOR THE BINDER AND IR FOR THE SOLVENT.

8. REQUIREMENTS
   A. BINDER - TGA - 99 ± 1% WT. LOSS.
   B. SOLVENT - IR - VERIFY SOLVENT THAT OF NOTE 4.

Figure 40. (Cont'd)

SCIENCE APPLICATIONS, INC. - MSO			
SCALE: NONE	APPROVED BY:		DRAWN BY RON JACOBS
DATE 6/8/79			REVISED 11/12/80
TITLE: REINFORCEMENT RODS			
SIZE	SHEET 2 OF 2	REV E	DRAWING NUMBER MSO [illegible]

examination of one sample from each lot of fiber and comparison to a standard and rod dimensional check. The dimensional check was carried out by direct measurement with a micrometer of the cross-section dimensions; sampling was per MIL-STD-105D. Spot checks of rod length were also carried out.

Preform weaving consisted of inserting the required number of axial rods in the hole pattern in the base plate. Only the two outer layers are inserted. Next approximately 9 layers of transverse rods are inserted in the appropriate channels between these axials. The remaining axials are next inserted into the interstices adjacent to the transverse rod cross-over points. The remaining transverse layers were then inserted and compacted until the required log height was obtained.

Inspection consisted of periodic layer spacing measurements during weaving plus preform final dimensional measurements. In addition, the preform was inspected using a light box. Due to the nature of the preform construction, any missing rod will leave a channel and by backlighting such a channel can be easily detected. After weaving, the cage was installed for powder fill.

Powder Fill. - The next step is to powder fill the preform. This was carried out by flowing powder into the top center of the caged preform. The caged preform with the top plate assembly was placed on a vibrating table to stimulate the powder flow. Figure 41 is a plot of a typical filling history. The powder flow rates were adjusted by trial and error to maintain the difference in powder height between outside and inside to less than 10 cm (4 in). The break between 19 and 29 hours was overnight when the filling was left on which resulted in a slight inside overfill condition in this case which was rectified by lowering the flow rate to allow the outside to catch up.

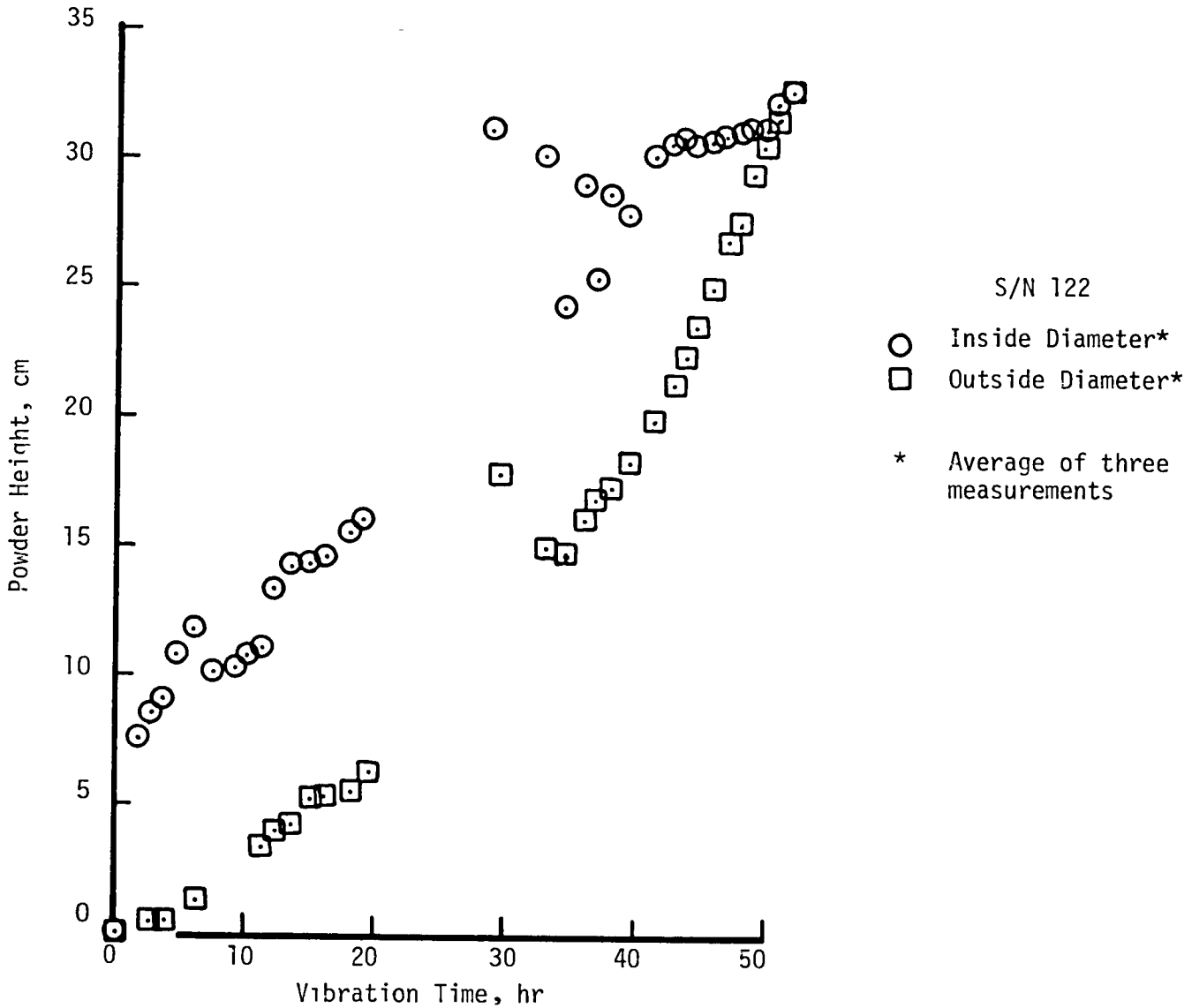

Figure 41. Typical Powder Fill History

Considerable time was required to fill some preforms, i.e. up to 200 hours. This was attributed to two reasons. First the powder was fed into the preform in a thin stream at the center of the preform. Consequently the powder had to flow down the preform length and then radially to the outside in order to fill the preform completely. Subsequent work has shown that the powder can be fed uniformly over the top surface without adverse effects. Secondly, the powder used, BB4, is poorly shaped for good flowing characteristics, since it consists of long needle like particles. Recent in-house work has yielded a better flowing powder, one more spherically shaped. Use of this powder would decrease the filling time for this size log to approximately 10 hours.

Once the preform is filled, the powder holds it in place thus there is no further need for the binder in the rods. Thus the next step is to heat clean the caged, powder filled preform to remove the binder so that the rods can be infiltrated by the liquid pitch impregnant. Figure 42 presents a plot of the heat cleaning cycle used. This too was accomplished at Haveg using an argon atmosphere. The argon gas conformed to MIL-A-18455.

Densification. - Liquid densification consists of three distinct operations; impregnation, carbonization and graphitization. For the Antares III logs, a total of four cycles of these three operations was carried out.

For the impregnation operation, the caged powder filled preform and/or partially densified billet is placed in a stainless steel can. A thermocouple is inserted in the annulus between the cage and the preform. To minimize the amount of pitch, graphite filler blocks are used to reduce the free volume inside the can. The object is not to save pitch per se but to minimize

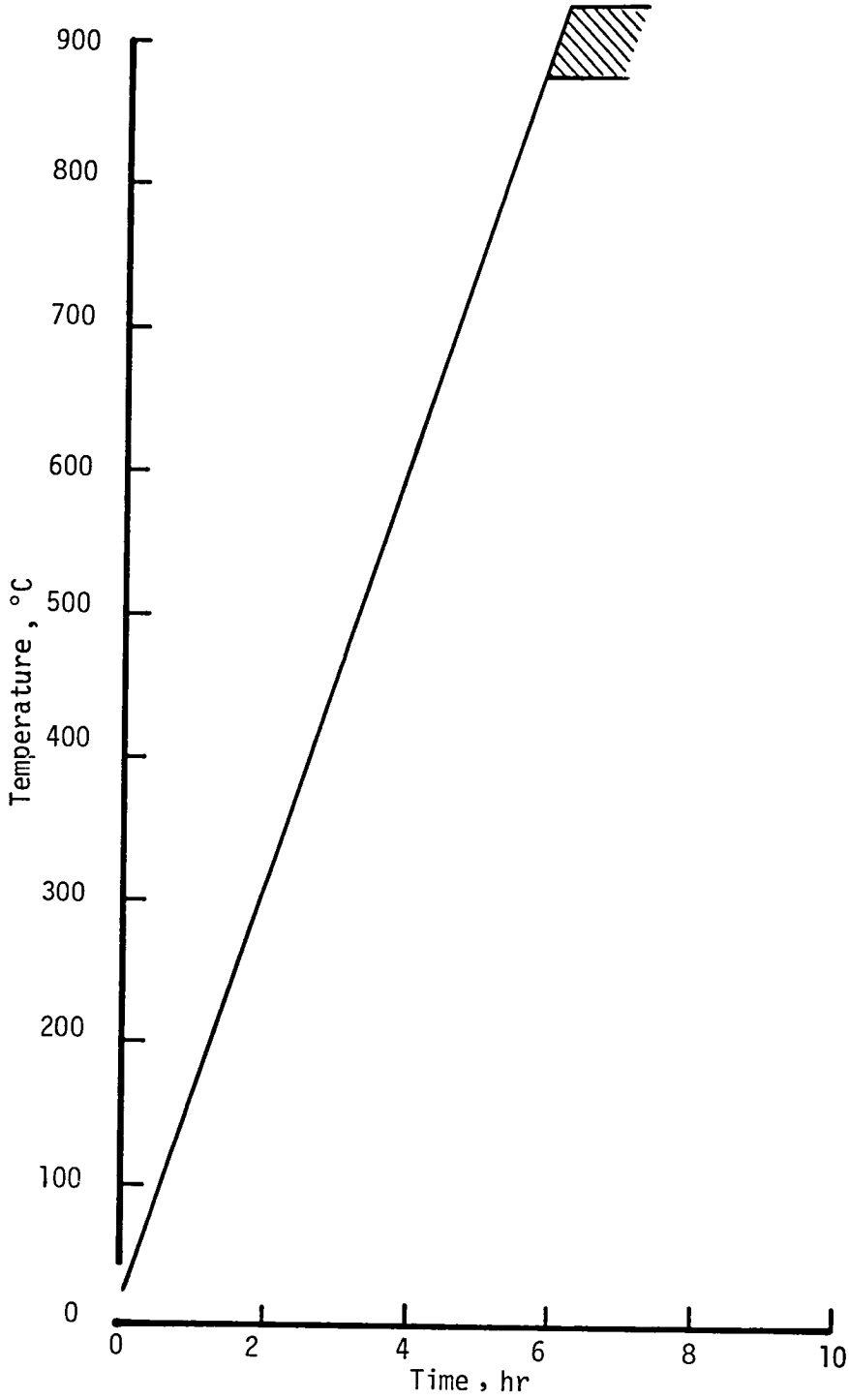

Figure 42. Heat Cleaning Cycle

the amount of decomposition products. For cycle 1, the preform, and cycle 3 the billet is placed with the forward end up while for cycles 2 and 4 the forward end is placed down. The can is weighed, placed in the main tank of the impregnator, the lid is closed and a vacuum of 2 torr is pulled. The tank is backfilled with argon to atmospheric pressure and the load is heated to 250 + 20-0°C (480 $\pm$ 36-0°F) as indicated by the internal thermocouple. Simultaneously, the side loader tank containing the heat treated pitch is heated to the same temperature and agitated. When both temperatures are as specified, the pitch is transferred to the steel can to a level about 5 cm (2 in) above the top of the load. The pressure is increased to 6.895 x 10^5 Pa (100 psi) and the main tank heaters shutoff.

Early in the program a discrepancy was encountered with S/N 105. After the first cycle, during rough machining, visual inspection revealed a region where there was 0.76 cm (0.3 in) separation of the U, V,W, layers extending through the diameter of the log, Figure 43. At the time this was attributed to movement of the transverse layers during the vibratory powder fill. Various alterations to the tooling used during powder fill were instituted to provide a positive downward force upon the transverse layers during vibration to prevent their movement.

S/N 109 suffered a highly anomalous occurrence on the first impregnation cycle. After removal of the cannister from the impregnator main tank, visual inspection revealed that the bottom of the can was convex. After carbonization this convex shape still existed, Figure 44. In addition, the pitch level had dropped approximately 12.7 cm (5 in). Inspection of the cage after removal from the cannister revealed the following:

1. The bottom plate was separated 3.8 to 5.1 cm (1.5 to 2.0 in) the bottom end of the cage and cracked, Figure 45.

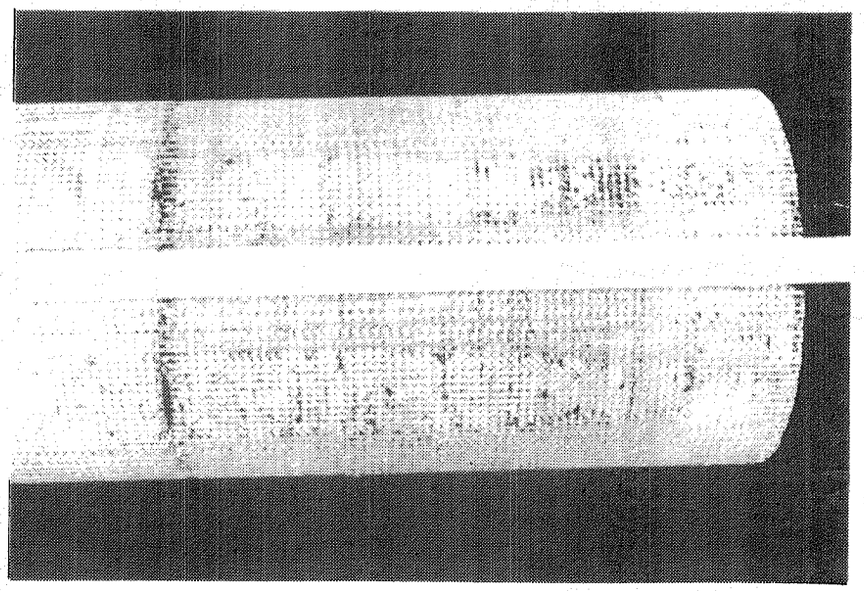

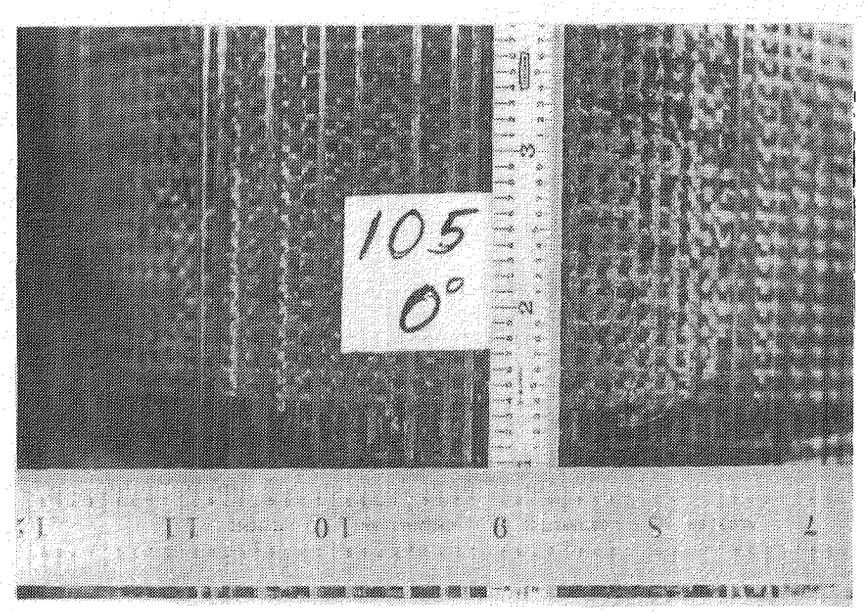

Figure 43. Separations in Log S/N 105

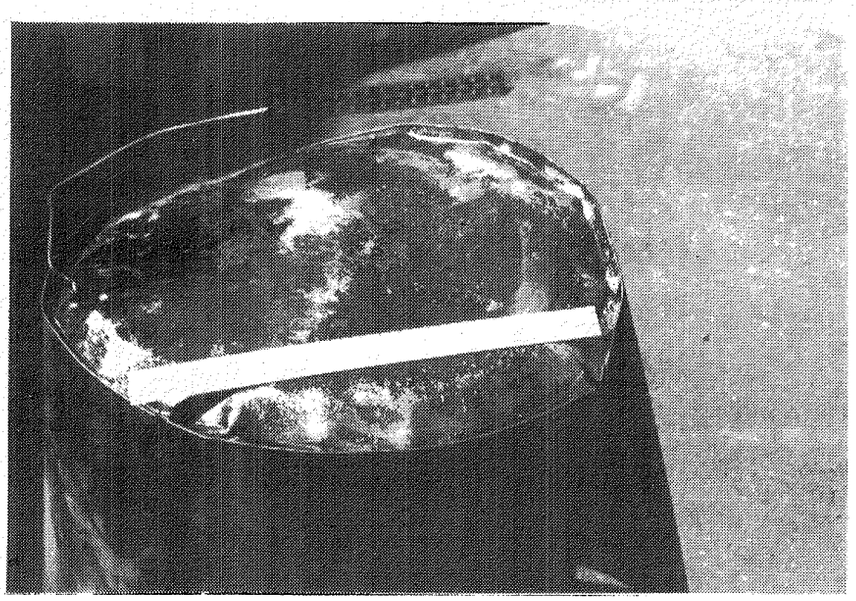

Convex bottom of canister after impregnation and carbonization cycles. Preform has been removed.

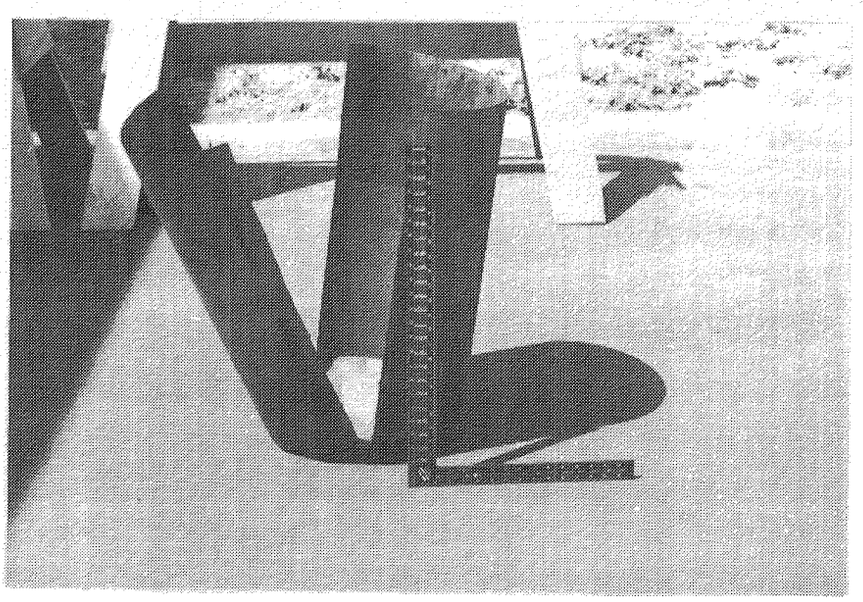

Split canister after removal of preform

Figure 44. Log S/N 109 Canister

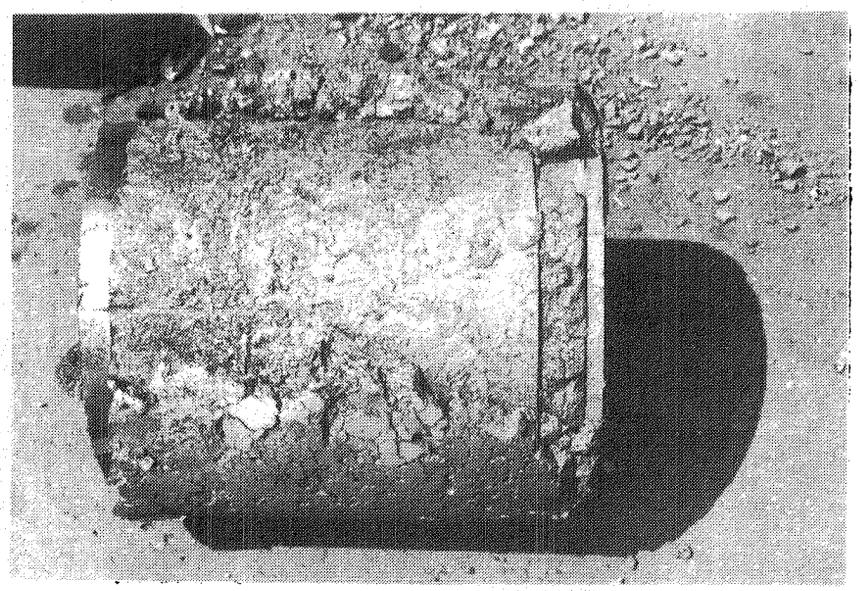

Separation of the base plate from the preform cage.

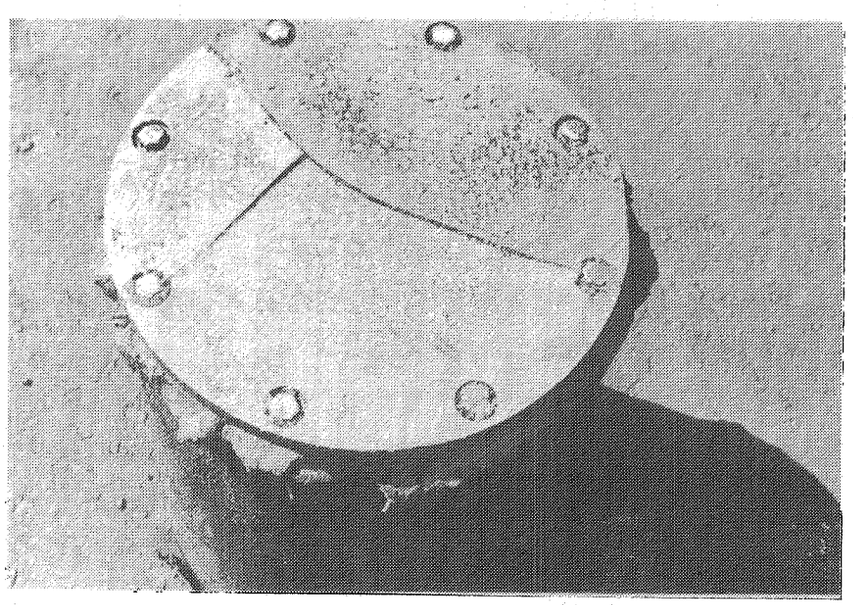

Base plate cracked.

Figure 45. Log S/N 109 Caged Preform Assembly

2. The volume between the base plate and cage was filled with carbonized pitch and powder, Figure 46.

It was suspected that there were dry regions in the bottom of the powder filled preform and that this somehow caused an unbalanced pressure during impregnation or carbonization. The fix was to ensure that the temperature was uniform throughout the load and holes were added to the top lid.

Visual inspection of S/N 119 revealed the presence of three separated regions similar to those of S/N 105. It was decided at this point to institute a detailed assessment of the condition of the billet after each process step by using x-ray inspection. X-rays were taken after powder fill, heat clean, impregnation, and first carbonization in addition to those already scheduled after first graphitization.

S/N's 121, 122, 120, 124, 125, 126, 123 and 127 were densified in order. S/N 126 was the next to show a separation of 1.9 cm (0.75 in), 7.29 cm (2.87 in) from the aft end. This separation was detected after impregnation, Figure 47. Since no separation was detected after heat clean, clearly the process causing the separation was impregnation.

The can containing S/N 126 had required pitch topping off after pressurization to 1.034×10^5Pa (15 psia), a not uncommon occurrence. This was accomplished by evacuating the main tank, drawing in sufficient pitch from the side loader, and repressurizing to 1.034×10^5Pa (15 psia). It was suggested that the preform had not completely impregnated as evidenced by the need to add pitch and that the "bumping" of the pressure from atmospheric to vacuum to atmospheric may have resulted in pressure gradients causing the compression of the transverse bundles and the attendent formation of a separation.

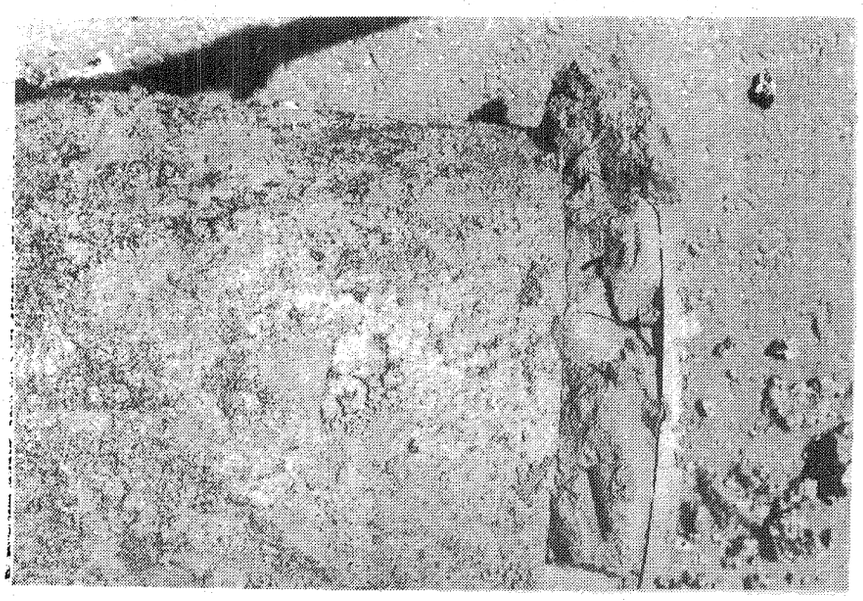

Separation of the base plate from the preform cage.

Figure 46. Log S/N 109 Caged Preform Assembly Close-Up

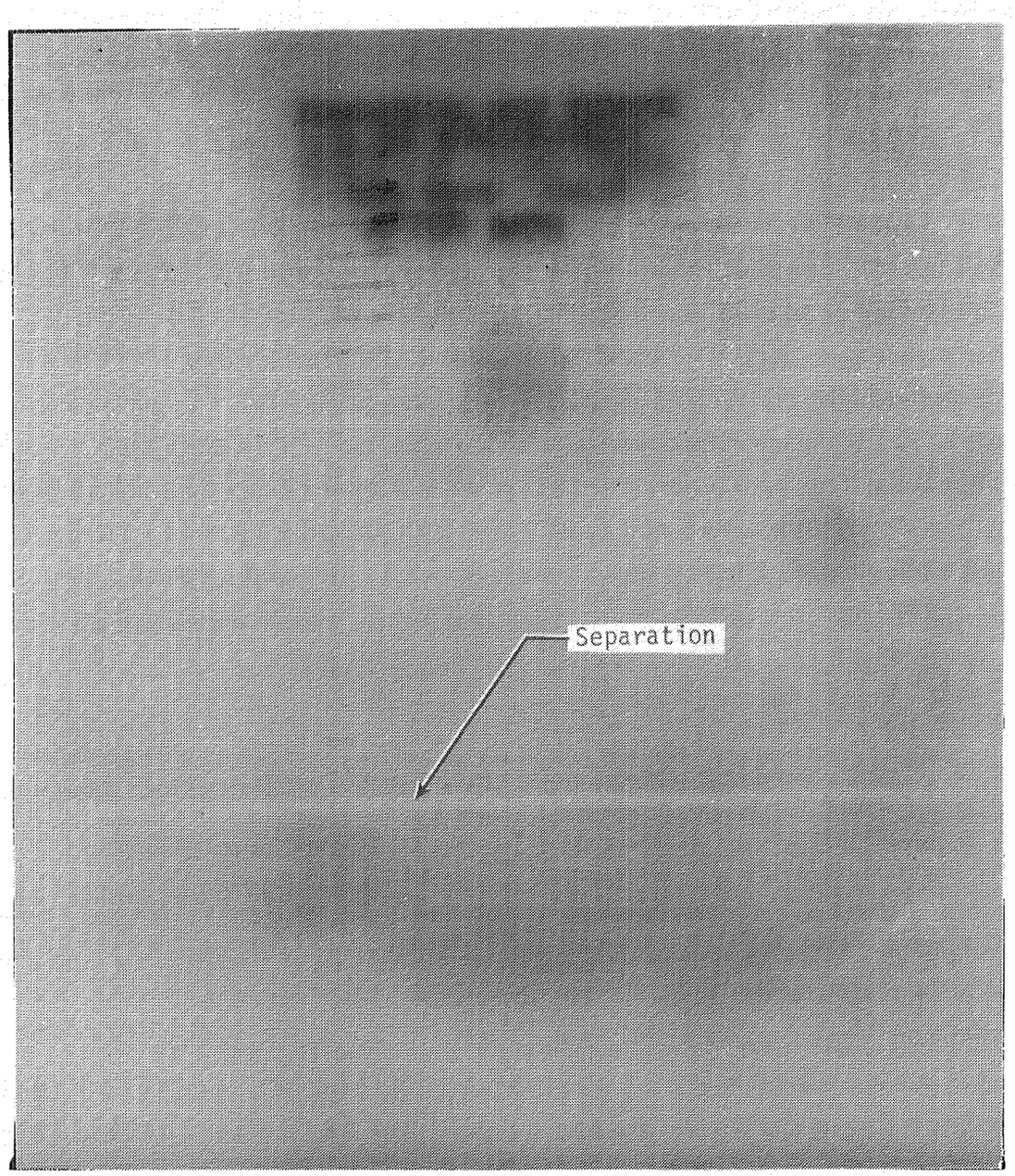

Figure 47. X-Ray of Log S/N 126 After First Impregnation

S/N 123 which was impregnated almost immediately after S/N 126 also had a separation formed during impregnation. This time, however, no "bumping" of the pressure occurred. It appears that the powder filled preform was not uniformly impregnated at the time of pressurization to 6.89 x 10^5Pa (100 psia). It is speculated that at the time of pressurization there were wet and dry regions in the preform, Figure 48. Since the impregnation is largely a radial process, it is conceivable that there may be locations of complete impregnation forming essentially a stratum of fully impregnated material bounded above and below by dry material. However, this dry region(s) is incapsulated within impregnated regions, effectively sealing it off. This is no problem as long as a vacuum is maintained. However, upon pressurization, the impregnated material is pressurized while the dry remains at vacuum, and a large pressure unbalance occurs. It is this large pressure gradient that caused the transverse bundle compaction and separation of the layers.

The most puzzling question is why does it take so long to impregnate these logs? The answer is that the powder filled preform is encased in a layer of powder. Recent work has shown that the capillary pressure of this powder is about a fourth to a third of that of the yarns. Thus this powder surrounding the preform forms a layer of material resistant to the flow of the impregnant into the preform since under vacuum conditions capillary action is the only mode of flow. Calculations show that complete impregnation requires on the order of 6-8 hours under vacuum conditions. Since typically pressurization was occurring within a hour or so of pitch transfer it seems likely that impregnation was not complete at pressurization.

The carbonization step was carried out in an autoclave capable of temperatures up to 650°C (1200°F) and 200 atm pressure in an argon atmosphere. The impregnated load was placed in the auto-

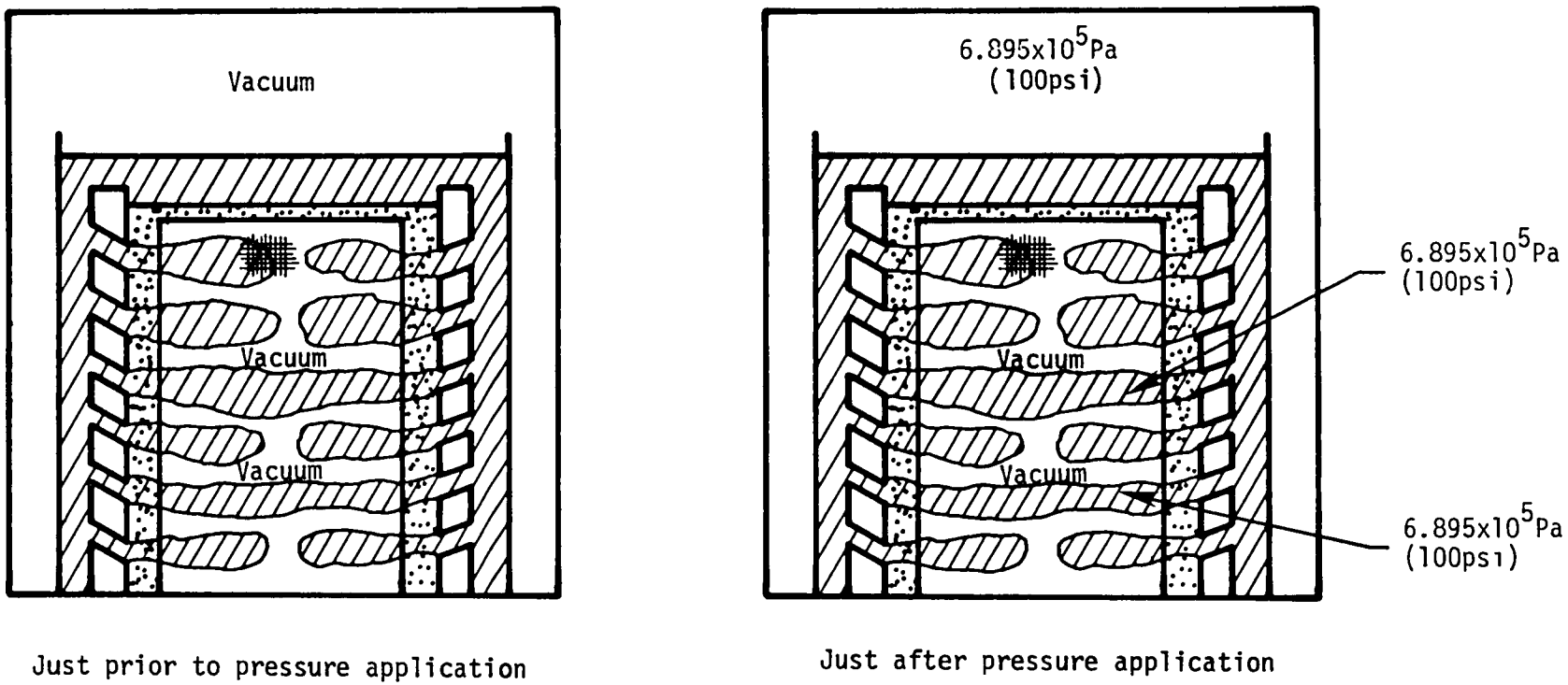

Figure 48. Separation Formation Scenario

clave with an internal thermocouple. The temperature and pressure history shown in Figure 49 was then applied. The temperatures in this case are furnace wall temperatures. The cycle starts by pressurizing to 5 atm and heating to 300 ± 30°C (570 ± 50°F), at which point a four hour hold is inserted to allow the pitch to melt and reach at least 200°C (390°F). The pressure is increased to 33 ± 3 atm and held for an hour during which time the pressure system and instrumentation is verified as functioning properly. The pressure is increased to 200 atm and another one hour hold is inserted for final systems check. The temperature is ramped to 525 ± 25°C (980 ± 45°F) at 75°C/hr (135°F/hr). Another 4 hour hold is inserted to allow the internal temperatures to equilibrate, then a final heating ramp to 675 ± 30°C (1250°F ± 54°F) at 50°C/hr (90°F/hr) is performed. After holding at this temperature for 4 hours, the power is shut off.

The critical portions of the run are the temperature ramps after full pressurization. Figure 50 presents the control and internal temperature histories for the carbonization runs utilized in the program. The control thermocouples are on the furnace outside wall and the data indicate all runs were within tolerance and were very repeatable. The internal temperatures are less repeatable particularly at the higher end. The reason for this is not obvious. Total load weights varied from a low of 35 kg (77 lb) for run 83 to a high of 137 kg (302 lb) for run 60. However, the slowest response is seen to be run 17 at 77.6 kg (171 lb) while the fastest response was run 43 at 104 kg (229 lb). Other comparisons bear out that load weight was not the cause. For instance, internal thermocouple location is either near the can wall for loads with caged preforms or in the center for all others, but similar comparisons show no correlation.

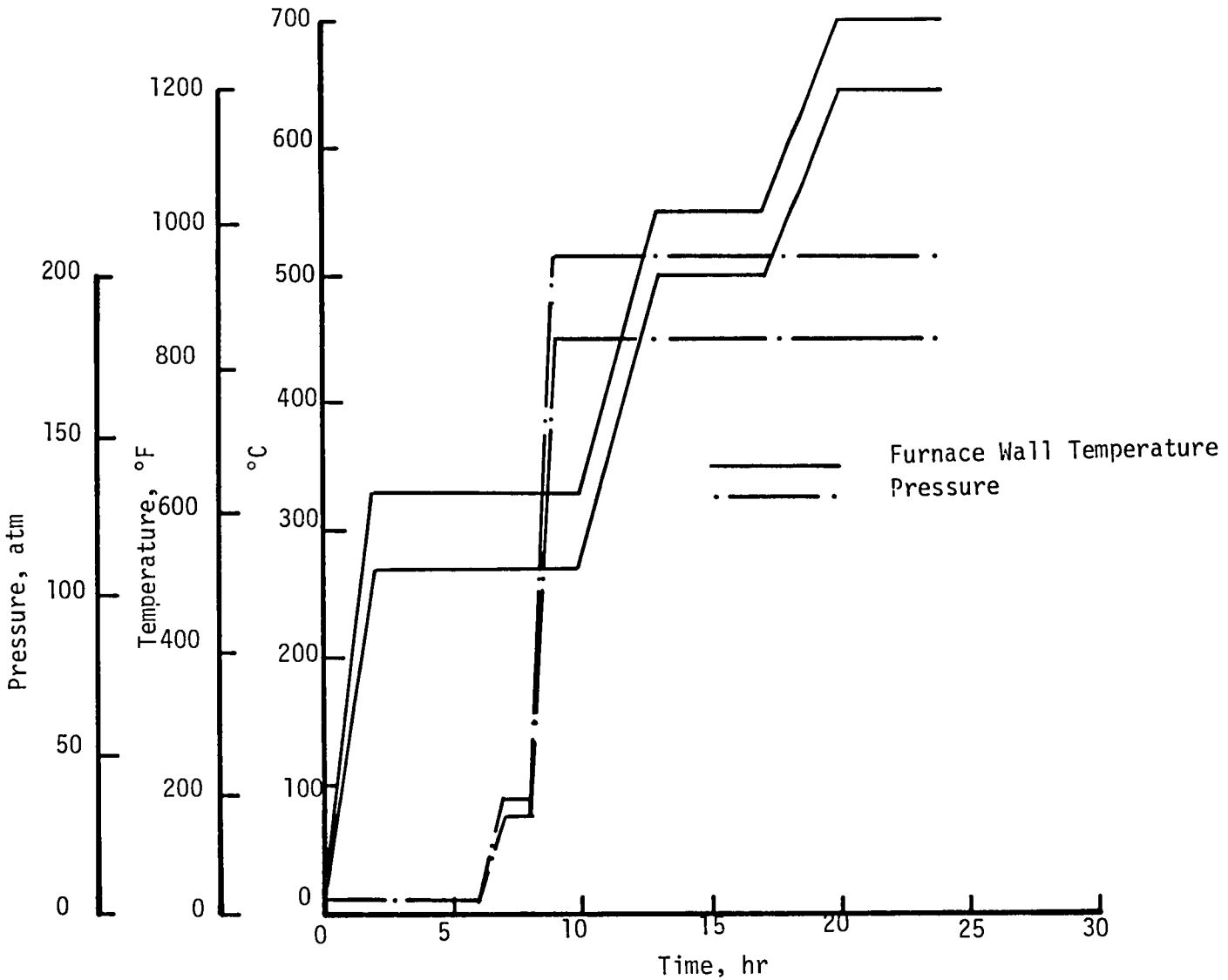

Figure 49. Carbonization Cycle

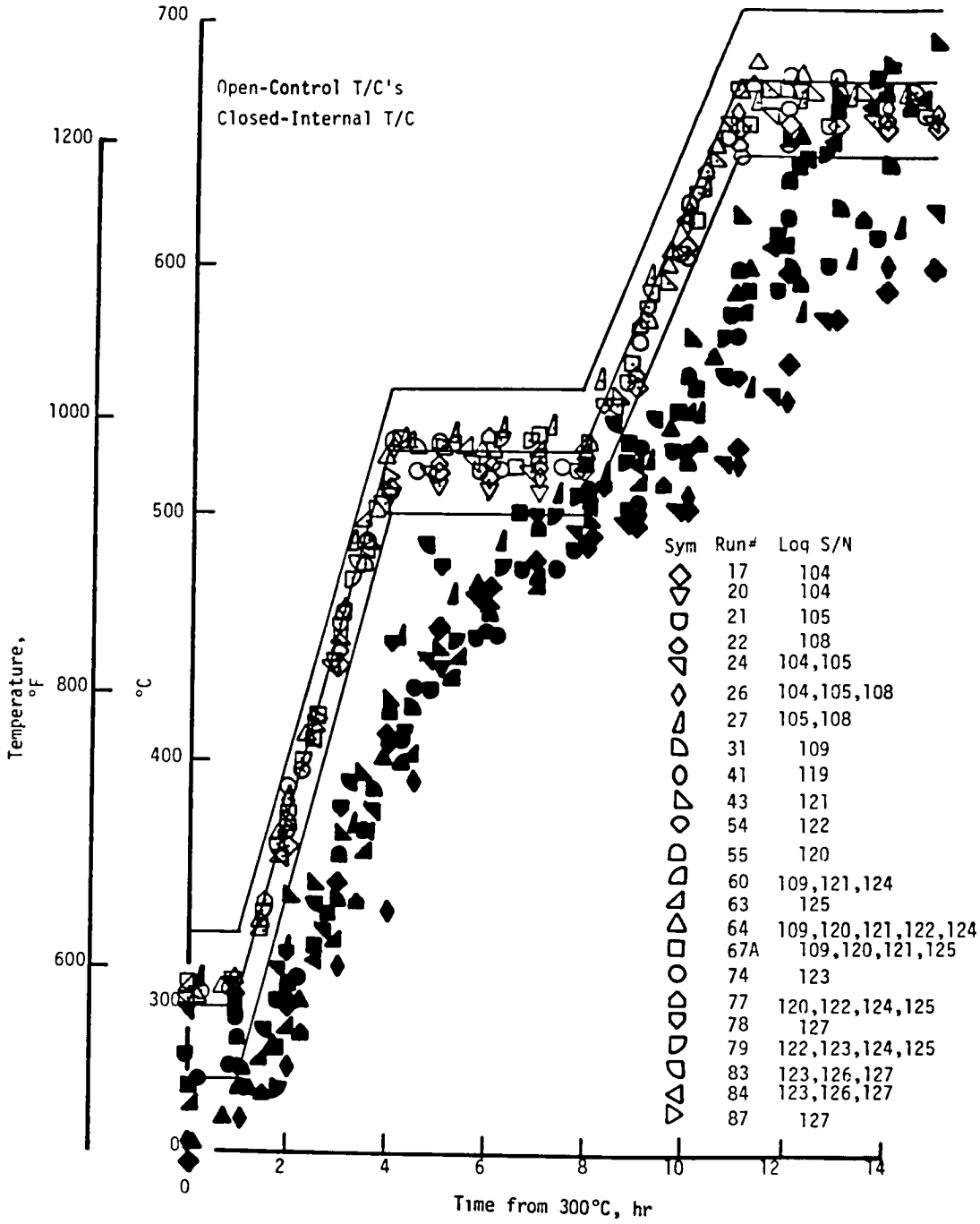

Figure 50. Summary of Carbonization Temperature Data

The above variations are not of any great consequence since the next step is to graphitize, thus each log will eventually be processed to the same temperature. Once the log has exceeded 500°C (930°F), conversion to solid carbon is complete and further mass loss is minimal.

The graphitization was carried out at Haveg Industries using an argon atmosphere similar to that used in the heat clean and carbonization cycles. Figure 51 presents the graphitization cycle used; in this case the temperature is the part temperature. Also shown are the data from a sampling of the runs. Not all the graphitization runs are shown because they are so close one cannot tell the difference between one and another. In all runs, the data fell within the tolerances of Figure 51.

Machining. - There were three separate machining steps. Rough machining was performed after the first graphitization to remove most of the selvage from the ID, OD and ends, Figure 52. Interim machining was performed after the third cycle to remove any skin build-up due to insoluble filtering as previously described, Figure 53. Typical log sectioning and final machining are shown in Figures 54 and 55. Where each billet was taken from the log was varied to avoid low quality regions. Thus billet numbering was not consistent.

Final Inspection. - After final machining each billet was subjected to a final x-ray inspection. Figure 56 presents the lay-out of shots. Single wall radial shots were taken every 30° around the OD with the film on the ID at three longitudinal locations. Tangential shots and axial shots were taken also as shown in Figure 56. Table 10 gives a summary of the acceptance criteria for these billets and Table 11 gives a summary of the x-ray inspection results for each billet.

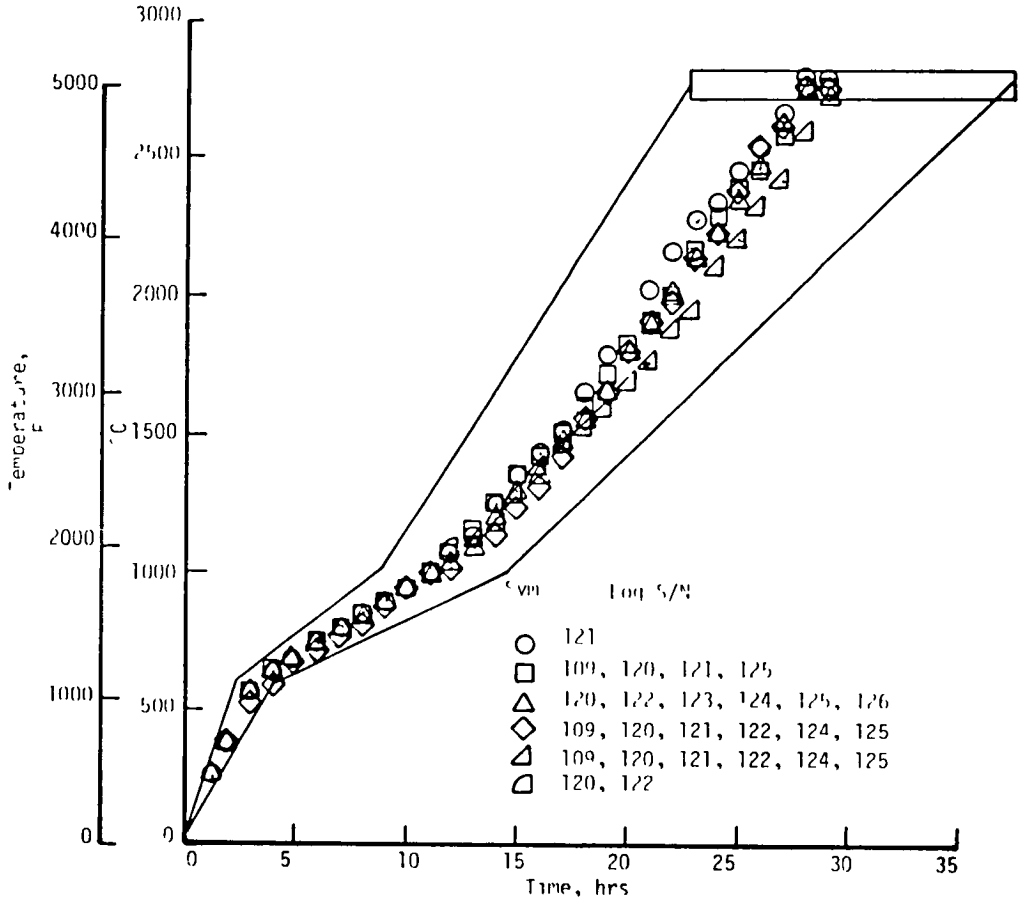

Figure 51. Graphitization Cycle

Rev	DESCRIPTION	DATE
A	DIMENSION CHANGE ON END VIEW ADD L DIMENSION LEGEND	12/11/78
B	[illegible]	[illegible]

NOTES FOR ROUGH MACHINING OPERATION

1. EACH PART HAS AN IDENTIFICATION TAG WHICH MUST STAY WITH THE PART UNTIL IT IS PERMANENTLY MARKED
2. THE PART IS SHIPPED WITH ONE END PAINTED WHITE WHICH INDICATES THE FORWARD (TOP) DIRECTION
3. THE PAINTED END HAS A CENTER ROD WHICH LOCATES THE GEOMETRIC CENTER OF THE PART
4. OPERATOR MUST GRIP UNPAINTED END AND PLACE A LINE CENTER AT GEOMETRIC CENTER WHICH IS LOCATED IN THE PAINTED END
5. THE SERVICE O THE OUTSIDE DIAMETER OF THE PAINTED END MUST BE REMOVED TO APPROXIMATE OUTSIDE DIAMETER BY USING THE LINE CENTER AS A REFERENCE
6. AFTER THE OUTSIDE DIAMETER OF THE PAINTED END HAS BEEN TURNED TO THE APPROXIMATE SIZE THE PART WILL THEN BE CHUCKED ON THE PAINTED END AND THE ENTIRE CYLINDER WILL BE TURNED TO REQUIRED DIMENSIO S
7. THE UNPAINTED END WILL BE FACED FLAT AND PARALLEL TO THE SIDES OF THE CYLINDER DURING THIS OPERATIO O MORE THAN 1 26 (0 5) WILL BE REMOVED FROM UNPAINTED END
8. THE PAINTED END WILL THEN BE FACED FLAT AND PARALLEL WITH THE SIDES OF THE CYLINDER DURING THIS OPERATION NO MORE THAN 1 89 (75) WILL BE REMOVED FROM THE PAINTED END
9. AT THIS TIME THE IDENTIFICATION INFORMATION ON THE ATTACHED TAG WILL BE TRANSFERRED TO ONLY THE FORWARD END THIS WILL BE DONE IMMEDIATELY AFTER THE PAINTED END IS FACED USE A VIBRO-ETCH PENCIL TO INSTALL IDENTIFICATION
10. INSTALL CENTER HOLE AFTER IDENTIFYING PART THE CENTER HOLE SHALL BE CONCENTRIC WITH THE OUTER DIAMETER WITHIN 0 25 (0 10)

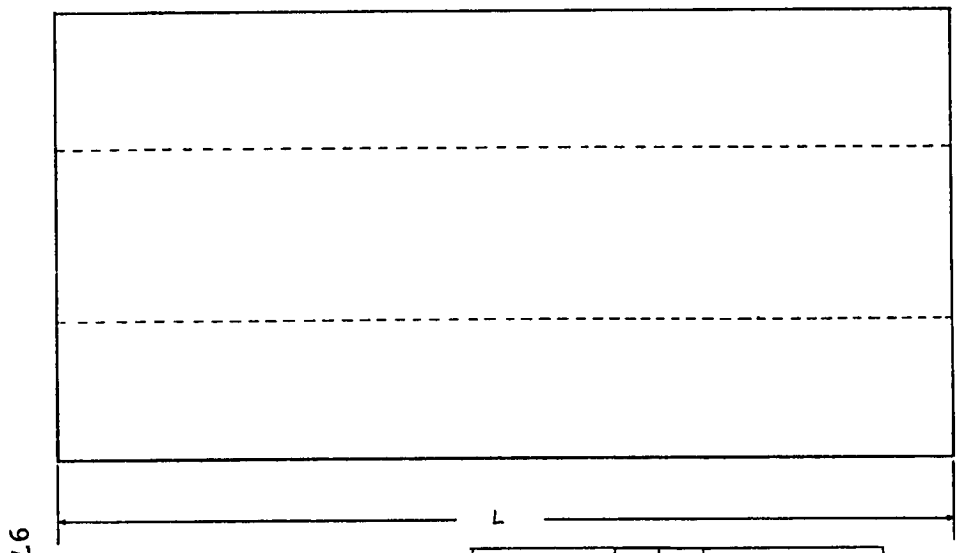

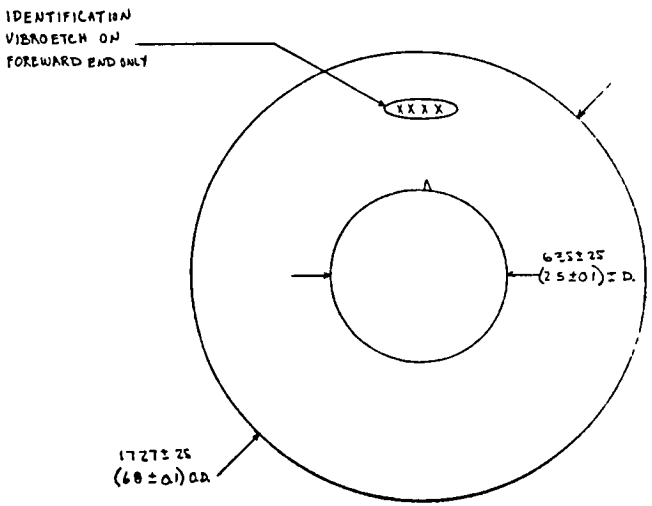

COMPONENT ID		L MIN	MAKE FROM
MSO-MC-0003	-01	21.75 (12.5)	MSO MC 0002-01
MSO MC 0003	-02	29.21 (11.50)	MSO MC-0002-02

Figure 52. Rough Machining

UNLESS OTHERWISE SPECIFIED DIMENSIONS ARE IN CM (IN) AND TOLERANCES ON
FRACTIONS = ± 1/16 X = ± .25 (.10)
ANGLES = ± 0.5 DEG XX = ± .076 (.030)
XXX = ± .025 (.010)

SCIENCE APPLICATIONS, INC-MSO

SCALE 2/1 APPROVED BY [signature] DRAWN BY [illegible]
DATE 11-2-78 REVISED [illegible]

BILLET - ROUGH MACHINING

CONTRACT NO	NEXT ASSEMBLY	SIZE		REV	DRAWING NUMBER
DAAA18-73 A-0127	MSO MC-0004		SHEET _ OF 1	B	MSO MC-0003

NOTES FOR INTERIM MACHINE OPERATION

1 PART IS IDENTIFIED ON FORWARD END WITH SERIAL NUMBER AND NOTCHED ON BOTH ENDS FOR DEGREE ORIENTATION IF AT ANY TIME DURING THIS OPERATION THE S/N OR EITHER OF THE DEGREE NOTCHES IS REMOVED IT MUST BE REPLACED BEFORE NEXT OPERATION

2 THIS OPERATION IS DESIGNED TO REMOVE ONLY THE OUTER 0.064 (0 025) SURFACE OF THE PART THIS APPLIES TO ENDS ID AND OD

3 'L OD and ID' ARE DIMENSIONS OF PARTIALLY PROCESSED PART AS RECEIVED AT VENDOR MATERIAL SHALL BE REMOVED FROM THESE DIMENSIONS

86

Rev	DESCRIPTION	DATE
A	ADD SEE NOTE 3	12/11/78
2	* DUPLICATE METRIC EQUIVALENT UNITS	11/18/80

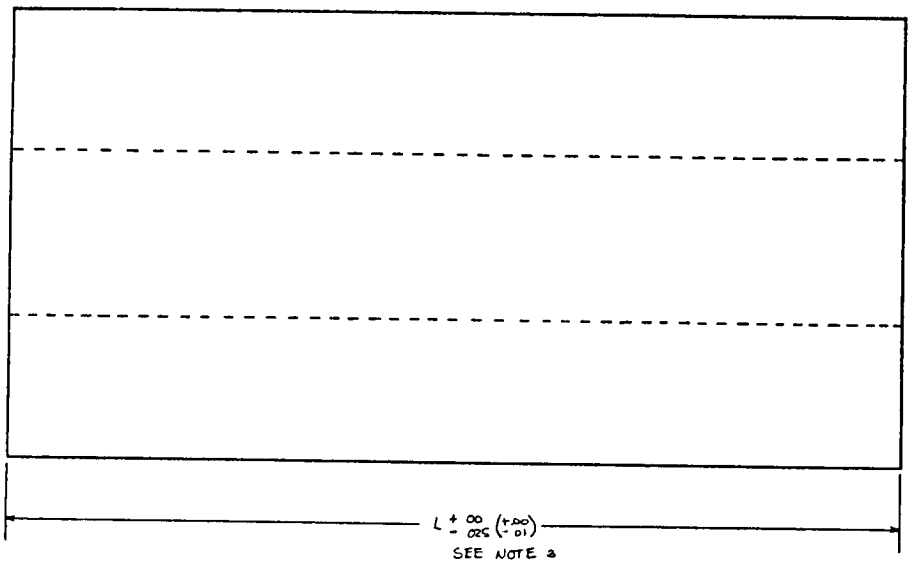

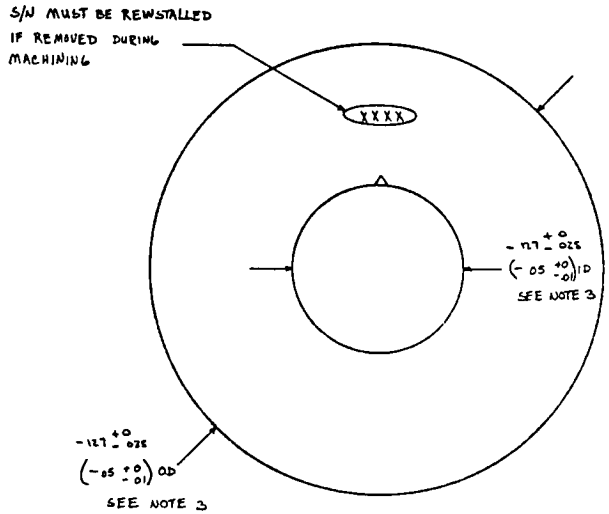

Figure 53. Interim Machining

UNLESS OTHERWISE SPECIFIED DIMENSIONS ARE IN CM (IN) AND TOLERANCES ON
FRACTIONS = ± 1/16 X = ± .25 (.10)
ANGLES = ± 0 5 DEG XX = ± .076 (.030)
XXX = ± .025 (.010)

SCIENCE APPLICATIONS, INC.-MSO

SCALE 4/1 = 1 | APPROVED BY: | DRAWN BY: | DATE 11-2-79 | REVISED 11/

BILLET - INTERIM MACHINING

CONTRACT NO DAEA18 79 A 0127 | NEXT ASSEMBLY MSO MC 0005 | SIZE | SHEET 1 of 1 | REV 2 | DRAWING NUMBER MSO MC 0004

REV	DESCRIPTION	DATE
A	ADD NOTE TO ADD E	8/22 [illegible]
B	ISSUED WITH METRIC EQUIVALENT UNITS	11/18/80

NOTES FOR REMOLDING SECTION OF PART

1 PART IS IDENTIFIED ON FORWARD END WITH SERIAL NUMBER AND NOTCHED ON BOTH ENDS FOR DEGREE ORIENTATION IF AT ANY TIME DURING THIS OPERATION THE S/ OR EITHER OF THE DEGREE NOTCHES IS REMOVED IT MUST BE REPLACED BEFORE THE NEXT OPERATION

2 AS RINGS SECTION OR SEGMENTS ARE PARTED THEY MUST BE IDENTIFIED AS TO FORWARD END AND DEGREE ORIENTATION EACH PART WILL BE ASSIGNED A DASH NUMBER WHICH MUST BE INCLUDED ON EACH PART

3 NEWLY PARTED SURFACES MUST BE P WORKED WITH 500 GRIT OR FINER PAPER

4 BREAK SHARP EDGES

5 THE PART SERIAL NUMBER DASH NUMBER AND ZERO DEGREE LOCATION SHOULD BE IDENTIFIED ON THE FORWARD FACE OF EACH PART WITH A WATER BASE WHITE MARKING SUBSTANCE

6 DEFORMED MATERIAL NOT TO BE INCLUDED IN BILLET THICKNESS TO BE DETERMINED BY QA USING X-RAY AND VISUAL INSPECTION

7 REMAINING MATERIAL TO BE USED FOR QC TESTING

NOTE TO 1 AND 5 THE NOTCH METHOD FOR IDENTIFICATION IS USED DURING THE PROCESSING OF THE LOG AFTER FINAL MACHINING A WHITE PAINT IS USED FOR IDENTIFICATION WITHOUT DEFACING BILLET

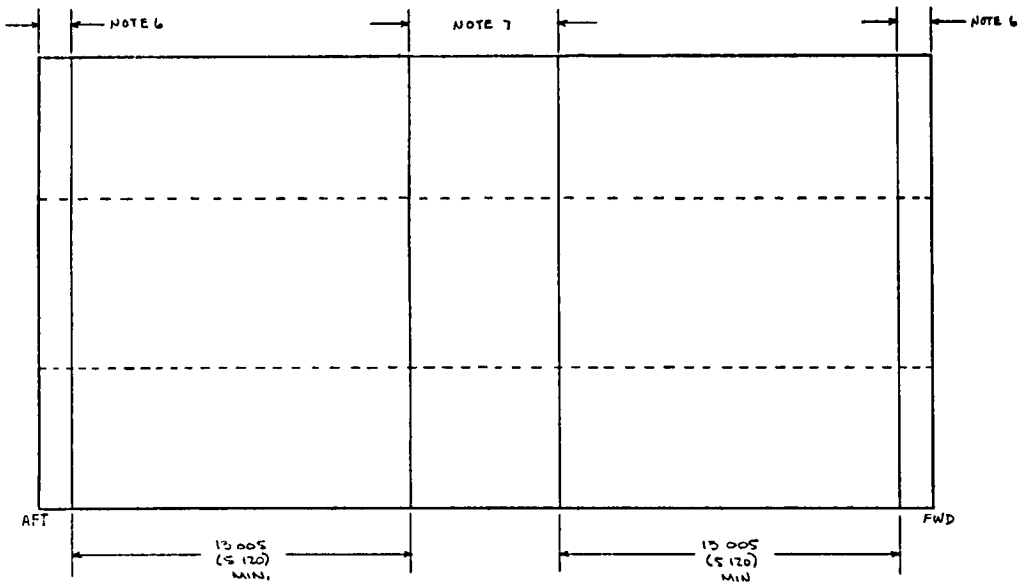

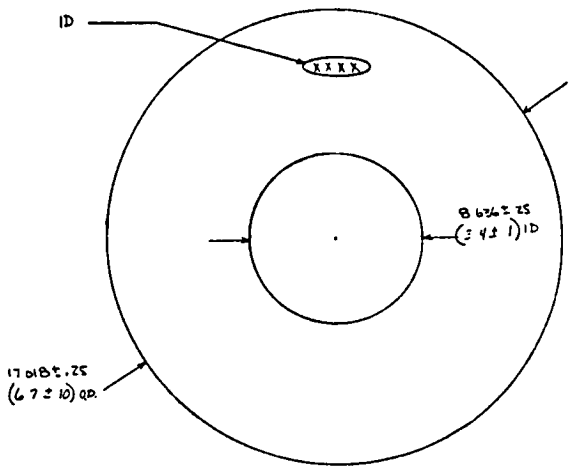

Figure 54. Log Sectioning

UNLESS OTHERWISE SPECIFIED DIMENSIONS ARE IN mm (in) AND TOLERANCES ON FRACTIONS ±1/16 ANGLES ±0.5 DEG X ±.25 (.01) XX ±.076 (.03) XXX ±.025 (.010)	SCIENCE APPLICATIONS, INC - MSO	
	SCALE: 1/4" = 1" APPROVED BY [signature] DRAWN BY [illegible]	
	DATE 11 2 18 REVISED [illegible]	
	BILLET - SECTIONING PLAN	
CONTRACT NO DREA18 73-A 0127	NEXT ASSEMBLY MSO-MC-0006	SIZE B SHEET 1 OF 1 DRAWING NUMBER MSO-MC-0005

NOTES

1 Billet(s) are to each be identified on the forward end of billet with the serial number, dash number and zero degree location White water base paint to be used for identification.

2 Surfaces must be finished with 500 grit or finer paper

3 Part must be free of sharp edges

4 Defect criteria to be

A) Broken rods (perpendicular to rod length) are not permitted

B) Separation between rods to matrix and within rods (parallel to rod length) are acceptable.

C) Low density, porous areas or non-uniform appearance shall not exceed 1 27 (50) in any direction.

D) Cracks in matrix are acceptable

F) U,V,W rod shall be ⊥ A within ±7°, z rods shall be // A within ±3° and ⊥ B within ±2°

F) Rods shall be uniform and straight in appearance

Rev	DESCRIPTION	DATE
A	ADD FLAGS AAR TO DRAWING	1/13/80
B	[illegible]	[illegible]
C	[illegible]	11/84

100

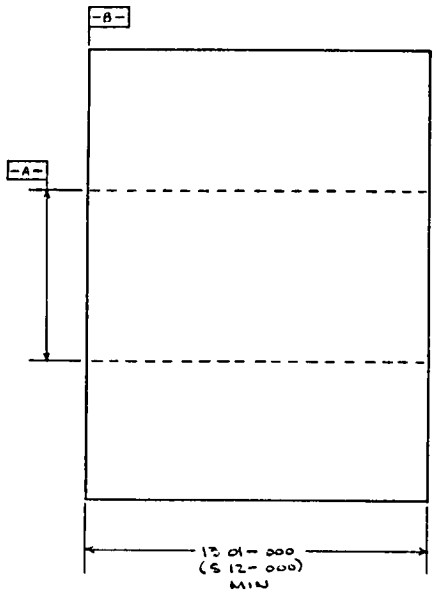

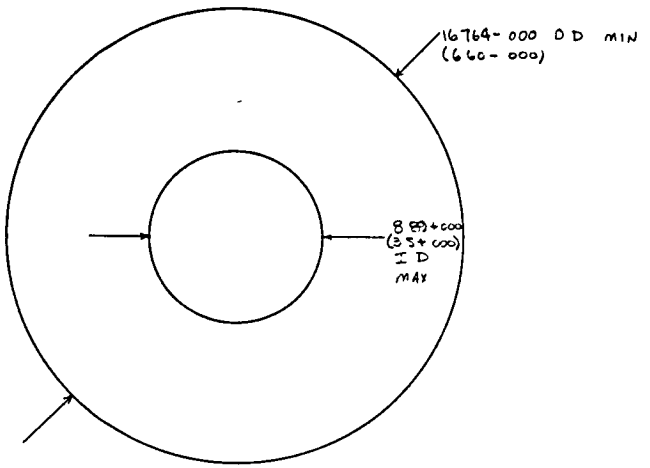

Figure 55. Final Machining

UNLESS OTHERWISE SPECIFIED DIMENSIONS ARE IN CM (IN) AND TOLERANCES ON FRACTIONS = ± 1/16 ANGLES = ± 0 5 DEG X = ± 25 (10) XX = ± 076 (03) XXX = ± 010 (005)	SCIENCE APPLICATIONS, INC.	
SCALE 1/1 1	APPROVED BY	DRAWN BY
DATE		REVISED
	BILLET - 1"	
CONTRACT NO DAEA18 73-A 0127	NEXT ASSEMBLY NONE	SIZE C
	SHEET 1 OF 1	DRAWING NUMBER

NOTES FOR X-RAY INSPECTION

1 EACH TUBE [illegible] LABELED ON THE FORWARD END WITH A SERIAL NUMBER AND A NOTCH FOR DEGREE ORIENTATION ALL RADIOGRAPHIC X-RAYS MUST BE REFERENCED TO THESE LOCATIONS

2 RADIAL IN SECTION PERFORMED PRIOR TO CUTTING

ITEM 1 EACH PART WILL BE X-RAYED THROUGH THE SINGLE WALL EVERY 30° AT THREE PLACES

ITEM 2 EACH PART WILL BE X-RAYED THROUGH THE DOUBLE WALL AT TANGENTS OF 0 30, 60 90 120 and 150° AT TWO PLACES

3 AXIAL INSPECTION PERFORMED AFTER SECTIONING

ITEM 3 EACH PART WILL BE X-RAYED THROUGH THE LENGTH AT 45° INCREMENTS MAX

4 WHEN PARTS ARE RETURNED VENDOR WILL INCLUDE, BUT NOT BE LIMITED TO X-RAYS, X-RAY SOURCE, DISTANCE FROM PART FILM TYPE AND ANY ADDITIONAL PERTINENT INFORMATION

5 X-RAY FILM SHOULD BE LOCATED AS SHOWN

[illegible]	[illegible]	DATE
1	[illegible]	2/4/77
2	[illegible]	1/14/80

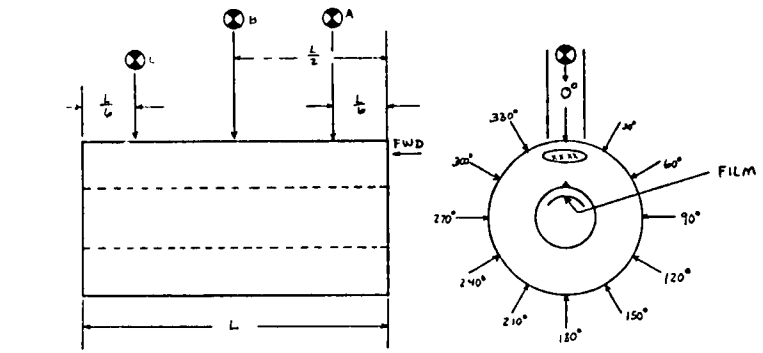

ITEM 1 SKETCH SHOWS WHERE SINGLE WALL X RAYS SHALL BE TAKEN TOTAL 36 SHOTS

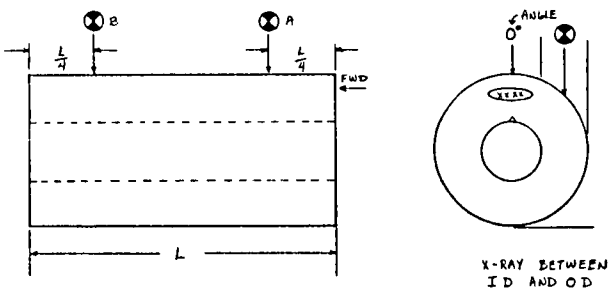

ITEM 2 SKETCH SHOWS WHERE DOUBLE WALL TANGENTIAL X RAYS SHALL BE TAKEN
TOTAL 12 SHOTS
6 VIEWS 2 PLACES

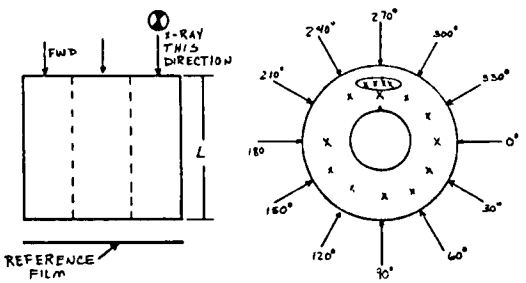

ITEM 3 AXIAL VIEWS SKETCH WHERE LENGTHWISE X-RAYS SHALL BE TAKEN TOTAL 12 VIEWS EACH PART

101

Figure 56. X-Ray Inspection

UNLESS OTHERWISE SPECIFIED DIMENSIONS ARE IN CM (IN) AND TOLERANCES ON FRACTIONS = ± 1/16 ANGLES = ± 0 5 DEG X = ± 25 (.10) XX = ± 076 (.030) XXX = ± 025 (.010)	SCIENCE APPLICATION, INC-MSO		
	SCALE 1/1 = 1"	APPROVED BY [signature]	DRAWN BY [illegible]
	DATE 3-16-79		REVISED 11/213
	BILLET / X-RAY INSPECTION		
CONTRACT NO DAE18-73-A-0127	NEXT ASSEMBLY NONE	SIZE	SHEET 1 OF 1
		REV B	DRAWING NUMBER MS.? SI-0003

Table 10. Acceptance Criteria for Production Antares III 4-D Carbon-Carbon

Dimensions in cm (in)

INDICATION (After final graphitizatio)	ACCEPTANCE CRITERIA	INSPECTION METHOD
Missing rods on machined surfaces (dislodged by machining)	O.D. Bonding Surface: Less than 1.27 (.5) long throat: Radial depth less than .051 (.02) I.D. surfaces (except throat): less than 1.27 (.5) long	Visual
Missing Rods	Five per log, no two rods can be missing within one inch of each other in any direction	Visual, Radiography
Broken Rods	None allowed	Visual, Radiography
Separations: Rod-to-matrix and within rods (between tows)	Separations parallel to rod length are acceptable	Visual, Radiography
Low density, porous areas, or nonuniform appearance	Less than 1.27 (.5) in any direction except none allowed within plus or minus 1.27 (.5) of estimated throat plane	Visual, Radiography
Scratches on ID surfaces	Less than .051 (.02) depth	Visual
UVW Rod Spacing	Average Spacing: .145 (.057) maximum for any layer/increment divided by nine Maximum separation between adjacent layers .051 (.02)	Visual, Radiography
Cracks in matrix	Matrix cracks in areas having acceptable UVW and Z rod spacing are acceptable. Cracks in matrix in areas of unacceptable rod spacing are not allowed	Visual, Radiography
Rod orientation	UVW Rods: perpendicular to & within 7° Angle of twist in Z rods shall be less than 3°	Visual, Radiography
Density	1.82 to 1.90 g/cm^3 (113.6 to 118.6 lb/ft^3)	--

Table 11. Final X-Ray Inspection Results

Billet S/N	Observations	Comments
104-1	No anomalies	
104-2	No anomalies	
105-1	Low density areas visible around 90% of circumference	Accepted
105-2	Low density area visible around 70% of circumference	Accepted
108-1	No anomalies	
108-3	No anomalies	
109-1	Slight low density areas 7.6cm from aft end of log	Accepted
109-2	See 109-1	
119-1	Separation	Rejected
119-2	Separation	Rejected
120-1	No anomalies	
120-3	No anomalies	
121-1	Low density striations at forward end	Accepted
121-3	No anomalies	
122-2	Slight low density areas	Accepted
122-3	Low density regions and distorted reinforcements	Rejected
123-1	Separation	Rejected
123-2	Slight low density areas and distorted axial rods	Accepted
124-1	No anomalies	
124-3	No anomalies	
125-2	No anomalies	
125-3	No anomalies	
126-1	No anomalies	
126-3	Separation	Rejected
127-2	No anomalies	
127-3	No anomalies	

Table 12. Final Visual Inspection Results

Billet S/N	ID, cm (in)	OD, cm (in)	Length, cm (in)	Weight, gm (lb)	Density, g/cm^3 (lb/in^3)	Reinforcement Spacing: Axial-Row, cm (in)	Reinforcement Spacing: Axial C-C, cm (in)	Reinforcement Spacing: Transverse, cm (in)	Max. Axial Twist, deg
103-1	8.898(3.503)	17.013(6.698)	13.033(5.131)	3947(8.694)	1.834(114.442)	NM	NM	.134(.053)	NM
103-2	9.055(3.565)	16.990(6.689)	13.058(5.141)	3882(8.551)	1.832(114.317)	NM	NM	.132(.052)	NM
104-1	8.573(3.375)	17.010(6.697)	13.040(5.134)	4085(9.006)	1.848(115.315)	NM	NM	.117(.046)	NM
104-2	8.570(3.374)	17.056(6.715)	13.559(5.338)	4219(9.301)	1.822(113.693)	NM	NM	.122(.048)	NM
105-1	8.588(3.381)	17.026(6.703)	13.190(5.193)	4085(9.006)	1.825(113.880)	NM	NM	.124(.049)	NM
105-2	8.555(3.368)	17.051(6.713)	13.066(5.144)	4082(8.999)	1.828(114.067)	NM	NM	.137(.054)	NM
108-1	6.406(2.522)	17.463(6.875)	21.694(8.541)	8286(18.267)	1.840(114.816)	NM	NM	.122(.048)	NM
108-3	6.375(2.510)	17.508(6.893)	3.023(1.190)	1173(2.586)	1.850(115.440)	NM	NM	.122(.048)	NM
109-1	8.623(3.395)	17.064(6.718)	12.758(5.032)	3991(8.799)	1.833(114.379)	.650(.256)	.368(.145)	.112(.044)	.62
109-2	8.618(3.393)	17.051(6.713)	12.705(5.002)	3980(8.774)	1.840(114.816)	.632(.249)	.363(.143)	.124(.049)	1.13
120-1	8.588(3.381)	16.815(6.620)	13.305(5.238)	4012(8.845)	1.837(114.629)	.632(.249)	.361(.142)	.124(.049)	1.92
120-3	8.585(3.380)	16.830(6.626)	13.139(5.173)	3974(8.761)	1.837(114.629)	.632(.249)	.363(.143)	.127(.050)	1.72
121-1	8.623(3.395)	17.043(6.710)	13.259(5.220)	4164(9.180)	1.850(115.440)	NM	NM	.119(.047)	NM
121-3	8.631(3.398)	17.054(6.714)	13.277(5.227)	4186(9.228)	1.855(115.752)	NM	NM	.130(.051)	NM
122-2	8.623(3.395)	16.866(6.640)	12.852(5.060)	3919(8.640)	1.849(115.378)	.630(.248)	.363(.143)	.117(.046)	1.25
123-2	8.611(3.390)	16.985(6.687)	13.007(5.121)	4101(9.041)	1.873(116.875)	.653(.257)	.376(.148)	.119(.047)	2.10
124-1	8.626(3.396)	16.894(6.651)	13.294(5.234)	4052(8.933)	1.839(114.754)	.645(.254)	.366(.144)	.122(.048)	.50
124-3	8.623(3.395)	16.894(6.651)	13.109(5.161)	4015(8.851)	1.848(115.315)	.640(.252)	.368(.145)	.127(.050)	.80
125-2	8.626(3.396)	16.805(6.616)	13.104(5.159)	3935(8.675)	1.838(114.691)	.630(.248)	.366(.144)	.124(.049)	.37
125-3	8.628(3.397)	16.805(6.616)	13.162(5.182)	3960(8.730)	1.841(114.878)	.635(.250)	.368(.145)	.127(.050)	.72
126-1	8.679(3.417)	17.010(6.697)	13.254(5.218)	4057(8.944)	1.821(113.630)	.632(.249)	.363(.143)	.127(.050)	.60
127-2	8.580(3.378)	17.028(6.704)	13.096(5.156)	4067(8.966)	1.827(114.005)	.632(.249)	.366(.144)	.130(.051)	.65
127-3	8.641(3.402)	17.054(6.714)	13.106(5.160)	4087(9.010)	1.836(114.566)	.627(.247)	.366(.144)	.127(.050)	.50
Required	8.870(3.500) Max.	16.764(6.600) Min.	13.005(5.120) Min.	None	1.820(113.568) Min.	.616(.247 +.051+.020 -.013-.005)	.363(.143 +.025+.010 -.013-.005)	.137(.054) Max.	3.00 Max.

Note: Rejected billets not subjected to final inspection

In addition to x-ray inspection, visual inspection was also performed. This consisted of a qualitative portion for overall appearance and a quantitative portion for final dimensions, final weight, final density, reinforcement spacings and log twist. Table 12 summarizes this data for each billet. Billets S/N's 108-1 and 108-3 were non-standard since they were used for material characterization studies at SoRI. Where differences occur from the required values, the billets were accepted by Vought Corporation, except as noted.

Table 13 and Figure 57 presents the density of each log after each densification cycle. With the exception of log S/N's 103 and 121 after the first cycle, the data forms a tight grouping verifying the very reproducible processing as indicated earlier. Figure 58 is a plot of density increase on a given cycle as a function of the density at the beginning of that cycle.

Table 13. Density Histories

Log S/N	Cycle* 1	2	3	4
103	1.29(80.50)**	1.55(96.72)	1.71(106.70)	1.83(114.19)
104	1.34(83.62)	1.59(99.22)	1.74(108.58)	1.82(113.57)
105	1.33(82.99)	1.57(97.97)	1.71(106.70)	1.83(114.19)
108	1.34(83.62)	1.57(97.97)	1.75(109.20)	1.85(115.44)
109	1.32(82.37)	1.57(97.97)	1.74(108.58)	1.84(114.82)
119	1.32(82.37)	Log rejected after first cycle		
120	1.32(82.37)	1.57(97.97)	1.73(107.95)	1.82(113.57)
121	1.27(79.25)	1.61(100.46)	1.76(109.82)	1.85(115.44)
122	1.35(84.24)	1.56(97.34)	1.76(109.82)	1.84(114.82)
123	1.36(84.86)	1.60(99.84)	1.75(109.20)	1.87(116.69)
124	1.33(82.99)	1.58(98.59)	1.75(109.20)	1.84(114.82)
125	1.34(83.62)	1.58(98.59)	1.75(109.20)	1.84(114.82)
126	1.33(82.99)	1.58(98.59)	1.73(107.95)	1.84(114.82)
127	1.38(86.11)	1.57(97.97)	1.73(107.95)	1.84(114.82)

* After Graphitization

** g/cm^3 (lb/ft^3)

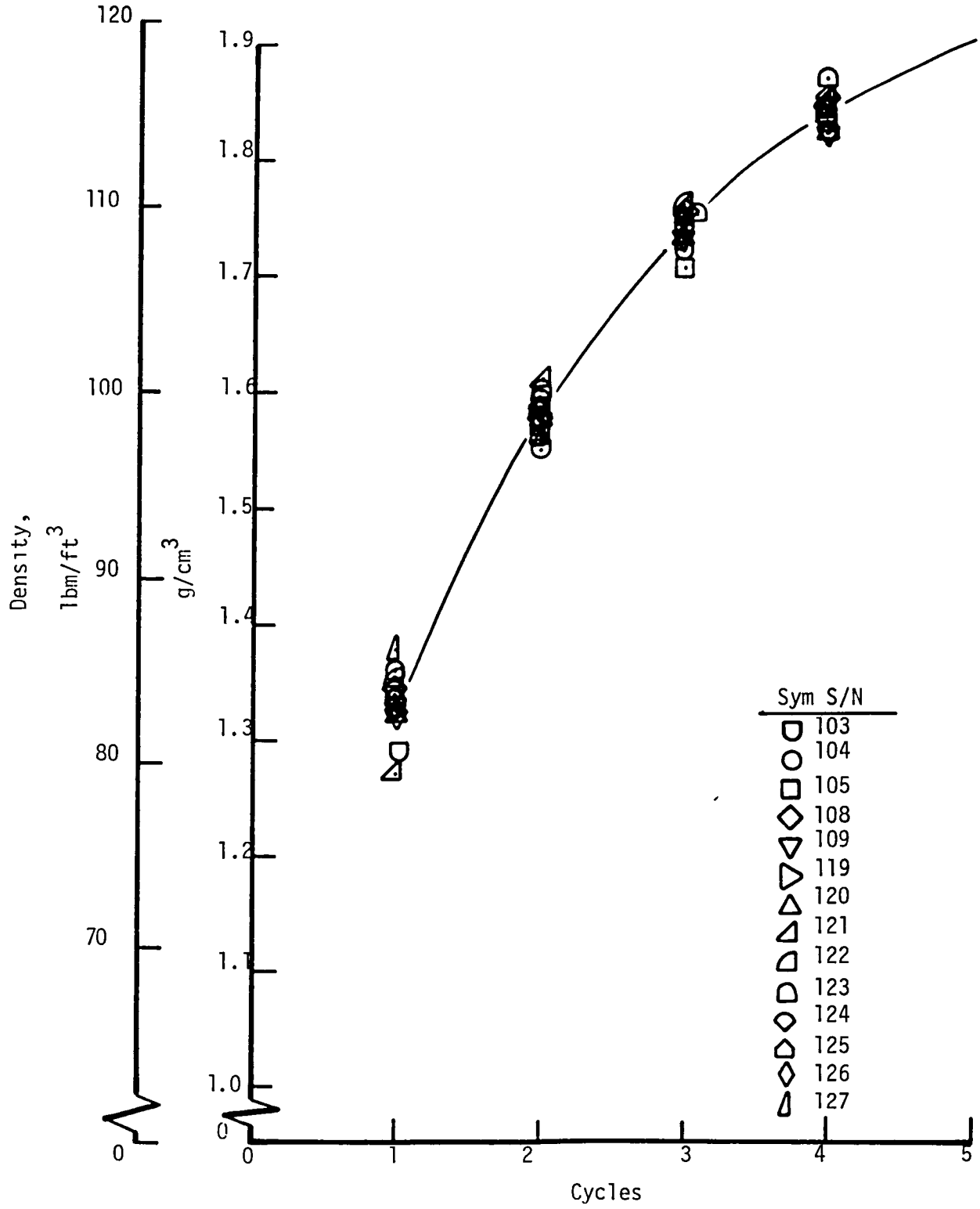

Figure 57. Density Histories

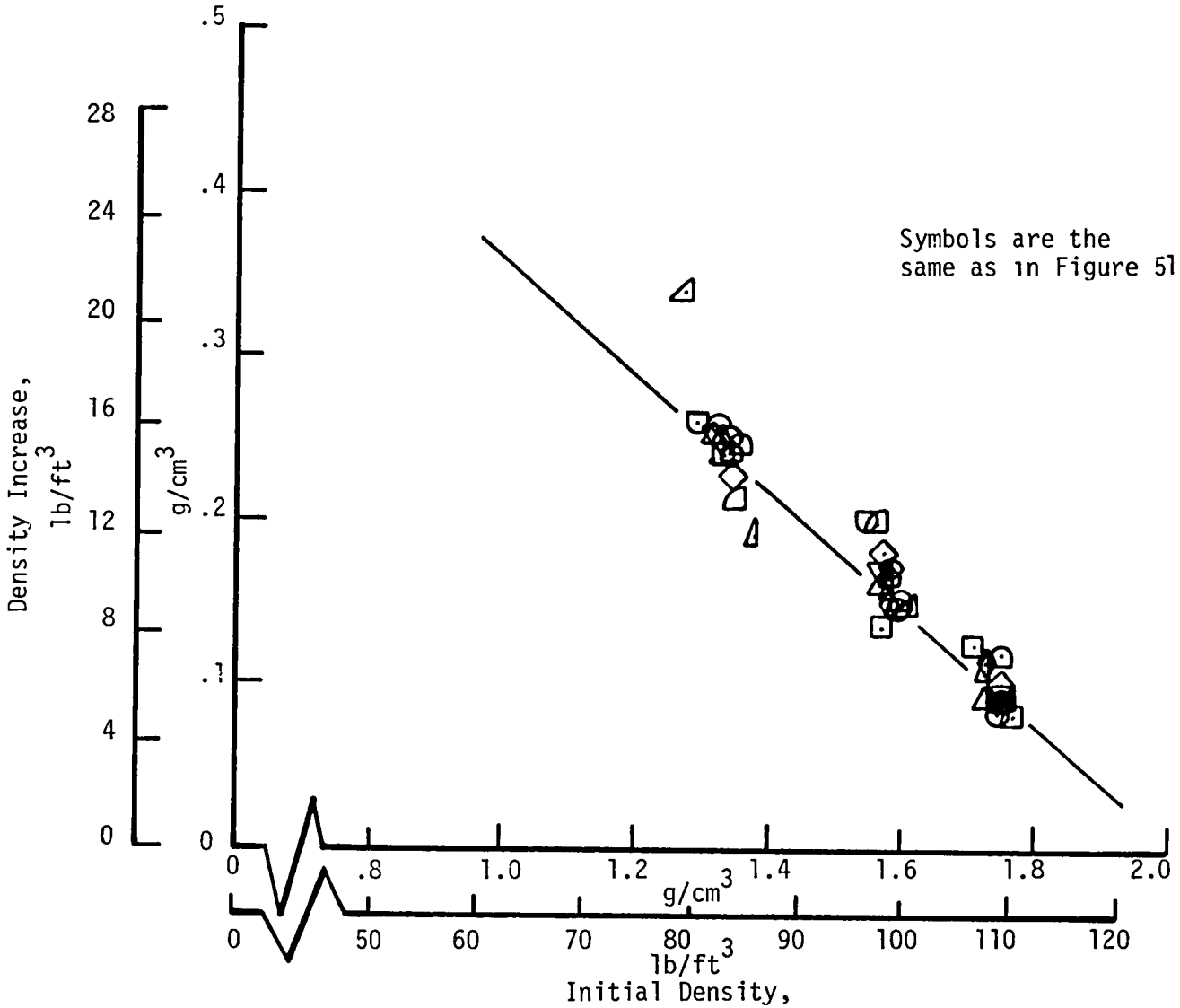

Figure 58. Densification Efficiency

MATERIAL CHARACTERIZATION

A thorough characterization of the material was carried out during the program. This consisted of microstructural, mechanical and thermal properties evaluations.

Microstructural Evaluation

Figures 59 and 60 present photomicrographs of log S/N 108 at two magnifications in two directions. Figure 59 presents the view parallel to the transverse direction showing the U fibers in the plane of the photo and the ends of the V and W bundles. The microcracking within the bundles, Figures 59a and 60a, is typical of all carbon-carbons of this general type. Of particular interest is the regularity of the bundle shapes, the lack of bundle billowing into the matrix pockets and the fine scale of the porosity in the matrix phase. This latter is a direct result of the use of powder as the initial "impregnant."

Tables 14 and 15 present the microstructural unit cell measurements; Figure 61 defines the measured quantities. Data were taken at five locations along the length of S/N 108 and all measured values are quite uniform along the length. The data in Table 15 represent the amount of shrinkage in bundle size that occurred during processing.

Macrostructural Evaluation

The mechanical properties were characterized with two goals in mind. The first was to obtain the various design properties of the material in each principal direction over the temperature range expected during use. This testing was conducted at SoRI. The second goal was to obtain a simple room temperature tag end evaluation of each log as a quality assessment indicator. This testing was conducted at SAI.

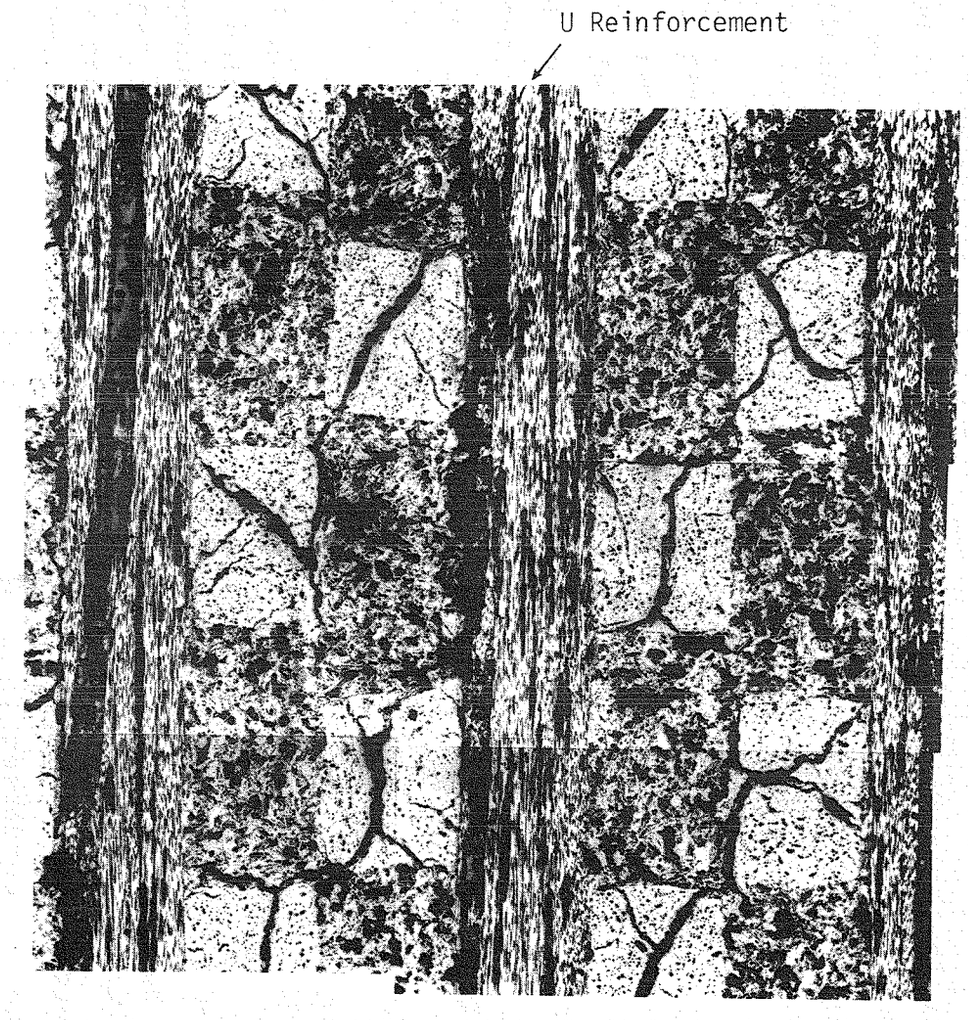

a. 26X

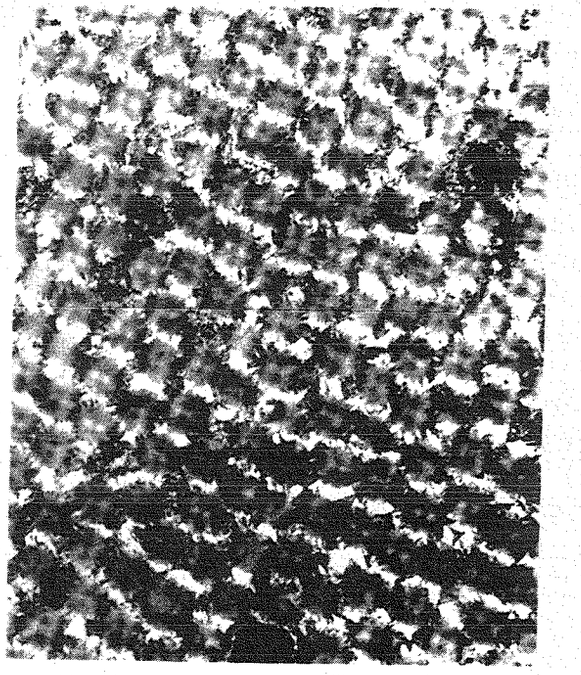

b. 1300X

Figure 59. Microstructure, Log S/N 108

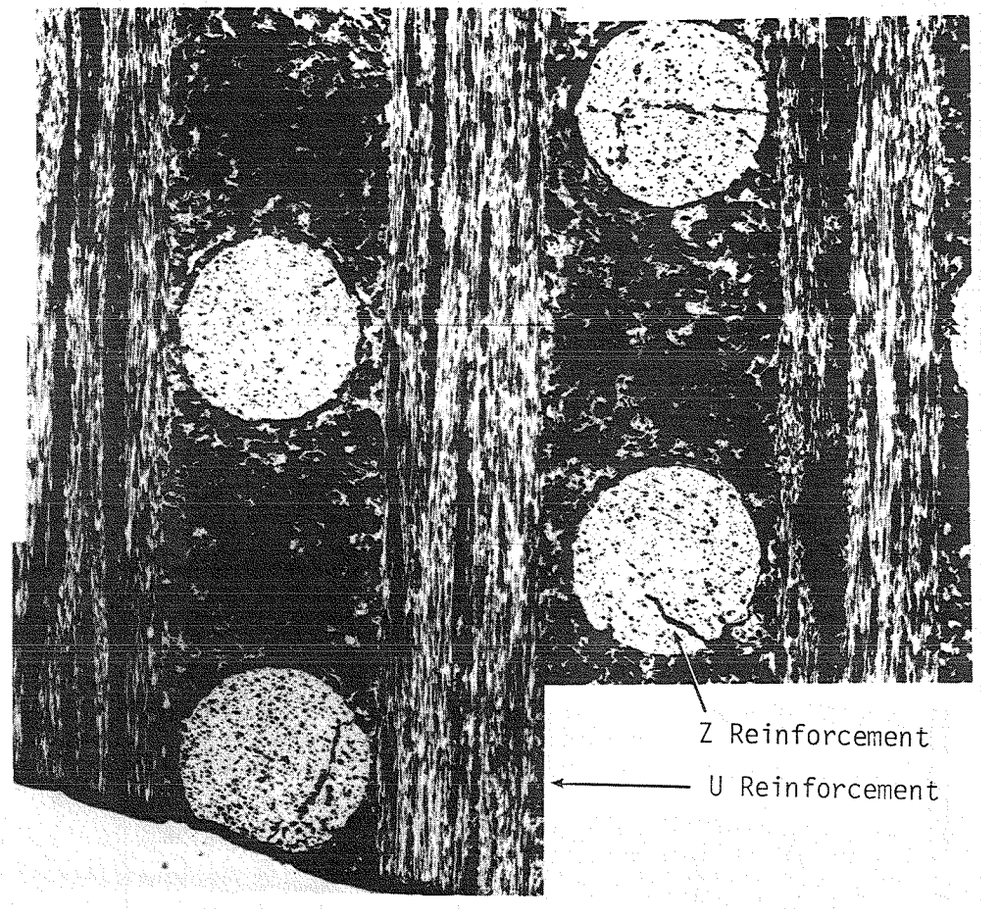

a. 26X

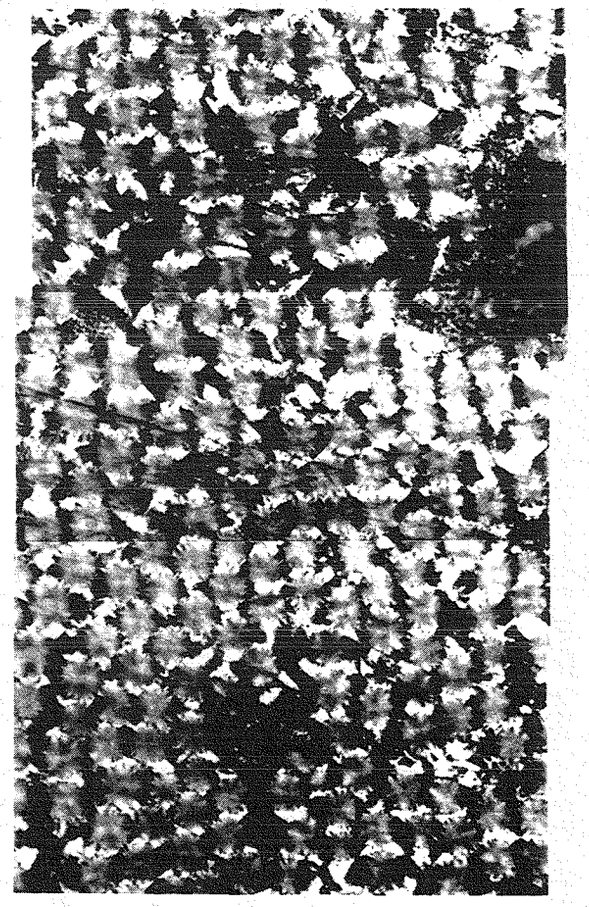

b. 1300X

Figure 60. Microstructure, Log S/N 108

Table 14. Log S/N 108 Microstructural Dimensions
-cm(in)-

Location	ΔL	ΔU	ΔZ	u_u	u_z	d_z
Top	.381(.150)	.323(.127)	.366(.144)	.132(.052)	.117(.046)	.165(.065)
Mid-Top	.384(.151)	.328(.129)	.368(.145)	.132(.052)	.119(.047)	.173(.068)
Middle	.356(.140)	.325(.128)	.376(.148)	.130(.051)	.122(.048)	.170(.067)
Mid-Bottom	.376(.148)	.323(.127)	.381(.150)	.127(.050)	.119(.047)	.173(.068)
Bottom	.358(.141)	.325(.128)	.406(.160)	.127(.050)	.127(.050)	.170(.067)
Average	.325(.146)	.325(.128)	.378(.149)	.130(.051)	.122(.048)	.170(.067)

Table 15. Microcrack/Matrix Pad Thicknesses
-cm(in)

Location	Axial/Transverse $(\Delta U-u_u-d_z)/2$	Transverse/Transverse $(\Delta Z-3u_z)/3$
Top	.0127(.0050)	.0051(.0020)
Mid-Top	.0114(.0045)	.0033(.0013)
Middle	.0127(.0050)	.0033(.0013)
Mid-Bottom	.0114(.0045)	.0076(.0030)
Bottom	.0140(.0055)	.0084(.0033)
Average	.0124(.0049)	.0055(.0022)

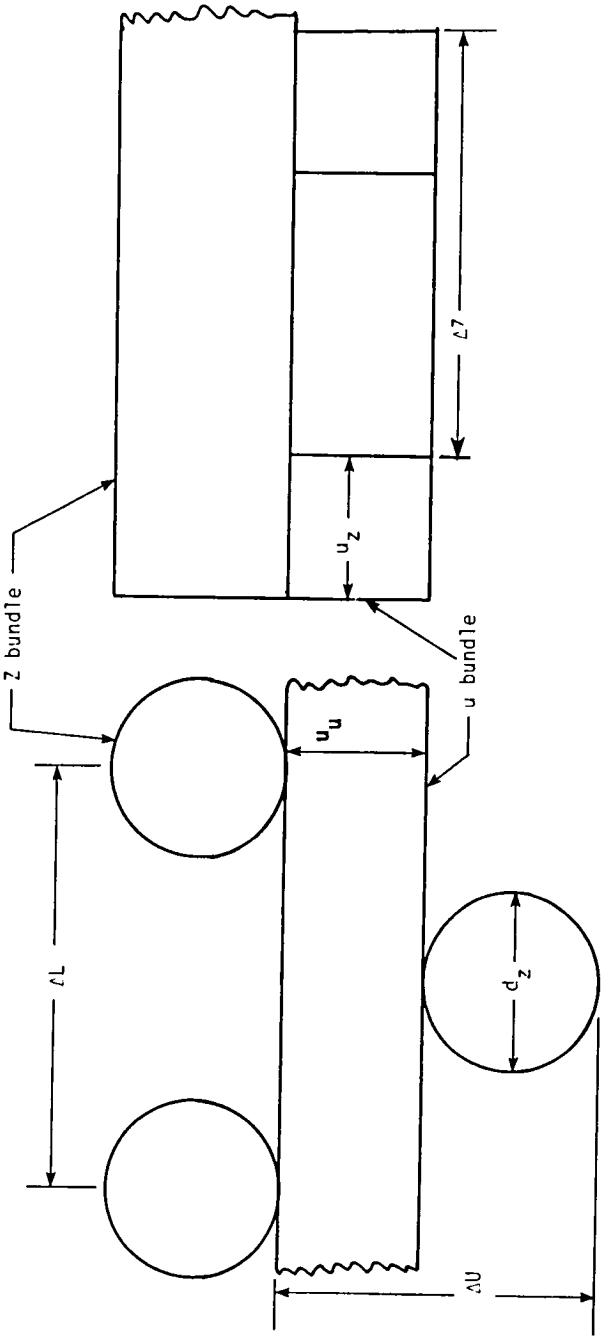

Figure 61. Unit Cell Measurements

Design Properties. - The determination of design properties was carried out in two distinct steps. Early in the program properties were required for use in the design analysis. Since no material had yet been made for this program, it was decided to perform a limited characterization of log S/N 102 which was available off-the-shelf. The primary differences between this material and that ultimately used on Antares III was its higher density of about 1.9-1.93 g/cc (118.56-120.43 lb/ft^3). In addition to the data collected in the present program, data on this same log were collected at SoRI under the CCAN program, Reference 27. Tables 16 and 17 contain the test matrices for these two evaluations of log S/N 102.

The main characterization carried out under this program was performed on log S/N 108, Reference 28. Table 18 contains the test matrix. This log was cut into the two billets shown in Figure 62.

Based on the results obtained with log S/N 102, a particular concern prior to testing log S/N 108 was the tensile specimen design. Past experience with carbon-carbon materials and log S/N 102 had shown that it is difficult to obtain pure test section tensile failure due to the vast differences between the tensile strength of the aligned fiber bundles and the interfacial and cross-fiber shear strengths. More often than not either the longitudinal fibers pull out of one of the heads or the heads shear in the grip region. Figure 63 is a sketch of these two failure modes. The only solution to avoiding either failure mode is to increase the shear load carrying capability within the specimen head either by increasing the head length or the shear strength.

Appendix A contains an approximate analysis of these two problems to guide the design of the tensile specimens for the axial, Z, and

Table 16. Test Matrix, Billet S/N 102

Test	Temp,°C (°F)	Direction	No. of Tests
Tension	20 (70)	Z	3
		U	3
		U+30	3
	1370 (2500)	Z	3
		U	3
		U+30	3
Compression	20 (70)	Z	2
		U	3
		U+30	2
	540 (1000)	Z	2
		U	2
		U+30	2
	1650 (3000)	Z	2
		U	2
		U+30	2
	2750 (5000)	Z	2
		U	2
		U+30	1
Shear (Cross-Fiber)	20 (70)	UZ	2
		UZ+30	2
	1650 (3000)	UZ	2
	2750 (5000)	UZ	2
Thermal Expansion	20-2750 (70-5000)	Z	1
		U	2
		U+30	2
Thermal Conductivity	20-800 (70-1500)	Z	1
		U	1
		U+30	1

Table 17. Test Matrix, Billet S/N 102 (CCAN)

Test	Temp, °C (°F)	Direction	No. of Tests
Tension	20 (70)	Z	3
		U	2
Compression	20 (70)	Z	2
		U	2
	2750 (5000)	Z	2
		U	2
Thermal Expansion	20-2750 (70-5000)	Z	1
		U	1

Table 18. Test Matrix, Log S/N 108

Test	Temp, °C (°F)	Direction	No. of Tests
Tension	20 (70)	Z	3
		U	3
	1200 (2200)	Z	3
		U	3
		U+30	2
	2650 (4800)	Z	3
		U	2
		U+30	2
Compression	20 (70)	Z	3
		U	3
		U+30	3
	1200 (2200)	Z	3
		U	3
		U+30	3
	2650 (4800)	Z	3
		U	3
		U+30	3
Shear (Axial Torsion)	20 (70)	UZ	3
	1200 (2200)	UZ	2
	2650 (4800)	UZ	2
45° Compression	20 (70)	UZ	2
	1200 (2200)	UZ	2
	2650 (4800)	UZ	2
Thermal Expansion	20-2750 (70-5000)	Z	2
		U	2
		U+30	2
Thermal Conductivity	20-2750 (70-5000)	Z	1
		U	1
		U+30	1
Flexure	20 (70)	Z	2
		U	2
		U+30	2

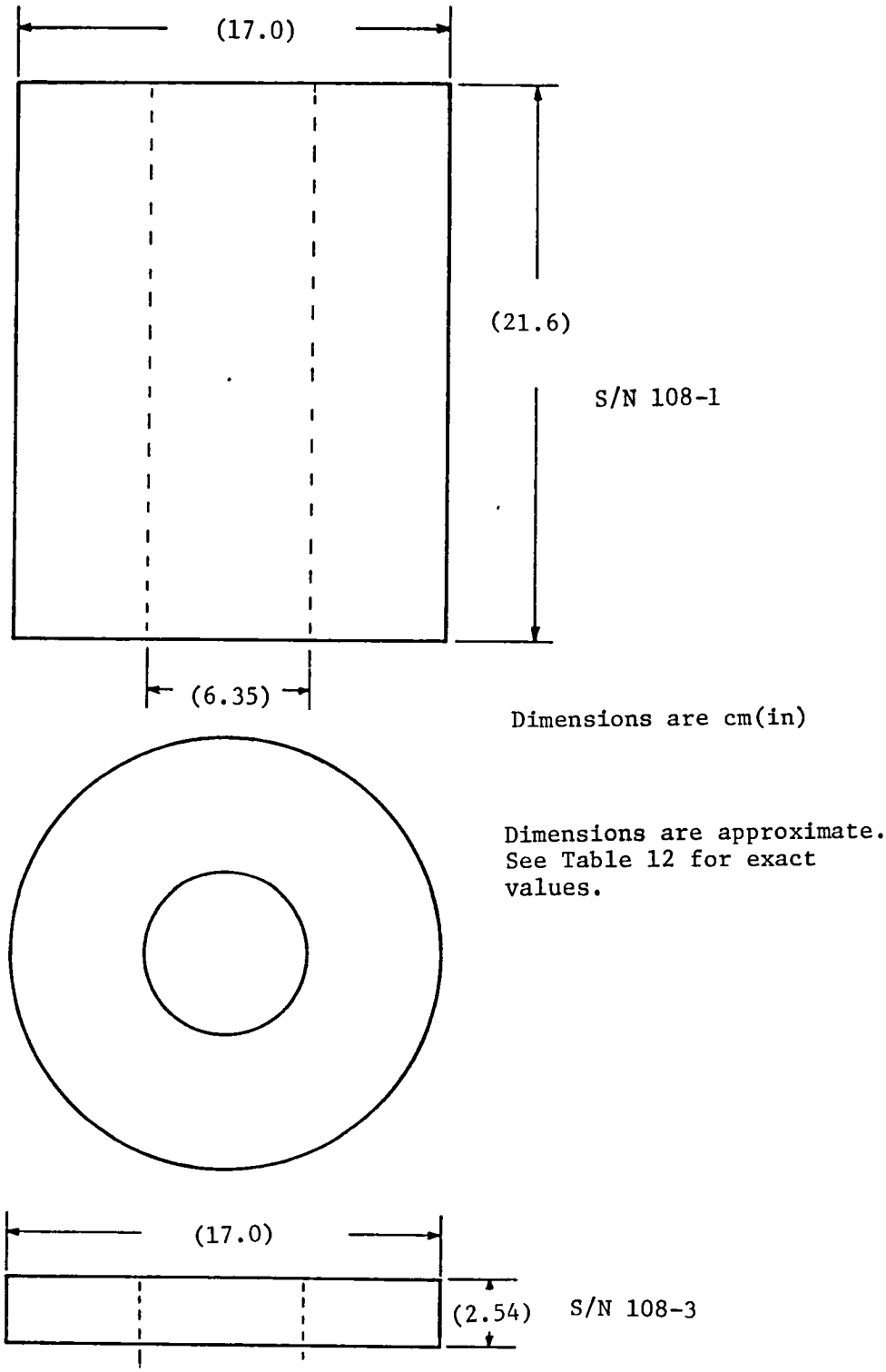

Figure 62. Schematic of Available Materials

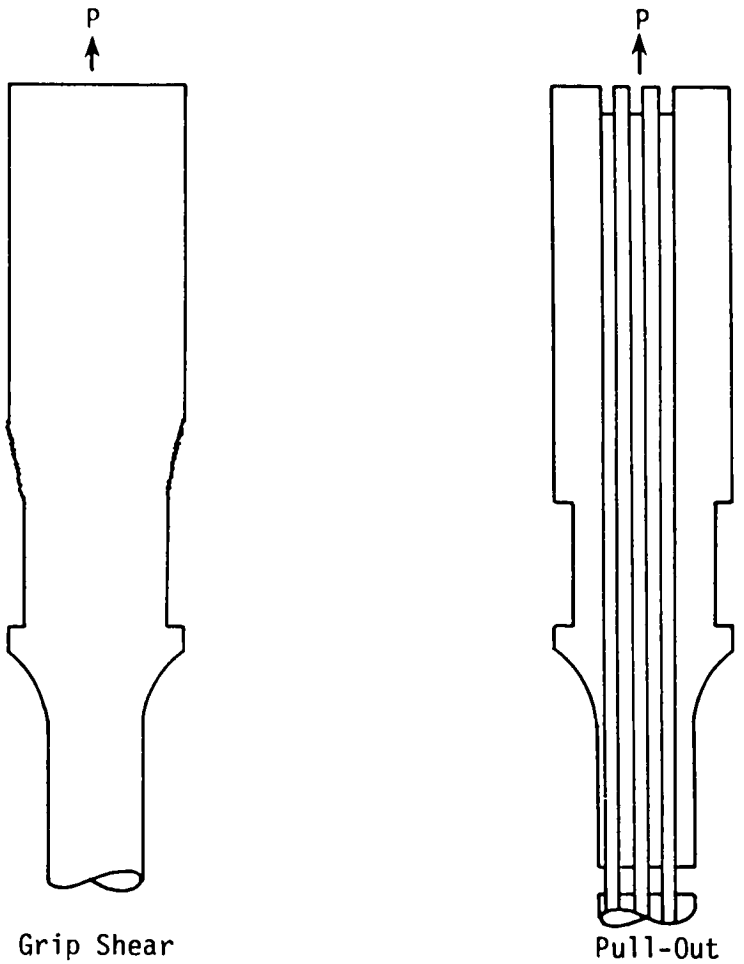

Figure 63. Non-Tensile Failure Modes

transverse, U,V,W, directions. The object was to see how long the head section should be to eliminate these non-tensile failure modes given the constraints of reasonable overall specimen lengths and diameters. The analysis showed that head shear could be avoided but that pullout probably could not without using unrealistically long specimens.

To check that the above conclusions were valid, a Z specimen was machined as shown in Figure 64. This specimen suffered rod pull-out lending credence to the above analysis.

The remaining alternative of increasing the interfacial shear strength of the longitudinal rods was investigated by the specimen design shown in Figure 65. Obviously, such an approach will only work at low temperature since, at elevated temperature, the epoxy will decompose. However, the interfacial shear strength tends to increase with temperature and the hope was that that increase would be enough to prevent pull-out under those conditions.

In any case, some success was achieved with this approach in that one room temperature tension failure was obtained in the U,V,W direction. Of the two remaining specimens, one suffered pull-out and one broke in machining. All three Z direction specimens suffered pull-out.

The specimens shown in Figures 66 through 74 were used for the balance of the testing. The objective in sizing the test cross-sections was to obtain a representative cross-section of the material and in most cases where only a few unit cells could be accommodated the specimen was centered on a yarn bundle. Figure 75 presents the cutting diagram for log S/N 108.

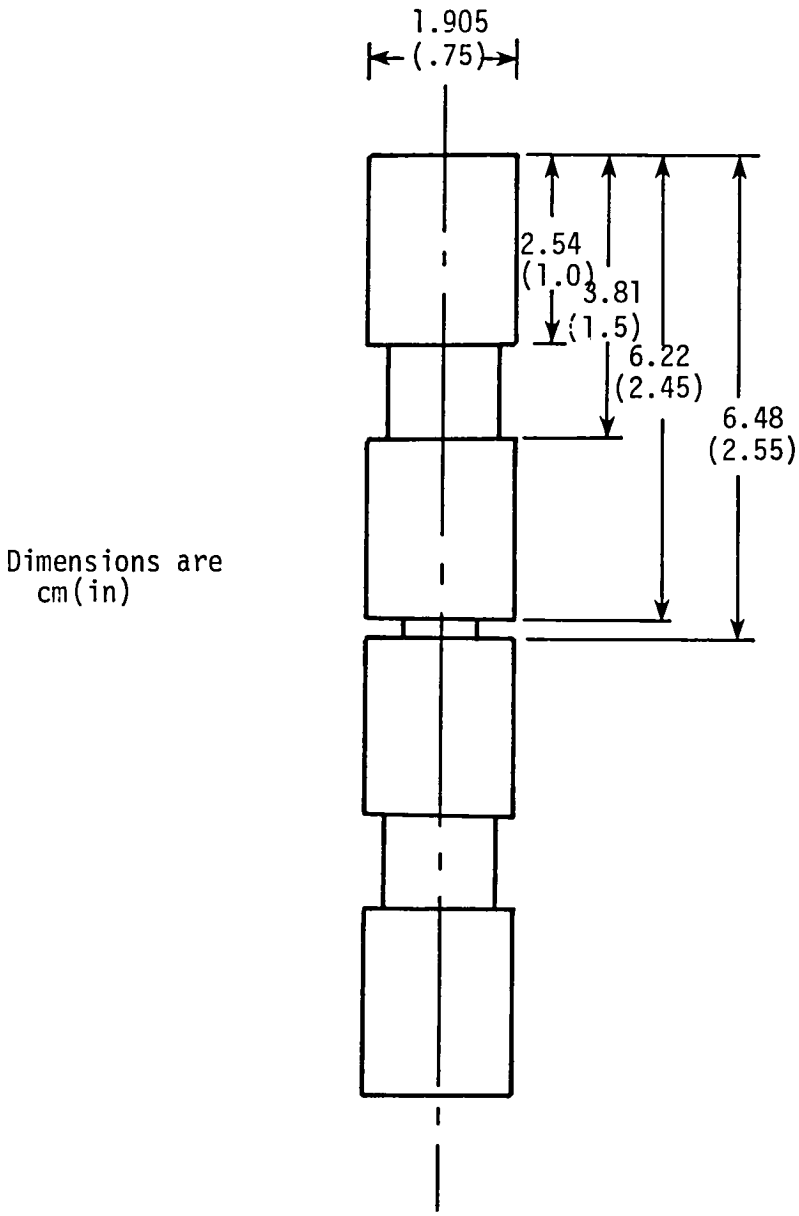

Figure 64. Experimental Tensile Specimen

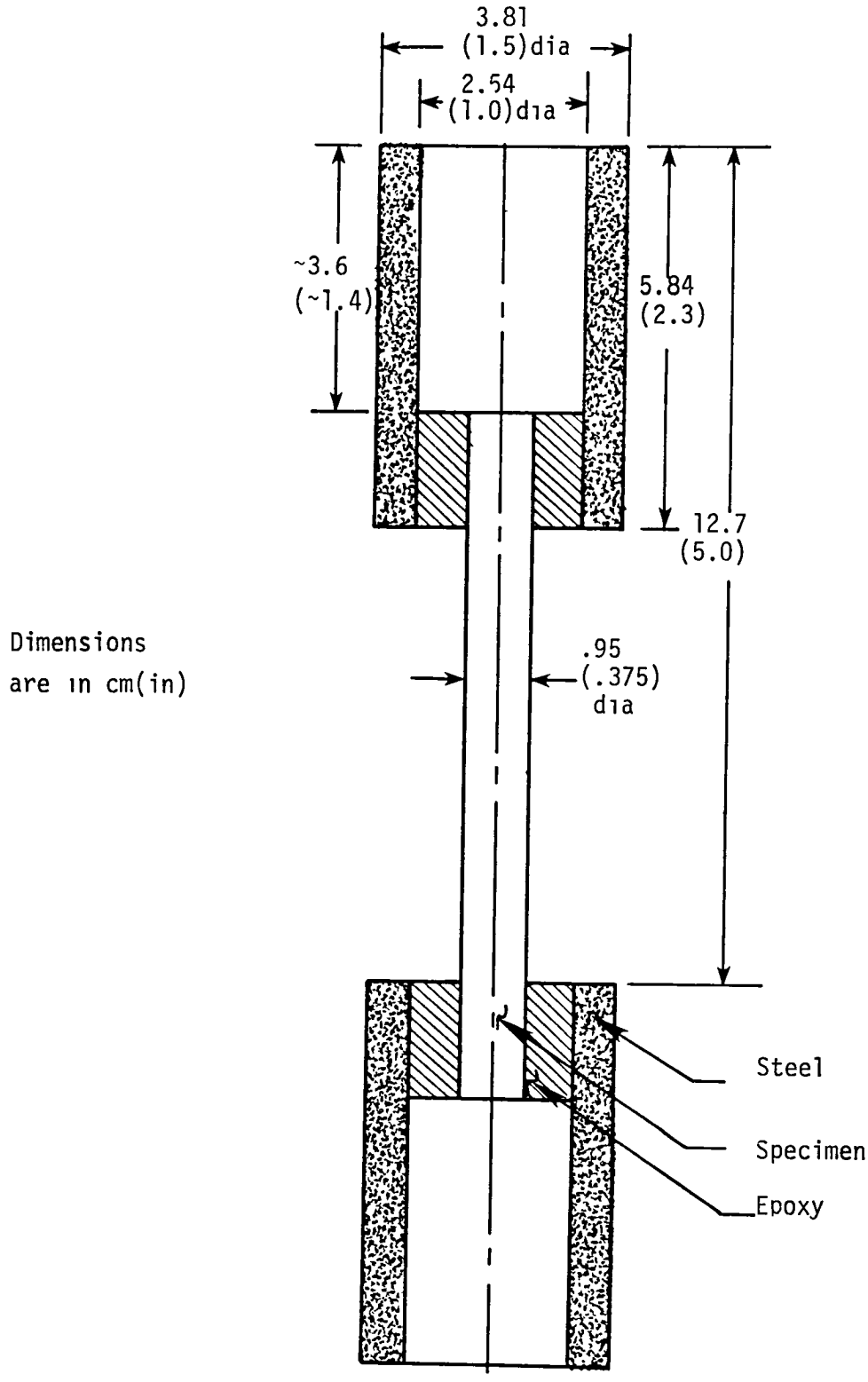

Figure 65. Experimental Tensile Test Specimen

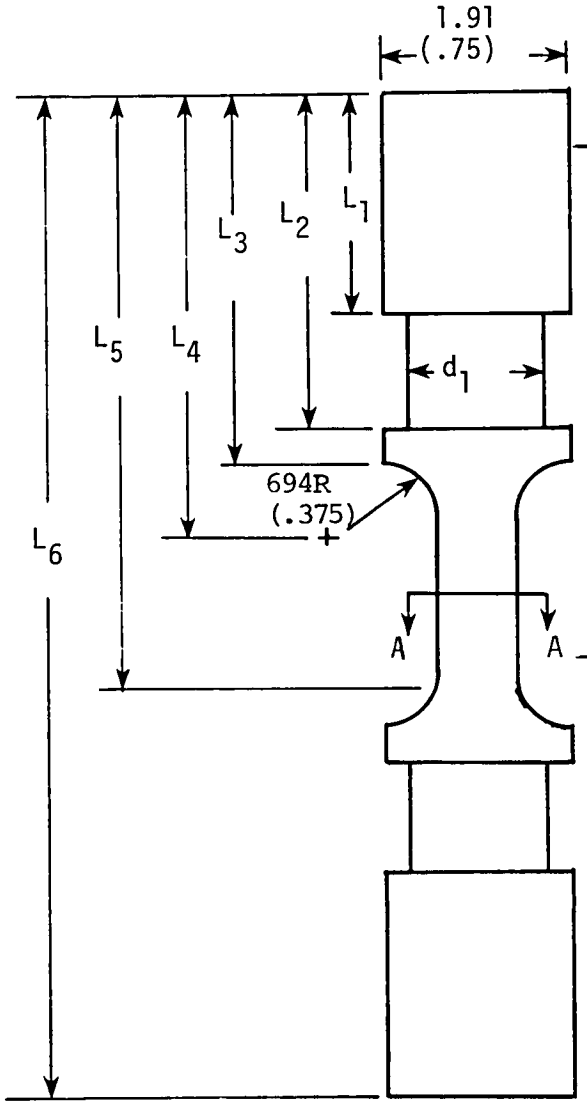

Direction	Dimension	Log S/N 102	Log S/N 108
Z	d_1	1.694 (.667)	1.575 (.620)
	L_1	2.248 (.885)	4.572 (1.800)
	L_2	3.556 (1.400)	5.880 (2.315)
	L_3	4.064 (1.600)	6.134 (2.415)
	L_4	5.080 (2.000)	6.939 (2.732)
	L_5	8.636 (3.400)	8.463 (3.332)
	L_6	13.720 (5.400)	15.240 (6.000)
U & U+30	d_1	1.694 (.667)	1.694 (.667)
	L_1	1.486 (.585)	2.604 (1.025)
	L_2	2.794 (1.100)	3.749 (1.440)
	L_3	2.883 (1.135)	4.166 (1.640)
	L_4	3.683 (1.450)	4.971 (1.957)
	L_5	7.493 (2.95)	7.049 (2.775)
	L_6	11.180 (4.40)	12.192 (4.800)

A-A Sections	Dir.	102	108
Modulus	Z	1.02x1.02(.4x.4)	1.02x.406(.4x.16)
Ultimates		1.02x1.02(.4x.4)	1.02x.406(.4x.16)
Modulus	U& U+30	1.27x1.27(.5x.5)	1.02x.381(.4x.15)
Ultimates		1.27x1.27(.5x.5)	1.02x.381(.4x.15)

Dimensions are in cm(in)

Figure 66. Tensile Specimens

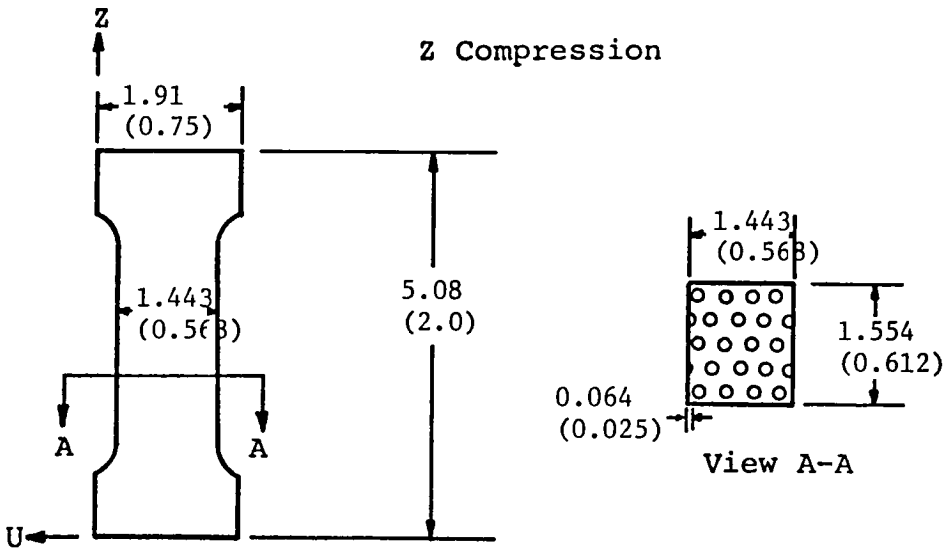

Dimensions are in cm(in)

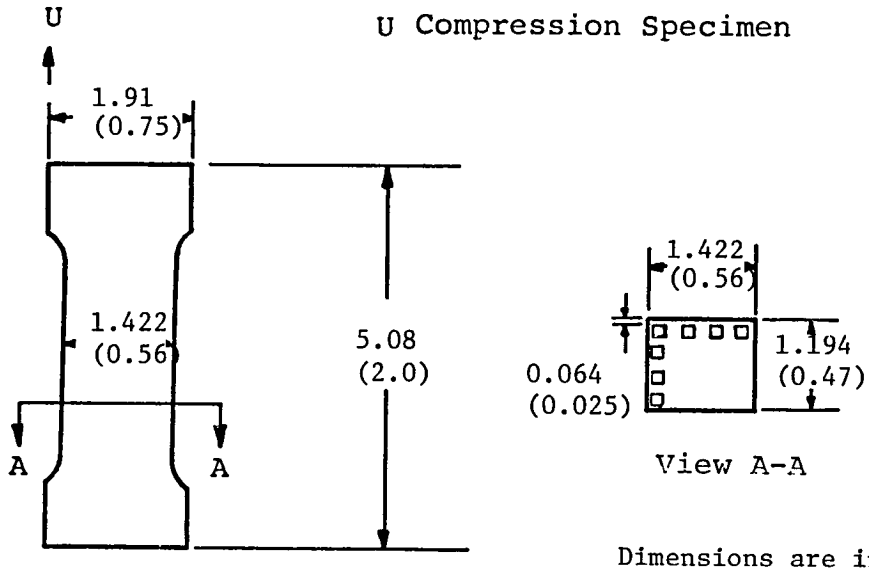

Dimensions are in cm(in)

Figure 67. Compression Specimens, Log S/N 108

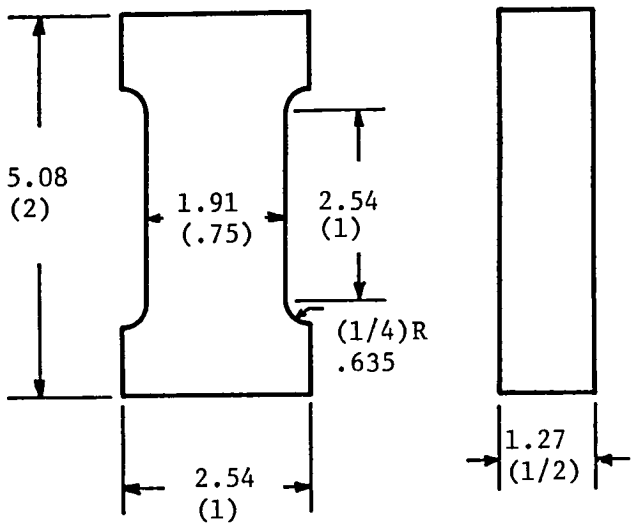

Dimensions are cm(in)

Figure 68. U+30 and Z+45 Compression Specimens, Log S/N 108

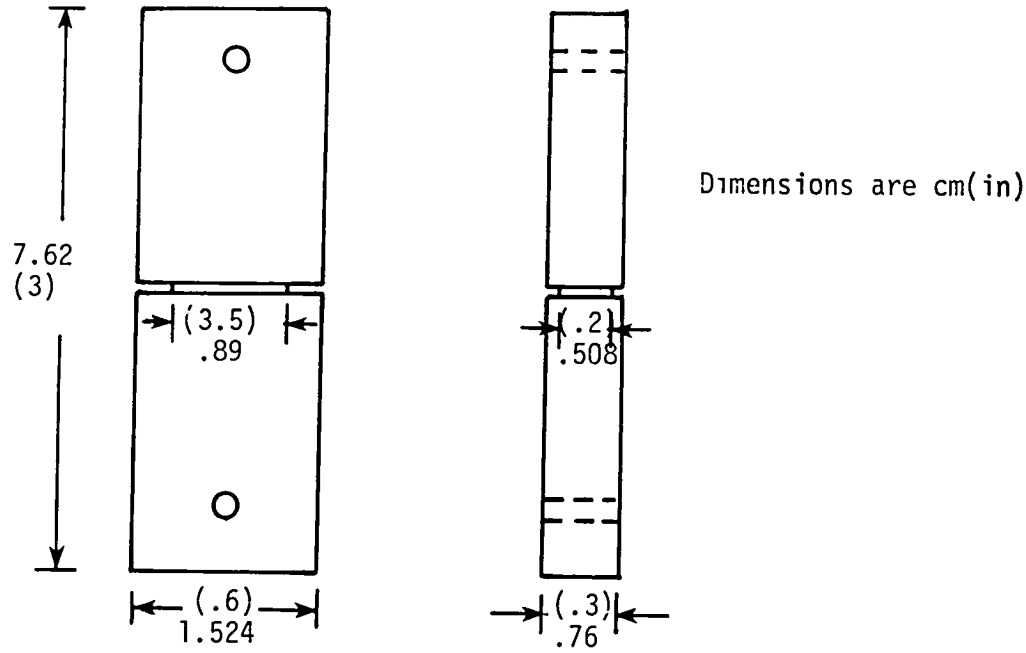

Figure 69. Shear Specimen, Log S/N 102

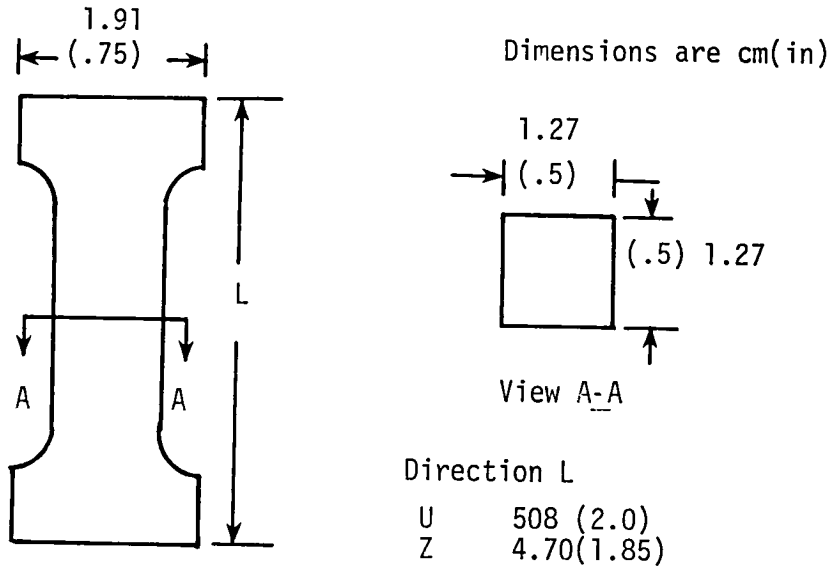

Figure 70. Compression Specimen, Log S/N 102

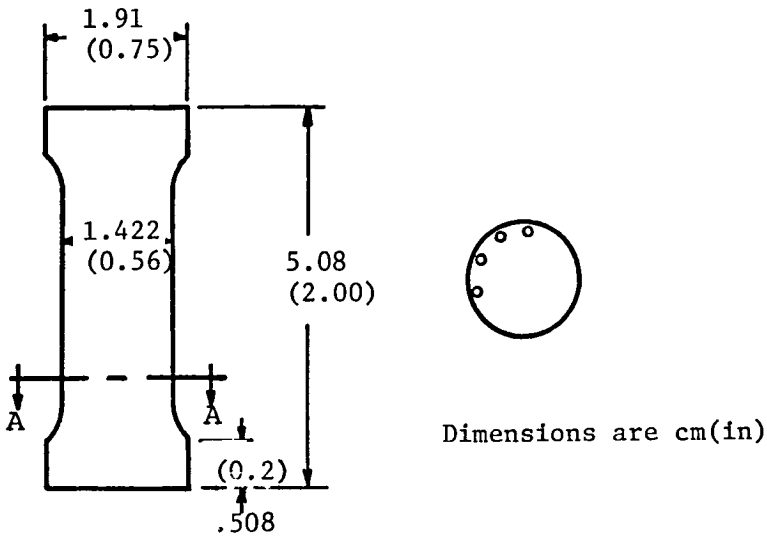

Figure 71. Torsional Shear Specimen, Log S/N 108

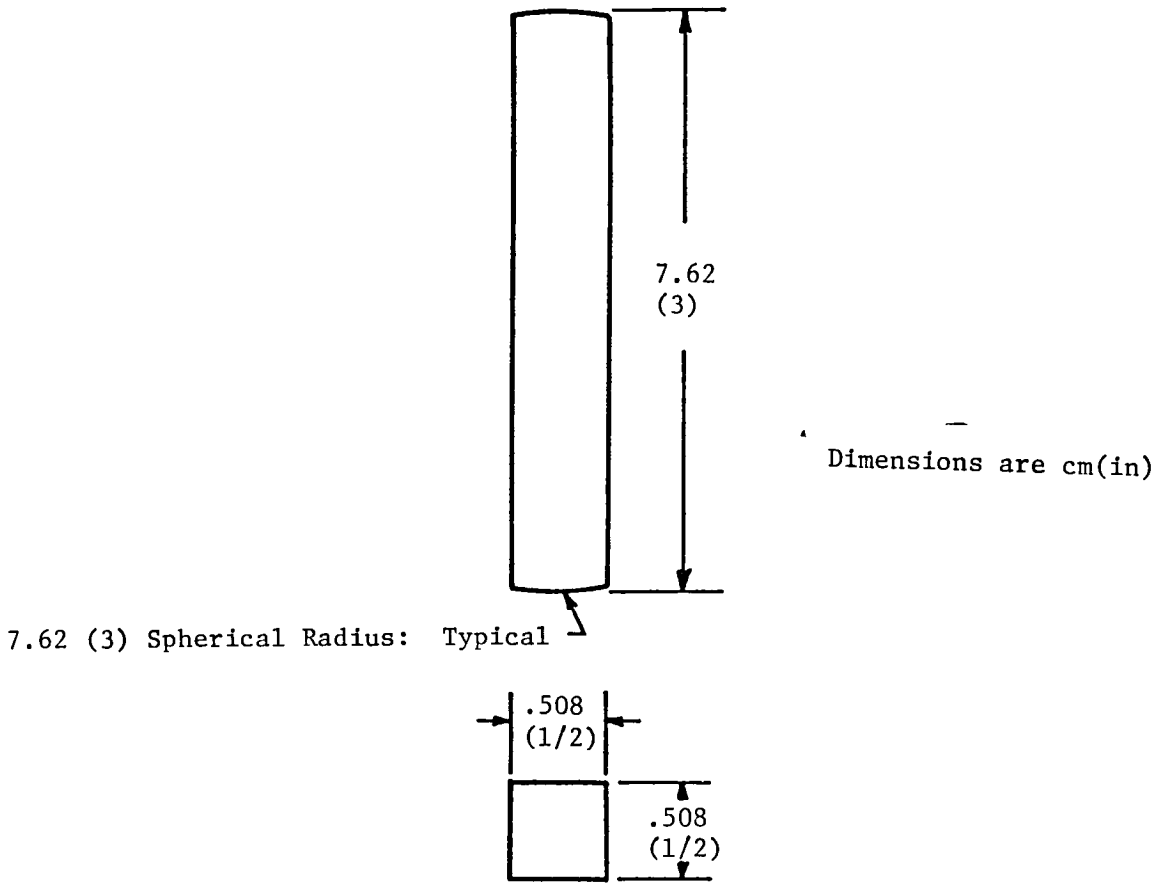

Figure 72. Thermal Expansion Specimen

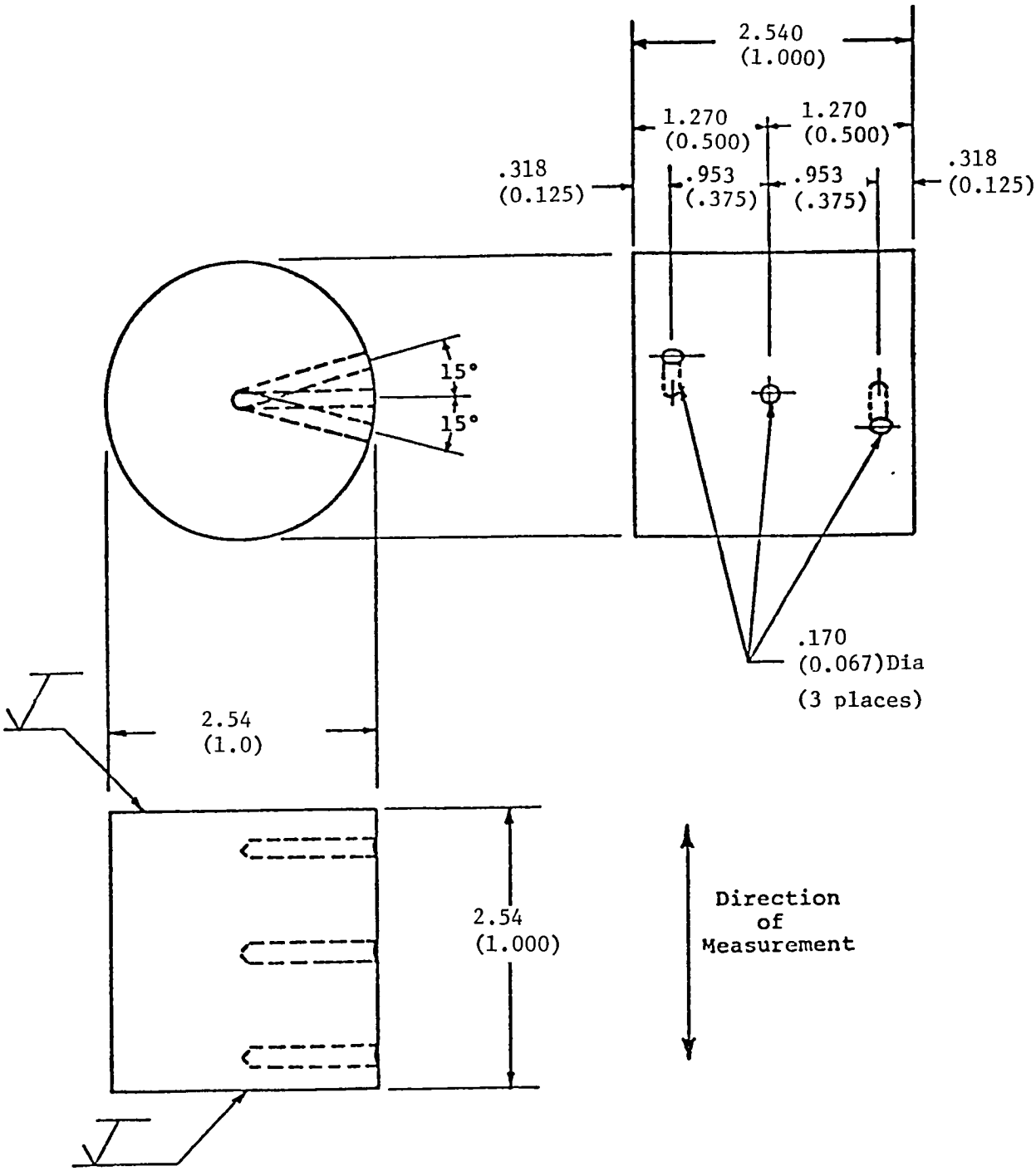

Note: All dimensions ±0.0127 except where noted

Dimensions in cm(in)

Figure 73. Drawing of Specimen for Thermal Conductivity Measurements in Comparative Rod Apparatus to 1800°F

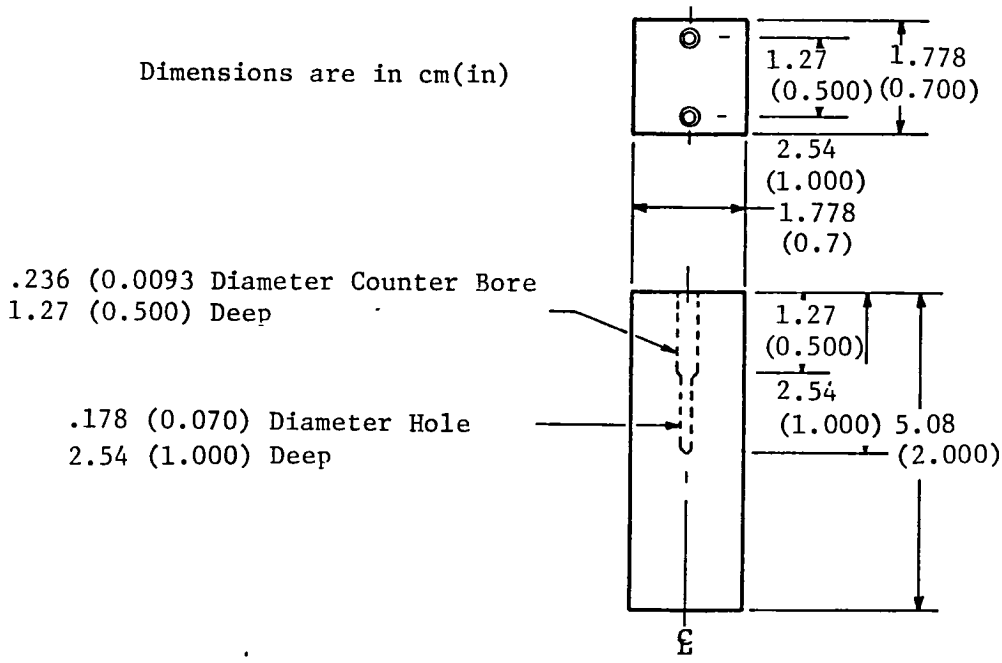

Figure 74. Radial Inflow Specimen Strip

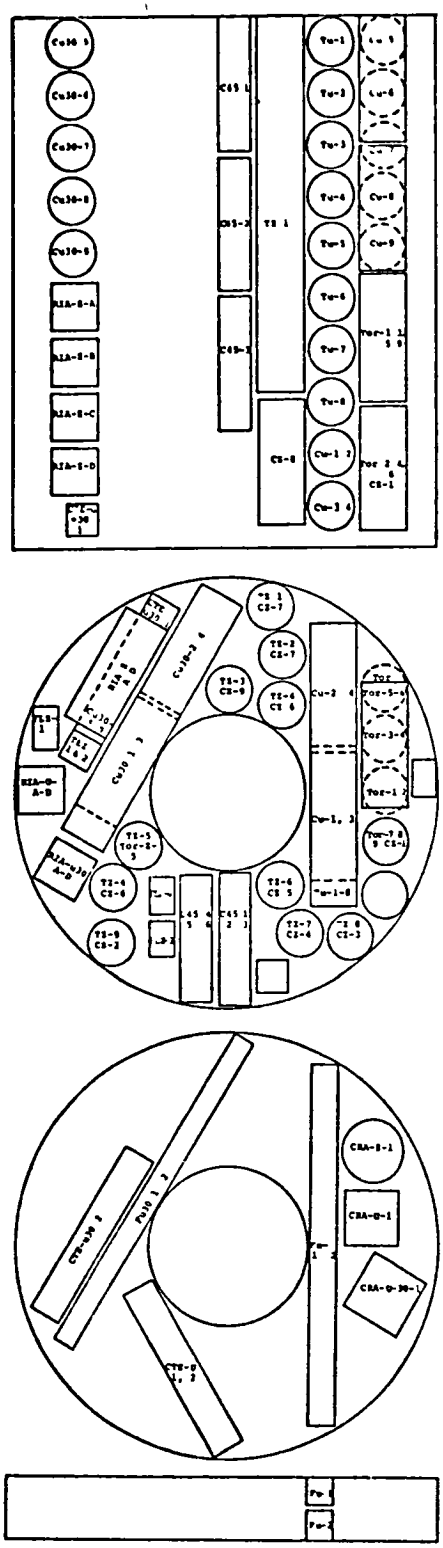

S/N 108-1

S/N 108-3

Figure 75. Cutting Diagram for Billet S/N's 108-1 and 108-3

The data obtained are presented in Tables 19 through 28. Tables 19, 20 and 21 present the tensile results. For log S/N 102, because of the limited amount of material available the room temperature tests were confined to determination of initial modulus only in each direction. As can be seen only 3 out of 9 specimens exhibit a tensile failure in the test section, the others suffered either rod pull-out or head shear. The S/N 102 (CCAN) data show similar results. For specimens where such a non-tensile failure occurs the ultimate data can be taken as representing a lower bound.

For log S/N 108, all room temperature tests were run using the epoxy technique and were not instrumented for strain. The room temperature modulus data for both the U and Z directions were obtained on the standard specimen design used at 1200°C (2200°C) by running a low load pre-test at room temperature. Fairly good strength data were obtained for the U direction; however in the Z direction, pull-out occurred at all temperatures thus the strength and strain-to-failure data represent lower bounds.

The U+30 direction data are shown as pull-out; however the pull-out in this case occurs in the test section itself. Essentially the specimen fails in interfacial shear in the test section and this may be the correct failure mode for this specimen.

SoRI has reported the interfacial shear strengths based upon those specimens where pull-out occurred by dividing the maximum load per bundle by the interfacial area in the specimen head per bundle. For S/N 102 the values for the U and Z directions were the same with an average of 4.8×10^6 Pa (700 psi) and for S/N 108 a value about 4.5×10^6 Pa (650 psi). Interestingly, if one were to use the peripheral area for the two off-axis bundles in the test sections of the U+30 specimens instead of the test section cross-sectional area the strength values in Table 21 become

Table 19. Tensile Data, Billet S/N 102

Direction	Specimen No.	Temp., °C (°F)	Ultimate Strength, Pax10^7(psix10^3)	Initial Modulus, Pax10^{10}(psix10^6)	Strain-at-Failure, 10^{-3}cm/cm	Comments
U	1	20 (70)	-	4.45 (6.45)	-	Low Load Test
	2		-	4.45 (6.45)	-	Low Load Test
	3		-	4.32 (6.27)	-	Low Load Test
	1	1370 (2500)	7.3 (10.6)	2.68 (3.88)	3.4	
	2		>7.6 (>11.0)	3.50 (5.07)	>2.2	
	3		>6.3 (> 9.2)	-	-	
Z	1	20 (70)	-	6.12 (8.87)	-	Low Load Test
	2		-	5.50 (7.97)	-	Low Load Test
	3		-	6.00 (8.70)	-	Low Load Test
	1	1370 (2500)	>11.9 (>17.2)	5.41 (7.84)	>2.2	Pull-Out
	2		>6.3 (> 9.2)	4.67 (6.78)	-	
	3		>5.5 (> 8.0)	4.15 (6.02)	-	
U+30	1	20 (70)	-	1.50 (2.18)	-	Low Load Test
	2		-	1.74 (2.53)	-	Low Load Test
	3		-	1.61 (2.33)	-	Low Load Test
	1	1370 (2500)	3.5 (5.1)	1.90 (2.75)	3.2	
	2		>3.5 (5.0)	2.30 (3.33)	>3.0	
	3		3.7 (5.4)	1.49 (2.16)	6.1	

Table 20. Tensile Data, Billet S/N 102 (CCAN)

Direction	Specimen No.	Temp., °C (°F)	Ultimate Strength, Pax10^7(psix10^3)	Initial Modulus, Pax10^{10}(psix10^6)	Strain-at-Failure, 10^{-3}cm/cm	Comments
U	1	20 (70)	>6.8 (>9.9)	-	-	
	3		>6.1 (>8.8)	-	-	
Z	1	20 (70)	>8.5 (>12.3)	6.36 (9.23)		
	2		>9.6 (>13.9)	-	-	
	3		>9.1 (>13.3)	5.30 (7.69)	>2.0	

Table 21. Tensile Data, Log S/N 108

Direction	Specimen No.	Temp., °C (°F)	Ultimate Strength, Pax10^7(psix10^3)	Initial Modulus, Pax10^{10}(psix10^6)	Strain-at-Failure, 10^{-3}cm/cm	Comments
U	3	20 (70)	>1.4 (>2.0)	-	-	Pull-Out
	6		4.1 (5.9)	-	-	Epoxy Specimen
	4		-	2.44 (3.54)	-	Low Load Test
	4	1200 (2200)	5.8 (8.5)	2.85 (4.14)	-	
	7		8.3 (12.0)	4.87 (7.06)	1.8	
	1		4.7 (6.8)	3.36 (4.88)	2.6	
	2	2650 (4800)	6.7 (9.8)	2.77 (4.02)	-	
	8		10.9 (15.8)	1.72 (2.50)	-	
Z	1	20 (70)	>4.8 (>7.0)	-	-	Pull-Out
	2		>4.8 (>7.0)	-	-	Pull-Out
	3		>4.8 (>7.0)	-	-	Pull-Out
	6		-	4.80 (6.97)	-	Low Load Test
	9		-	4.89 (7.09)	-	Low Load Test
	5	1200 (2200)	-	3.54 (5.13)	>1.6	Stopped Loading
	6		>8.6 (>12.5)	4.94 (7.17)	>2.2	Stopped Loading
	9		>5.5 (> 8.0)	5.70 (8.26)	>1.2	Stopped Loading
	NA		>14.8 (>21.5)	-	-	One Yarn, Pull-Out
	7	2650 (4800)	>4.8 (>7.0)	1.32 (1.91)	>5.0	Stopped Loading
	8		>5.0 (>7.2)	2.70 (3.92)	>3.0	Stopped Loading
	4		>4.7 (>6.8)	1.90 (2.76)	>3.6	Stopped Loading
U+30	7	1200 (2200)	>1.4 (>2.0)	1.00 (1.43)	>2.4	Pull-Out
	5		>1.3 (>1.9)	0.63 (0.91)	>3.0	Pull-Out
	4	2650 (4800)	>2.8 (>4.0)	0.68 (0.99)	>3.9	Pull-Out
	6		>2.3 (>3.4)	0.76 (1.10)	>3.5	Pull-Out

* Specimen number not available

Table 22. Compressive Data, Billet S/N 102

Direction	Specimen No.	Temp., °C (°F)	Ultimate Strength, Pax10^7(psix10^3)	Initial Modulus, Pax10^{10}(psix10^6)	Strain-at-Failure, 10^{-3}cm/cm	Comments
U	4	20 (70)	-	2.31 (3.35)	-	Low Load Test
	6		-	3.48 (5.05)	-	Low Load Test
	6	540 (1000)	4.3 (6.3)	1.29 (1.87)	4.1	
	4		3.8 (5.5)	2.79 (4.04)	-	
	3	1650 (3000)	5.5 (8.0)	1.42 (2.06)	4.2	
	2		5.4 (7.8)	2.24 (3.25)	4.9	
	1	2760 (5000)	10.6 (15.4)	4.24 (6.15)	-	
	5		10.3 (15.0)	3.13 (4.54)	-	
Z	4	20 (70)	-	3.92 (5.68)	-	Low Load Test
	1		-	3.90 (5.66)	-	Low Load Test
	4	540 (1000)	7.4 (10.8)	4.92 (7.14)	3.5	
	1		6.6 (9.6)	2.76 (4.00)	2.9	
	2	1650 (3000)	8.1 (11.8)	3.39 (4.91)	3.4	
	5		8.0 (11.6)	2.55 (3.70)	3.8	
	6	2760 (5000)	>11.7 (>17.0)	1.77 (2.56)	-	
	3		>10.7 (>15.5)	3.06 (4.44)	-	
U+30	1	20 (70)	-	1.41 (2.04)	-	Low Load Test
	4		-	2.44 (3.54)	-	Low Load Test
	4	540 (1000)	2.4 (3.5)	0.88 (1.28)	4.6	
	1		2.7 (4.0)	1.05 (1.53)	4.0	
	5	1650 (3000)	-	1.74 (2.53)	3.0	
	2		4.3 (6.3)	1.60 (2.32)	4.1	
	3	2760 (5000)	>7.9 (>11.5)	1.27 (1.84)	-	
	NA		>8.1 (>11.7)	1.89 (2.74)	-	

Table 23. Compressive Data, Billet S/N 102 (CCAN)

Direction	Specimen No.	Temp., °C (°F)	Ultimate Strength, Pax10^7(psix10^3)	Initial Modulus, Pax10^{10}(psix10^6)	Strain-at-Failure, 10^{-3}cm/cm	Comments
U	2	20 (70)	>4.6(>6.6)	4.76(6.90)	1.6	Int. bulk failure
	3		>5.1(>7.4)	3.78(5.48)	2.3	Int. bulk failure
	1	2760(5000)	>11.0(>16.0)	1.95(2.83)	>4.1	Specimen barreled
	4		>9.8(>14.2)	2.00(2.90)	>6.2	Specimen barreled
Z	2	20 (70)	6.1(8.8)	-	-	
	4		4.4(6.4)	-	-	
	1	2760(5000)	>9.8(>14.2)	2.46(3.57)	>4.3	Specimen barreled
	3		>11.6(>16.8)	1.72(2.50)	>5.1	Specimen barreled

Table 24. Compression Data, Log S/N 108

Direction	Specimen No.	Temp., °C (°F)	Ultimate Strength, Pax10^7(psix10^3)	Initial Modulus, Pax10^{10}(psix10^6)	Strain-at-Failure, 10^{-3}cm/cm	Comments
U	1	20 (70)	4.1 (5.9)	3.54 (5.13)	2.0	Internal Failure
	4		4.1 (5.9)	2.72 (3.94)	3.3	Internal Failure
	7		2.9 (4.2)	1.84 (2.67)	2.7	Internal Failure
	5	1200(2200)	4.8 (4.2)	2.26 (3.28)	-	Internal Failure
	2		4.7 (6.8)	3.14 (4.55)	-	Internal Failure
	8		4.6 (6.6)	2.60 (3.77)		Bulk Shear
	3	2650(4800)	8.2 (11.9)	2.30 (3.33)	10.3	Yarn Buckle
	6		7.2 (10.5)	2.16 (3.13)	9.7	Yarn Buckle
	9		7.8 (11.3)	2.38 (3.45)	7.8	Yarn Buckle
Z	7	20 (70)	6.4 (9.3)	5.52 (8.00)	≈20.0	Bulk Shear
	4		-	5.87 (8.51)	-	Internal Failure
	1		5.8 (8.4)	2.76 (4.00)	4.3	Internal Failure
	8	1200(2200)	6.2 (9.0)	5.11 (7.41)	3.4	Internal Failure
	2		5.8 (8.4)	4.45 (6.45)		Internal Failure
	5		5.4 (7.8)	5.74 (8.33)		Internal Failure
	9	2650(4800)	9.4 (13.7)	1.72 (2.50)	19.2	Yarn Buckle
	3		10.5 (15.3)	2.65 (3.85)	10.0	Yarn Buckle
	6		9.4 (13.6)	2.30 (3.34)	9.8	Yarn Buckle
U+30	7	20 (70)	1.5 (2.2)	1.72 (2.50)	1.6	Internal Failure
	4		0.9 (1.3)	1.29 (1.87)	2.9	Internal Failure
	1		1.4 (2.0)	2.00 (2.90)	1.7	Internal Failure
	2	1200 (2200)	1.7 (2.5)	2.88 (4.17)	1.0	Internal Failure
	5		2.1 (3.1)	1.83 (2.65)	2.1	Yarn Scissoring
	8		1.8 (2.6)	8.62 (1.25)	2.5	Internal Failure
	9	2650 (4800)	3.6 (5.2)	1.06 (1.54)	9.5	Yarn Scissoring
	3		5.0 (7.2)	2.09 (3.03)	-	Yarn Scissoring
	6		6.2 (9.0)	1.97 (2.86)	5.4	Yarn Scissoring

Table 25. Cross-Fiber Shear Strength Data, Billet S/N 102

Direction*	Specimen No.	Temp, °C (°F)	Shear Strength, Pax10^7 (psix10^3)
U	3	20 (70)	1.14 (1.65)
	4		1.18 (1.71)
	5	1650 (3000)	1.41 (2.05)
	2		1.41 (2.05)
	6	2760 (5000)	2.86 (4.15)
	1		2.14 (3.10)
U+30	1	20 (70)	1.21 (1.76)
	2		1.07 (1.55)

* Z bundles are being sheared

Table 26. Torsional Data, Log S/N 108

Direction: Specimen torqued around Z direction

Specimen No.	Temp., °C (°F)	Initial Secant Modulus,* Pax10^{10} (psi x10^{6})	Secondary Modulus,** Pax10^{10} (psi x10^{6})	Shear Strength @ .2% strain, Pax10^{6} (psi)	Shear Strength @ 2% strain, Pax10^{6} (psi)
9	20 (70)	.058 (.084)	.018 (.026)	1.30 (188)	4.55 (660)
1		.122 (.178)	.026 (.038)	2.07 (300)	5.52 (800)
4		.054 (.078)	.024 (.035)	1.30 (188)	4.48 (650)
7	1200 (2200)	.059 (.085)	.040 (.058)	0.95 (138)	7.79 (1130)
2		.064 (.093)	.035 (.051)	1.55 (225)	7.45 (1080)
3	2650 (4800)	.145 (.210)	.117 (.170)	3.02 (438)	-
8		.200 (.290)	-	3.86 (560)	-

* at 1.72x10$_{6}$ Pa (250 psi)

** from 1.72x10^{6} Pa (250 psi) to 0.01 cm/cm

Table 27. 45° Compression Data, Log S/N 108

Note: 45° to Z direction

Specimen No.	Temp., °C (°F)	Ultimate Strength, Pax10^7(psix10^3)	Initial Modulus, Pax10^{10}(psix10^6)	Shear Modulus,* Pax10^{10}(psix10^6)	Comments
2	20 (70)	>1.2 (>1.7)	.24 (0.35)	.06 (0.09)	Stopped loading
1		1.9 (2.8)	.16 (0.23)	.04 (0.06)	
4	1200 (2200)	2.6 (3.7)	.17 (0.24)	.04 (0.06)	
5		1.7 (2.5)	.30 (0.44)	.08 (0.11)	
3	2650(4800)	4.1 (6.0)	.52 (0.76)	.13 (0.19)	
6		>3.3 (>4.8)	.34 (0.50)	.09 (0.13)	Stopped loading

* $G = E_{45}/4$

Table 28. Flexure Data, Log S/N 108

Direction*	Specimen No.	Stress @ Failure, P_a x10^7(psix10^3)	Ultimate Stress, P_a x10^7(psix10^3)	Initial Modulus, $P_a 10^{10}$(psix10^6)
U	1	3.88 (5.55)	4.10 (5.95)	2.39 (3.47)
	2	6.27 (9.10)	>7.24 (>10.50)	3.46 (5.02)
Z	2	6.69 (9.70)	6.69 (9.70)	4.00 (5.80)
	3	3.90 (5.65)	5.38 (7.80)	3.85 (5.58)
U+30	1	1.34 (1.95)	1.34 (1.95)	0.73 (1.06)
	2	-	-	

* Denotes direction of alignment of specimen longitudinal axis.

approximately 4.83×10^6 Pa (700 psi) at 1200°C (2200°F) and 8.93×10^6 Pa (1295 psi) at 2650°C (4800°F).

From the ultimate load data per bundle we can also calculate the strength of the aligned fiber bundles. Table 29 presents the results for log S/N's 102 and 108. It appears that the tensile strength of the bundles are about 60×10^7 Pa (86,800 psi) at room temperature and increase to about 75×10^7 Pa (110,000 psi) at elevated temperature.

The compression data are shown in Tables 22, 23 and 24; except for some barreling there was no problem with the testing and the data appear well behaved.

The cross-fiber shear strengths, Table 25 were run in such a manner as to shear the axial bundles. Thus, the shearing direction was in the transverse plane. Two load directions were used and as one might expect, there is little or no difference between them. The shear strength increases with temperature reflecting the greater contact area as the interfacial microcracks close with increasing temperature and the increasing fiber strength with temperature. The values for cross-fiber shear strengths are quite comparable to values for other carbon-carbons.

Table 26 presents the axial torsional results. The torsional shear modulus was measured with the centerline of the specimen in the axial direction, producing a coupled modulus. The specimens were evaluated in the gas-bearing torsional facility. This facility had gas-bearings in the load train to insure proper alignment of the specimen and load train. The torque was applied at one end of the load train by a synchronous constant speed motor through a double reduction chain drive to provide a constant shear deformation rate. The other end of the load train was restrained from rotating by an aluminum rod positioned so that it stopped on a load measuring device.

Table 29. Yarn Bundle Tensile Strengths

Log S/N	Test Direction	Temp., °C(°F)	Bundle Stress, Pax10^7(psix10^3)	Failure Mode
102	Z	20 (70)	49.1 (71.2)	Pull-out
	U	20 (70)	62.4 (90.5)	Pull-out
108	U	20 (70)	52.7 (76.4)	Pull-out
	Z	1200 (2200)	75.6 (109.7)	Pull-out
	U	20 (70)	59.8 (86.6)	Tensile
	U	1200 (2200)	76.9 (111.5)	Tensile
	U	2650 (4800)	75.8 (109.9)	Tensile

The angular rotation of the specimen was measured utilizing the following system. Two graphite rings with V-grooves around the circumference were positioned one inch apart on the specimen. Strings were attached to the rings and wound around the circumference in the V-grooves. The free ends of the strings were then attached to individual strain measuring devices which were calibrated to give the movement. Thus, as the specimen and load train rotated, the rings acted as spools and "rolled up" the string. The strain measuring devices were connected into a full bridge circuit which gave a millivolt response on the X-Y recorder proportioned to the difference of the two movements. In other words, the recorder was receiving and plotting the actual angular rotation of the specimen along the one-inch section versus applied torque.

The shear modulus was also evaluated utilizing a specimen oriented 45° to the Z direction of the material, Table 27. The specimen was loaded in compression. The modulus was calculated using the following equation:

$$\frac{1}{G} = \frac{4}{E_{45}} - \frac{1 - \nu}{E_{11}} - \frac{1 - \nu}{E_{22}}$$

G = Shear Modulus

E_{45} = Modulus from off-axis specimen

Note that Poisson's ratio (ν) and other Young's moduli (E) need to be known. For most carbon-carbons, the Poisson's ratio is small (<0.1) and the Young's moduli are large (>10×10^6). This enables a reduction of the above equation:

$$\frac{1}{G} = \frac{4}{E_{45}}$$

or $$G = \frac{E_{45}}{4}$$

The flexural evaluations were performed in the graphite flexure facility, Table 28. The evaluations were performed at room temperature only. The technique utilized was the four point bending method. The specimen, was loaded at two points and supported at two points. The following equation was utilized in reducing the data:

$$E = \frac{12}{ybh^3} \frac{P}{2} \left[\frac{a^3}{3} + \frac{ac}{2} (a + \frac{c}{4})\right]$$

The tensile mechanical response of carbon-carbons is controlled principally by the fibers because they are the stiffest and strongest components of the composite and because the interfacial strengths i.e. fiber-to-fiber and fiber-to-matrix, are quite low. Consequently, in order to insure that one is obtaining an accurate measurement of the material in any given test, one must use a specimen with a test section size large relative to the characteristic unit cell size. If such is not the case, then the data should be corrected for fiber volume fraction effects. This is accomplished by measuring the fiber bundle volume fraction in the actual test specimen test section, dividing this into that for the bulk material and multiplying the tensile strength and modulus. Table 30 presents the measurements made on the S/N 108 tensile specimens for the present program; those for S/N 102 did not require correction.

Figures 76 through 90 present the preceding data plotted versus temperature where the tensile data in the Z and U directions have been corrected as explained above. The agreement between S/N 102 and S/N 108 data is good indicating, by the lack of dependency on bulk density, that the fiber bundles are the major influence on mechanical response. The lines represent means of the data. In the case of Z direction tensile strength, the line was calculated using the values in Table 29 and the material bundle volume fraction.

Table 30. Tensile Test Section Aligned Fiber Bundle Volume Fraction, Log S/N 108

Specimen No.	Bulk Billet	Specimen Test Section
TZ-1	.19	.20
-2		.20
-3		NS*
-4		.16
-5		.19
-6		.20
-7		.16
-8		.16
-9		.16
TU-1	.14	.12
-2		.12
-3		.09
-4		.12
-6		.09
-7		.12
-8		.12

* No specimen available

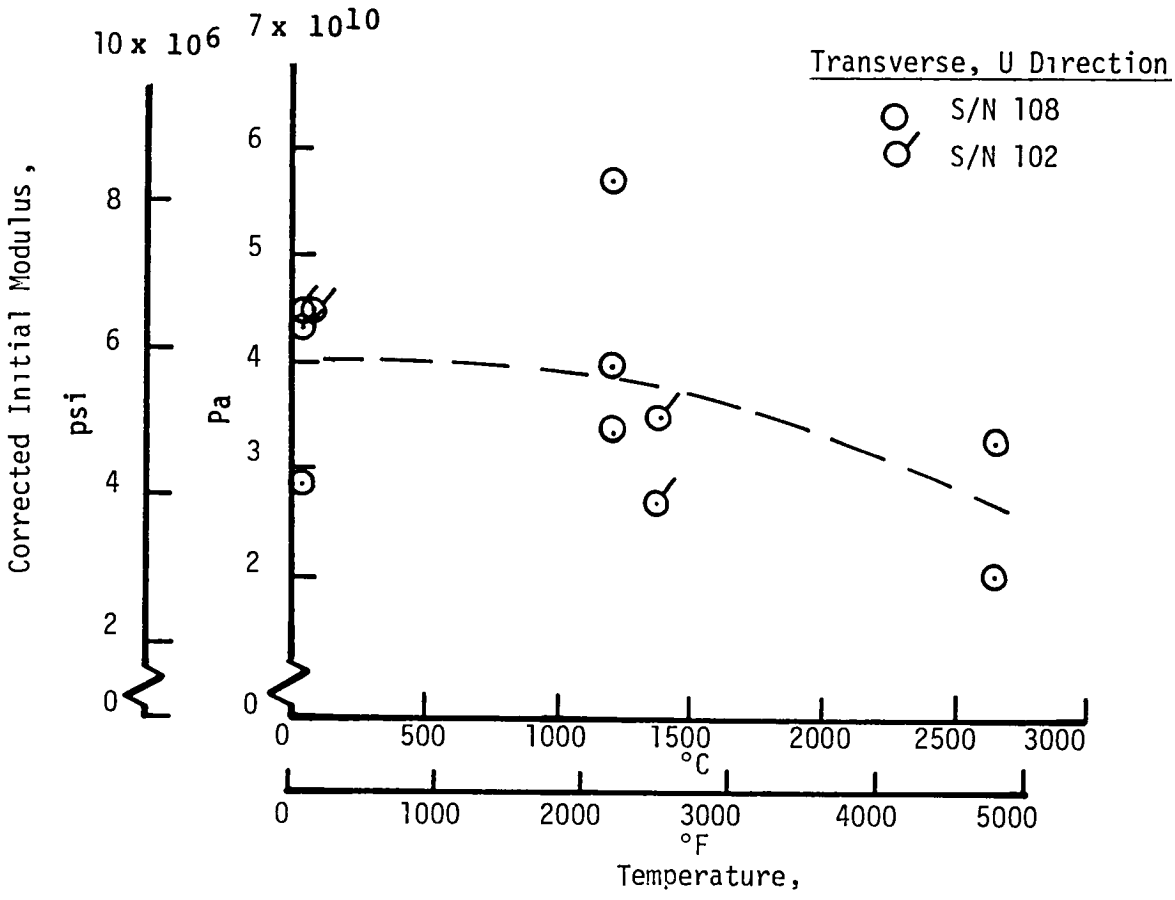

Figure 76. Tensile Modulus

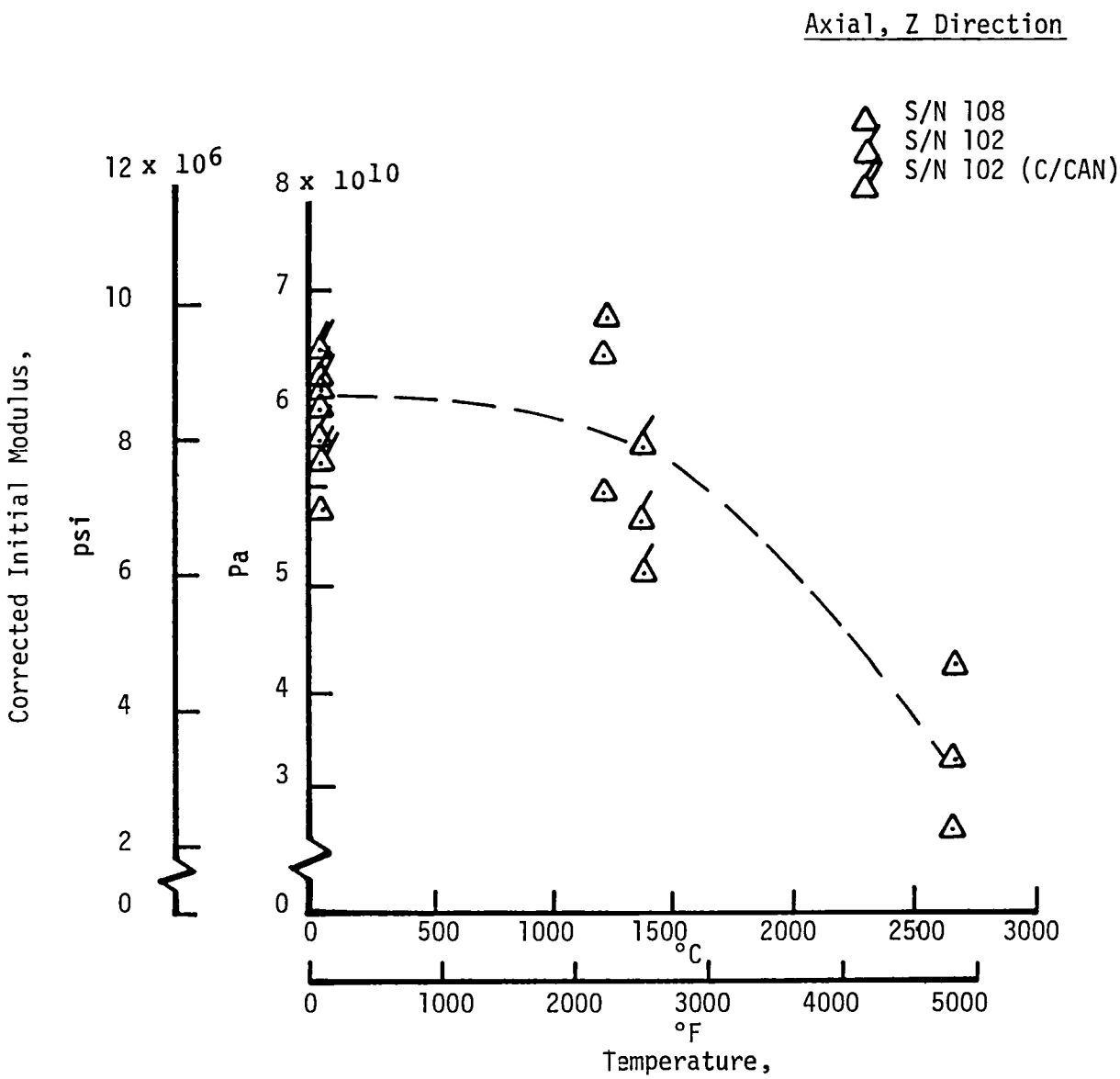

Figure 77. Tensile Modulus

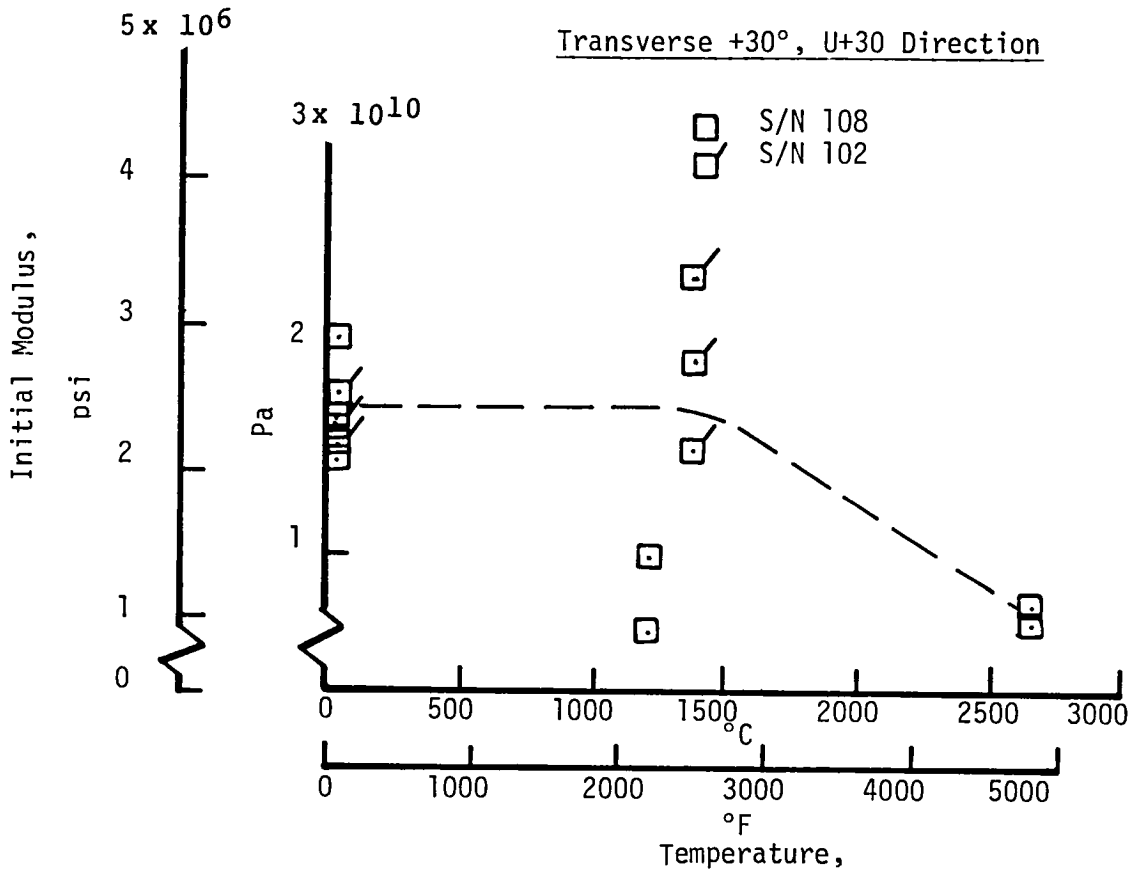

Figure 78. Tensile Modulus

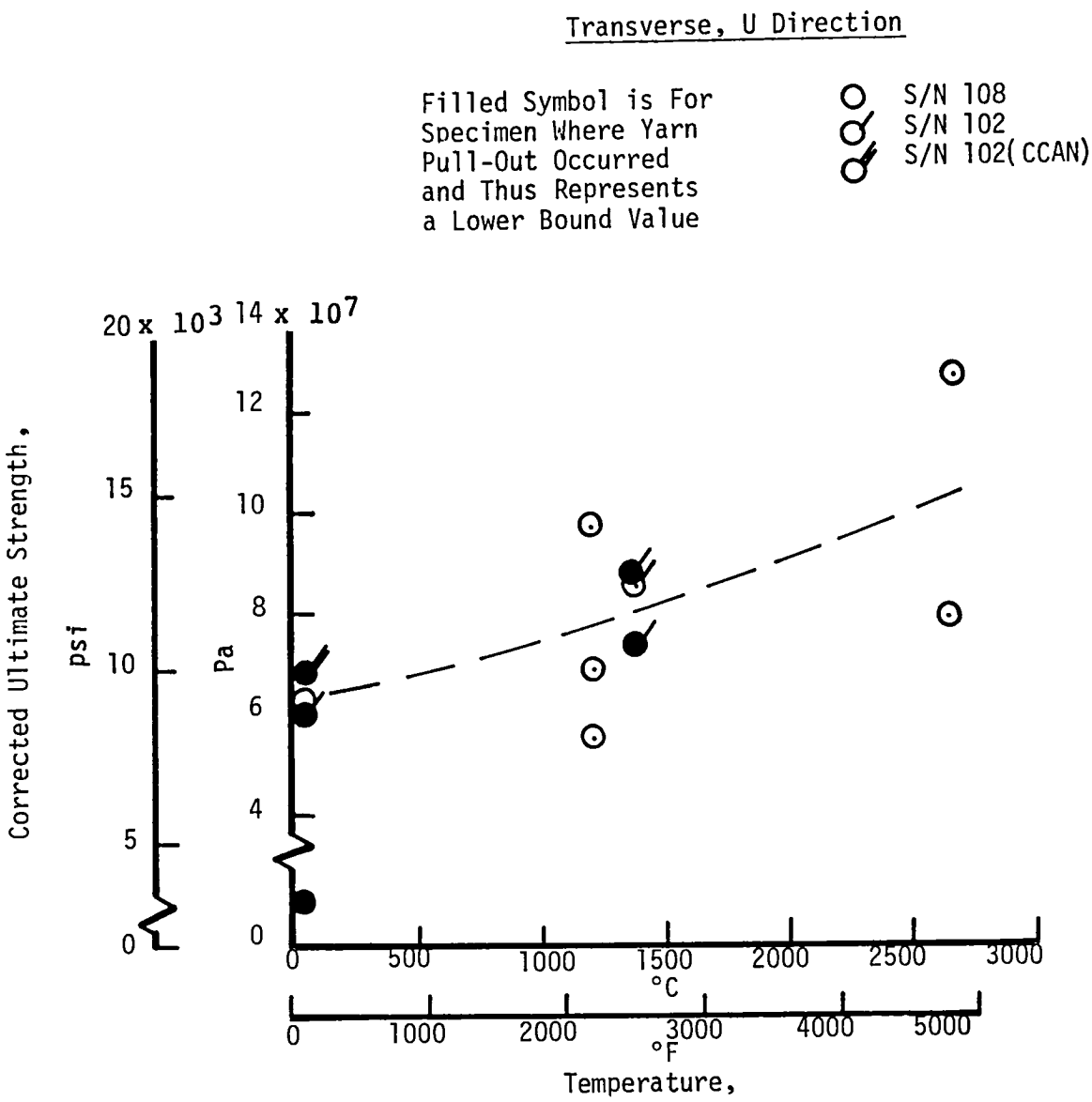

Figure 79. Tensile Strength

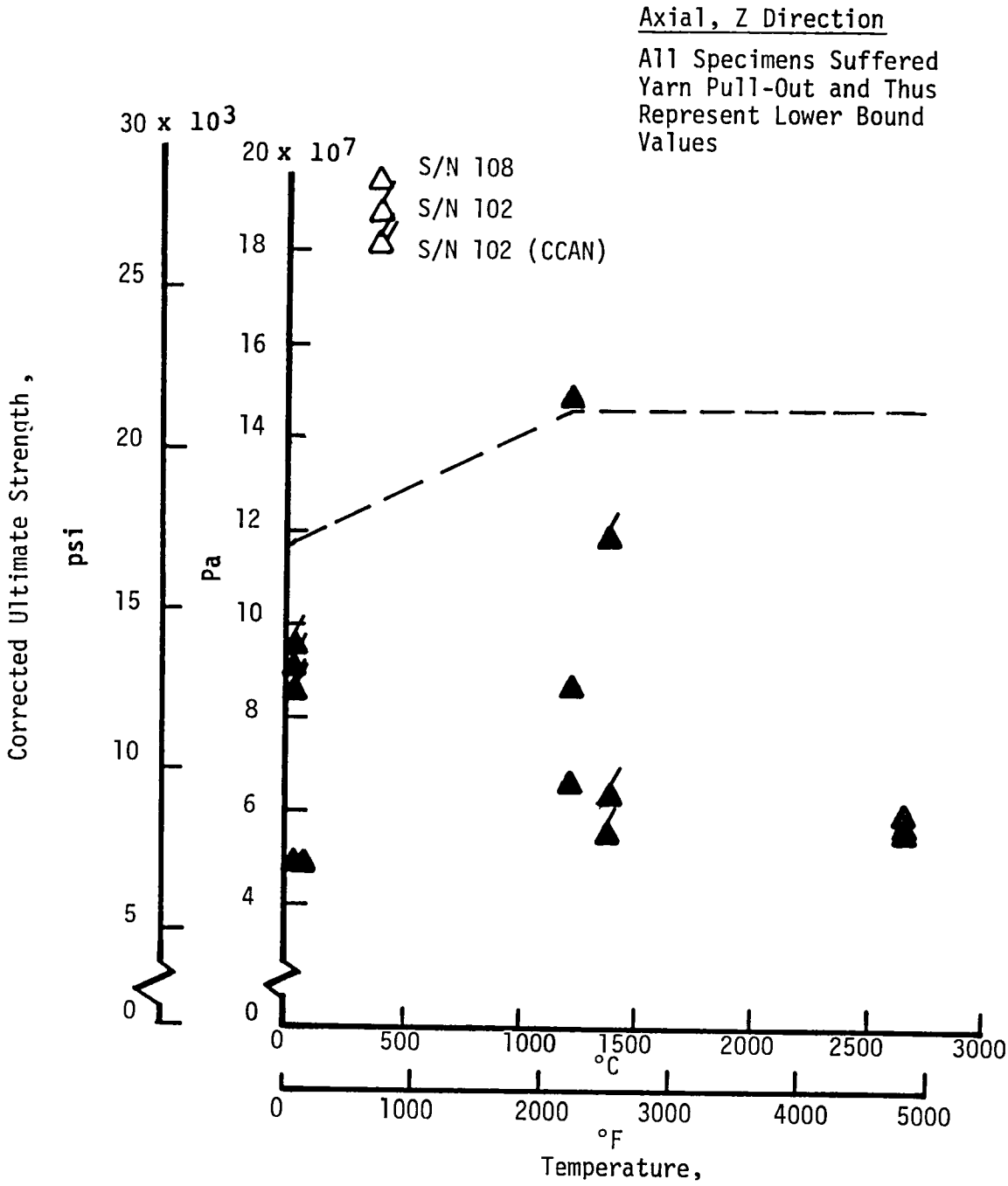

Figure 80. Tensile Strength

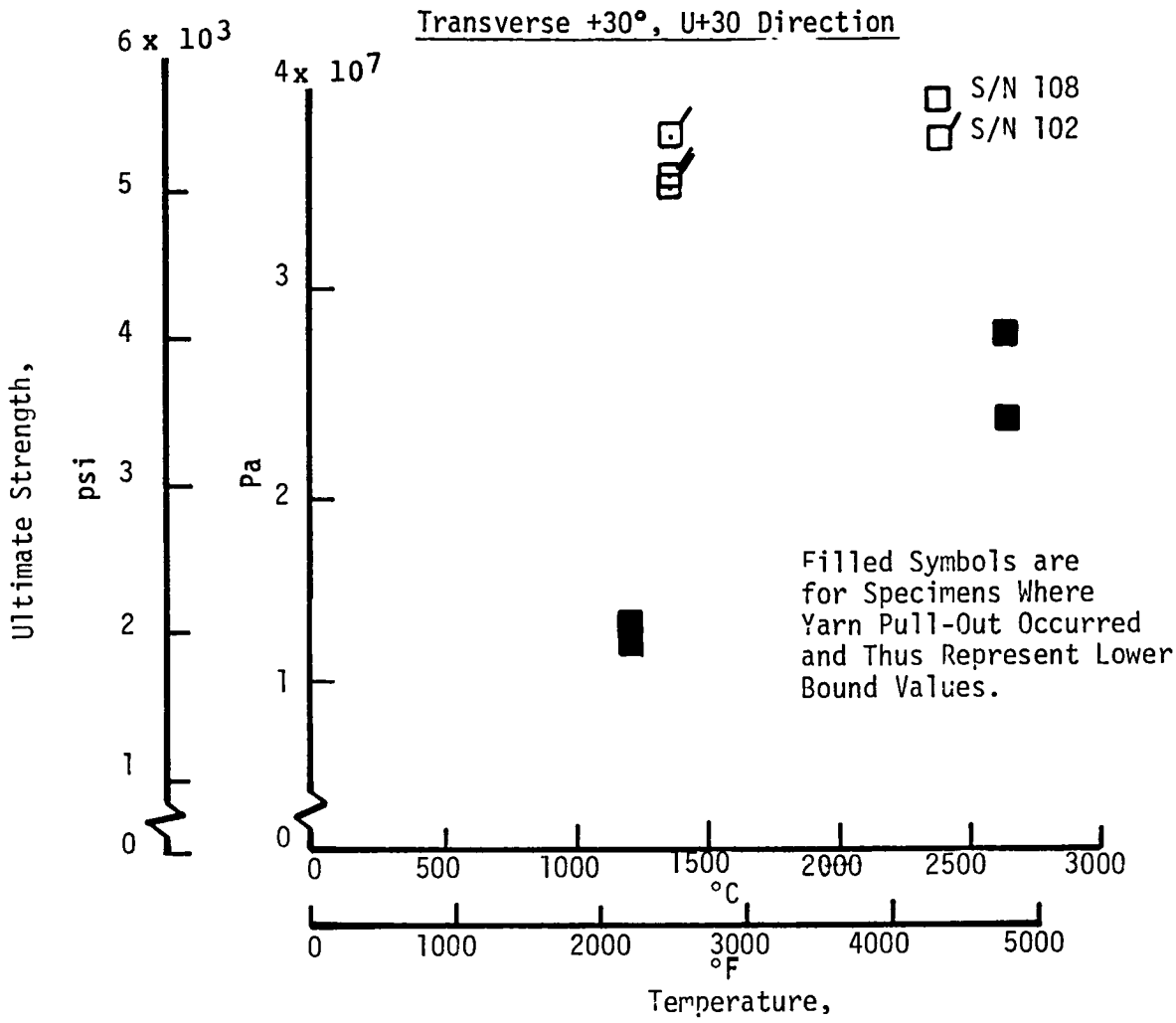

Figure 81. Tensile Strength

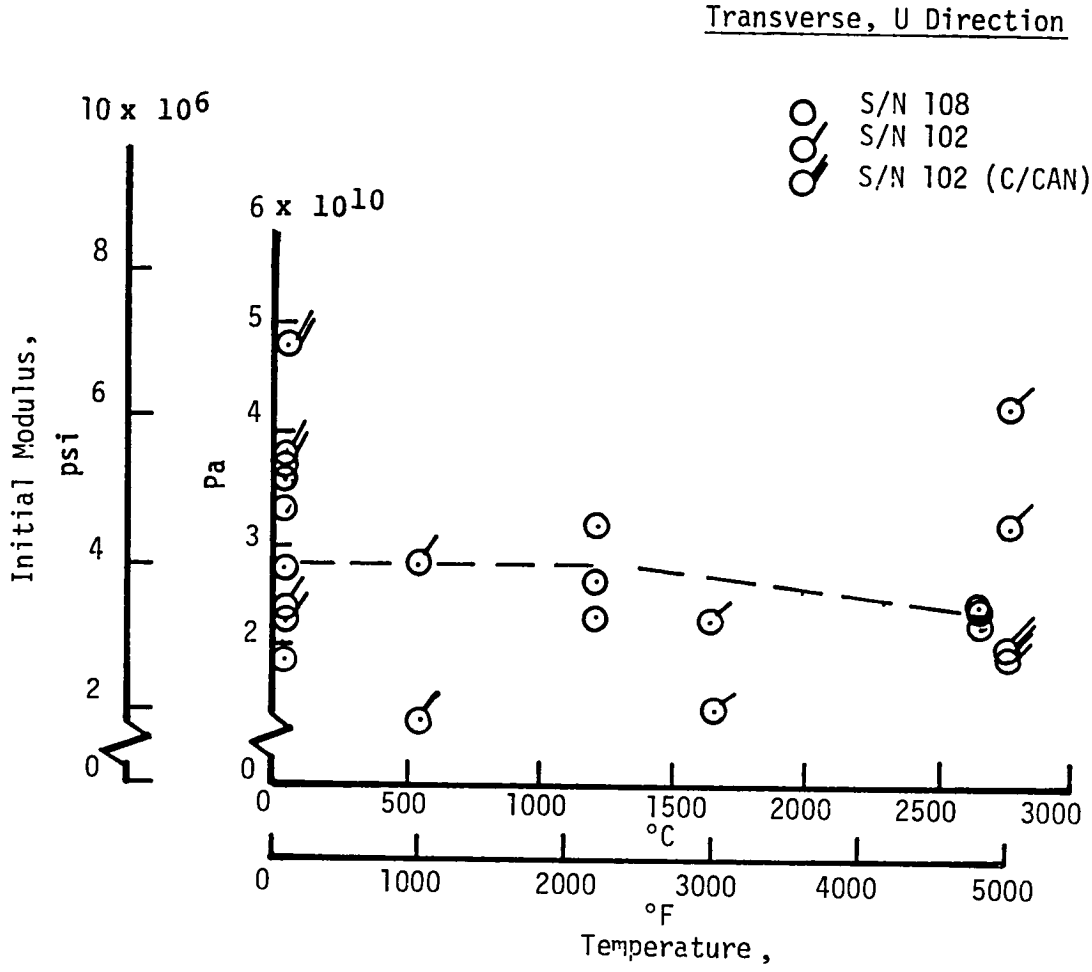

Figure 82. Compressive Modulus

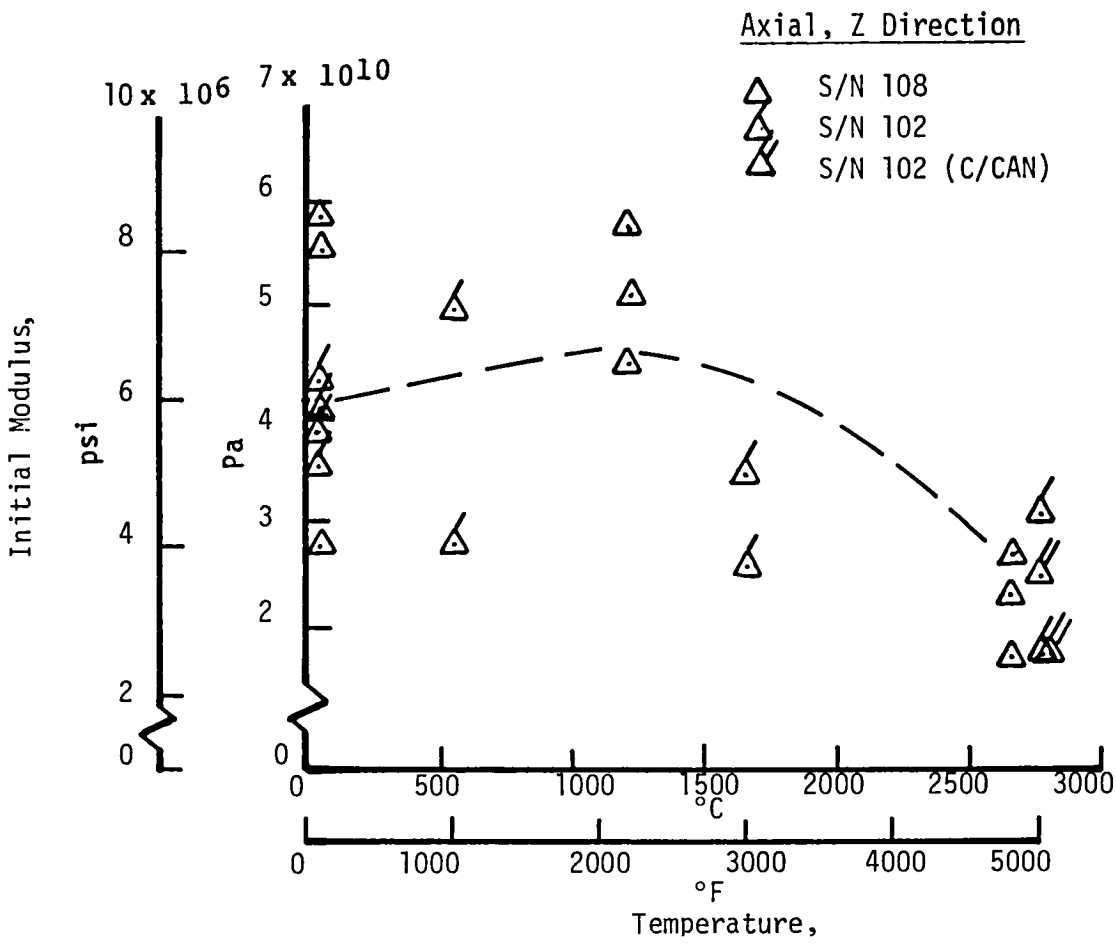

Figure 83. Compressive Modulus

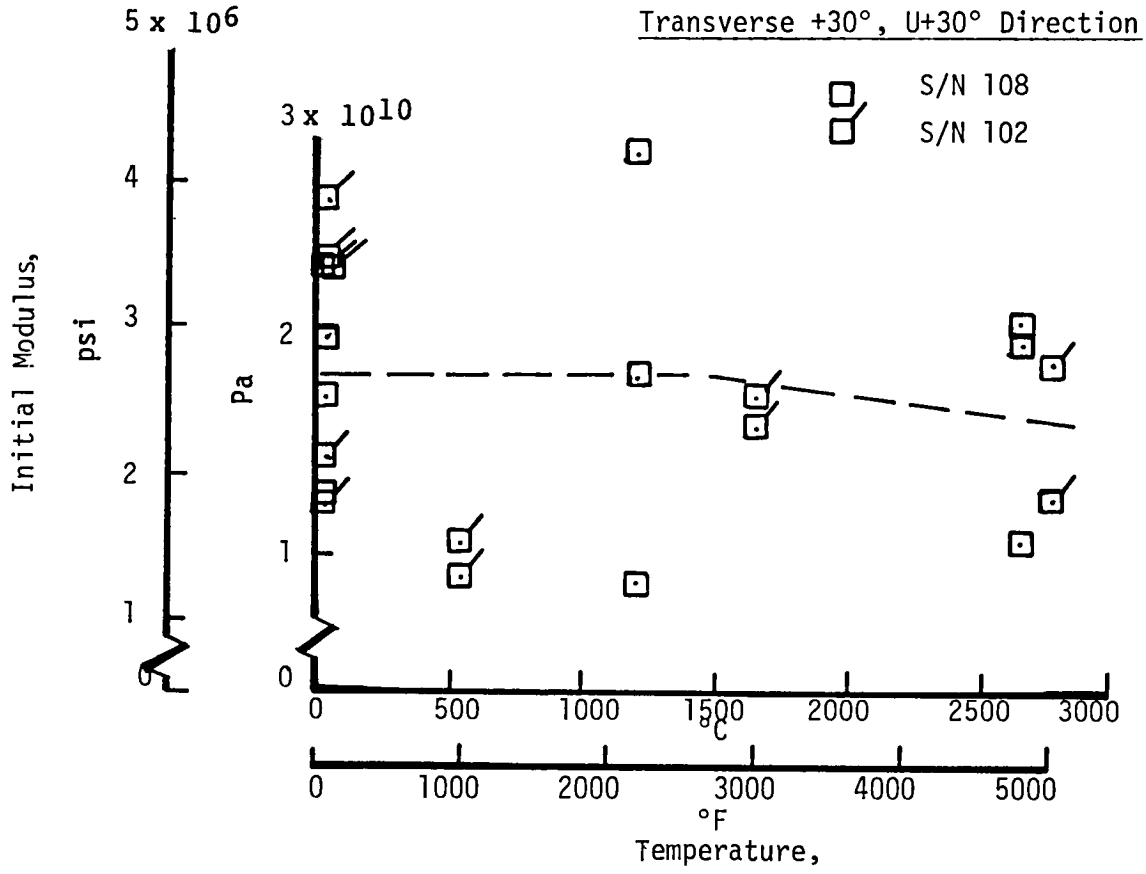

Figure 84. Compressive Modulus

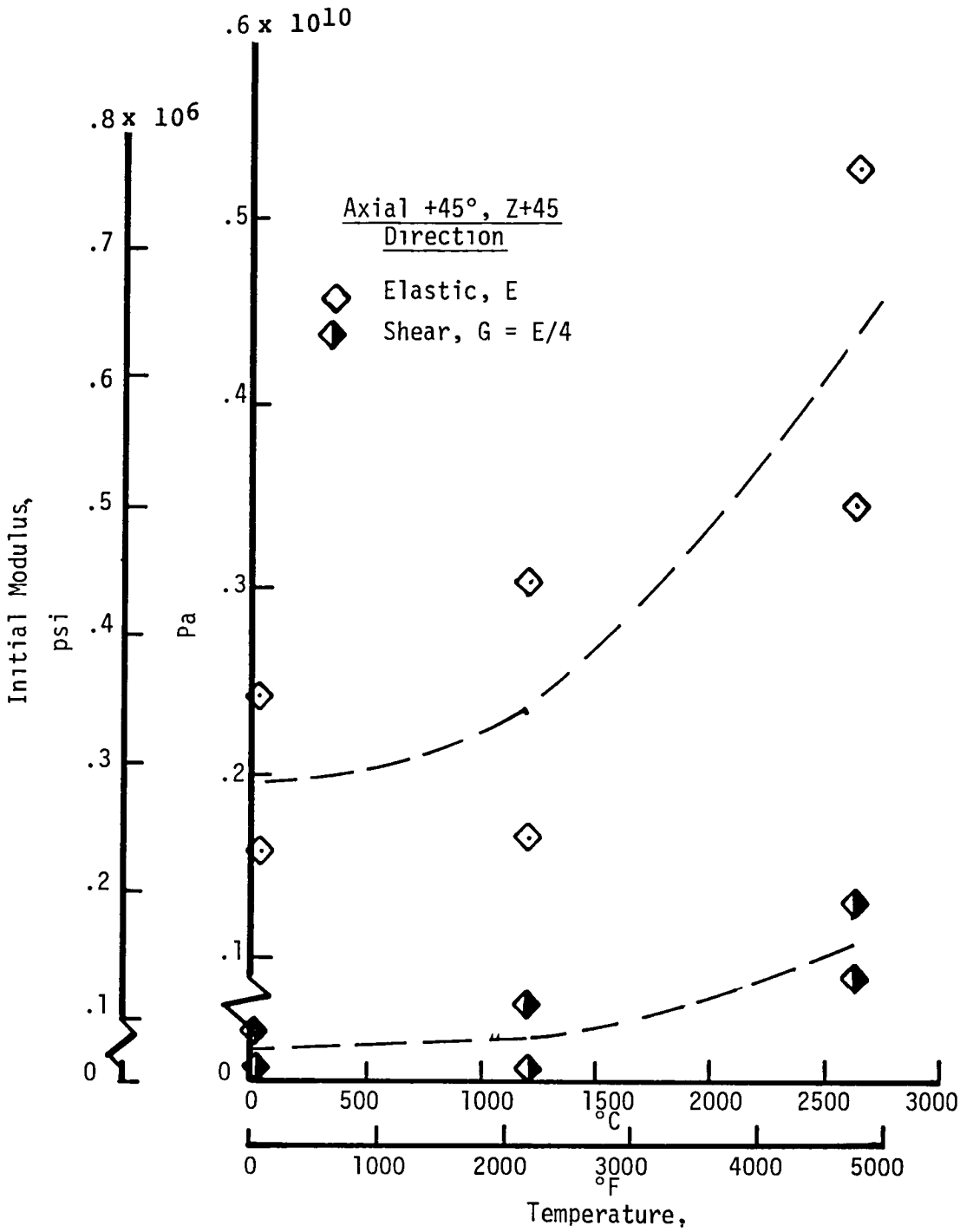

Figure 85. Compressive Modulus

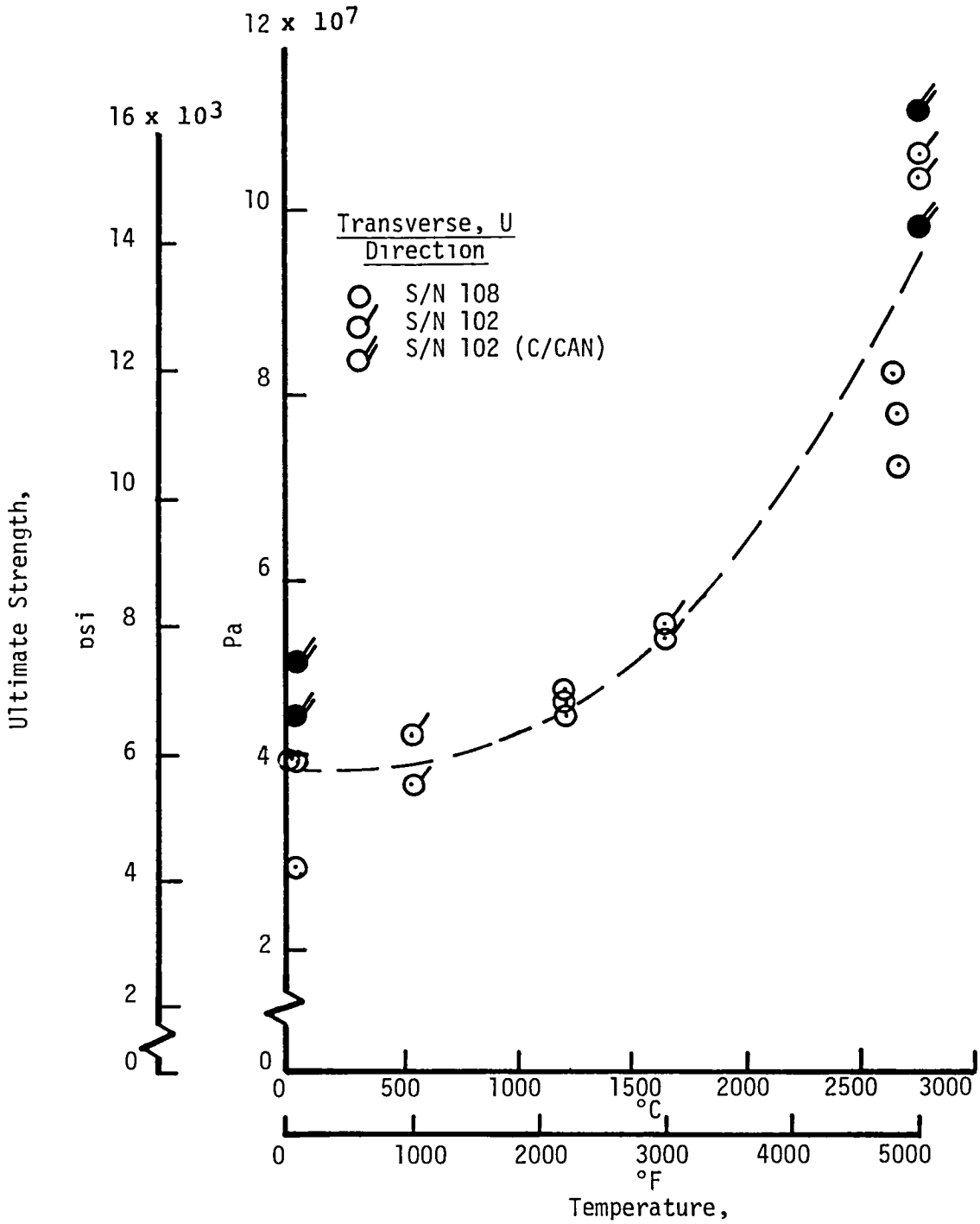

Figure 86. Compressive Strength

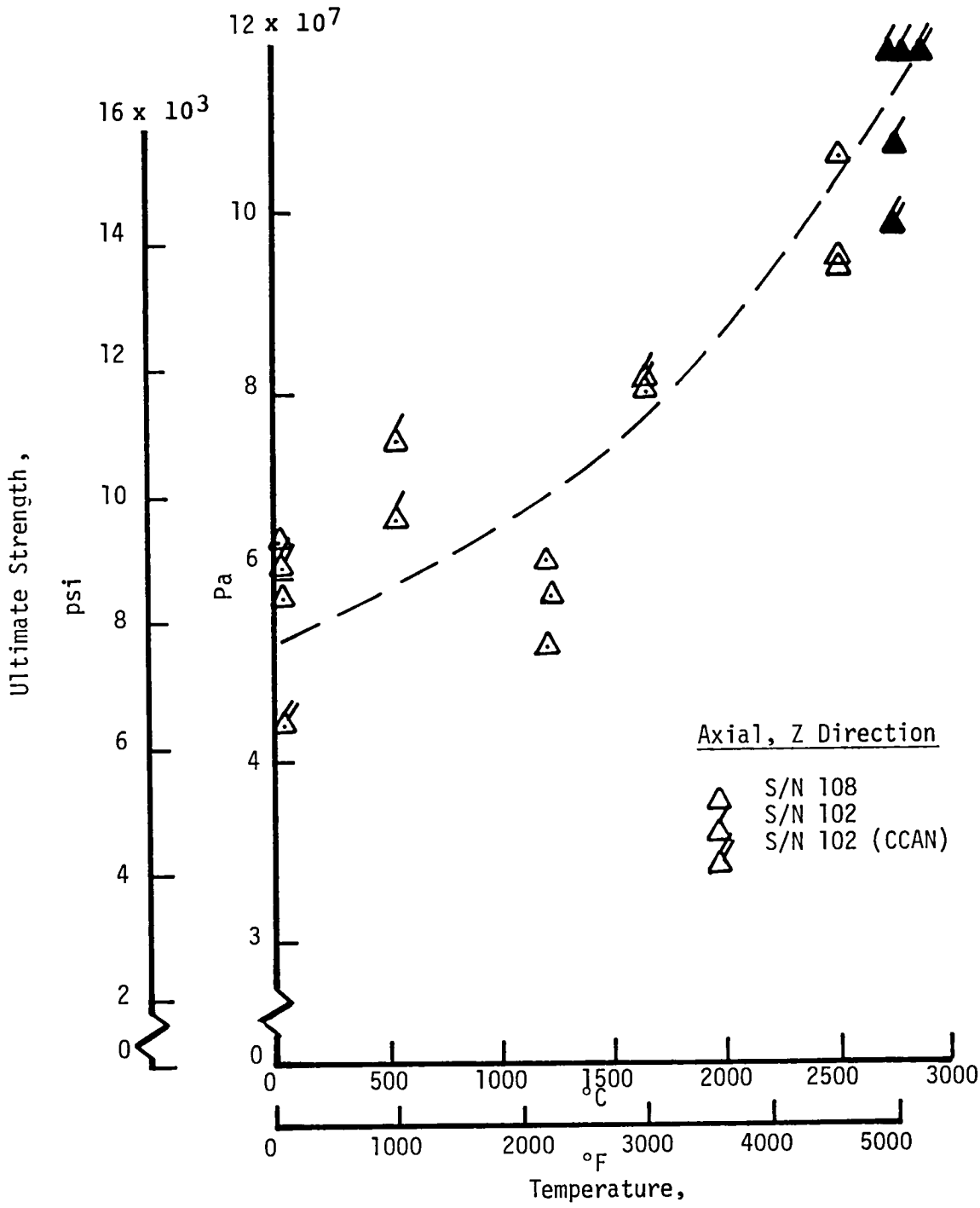

Figure 87. Compressive Strength

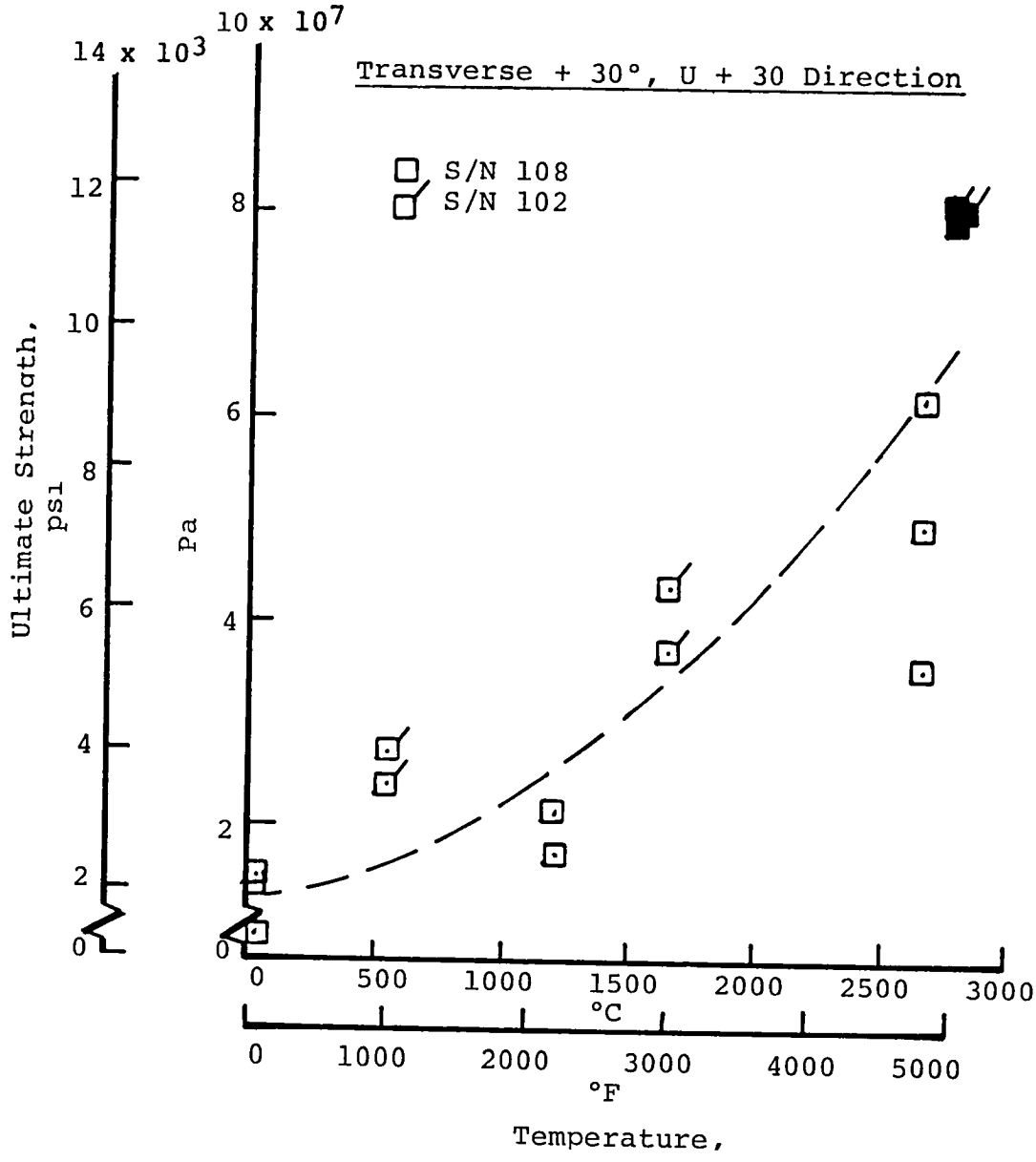

Figure 88. Compressive Strength

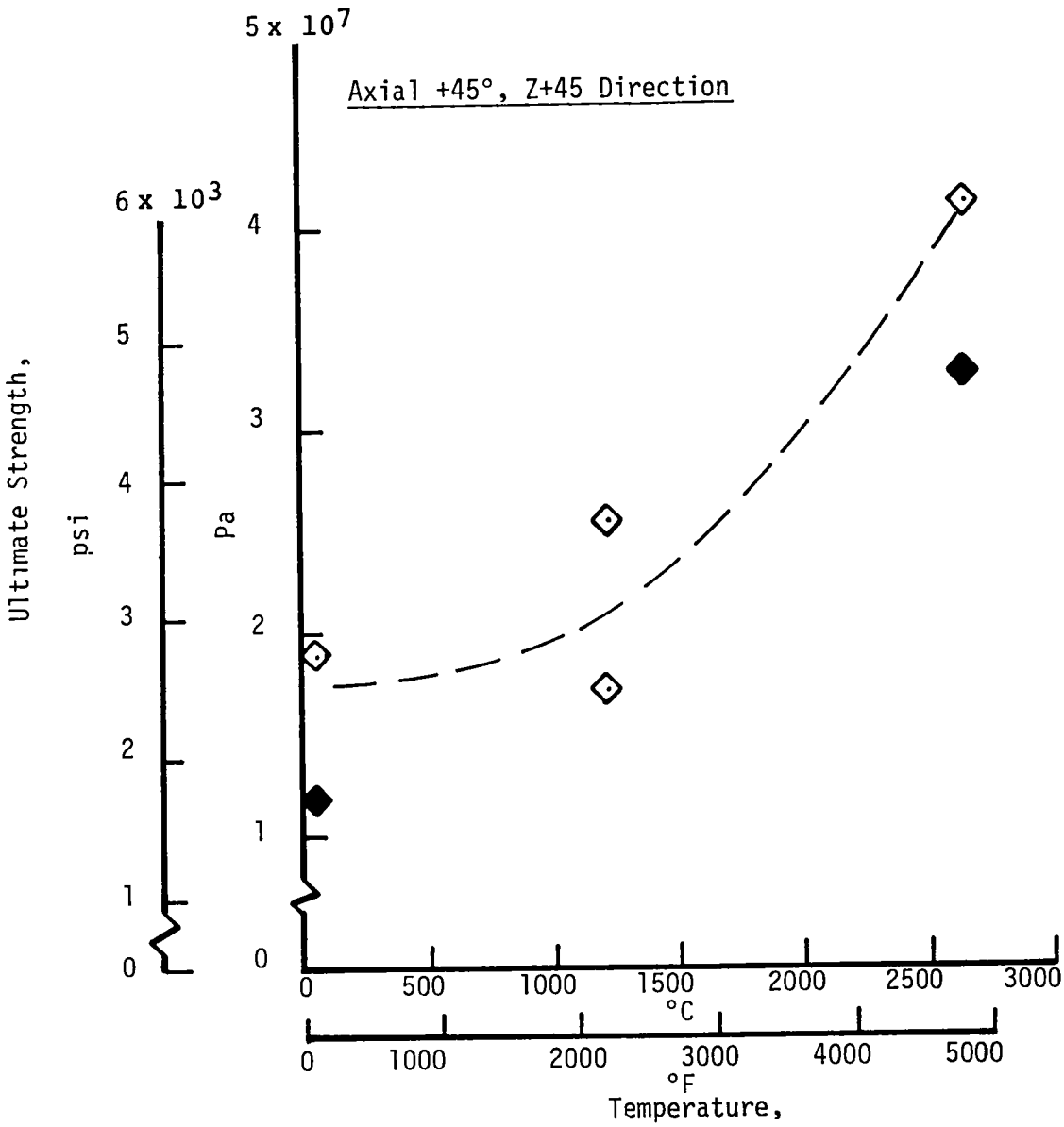

Figure 89. Compression Strength

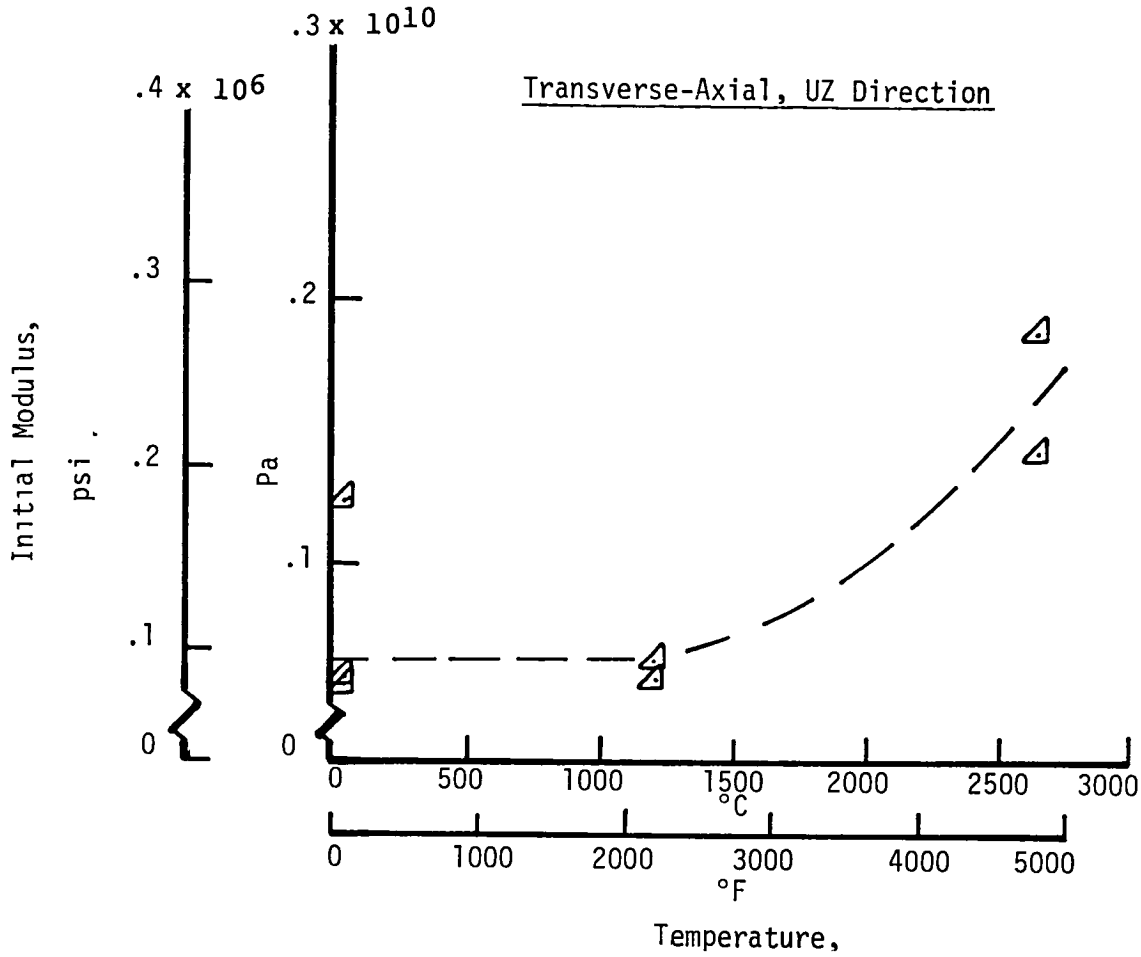

Figure 90. Torsional Modulus

Figures 91 through 93 present the thermal expansion data. Again the agreement between S/N's 102 and 108 is very good. A significant point to note is that there is very little permanent set in specimen length after cooling to room temperature. This is unusual compared to other coarse weave carbon-carbons where permanent elongations representing aligned fiber creep and end-effects can account for up to 40% of maximum thermal expansion, Reference 29.

The curves have been faired through the S/N 108 data and are replotted in Figure 94. The material appears to be isotropic in thermal expansion.

Figures 95 through 97 present the thermal conductivity data. In the U direction, again excellent agreement between S/N's 102 and 108 are obtained, while in the Z and U+30 directions, the S/N 102 data are higher. Again, the curves are faired through the S/N 108 data and are compared in Figure 98. As with thermal expansion, the material is isotropic in thermal conductivity.

Tag End Testing. - Two types of testing were explored for tag end quality assessment evaluation of the logs. The first was a ring tension test which was ultimately selected; the second a flexure test.

In developing the ring test, plane stress, linear elastic finite element analysis of the 4D ring was performed utilizing the MSO version of the SAAS III computer code, Reference 8. This analysis was conducted to provide design guidance and a correlation between the test results and an analytical material model.

The material model, shown in Figure 99, consisted of an orthotropic 4D ring with material property variation around the ring circumference having a periodicity of 60 degrees and symmetry

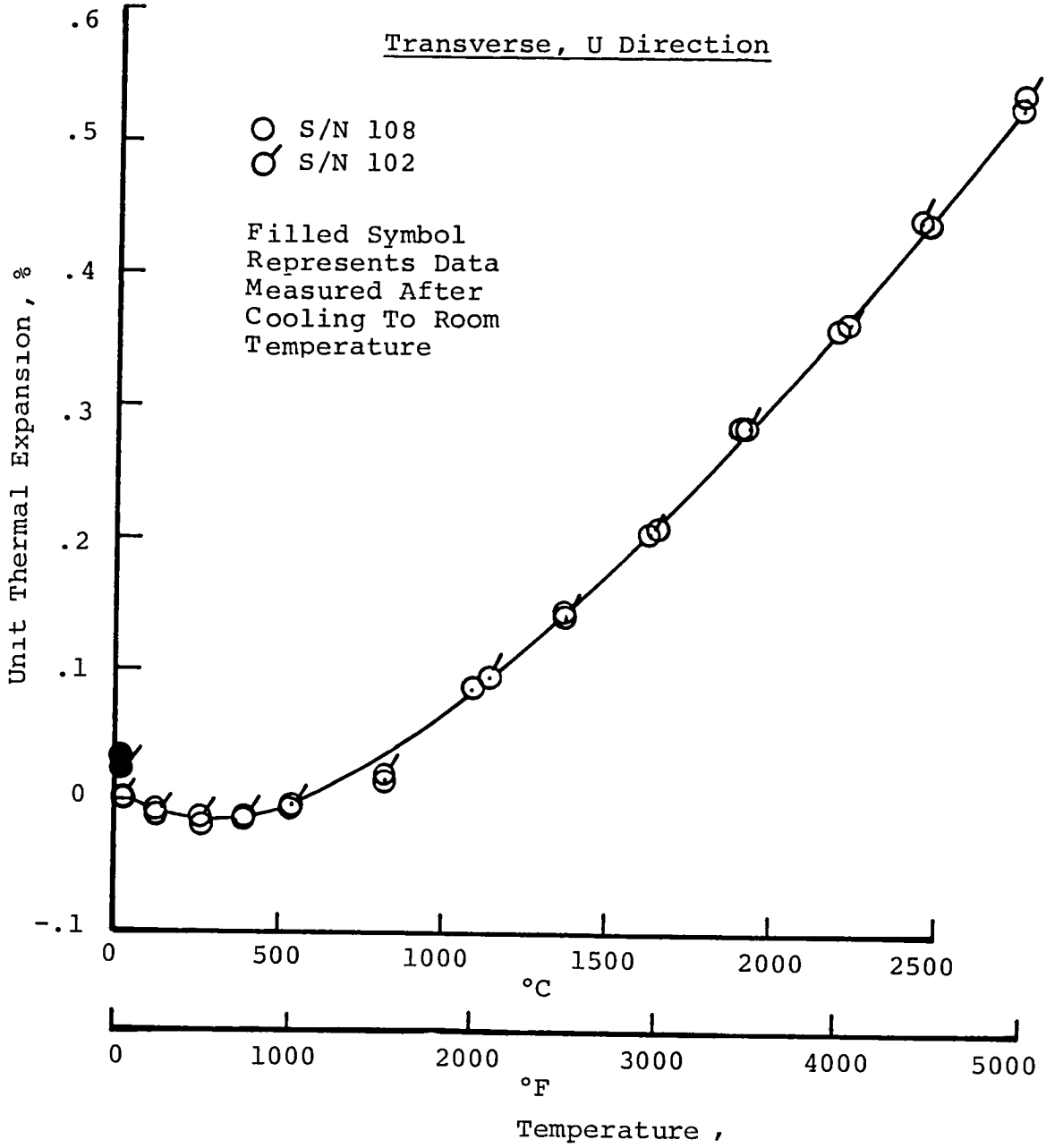

Figure 91. Thermal Expansion

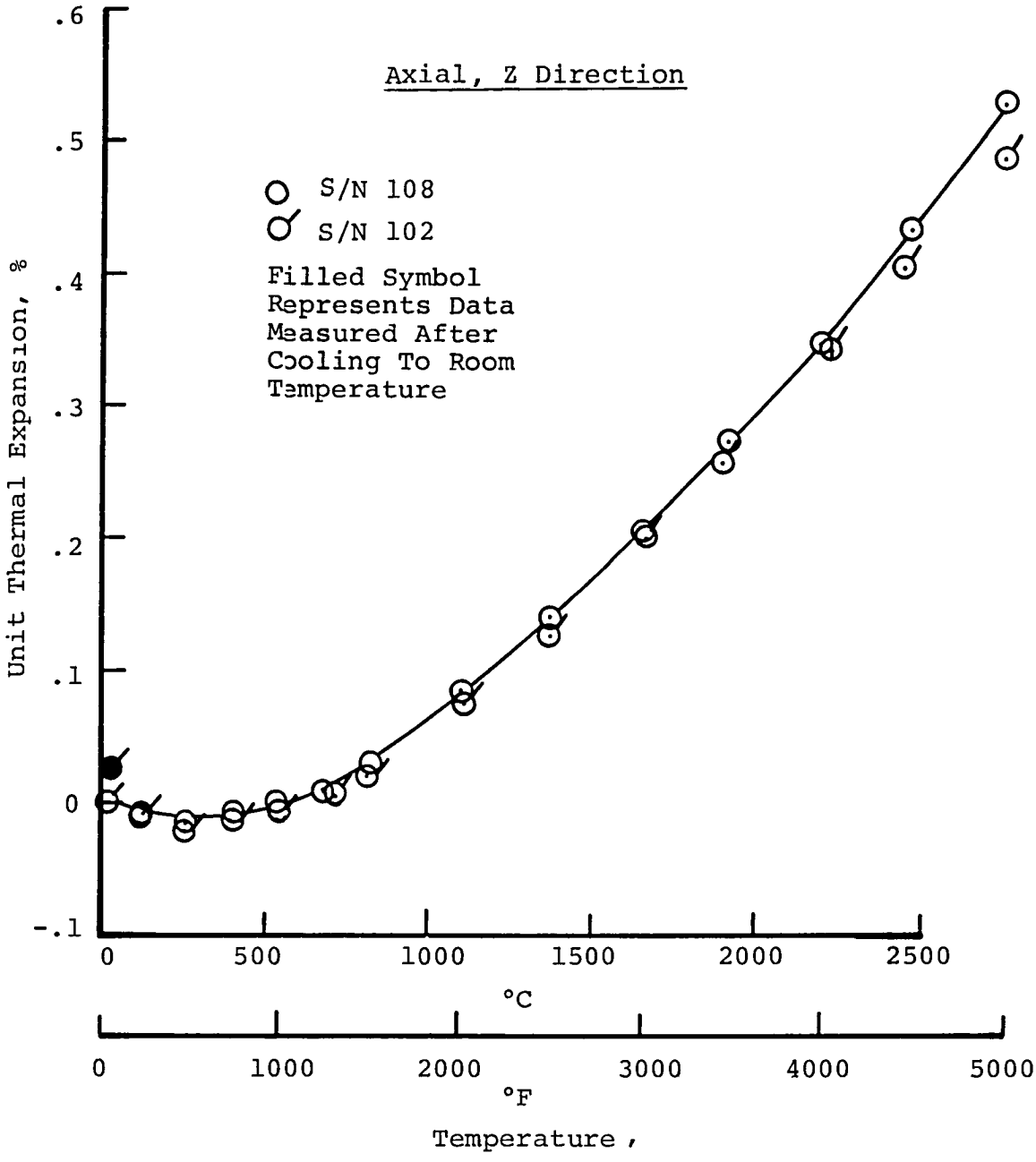

Figure 92. Thermal Expansion

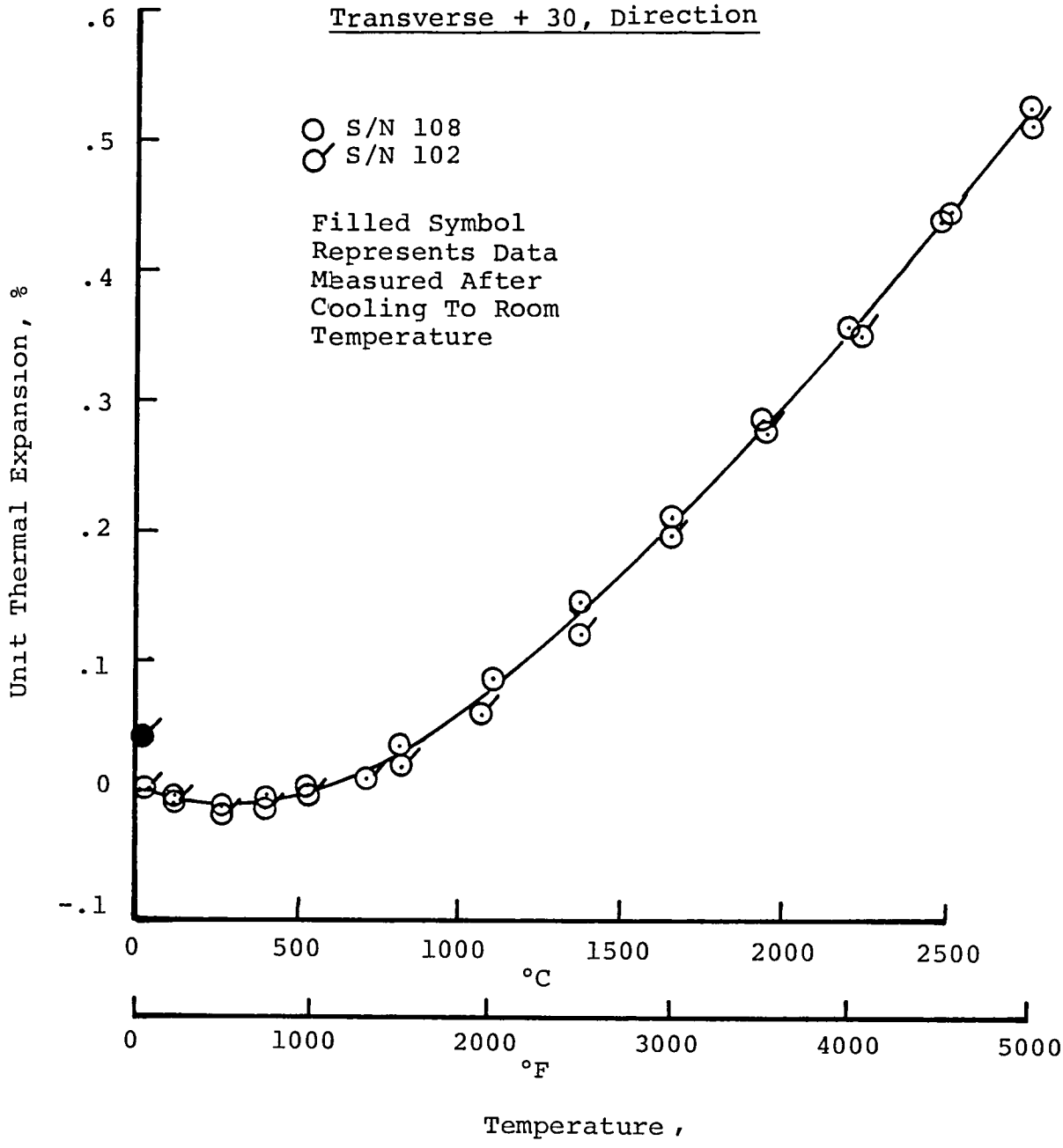

Figure 93. Thermal Expansion

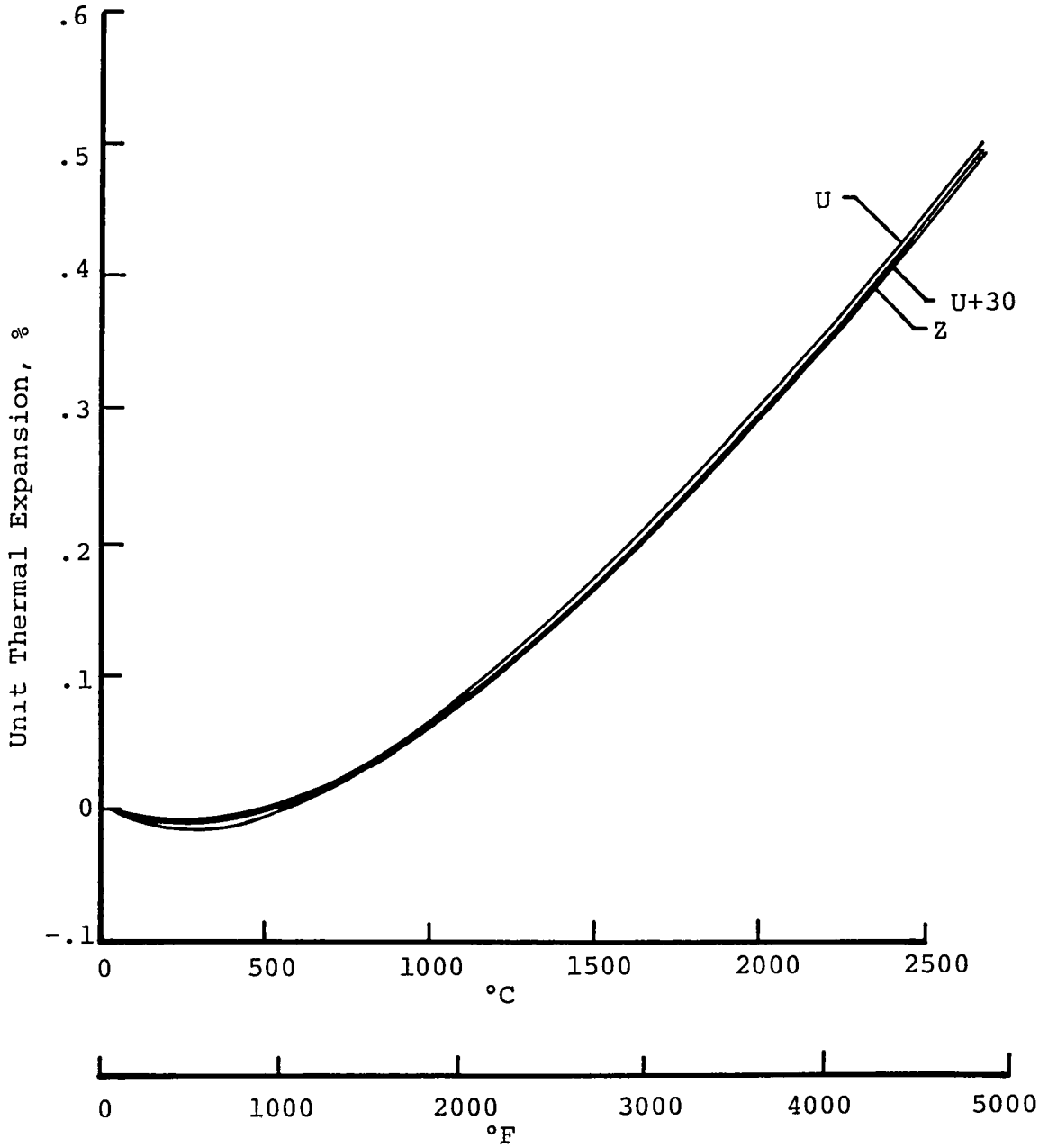

Figure 94. Thermal Expansion Comparison, Log S/N 108

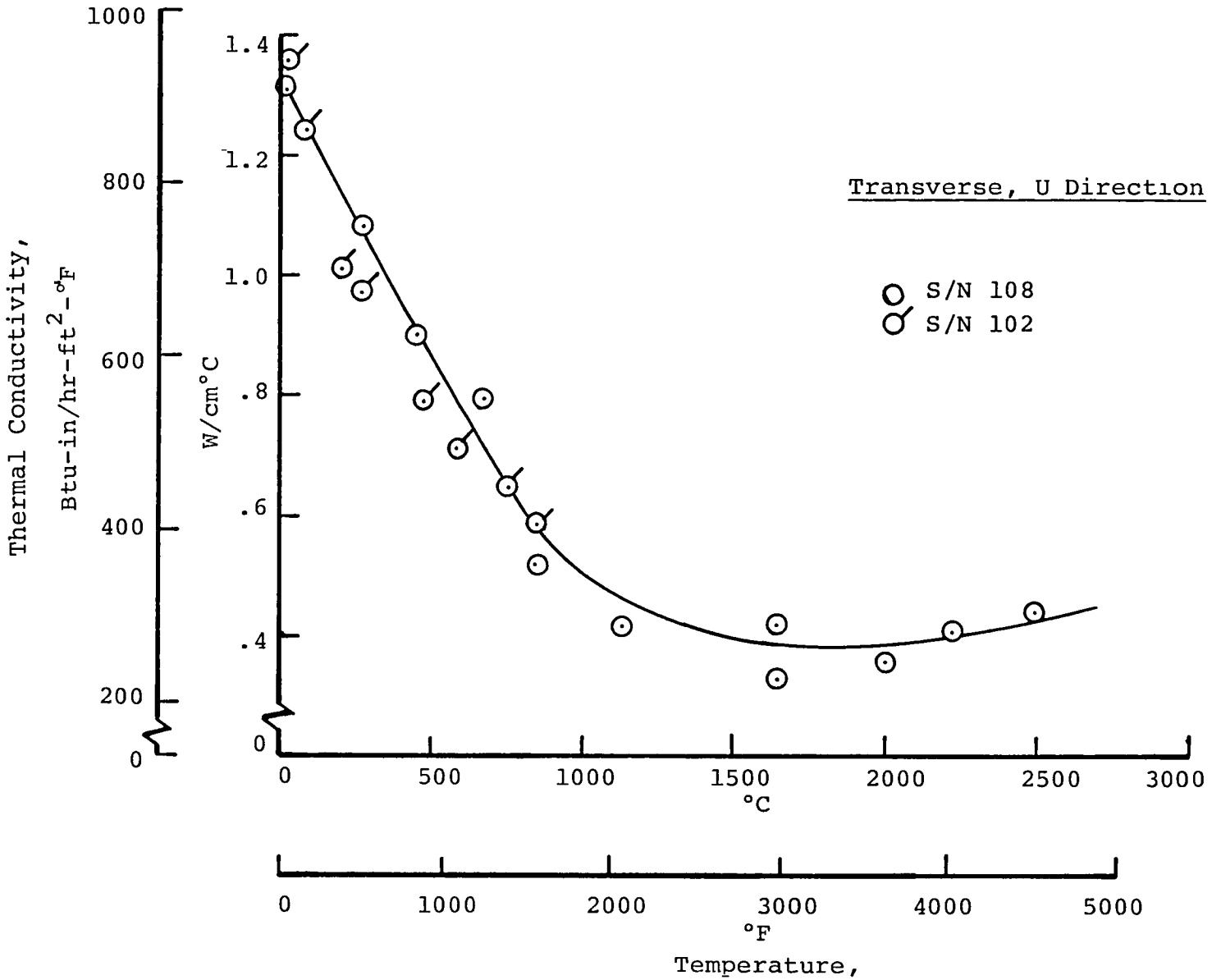

Figure 95. Thermal Conductivity

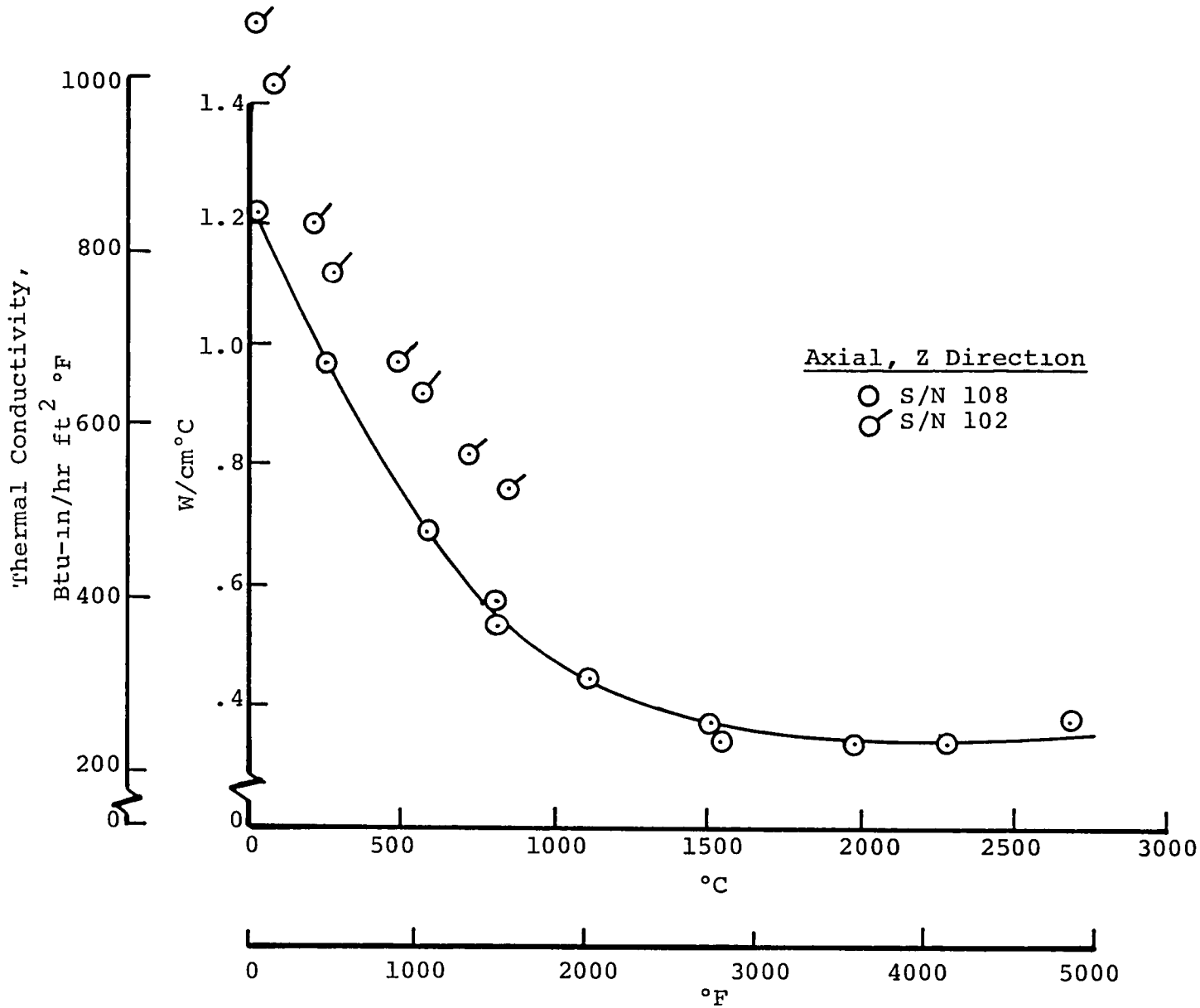

Figure 96. Thermal Conductivity

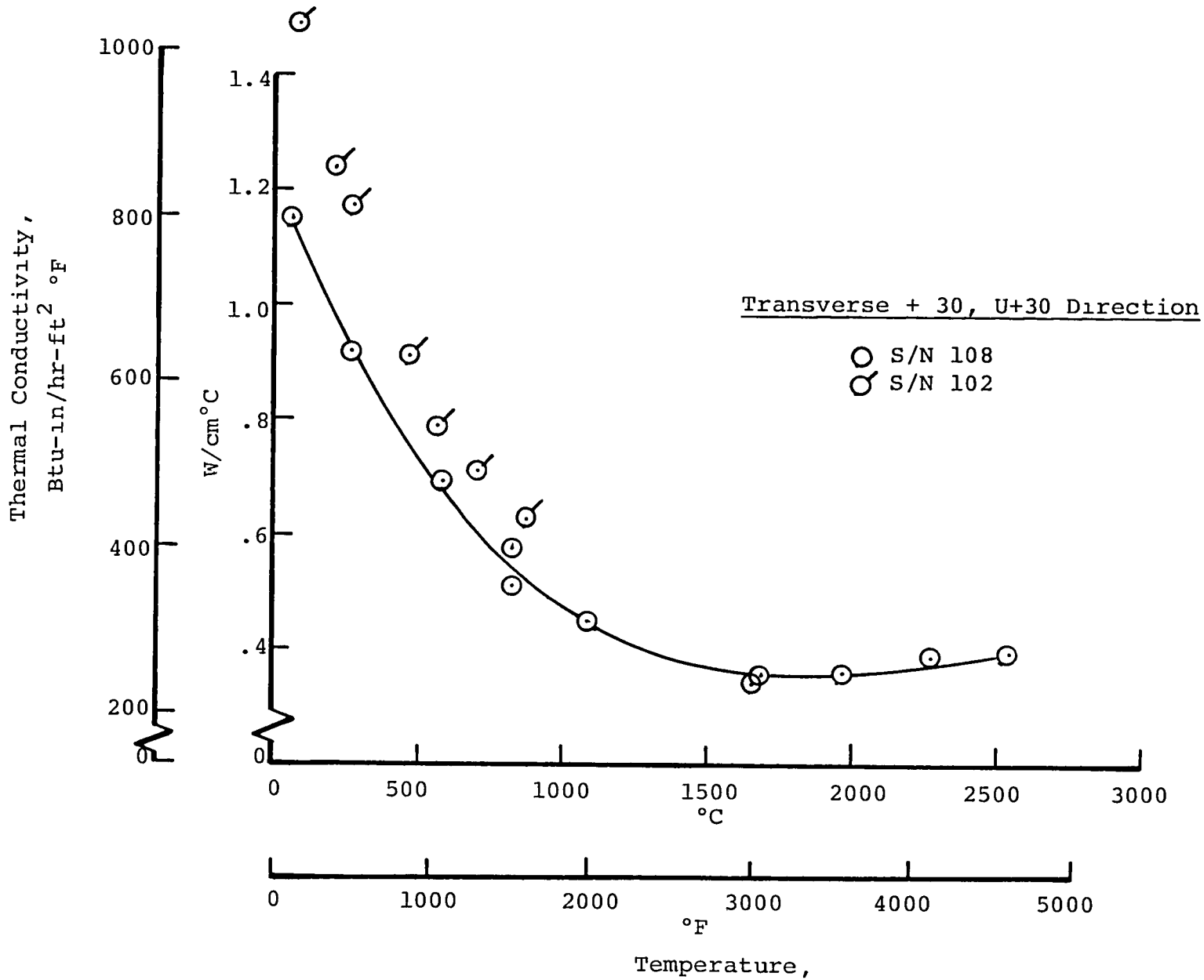

Figure 97. Thermal Conductivity

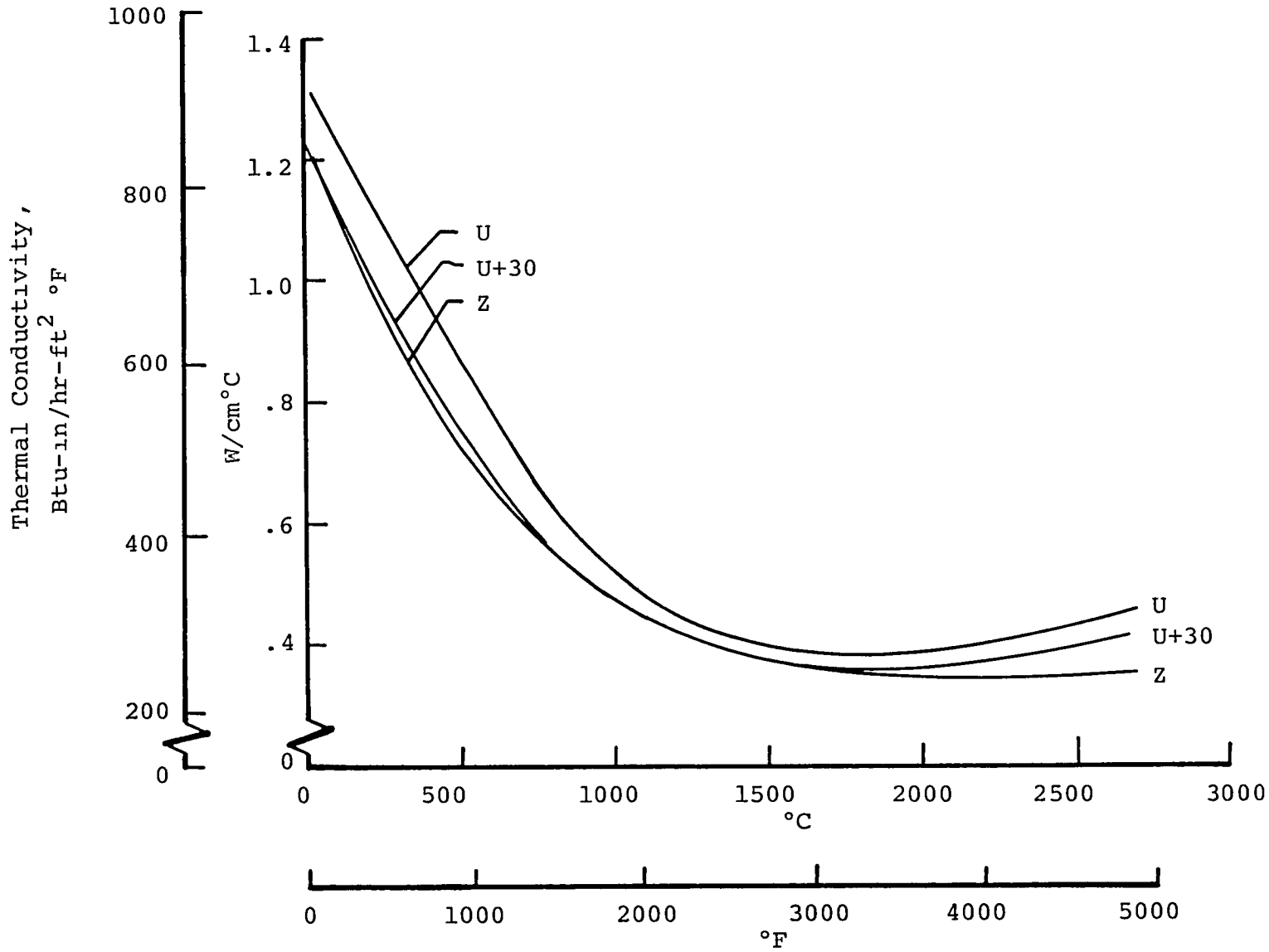

Figure 98. Thermal Conductivity Comparison, Log S/N 108

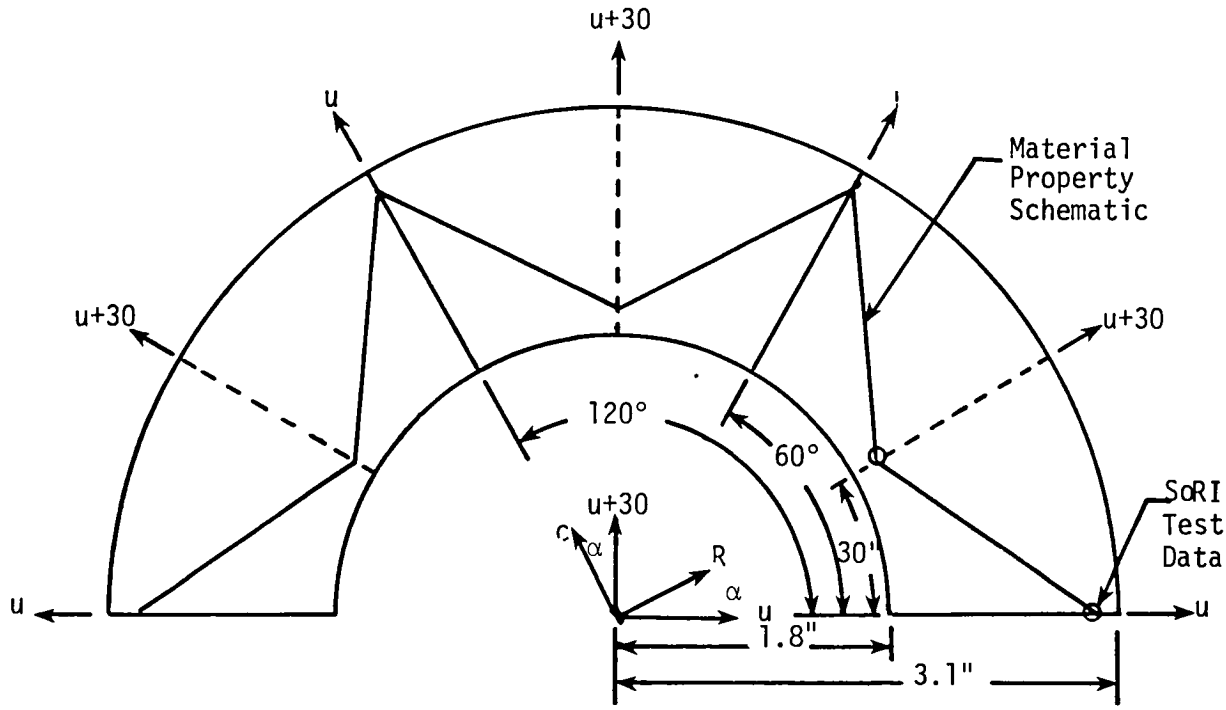

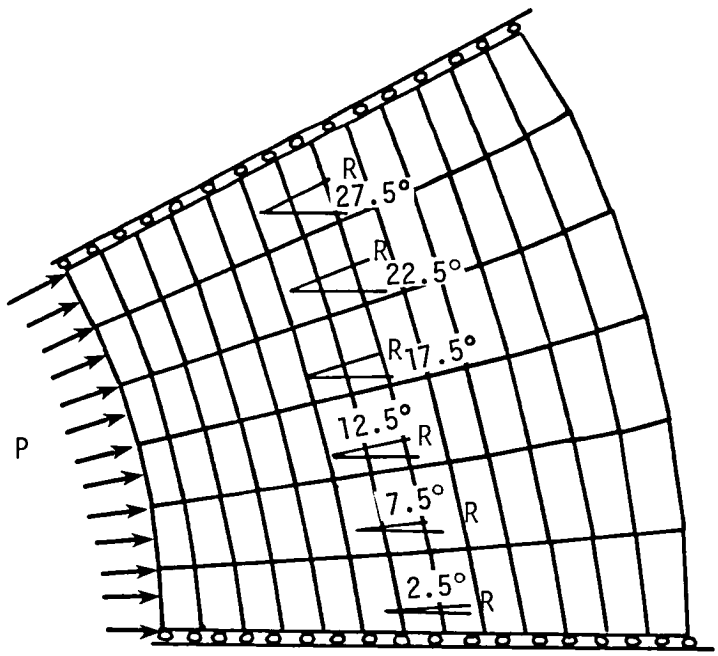

Figure 99. Analytical Model -4D Ring Test

at 30°. Because of the material property symmetry, only a 30° segment was required for the analysis. Rollers were placed on the circumferential faces of the ring which constrained the ring to radial displacement thereby allowing the internal pressure to be reacted by material constraints only. The plane stress condition is satisfied by having the test fixture design so that no load or constraint is placed on the specimen in the axial direction. The properties in the U and U+30 direction were obtained from SoRI test data. A linear property variation, shown in Figures 100 and 101, was assumed across the 30° arc. Note that because of the room temperature test environment, thermal strains for each material were zero. The material property variation was modeled incrementally across the 30° arc by incorporating 6 material blocks at 5° segments. The material characteristics of each 5° block were determined from the property variation data as a function of angle from the U axis. R is the principal material direction of each material block displaced from U by a material angle α, $2.5° \leq \alpha \leq 27.5°$. Each material block is orthotropic with the R direction corresponding to the average radial direction of that material block and the C direction corresonding to the circumferential direction, such that $E_R|_{2.5°} = E_c|_{27.5°}$ and $E_c|_{2.5°} = E_R|_{27.5°}$.

The allowable data associated with this material was developed by the same methodology as the material property data. Starting with SoRI orthotropic material allowable data for U and U+30° directions, a linear variation for ultimate strength and strain was assumed such that $\sigma_{R|_{U}} = \sigma_{C|_{U+30°}}$ and $\sigma_{C|_{U}} = \sigma_{R|_{U+30°}}$.

strength allowable data are presented in Figure 102. In the case of mechanical loading, for a linear elastic material model in particular, margins based on strength will predict the material behavior more closely than margins based on strain. This

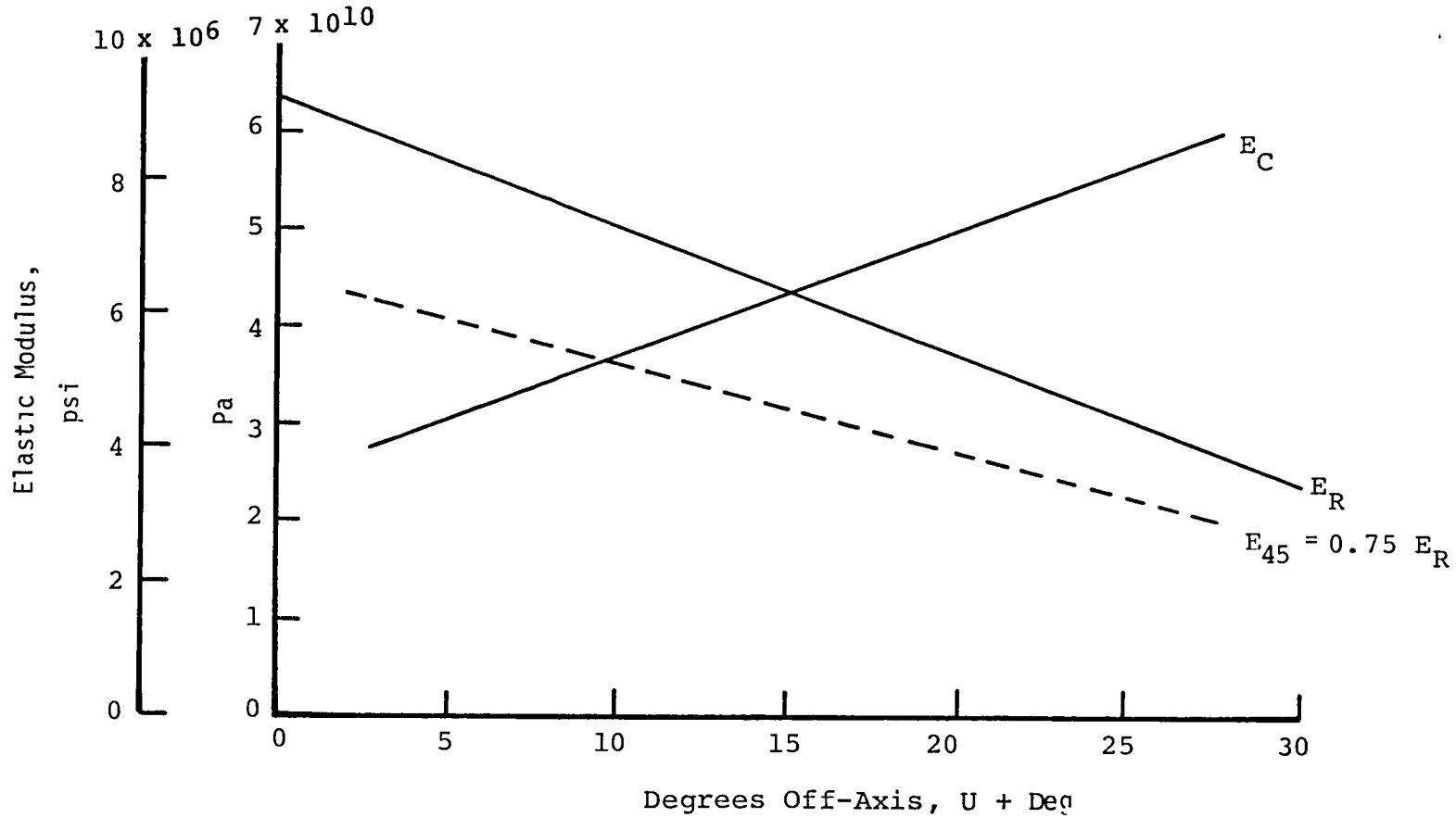

Figure 100. Elastic Modulus as a Function of Off-Axis Angle

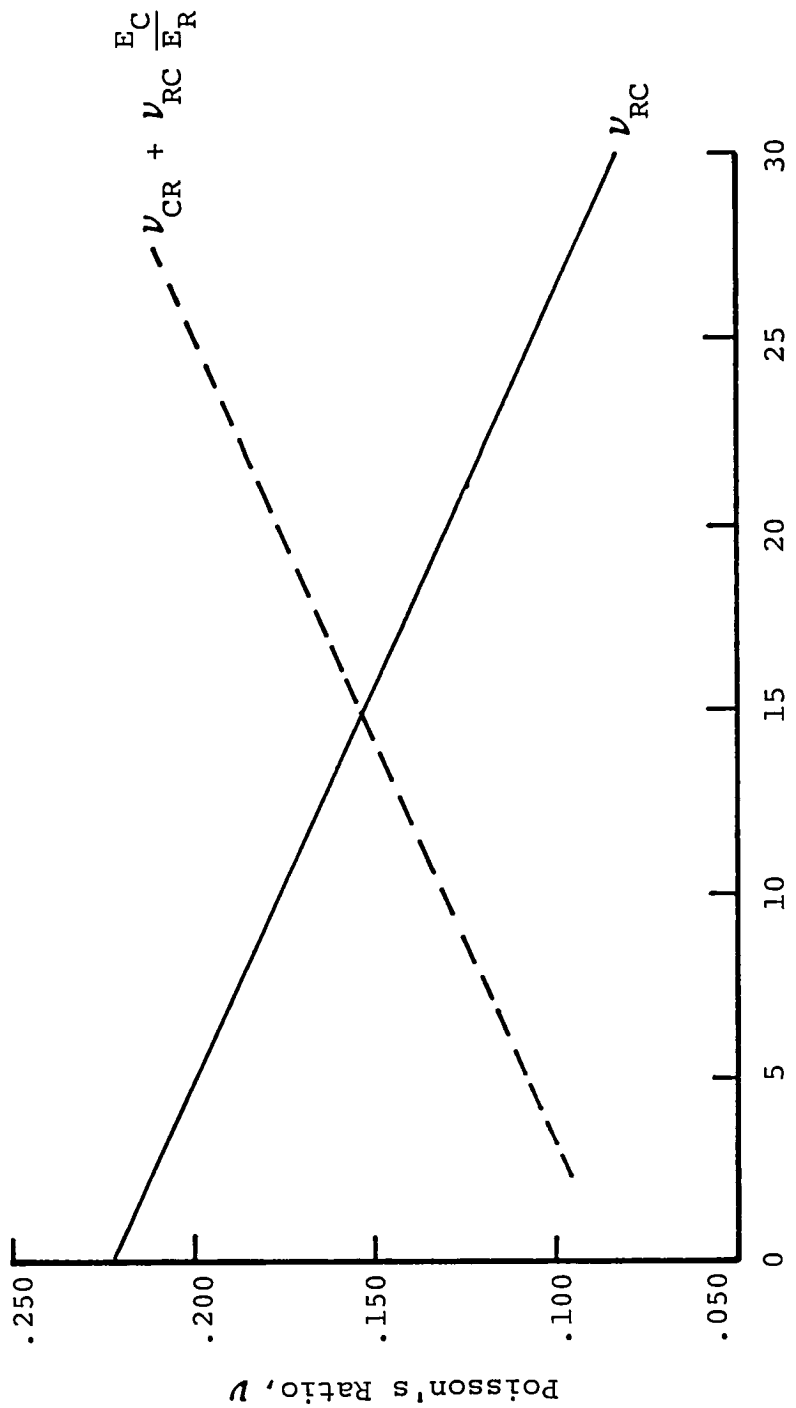

Figure 101. Poisson's Ratio as a Function of Degrees Off-Axis

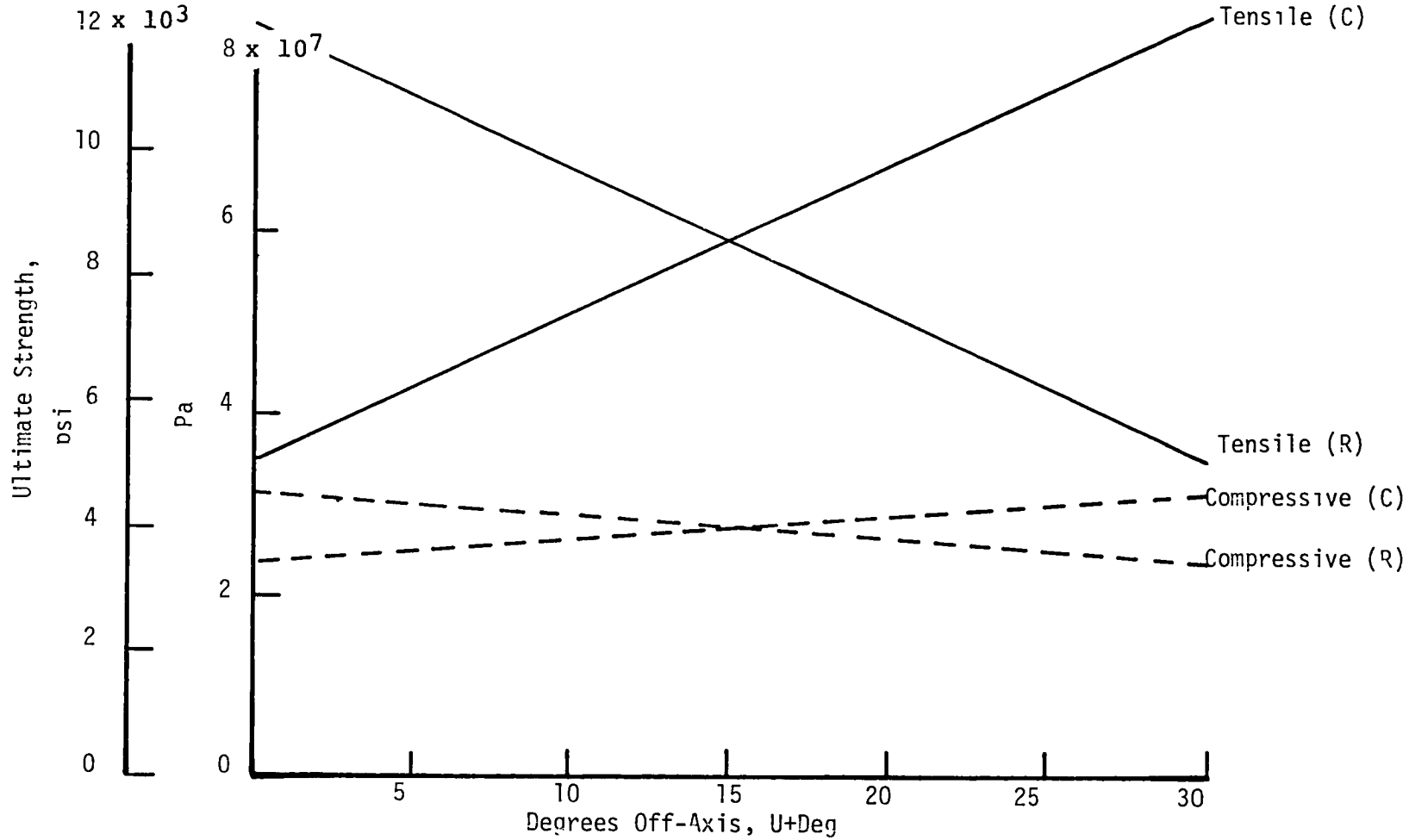

Figure 102. Ultimate Strength vs Degrees Off-Axis
4D Ring Test

is because the displacements used in the finite element analysis were derived from an applied force rather than an applied strain as would be in the case of thermal loading. Figure 103 shows the margin of safety plot based on strength as a function of internal pressure and material angle. This plot of circumferential tension margins shows the lowest of the two negative margin directions predicted by the analysis. The other case with negative margins indicated crushing of the inside diameter material at approximately 3.1×10^7 Pa (4500 psi) internal pressure. In both cases, the margins were the lowest at the I.D. Figure 103 indicates that, by extrapolating the material angle to zero degrees and the material radius to the I.D. rather than the inside element center, the ring will fail in circumferential tension at a "U" rod at an internal pressure of 1.65×10^7 Pa (2400 psi).

The test apparatus consists of two steel plates, sandwiching the thick ring test specimen, Appendix B. Four spacer blocks are used to ensure adequate clearance so that the specimen has no axial constraint. A rubber bladder is placed inside the ring to apply the internal pressurization. Initially instrumentation consisted of a dial pressure gage, a pressure transducer and "belly band" attached to an LVDT for OD circumferential deflection. These latter two were recorded on an x-y recorder in an attempt to obtain a load-deflection curve.

During check-out, considerable difficulty was encountered in obtaining repeatable deflection response. The cause of this was believed to be inadequate clearance between the specimen and the steel plates. Originally, this clearance was 0.025 cm (.010 in). During initial testing, the thin bladder was extruding through this opening at high pressures and failing. This was rectified by changing to a thicker bladder and decreasing the clearance to .002-.004 cm. (.001-.002 in). The specimen rings

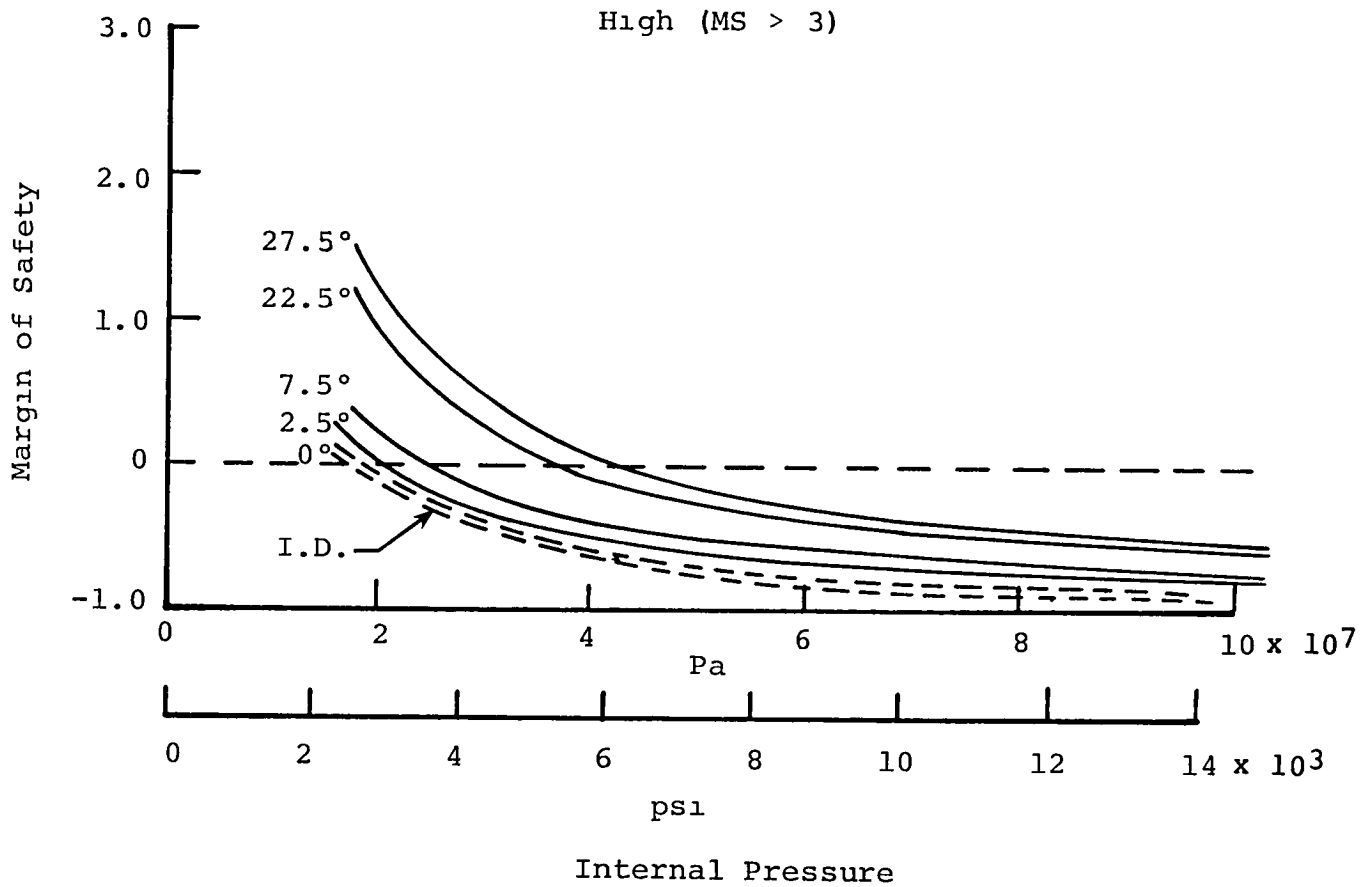

Figure 103. Strength Margin vs Internal Pressure
4D Ring Test - Circumferential Direction

were to be machined to +.000 -.004 cm (+.000-.002 in) tolerance so it was felt that adequate clearance was available. The rings were inspected using a micrometer every 30° of their circumference and found to fall within this tolerance.

However, in performing further testing, difficulties were experienced in consistently obtaining deflection measurements at low pressure loadings. It was felt at the time that this was due to "slop" in the belly band, LVDT system and efforts were focused upon improving this measurement technique.

When no consistent improvement was noted an alternative explanation was sought. The rings from log S/N's 103 and 104 were checked by laying them on a flat surface and checking their height dimension using a height guage. It was found that while their height at any location measured with a micrometer was within tolerance, when measured with a height gauge they were not flat. Thus, for rings 4D103 the spacers were shimmed to provide a clearance of .025 to .030 cm. In addition, once the test setup was assembled, a feeler gauge was used to verify that clearance existed around the specimen.

At this time it was also decided to eliminate the strain measurement for two reasons. The measurement is quite difficult and equipment set-up and calibration consumed inordinate amounts of time making the test quite expensive. More importantly, since the specimen is a thick ring lacking axisymmetry, how to interpret the OD strain measurement in terms of material quality was unclear.

Table 31 contains the ring data. Since S/N 103 was used in a development motor and S/N 104 was used in a qualification motor and for flight (MAGSAT, October 1979), one could establish approximately 1.15×10^7 Pa (1670 psi) as the minimum allowable

Table 31. Ring Test Data

Log S/N	Specimen No.	Maximum Internal Pressure, Pax10^7 (psix10^3)
ATJ	R1	1.310 (1.900)*
ATJ	R2	1.362 (1.975)*
107	R1	1.707 (2.475)*
107	R2	1.655 (2.400)*
107	R3	1.965 (2.850)*
107	R4	0.896 (1.300)*
105	R1	1.500 (2.175)*
103	1A	1.151 (1.670)
104	R1	1.407 (2.040)
108	2	1.758 (2.550)
108	4	1.724 (2.500)
120	2	1.345 (1.950)
121	2	1.448 (2.100)
122	3	1.276 (1.850)
123	3C	1.586 (2.300)
124	2	1.414 (2.050)
125	1	1.224 (1.775)
126	2	1.534 (2.225)
127	4	1.672 (2.425)
	Average	1.462 (2.120)

* Test may have suffered specimen binding therefore data suspect and not included in average.

burst pressure. All of the production logs delivered after S/N 103 had burst pressures in excess of this value. In addition, the results correlate well with the analysis both in location of the failure and pressure level.

In a parallel effort to the ring test, flexure testing was investigated as an alternate. All specimens were tested on an Instron model TM testing machine in three point bending at room temperature, see Figure 104. A constant crosshead speed (.05 cm/min) was used to apply the load to the specimen with load as a function of crosshead travel recorded on the Instron x-y strip chart. A dial gage mounted to the load train was placed in line with and directly opposite the applied force. The dial gage acted as a backup for the load train compliance in the elastic range and as a reference for total midspan deflection during plastic deformation.

As load is applied, the load train itself has deflection characteristics which must be taken into account when reducing raw test data. Also, material indentation at both support and load application points must be considered in defining the total load-deflection compliance. Load train and specimen indentation compliance was measured by using a flat .64 cm (.25 in) thick tool steel bar sandwiched between two flat pieces of test material loaded in three point bending, Figure 105. A 1.91 cm (.75 in) specimen length was used in the compliance calibration. This allowed a dial gage to be placed midspan in line with and opposite to the applied load. Any bending of the beam was subtracted out of the compliance curves. These data yielded load vs deflection curves for various test materials and orientations, Figure 106. In obtaining true beam deflection data, the compliance deflections at given loads were subtracted from the test load vs. deflection data. As can be seen by comparing Figure 106 with a typical test load-deflection curve shown in Figure

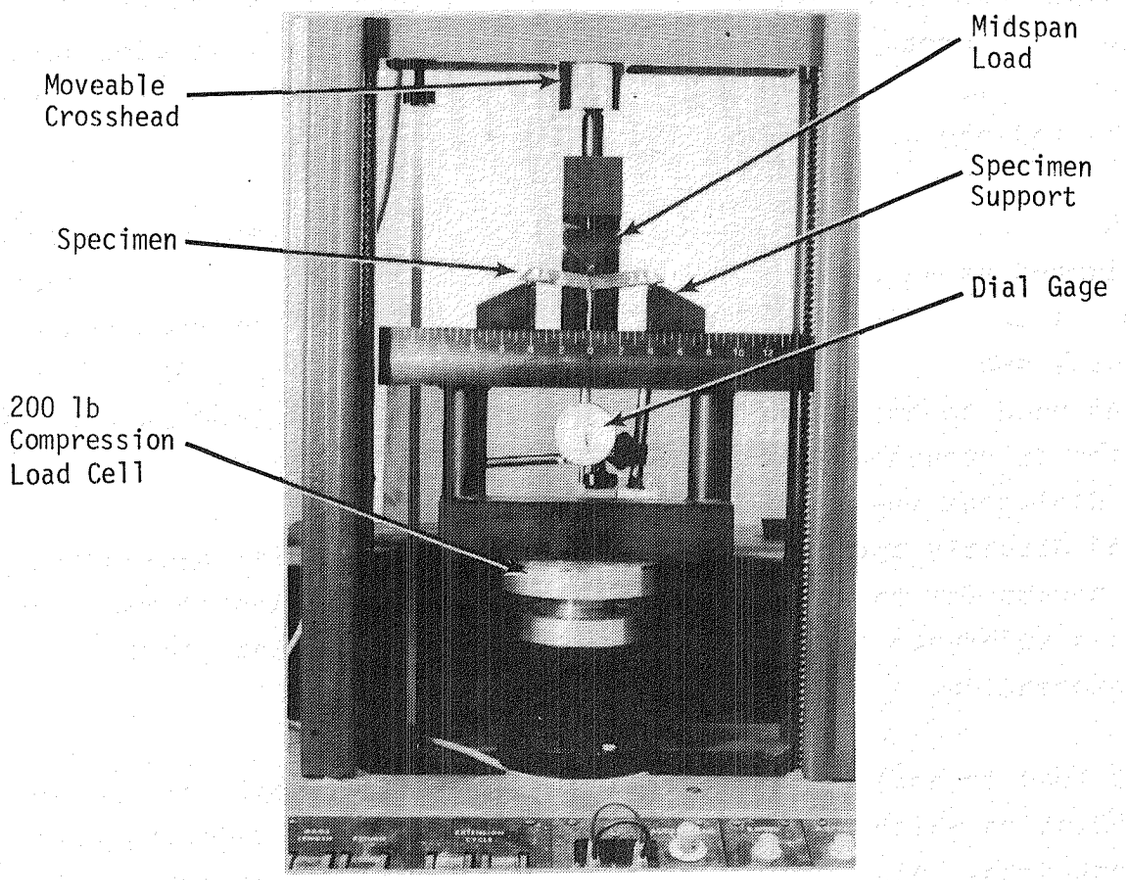

Figure 104. Flexure Test Load Train

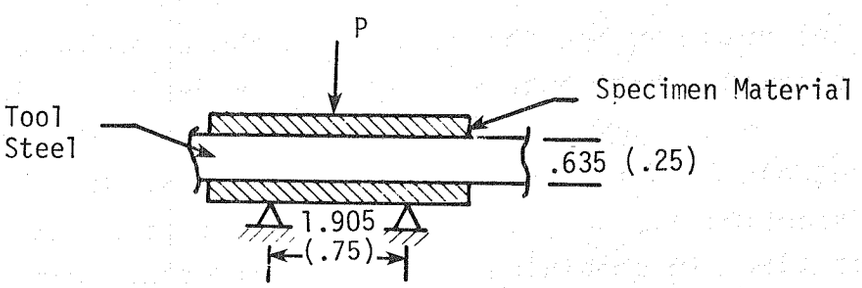

Figure 105. Compliance Test Specimen

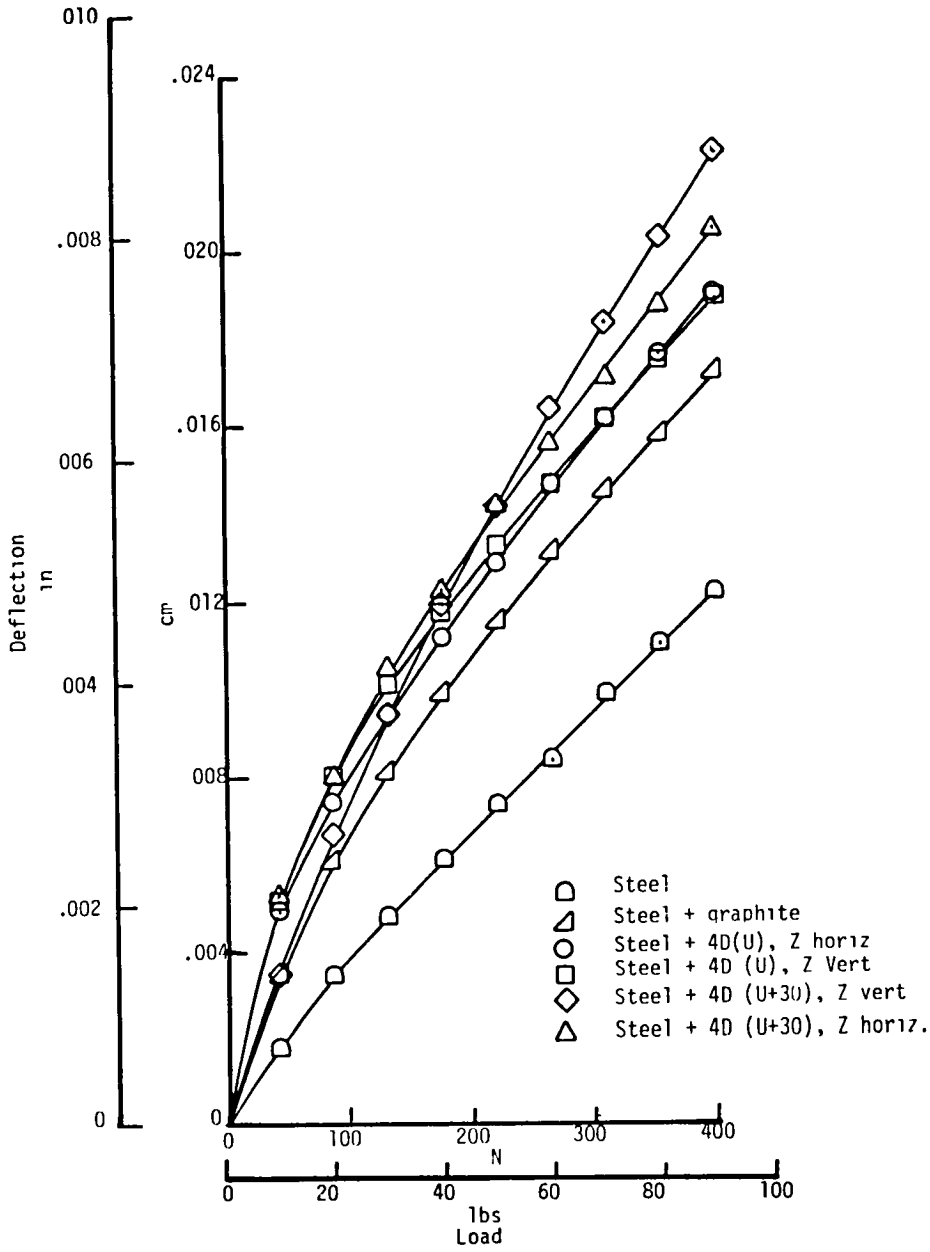

Figure 106. Instron Flex Test Load Train Deflection vs. Load

107, the compliance deformations are a considerable portion of the observed deflections during flexure tests.

Data reduction was carried out as follows. The modulus of elasticity, E, was determined by the relation

$$E = \frac{pl^3}{48vI}$$

where

p = load
l = span length
v = deflection
I = crosssection moment of inertia

The load-deflection characteristics were obtained in the linear portion of the curve after initial loading. The yield point was taken as the point where a substantial deviation from the initial linear curve was observed. The yield stress and strain were derived from Navier's flexure formula and Hooke's Law, respectively:

$$\sigma_y = \frac{My}{I} \quad , \quad \varepsilon_y = \frac{\sigma_y}{E}$$

where

M = midspan moment at yield
Y = distance from neutral axis to outer fiber

The maximum stress was approximated also using Navier's formula. However, the stress is underpredicted because the load-deflection curve is no longer linear, the effective cross sectional area has decreased and the neutral axis has shifted upward.

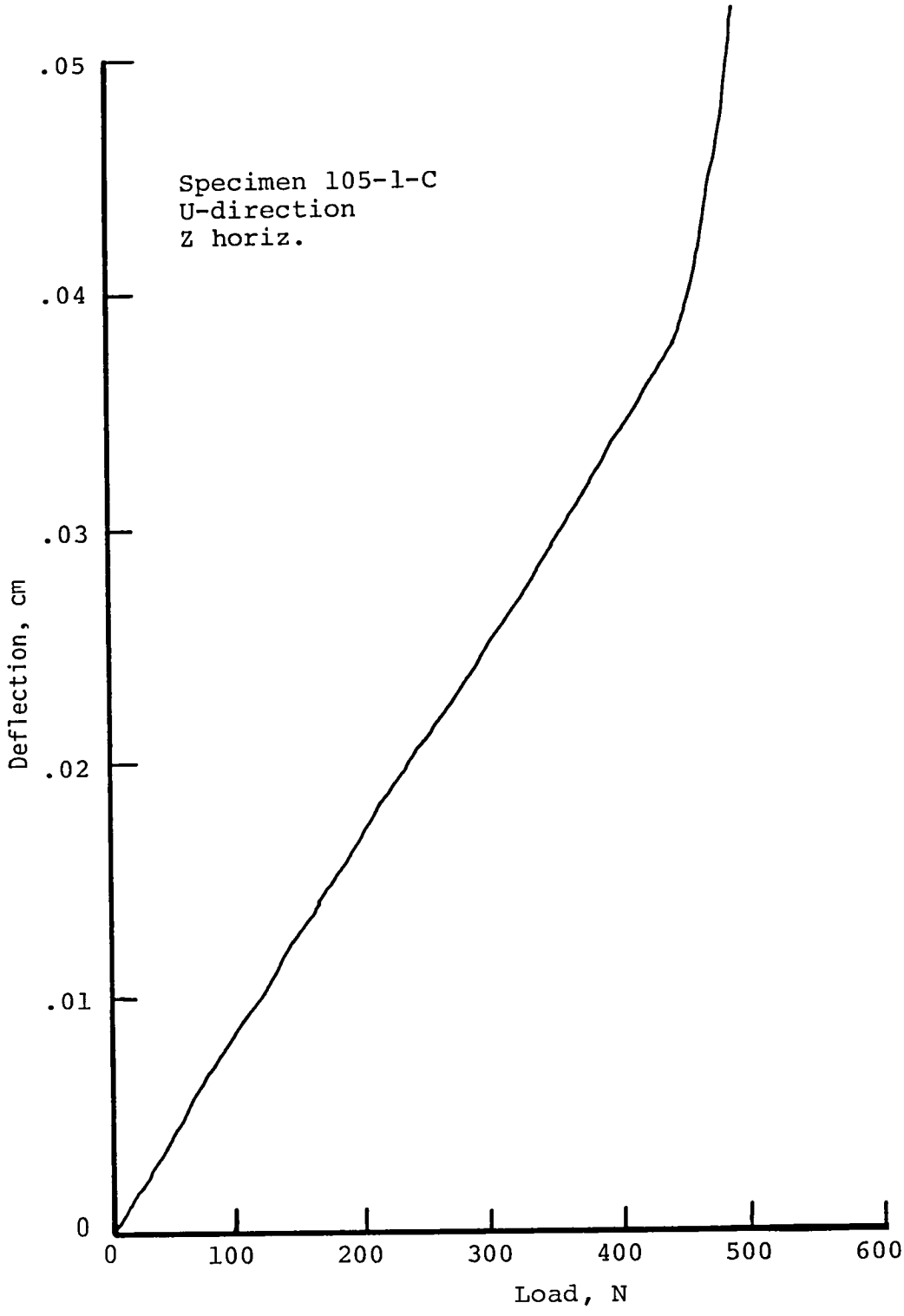

Figure 107. Instron Strip Chart Load - Deflection Curve

The strain at ultimate load and 50% ultimate load are estimates based on a ratio of strain to crosshead displacement at yield and strain to crosshead displacement at ultimate (or 50% ult) load such that:

$$\frac{\varepsilon_y}{\Delta y} = \frac{\varepsilon_{ult}}{\Delta y_{ult}}$$

This type of calculation gives a lower bound value and should be used for comparison only since strains may vary depending on yield point and Δy chosen.

Two series of tests were performed. The first testing was of log S/N's 103, 104, 105 and 107 and was done primarily to provide a checkout of the system. Table 32 presents this data. Most of the specimens came from rings that had been subjected to a burst test. Only for log S/N 105 was there enough virgin material to obtain specimens. In addition, all specimens were in the transverse direction and were tested mostly with the axial rods horizontal i.e. perpendicular to the load direction. It is obvious that material that has been ring tested has suffered damage. The moduli and ultimate stresses for the 105-3X series agree well with those obtained at SoRI.

A second series of tests was to provide a better data base on specimens excised from ring tested and virgin material. Table 33 presents this data which was gathered on log S/N 123. The data from log S/N 105 is repeated. Table 34 presents a summary of the averages for tested and virgin material data. These results are somewhat less clear. For specimens not from the region 180° from the failure location, the strength showed significant reduction compared to the virgin material. However, the strain was unaffected while the modulus was actually higher for the tested

Table 32. Flexure Data - Series I

	Specimen No.	Height, cm(in)	I, $cm^4(in^4 x 10^{-2})$	Gage Length, cm(in)	E, $Pa x 10^{10}$ ($psi x 10^6$)	σmax, $Pa x 10^7$ ($psi x 10^3$)	Strain @ 1/2 σmax, %	Strain @ σmax, %	Z Direct.[2]
T[1]	103-1AA	1.302(.513)	.209(.502)	10.16(4.0)	1.17(1.69)	3.80(5.51)	0.59	1.88	H
T	103-1AB	1.130(.445)	.158(.379)	10.16(4.0)	1.01(1.46)	3.90(5.66)	0.22	1.93	V
T	103-1AC	1.295(.510)	.215(.516)	10.16(4.0)	1.50(2.18)	3.54(5.14)	0.51	2.41	H
T	103-1AD	1.130(.445)	.150(.371)	10.16(4.0)	0.88(1.28)	4.05(5.87)	1.12	1.95	V
	Avg				1.14(1.65)	3.82(5.55)	0.61	2.04	
T	104-1A	1.361(.536)	.247(.593)	8.89(3.5)	1.36(1.97)	3.01(4.36)	0.60	1.52	H
T	104-1B	1.280(.504)	.200(.481)	8.89(3.5)	1.52(2.20)	3.82(5.54)	0.51	--	H
T	104-1C	1.285(.506)	.207(.497)	8.89(3.5)	1.71(2.48)	3.72(5.40)	1.15	2.10	H
T	104-1D	1.356(.534)	.251(.602)	8.89(3.5)	1.29(1.87)	3.23(4.69)	1.62	2.35	H
	Avg				1.47(2.13)	3.45(5.00)	0.97	1.99	
T	105-1A	1.311(.516)	.242(.582)	8.89(3.5)	0.93(1.35)	3.26(4.73)	0.90	2.59	H
T	105-1B	1.285(.506)	.225(.541	8.89(3.5)	1.81(2.62)	3.56(5.17)	0.15	1.70	H
T	105-1C	1.275(.502)	.189(.453)	8.89(3.5)	1.85(2.68)	4.16(6.03)	0.48	1.90	H
T	105-1D	1.298(.511)	.197(.473)	8.89(3.5)	1.41(2.05)	3.87(5.62)	0.86	2.22	H
	Avg				1.50(2.18)	3.71(5.39)	0.60	2.10	
U	105-3A	1.377(.542)	.267(.641)	11.43(4.5)	2.20(3.19)	4.23(6.13)	0.48	1.60	H
U	105-3B	1.351(.532)	.261(.627)	11.43(4.5)	3.32(4.81)	4.31(6.25)	0.25	1.46	H
U	105-3C	1.336(.526)	.253(.608)	11.43(4.5)	3.42(4.96)	4.16(6.03)	0.25	1.32	H
	Avg				2.98(4.32)	4.23(6.14)	0.33	1.46	
T	107-2A	1.278(.503)	.220(.528)	10.16(4.0)	2.90(4.21)	4.11(5.96)	0.10	1.19	H
T[3]	107-2B	1.229(.484)	.194(.467)	8.89(3.5)	0.79(1.14)	1.77(2.56)	0.19	3.08	V
T	107-2C	1.410(.555)	.236(.568)	8.89(3.5)	2.01(2.92)	3.70(5.37)	0.14	1.55	H
	Avg				1.90(2.76)	3.19(4.63)	0.14	2.06	

1 Material source: T-tested ring, U-untested ring

2 H-horizontal, V-vertical

3 U+30 specimen

Table 33. Flexure Data - Series II

Note: Z Direction Horizontal

	Specimen No.	Height, cm(in)	I, $cm^4(in^4x10^{-2})$	Gage Length, cm(in)	E, $Pax10^{10}$ (psix106)	σmax, $Pax10^7$ (psix10^3)	Strain @ 1/2σmax, %	Strain @ σmax, %
T[1]	105-1A	1.311(.516)	.242(.582)	8.89(3.5)	0.93(1.35)	3.26(4.73)	0.90	2.59
T	105-1B	1.285(.506)	.225(.541)	8.89(3.5)	1.81(2.62)	3.56(5.17)	0.15	1.70
T	105-1C	1.275(.502)	.189(.453)	8.89(3.5)	1.85(2.68)	4.16(6.03)	0.48	1.90
T	105-1D	1.298(.511)	.197(.473)	8.89(3.5)	1.41(2.05)	3.87(5.62)	0.86	2.22
	Avg				1.50(2.18)	3.71(5.39)	0.60	2.10
U	105-3A	1.377(.542)	.267(.641)	11.43(4.5)	2.20(3.19)	4.23(6.13)	0.48	1.60
U	105-3B	1.351(.532)	.261(.627)	11.43(4.5)	3.32(4.81)	4.31(6.25)	0.25	1.46
U	105-3C	1.336(.526)	.253(.608)	11.43(4.5)	3.42(4.96)	4.16(6.03)	0.25	1.32
	Avg				2.98(4.32)	4.23(6.14)	0.33	1.46
T	123-3C1F	1.229(.484)	.168(.403)	8.89(3.5)	2.17(3.14)	4.10(5.94)	0.40	1.66
T	123-3C1A	1.229(.484)	.181(.434)	8.89(3.5)	1.96(2.84)	3.96(5.74)	0.57	1.74
T	123-3C2F	1.290(.508)	.198(.476)	8.89(3.5)	1.69(2.45)	3.92(5.68)	0.42	1.30
T	123-3C2A	1.293(.509)	.201(.484)	8.89(3.5)	2.12(3.07)	4.07(5.91)	0.35	1.36
T[2]	123-3C3F	1.278(.503)	.196(.471)	6.35(2.5)	0.85(1.23)	2.86(4.15)	0.82	1.57
T[2]	123-3C3A	1.278(.503)	.177(.426)	6.35(2.5)	0.84(1.22)	3.08(4.46)	0.83	7.02
	Avg				1.61(2.33)	3.67(5.31)	0.57	2.44
U	123-3D1F	1.250(.492)	.170(.408)	8.89(3.5)	2.23(3.24)	4.20(6.09)	0.38	1.55
U	123-3D1A	1.273(.501)	.152(.366)	8.89(3.5)	1.61(2.34)	4.50(6.52)	0.65	1.42
U	123-3D2F	1.283(.505)	.201(.483)	10.16(4.0)	3.00(4.35)	4.41(6.39)	0.26	1.16
U	123-3D2A	1.273(.501)	.171(.412)	10.16(4.0)	1.88(2.73)	4.69(6.80)	0.34	1.19
U	123-3D3F	1.267(.499)	.189(.453)	10.16(4.0)	2.23(3.23)	4.56(6.61)	0.30	1.08
U	123-3D3A	1.191(.469)	.122(.294)	10.16(4.0)	1.74(2.52)	5.82(8.44)	0.53	1.08
U	123-3D4F	1.257(.495)	.201(.482)	8.89(3.5)	2.41(3.50)	3.95(5.73)	0.26	1.10
U	123-3D4A	1.267(.499)	.178(.428)	8.89(3.5)	1.84(2.67)	4.32(6.27)	0.36	1.19
U	123-3D5F	1.273(.501)	.205(.493)	7.62(3.0)	1.56(2.26)	3.34(4.85)	0.36	1.52
U	123-3D5A	1.252(.493)	.141(.338)	7.62(3.0)	1.30(1.88)	4.42(6.41)	0.82	2.14
U	123-3D6F	1.265(.498)	.190(.456)	7.62(3.0)	1.72(2.49)	3.56(5.16)	0.33	1.57
U	123-3D6A	1.273(.501)	.160(.385)	6.35(2.5)	0.74(1.07)	3.44(4.99)	0.68	2.25
	Avg				1.86(2.69)	4.27(6.19)	0.44	1.44

1 Material source: T-tested ring, U-untested ring

2 Specimen taken 180° from ring failure region

Table 34. Flexure Test Result Averages

	Tested			Untested		
Log S/N	E_{av}, Pax10^{10} (psix10^6)	ε_{av}, %	σ_{av}, Pax10^7 (psix10^3)	E_{av}, Pax10^{10} (psix10^6)	ε_{av}, %	σ_{av}, Pax10 (psix10^3)
105	1.50(2.18)	2.10	3.71 (5.39)	2.98 (4.32)	1.46	4.23 (6.14)
123*	1.99(2.88)	1.52	4.01 (5.82)	1.86 (2.69)	1.44	4.27 (6.19)
123**	0.85(1.23)	4.30	2.97 (4.31)	1.86 (2.69)	1.44	4.27 (6.19)

* Does not include 123-3C3F or 123-3C3A

** For 123-3C3F & 123-3C3A only

material. The material directly opposite the failure in the ring tested sample is obviously more seriously degraded than elsewhere in the ring.

GROUND TEST FIRINGS

A total of six ground test firings were conducted by Thiokol/Elkton. The first was a sea level demonstration test using an Altair III motor. In addition two sea level Antares III firings were conducted during the Development Phase. Finally, three Antares III qualification firings were conducted at AEDC. The following sections will present a brief summary of these results.

Demonstration Test

In order to demonstrate the performance of the SAI 4D carbon-carbon material for the throat insert in the redesigned Antares III motor nozzle, a static firing of an available Altair III motor was scheduled for the first week in August 1978. The nozzle insert billet S/N 102 was manufactured and densified to 1.81 g/cc by the Material Sciences Operation of SAI at Irvine, California and delivered to Edler Industries, the supplier of Altair nozzles, where it was installed in an Altair III nozzle in place of the standard G-90 insert (see Figure 108). The configuration of the carbon-carbon insert was the same as the G-90 insert in order to provide a direct comparison with previous Altair III static firing performance.

The static firing of the Altair III motor with the special nozzle described above was conducted by Thiokol Corporation at their Elkton, Maryland facility on 27 July 1978. All test objectives were met (Reference 30) and the carbon-carbon insert successfully survived the firing. Figure 109 shows pre- and post-test views of the nozzle. Post-test condition of the carbon-carbon insert was very good. The erosion rate was uniform around the circumference and there was no evidence of non-circularity at the throat due to the 4D weave construction (see Figure 110).

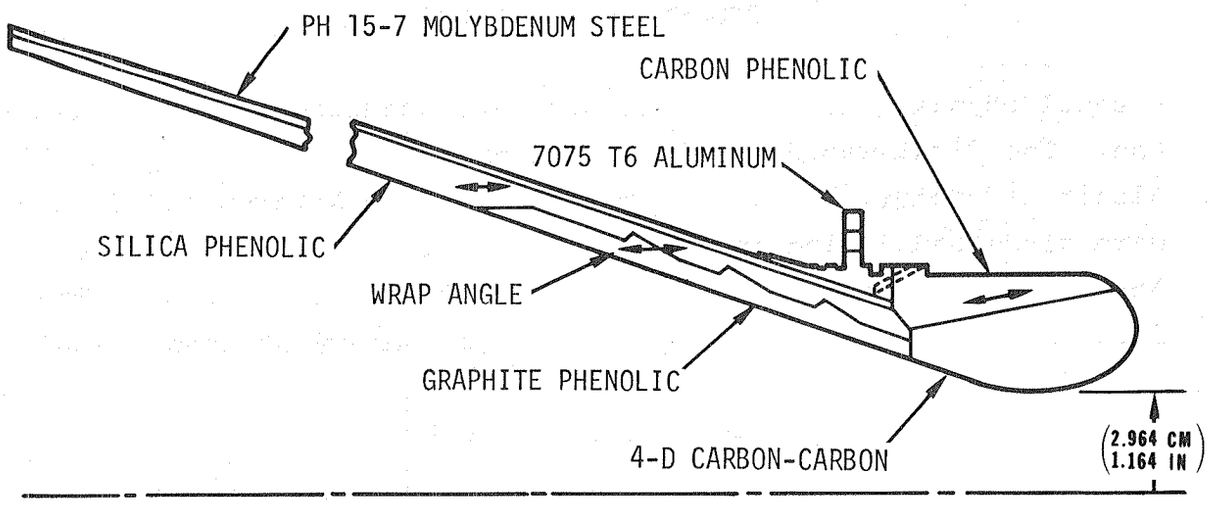

Figure 108. Altair III Nozzle

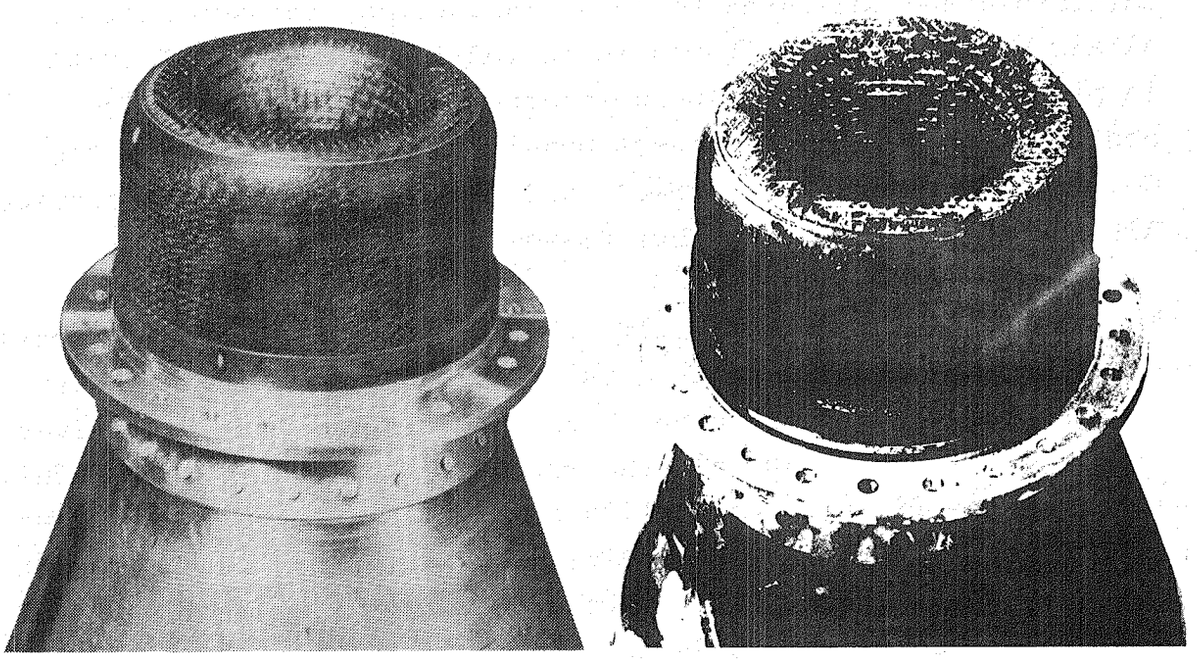

BEFORE FIRING AFTER FIRING

Figure 109. Altair III Nozzle With 4D C/C Insert Before Firing and After Firing

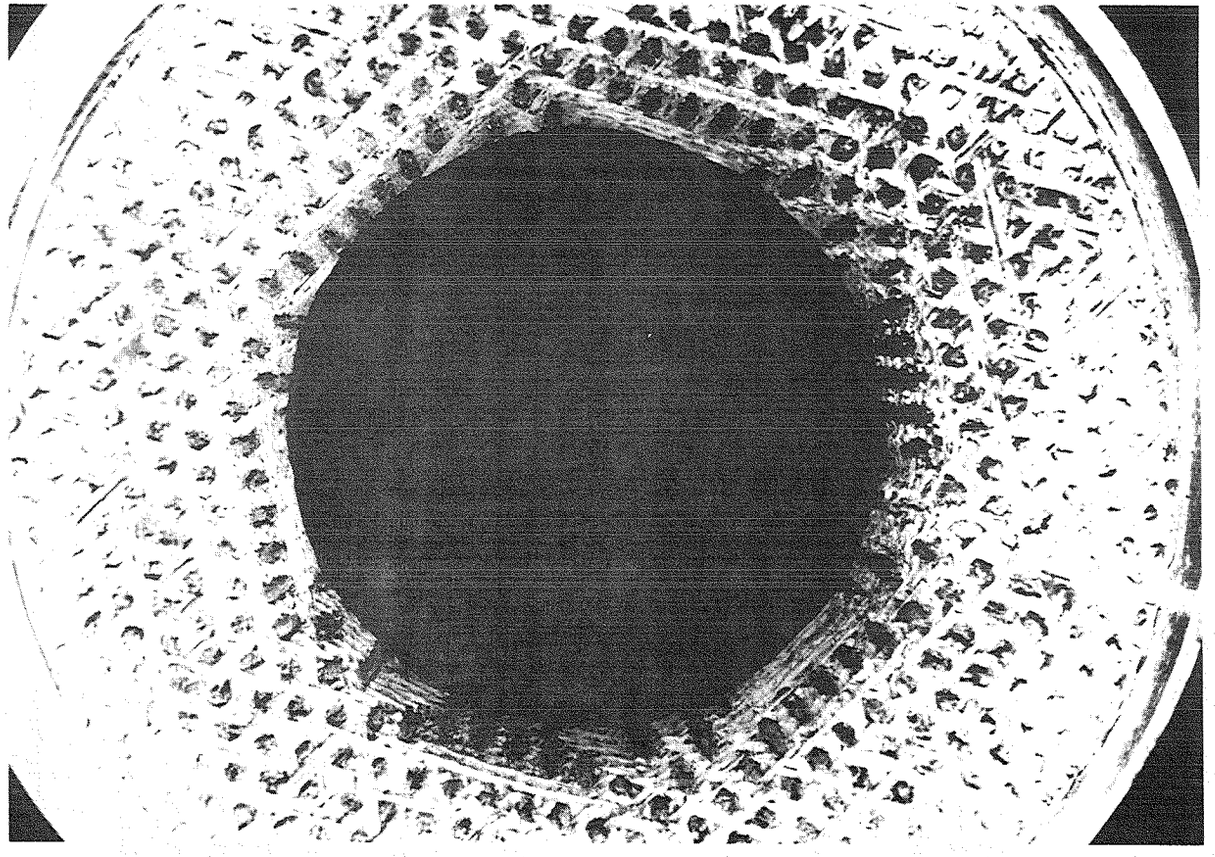

Figure 110. Altair III Carbon-Carbon Throat Insert (After Firing)

The average throat erosion rate was approximately forty percent higher than the average of previous firings with the G-90 insert, but virtually matched the pre-firing prediction of about 0.01 cm/sec (4 mil/ sec) (Reference 30). Figure 111 presents the predicted and measured chamber pressure histories.

Development Tests

Subsequent to the Altair III firing, the SAI 4D material was selected for the nozzle insert and taken into the Development Phase of the program. Two static firings at sea level were conducted by Thiokol/ Elkton, Reference 31. SAI provided both carbon-carbon billets, S/N's 103-1 and 103-2, to Thiokol who machined the inserts and assembled the nozzles, Figure 112. The only differences between D-2 and D-3 were the throat diameters, 10.206 cm (4.018 in) for D-2 and 9.162 cm (3.607 in) for D-3. Since use of carbon-carbon was new, the objective was to establish a throat diameter versus chamber pressure performance data base from which to select the final design throat diameter.

The firings occurred on September 21 and October 19, 1978 for D-2 and D-3, respectively. The carbon-carbon insert material performed as expected with good shape retention, Figure 113; the severe material loss aft of the insert evidenced in the D-1 firing was substantially reduced by the extention of the carbon-carbon insert into this region and the elimination of the dixie cup insulator part. There was no evidence of any cracks in the insert material due to thermostructural failure.

Figures 114 through 117 show the original and eroded profiles and the predicted and measured chamber pressure histories.

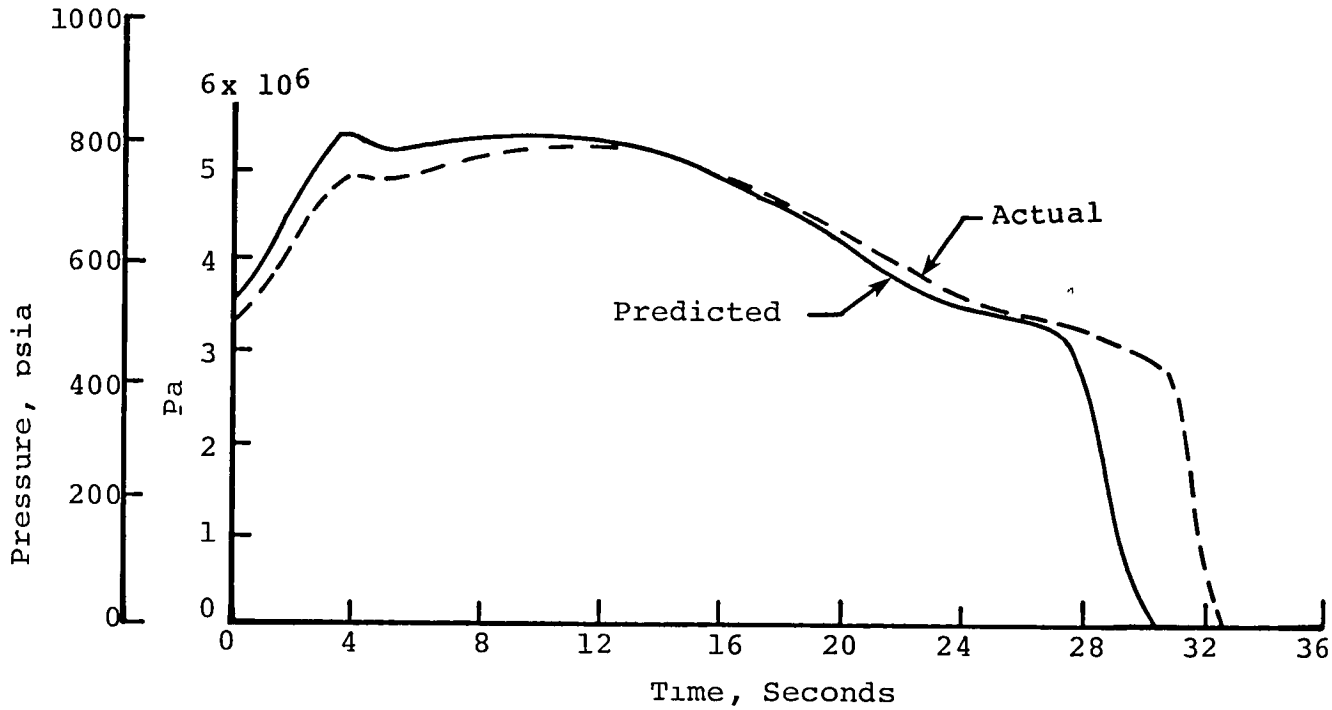

Figure 111. Pressure vs Time

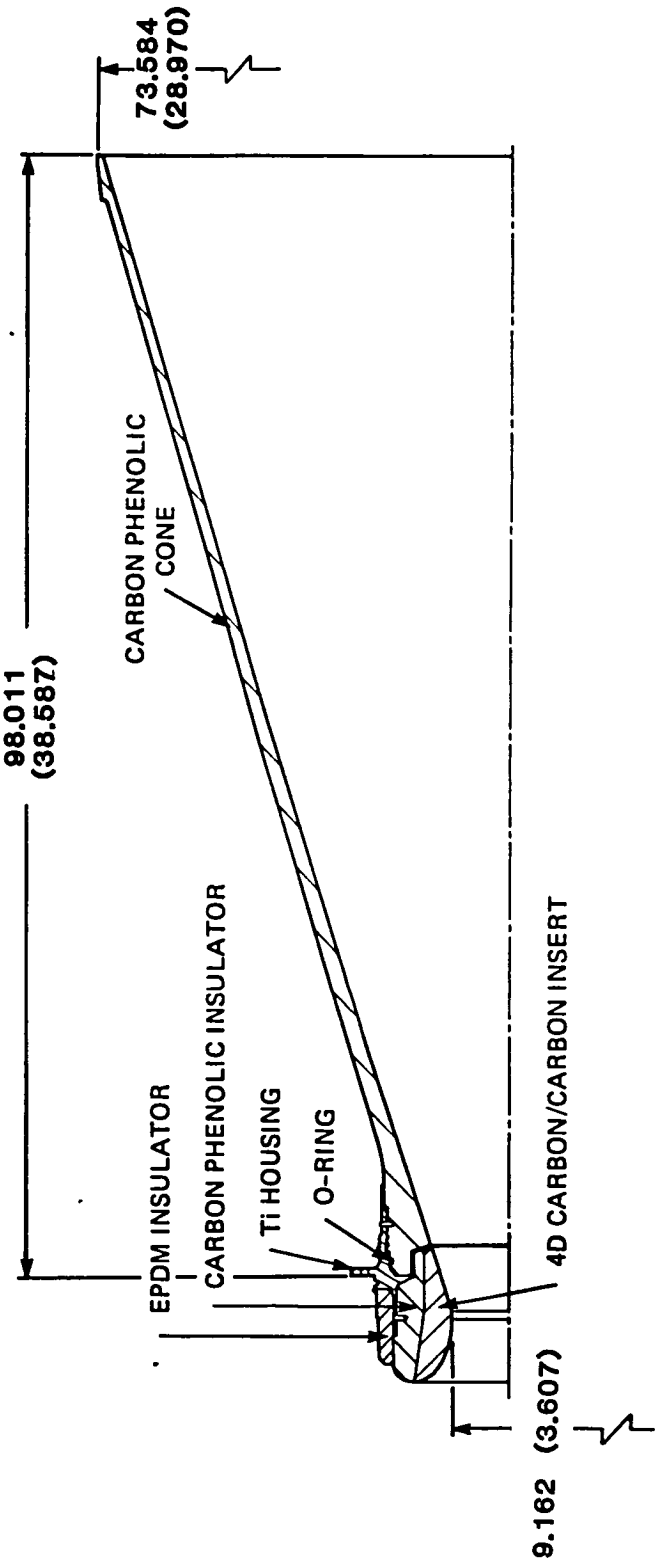

Figure 112. Nozzle Assembly, Motors D-2 and D-3

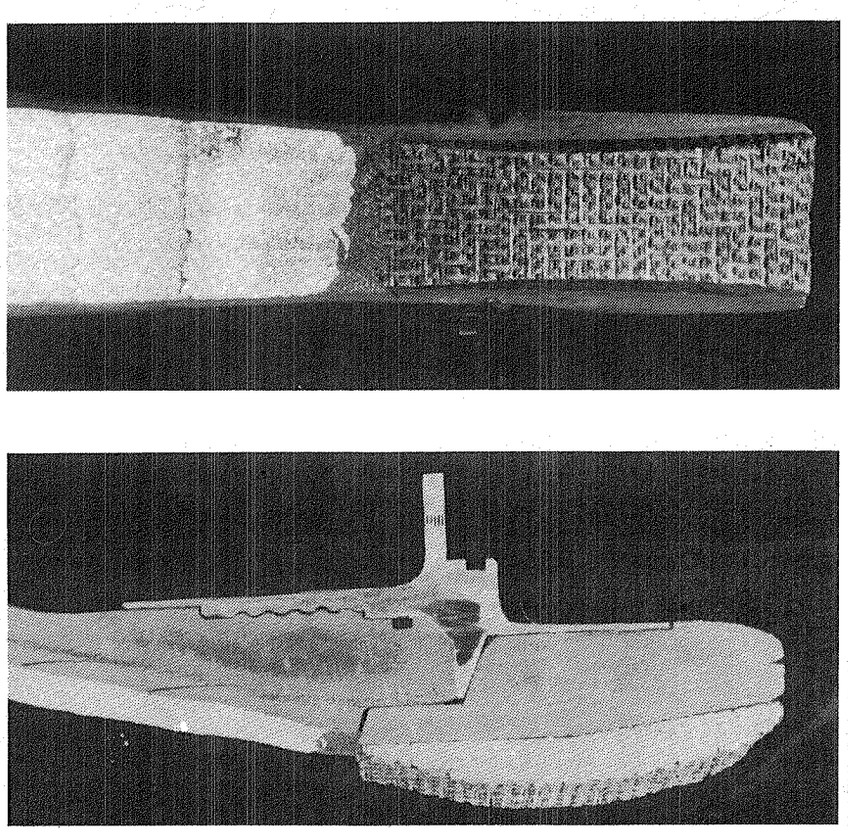

Figure 113. Post-Test Views of D-2 Nozzle

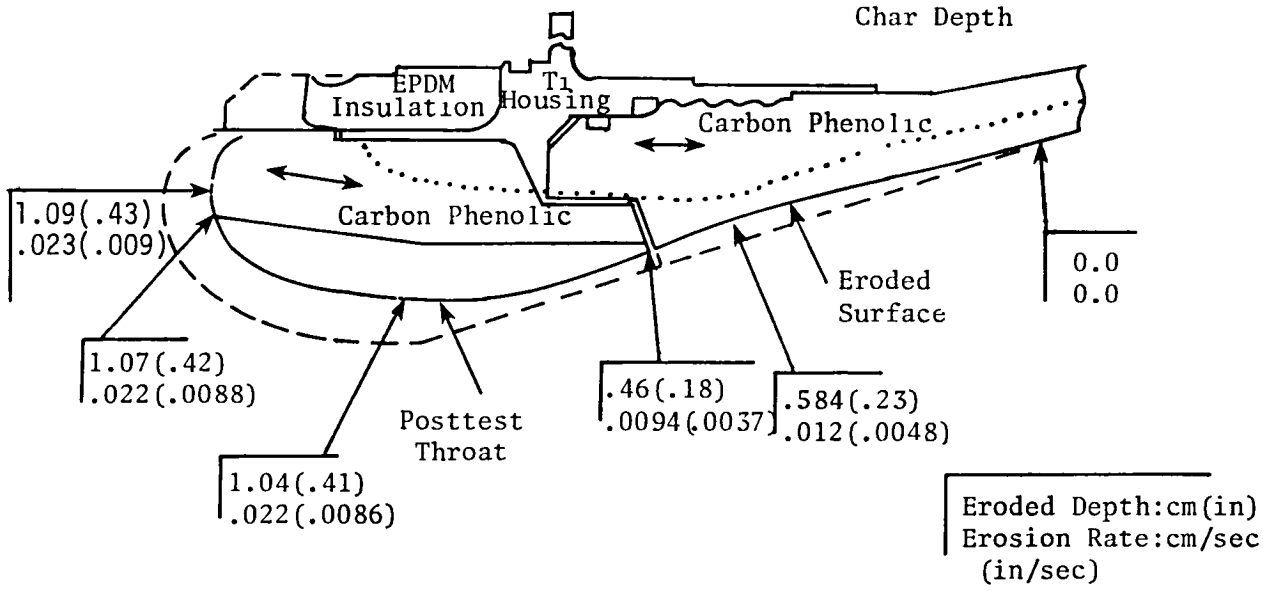

Figure 114. Nozzle Char And Erosion Profile, Motor D-2

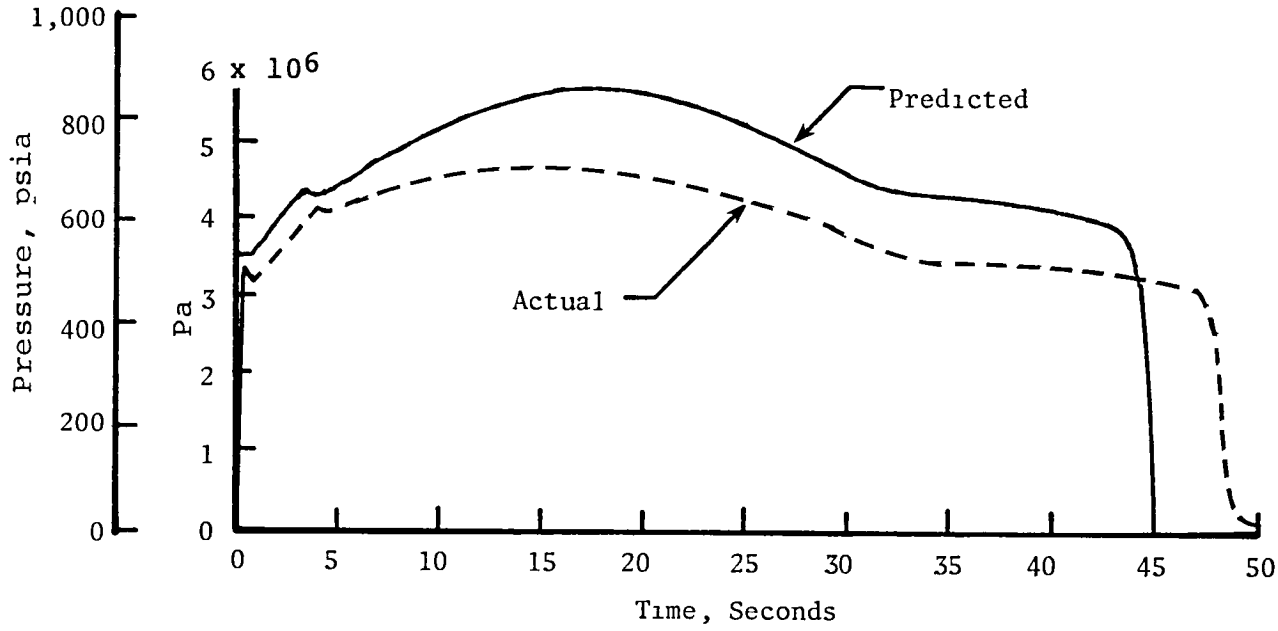

Figure 115. D-2 Predicted And Measured Chamber Pressure vs Time

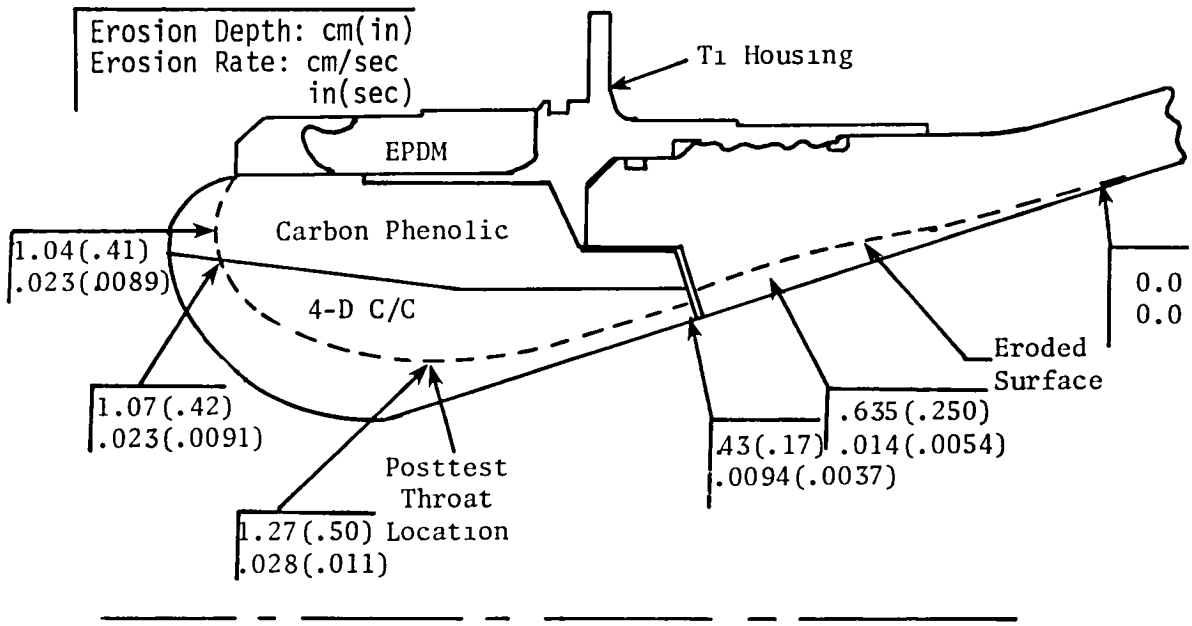

Figure 116. Nozzle Char And Erosion Profile, Motor D-3

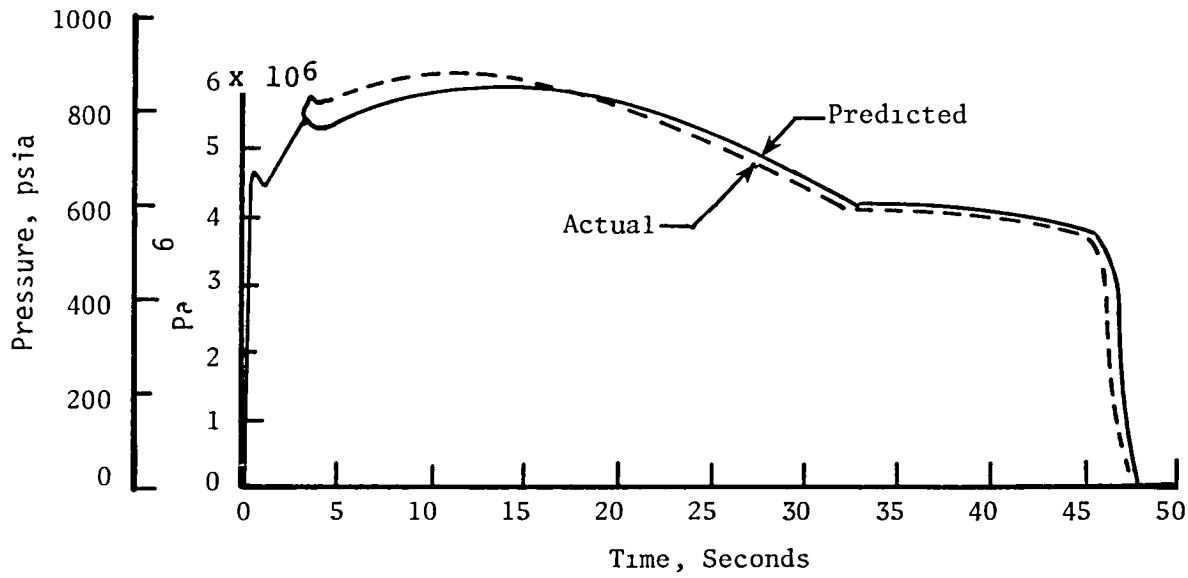

Figure 117. D-3 Predicted And Measured Chamber Pressure vs Time

Qualification Tests

Three ground tests were conducted on the final nozzle configuration at AEDC during the Qualification Phase, Reference 32. SAI furnished three billets to Thiokol, S/N's 104-1, 105-1 and 105-2 for Q-1, Q-2 and Q-3, respectively. Thiokol machined and assembled the nozzles which differed from those used in the Development Phase only in the throat diameter, 9.500 cm (3.74 in).

Again, the material performed flawlessly. Figure 118 presents the predicted and measured chamber pressure histories, the measured being slightly higher but quite repeatable. Table 35 presents a summary of the qualification test data and as can be seen throat erosion rate was repeatable within -2 to +3% while specific impulse was within $\pm$ .1% which is considered very good.

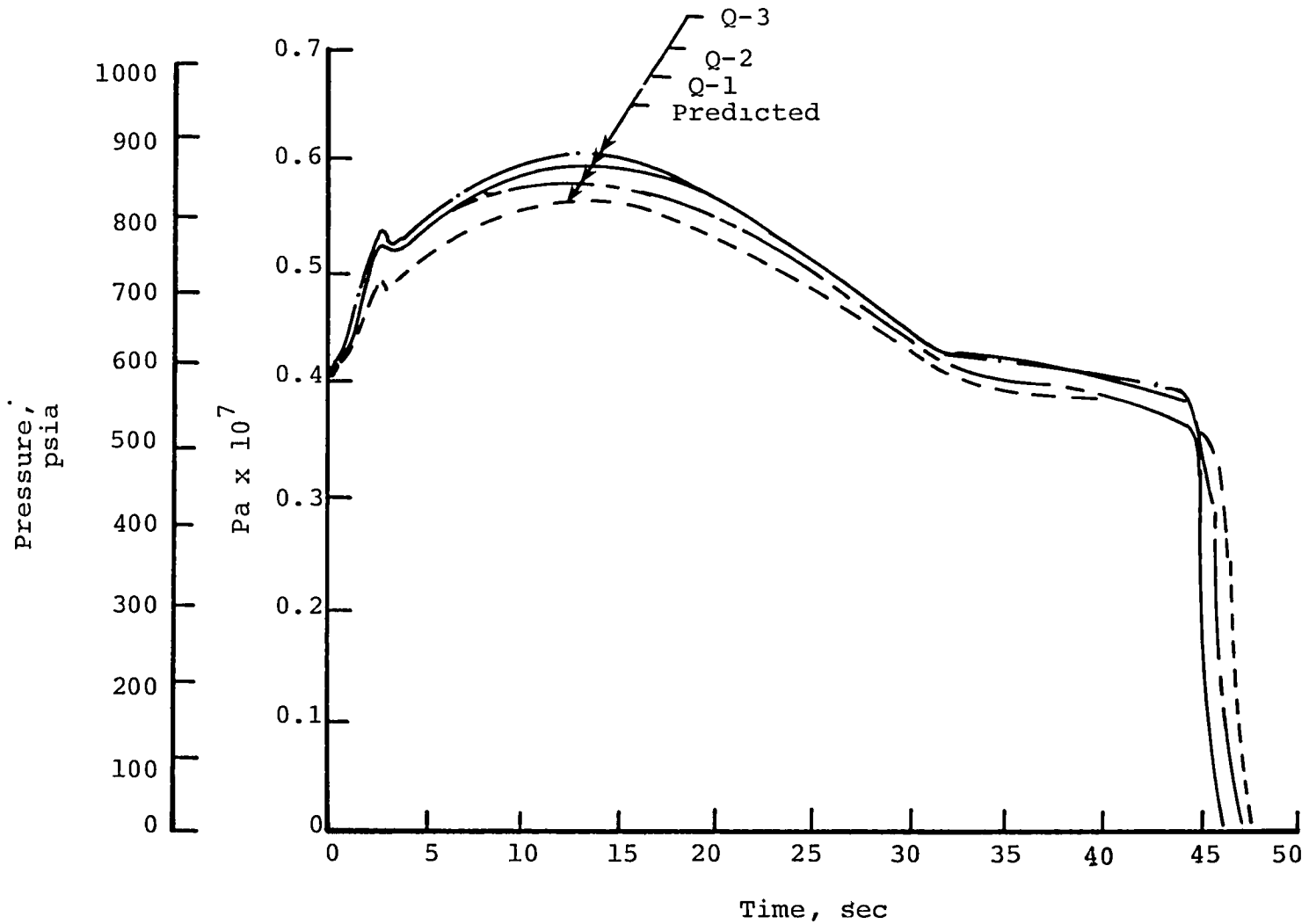

Figure 118. Qualification Firing Chamber Pressure Histories

Table 35. Measured Performance, Qualification Firings

Parameter	Q-1	Q-2	Q-3	Avg	Repeatability,%
Max. P_c, Pax10^6 (psi)	5.79(840)	5.94(861)	6.00(870)	5.91(857)	-2 to +2
Burn time, sec	45.50	44.48	44.04	44.67	-1 to +2
Throat Erosion Rate, cm/sec (in/sec)	.0264(.0104)	.0250(.0098)	.0252(.0099)	.0255(.0100)	-2 to +3
Max. Thrust, Nx10^4 (lbx10^4)	9.285(2.088)	9.447(2.124)	9.574(2.152)	9.435(2.121)	-2 to +1
Total Impulse, N-sec x10^6 (lb-secx10^5)	3.733(8.392)	3.739(8.405)	3.744(8.417)	3.738(8.405)	-.2 to +.2
Effective I_{sp}, sec	293.3	293.7	293.8	293.6	-.1 to +.1

CONCLUSIONS

A rational procedure has been developed and verified for the analysis of solid propellant rocket motor nozzles. The analysis methods employed include nozzle flow field prediction, radiative and roughwall convective heating, surface recession, and detailed thermal and mechanical response of all important nozzle components. The procedure was applied to the Antares III rocket motor nozzle during both the design and development phases and provided a rapid means of assessing the influence of configurational and material changes on the structural and thermal adequacy of the nozzle.

In particular, the analysis results obtained for the Antares III motor nozzle have demonstrated the following:

1. Thermostructural performance of G-90 bulk graphite nozzle throat inserts can be adequately predicted by linear elastic analysis methods if strain-to-failure (rather than ultimate strength) is used as the failure criterion.

2. Thermostructural response predictions require accurate material property data, particularly free thermal expansion and strain-to-failure.

3. Present kinetic ablation correlations developed for G-90 bulk graphite coupled with roughwall analysis methods adequately predict the erosion performance of this material. However, additional data and ablation modeling for the more porous, heterogeneous carbon-carbon materials are required.

Application of the analysis procedure to the Antares III nozzle has resulted in a design with an integral throat-entrance carbon-

carbon insert which provides a high degree of confidence thermostructurally, reduced number of parts, simplified assembly requirements, and an improved surface erosion contour. The SAI 4D carbon-carbon composite material chosen by the NASA Scout Project Office for the throat insert of the Antares III nozzle has provided additional verification of the viability of carbon-carbon materials for solid propellant rocket motor nozzles and demonstrated that low-cost carbon-carbon ITE's offer significant advantages for other future nozzle applications.

A complete manufacturing procedure for producing 4D carbon-carbon billets for Antares III has been constructed. Detailed documentation covering specifications, procedures and drawings have been written controlling every facet of the manufacture, i.e. raw materials, tooling, fabrication, processing, inspection and quality assurance. Using this plan, a total of 23 billets have been produced for use in the nozzle development, qualification and production. The end product was very reproducible in its physical characteristics.

A complete, detailed characterization of the 4D material was carried out. Mechanical and thermal design properties were measured on two separate logs and the agreement between these two sets of data was very good. While some testing and data interpretation difficulties in tension typical of this class of materials were encountered, the scatter in the data is considered nominal when compared to similar composites. Thermally, the material appears isotropic. Finally, a simple, inexpensive tag end ring test was developed and used to assess material repeatability in a gross structural sense.

A total of six ground tests were performed. In each case, the material performed as expected with no evidence of structural damage. Higher recession rates were obtained than with the G-90

graphite; however, this was expected since all carbon-carbons exhibit higher recession than bulk graphites. The erosion performance was repeatable within $\pm$ 3% and the motor specific impulse to within $\pm$ .1%.

REFERENCES

1. Dirling, Jr., R.B., A Method for Computing Roughwall Heat Transfer Rates on Reentry Nosetips, AIAA No. 73-763, May 1973.

2. Nikuradse, J., Laws for Flows in Rough Pipes, VDI-Forschungsheft 361, Series B, Vol. 4, 1933; Trans. NACA TM 1292, 1950.

3. Dipprey, D.F. and R.H. Sabersky, Heat and Momentum Transfer in Smooth and Rough Tubes at Various Prandtl Numbers, International Journal of Heat Mass Transfer, Vol. 6, pp. 239-353, 1963.

4. Sheldahl, R.E. and G.F. Wright, Effect of Fabric Orientation on the Ablation Performance of Carbon Phenolic, SANS-75-6088, Sandia Laboratories, Albuquerque, New Mexico, 1975.

5. Hender, D.R., Aft-facing Ablation Step Analysis and Computer Program, McDonnell Douglas Corporation, Santa Monica, CA MDC-G1195, October 1969.

6. Aerotherm Charring Material Thermal Response and Ablation Program Version 3 User Manual, Aerotherm Report No. UM-70-12, April 1970.

7. Chu, E. and H. Tong, Aerotherm Graphite Surface Kinetics Computer Program (GASKET2), AFRPL-TR-76-62, December 1976.

8. Crose, J.G. and R.M. Jones, SAAS III, Finite Element Stress Analysis of Axisymmetric and Plane Solids with Different, Orthotropic, Temperature-Dependent Properties in Tension and Compression, Air Force Report No. SAMSO-TR-71-103, June 21, 1971.

9. Pears, C.D., H.S. Starrett, and H.G. Sanders, More on Strength Analysis of Polygraphites, AFML-TR-73-212, January 1977.

10. The Thermal and Mechanical Properties of Graphitite G-90, Southern Research Institute Report A-883-2690-I-F, October 22, 1971.

11. The Thermal and Mechanical Properties of Graphitite G-90, Southern Research Institute Report 217-3034-I-F, July 3, 1973.

12. Tensile, Compressive, and Thermal Expansion Properties of Graphitite G-90, Southern Research Institute Report A-636-2612I, May 3, 1971.

13. The Thermal Expansion and Tensile Properties of Graphitite G-90, Southern Research Institute Report 8699-2032-I, Sept. 21, 1967.

14. Mechanical Properties and Thermal Expansion of Graphitite G-90, Southern Research Institute Report 9023-2032-II, April 19, 1968.

15. Buch, J.D., E.H. Zehms, and R.C. Rossi, Thermomechanical Properties of a Graphite Phenolic Composite, Air Force Report No. SAMSO-TR-70-219, June 15, 1970.

16. Data on Carbon Phenolic Material Fabricated by HITCO, unpublished data from the Scout Project Office, NASA-Langley Research Center.

17. Reentry Materials Handbook. Vol. 8, Aerospace Corporation Report POR-1001 (S 2855-20(-3)), December 1967.

18. Driggers, G., Ring and Flat Panel Carbon-Phenolic Properties, AIAA Paper No. 76-695, Presented at the AIAA Propulsion Conference, July 1976.

19. Loomis, W.C., et al, Antares III Nozzle Analysis, Science Applications, Inc. Report No. SAI-061-78-02-003, Prepared for NASA-Langley Research Center, February 28, 1978.

20. Metallic Materials and Elements for Aerospace Vehicle Structures, Military Handbook 5B, Vol. 1 and Vol. 2, August 1974.

21. Kessler, S., Evaluation of G-90 Graphite, Letter to R. Reames, Vought Systems Division, Document No. E147-78, Thiokol/Elkton Division, Elkton, Maryland, November 2, 1978.

22. Starrett, H.S., and C.D. Pears, Probable and Average Properties of ATJ-S (WS) Graphite, Air Force Report No. AFML-TR-73-14, Vol. 1, February 1973.

23. Buch, J.D., J.G. Crose, and E.Y. Robinson, Failure Criteria in Graphite Program, Air Force Report No. AFML-TR-77-16, March 1977.

24. Dull, R.B., Research and Development on Advanced Graphite Materials, Vol. XXVI, Physical Properties of Some Newly Developed Graphite Grades, Air Force Report No. WADD-TR-61-72, May 1964.

25. Letter to David Guthrie, NASA-Langley Research Center, Hampton, Virginia, WCL-061-115-78, Science Applications, Inc., Irvine, California, August 4, 1978.

26. Antares III Nozzle Redesign, Briefing Manual for SAI Presentation to Scout Project Office, NASA-Langley Research Center, August 24, 1978.

27. Canada, C.R. and C.D. Pears, The Evaluation of the Virgin, Tag-End, and Post-Fired Properties of the Candidate Materials in the Carbon-Carbon Advanced Nozzle Program, AFML-TR-4024, Part II, June 1980.

28. Canada, C.R., Letter Report No. SoRI-EAS-80-218-4380-F, March 1980.

29. Clayton, F.I., Cylindrical Carbon-Carbon ITE Nozzle Investigation, Monthly Progress Report No. 27, August 1980.

30. Carbon/Carbon Nozzle Insert Evaluation Test Report, E 122-78, Thiokol/Elkton Division, Elkton, Maryland, August 1978.

31. Antares III Development Program, Final Report, E34-79, Thiokol/ Elkton Division, July, 1979.

32. Antares III Qualification Review, Briefing Manual, July, 1979.

APPENDIX A

TENSILE SPECIMEN DESIGN
AND
ANALYSIS

Assume:

Total yarn bundle volume fraction =	.647
Z-yarn bundle volume fraction =	.233
U,V, or W yarn bundle volume fraction =	.138

If we further assume a filament packing fraction of .6, we get

Z-filament volume fraction, ν_Z =	.140
U,V, or W filament volume fraction, $\nu_{U,V,W}$ =	.083

Since the fibers are straight, we will use the "wound and woven-axial" curve of Figure A-1. Thus

$$\nu_Z \sigma_f = 1.52 \times 10^8 \text{ Pa } (2.2 \times 10^4 \text{ psi})$$

$$\nu_{U,V,W} \sigma_f = 8.96 \times 10^7 \text{ Pa } (1.3 \times 10^4 \text{ psi})$$

yielding in tension

$$\sigma_Z = 1.38 \times 10^8 \text{ Pa } (2.0 \times 10^4 \text{ psi})$$

$$\sigma_{U,V,W} = 8.96 \times 10^7 \text{ Pa } (1.3 \times 10^4 \text{ psi})$$

The interfacial shear strength for the SAI 4D material was backed out of available test data as

$$\tau_i = 1.379 \times 10^6 \text{ Pa } (200 \text{ psi})$$

while for other carbon-carbons (higher density)

$$\tau_i = 3.45 \times 10^6 \text{ Pa } (500 \text{ psi})$$

has been found. These will be used as lower and upper bounds re-

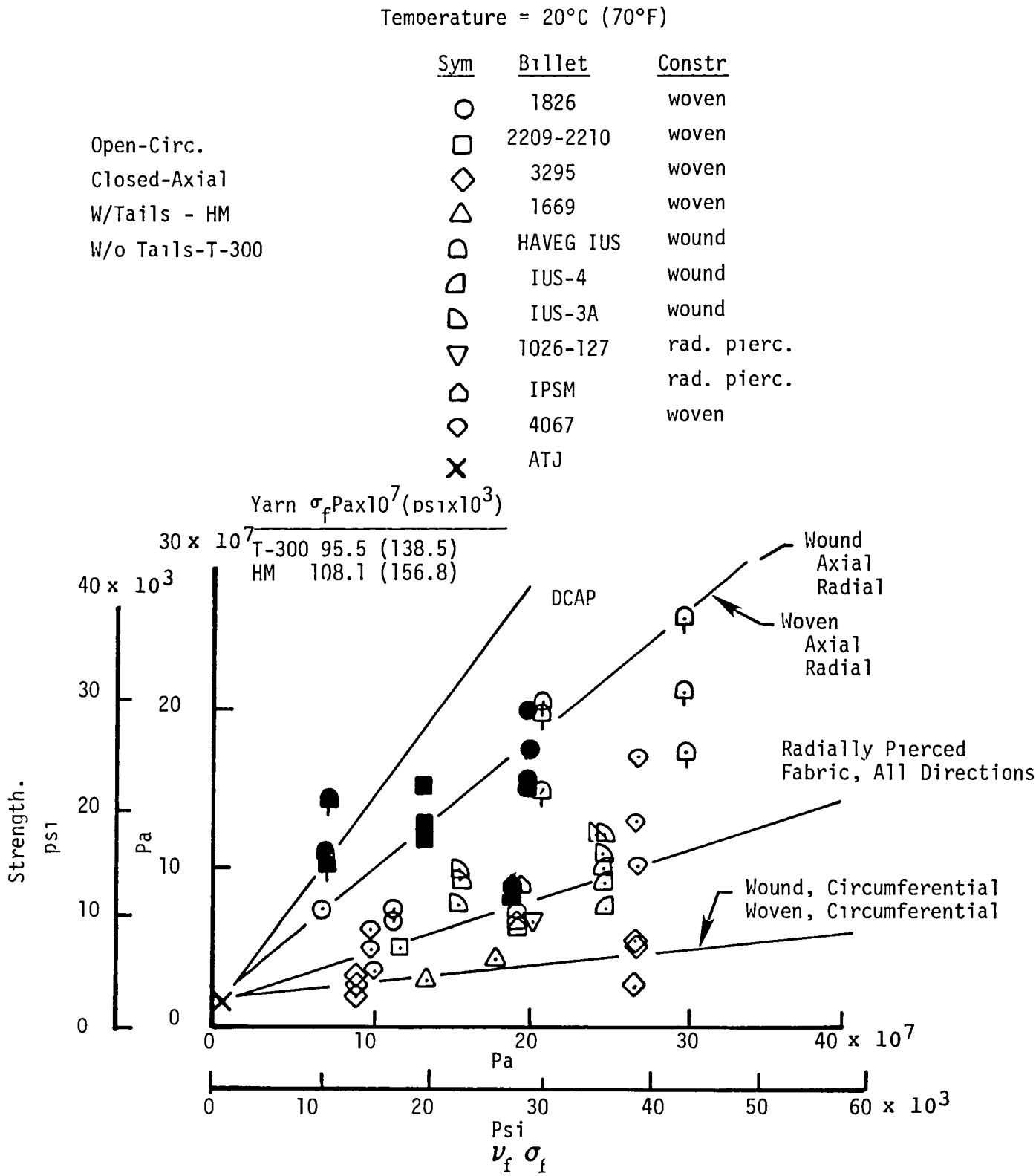

Figure A-1. Tensile Strength Correlation

spectively. The cross-fiber shear strength can also be obtained from the available 4D data as

$$\tau_c = 4.83 \times 10^6 \text{ Pa (700 psi)}$$

while an upper bound can be obtained from Figure A-2 as

$$\tau_{c_U} = 1.034 \times 10^7 \text{ Pa (1500 psi)}$$

$$\tau_{c_Z} = 1.586 \times 10^7 \text{ Pa (2300 psi)}$$

where Z and U refer to the fiber direction sheared.

For longitudinal rod pull-out:

$$L_a = A\sigma_u$$

$$L_s = n_1 c_1 l_h \tau_i$$

where

L_a = applied load required for tensile failure in test section

L_s = load carried in interfacial shear by bundles in specimen head

A = cross-section area of test section

σ_u = ultimate strength in tension = σ_Z or $\sigma_{U,V,W}$

n_1 = number of longitudinal fibers carrying the shear load in specimen head

c_1 = circumference of the longitudinal bundles carrying shear load in specimen head

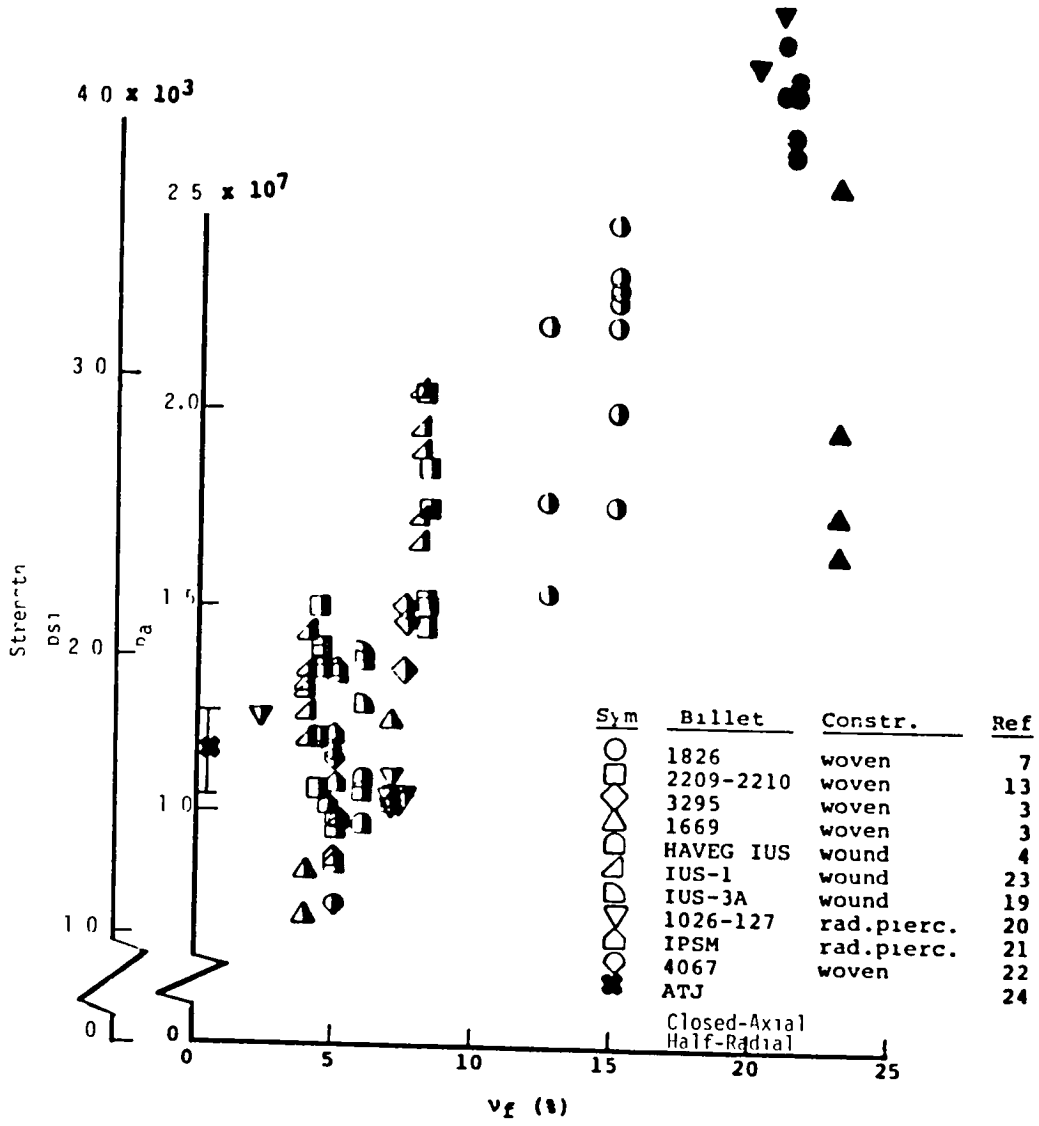

Figure A-2. Core Shear Data

l_h = head length of specimen

τ_i = interfacial shear strength of bundles in specimen head

We wish to solve for the minimum l_h which is when $L_a = L_s$. Thus,

$$l_{h_{min}} = \frac{A\sigma_u}{n_1 c_{1\ i}}$$

For head shear-off i.e. shearing of fibers transverse to the load direction

$$L_a = A\sigma_u$$

$$L_c = \pi d_1 l_h \tau_c$$

where

L_c = load carried in cross-fiber shear in specimen head

d_1 = minimum head diameter

τ_c = shear strength across fibers

as above

$$l_{h_{min}} = \frac{A\sigma_u}{d_{1\ e}}$$

For the SoRI test specimens, Figure 63, we have

Z Specimen	U,V or W Specimen
d_1 = 1.575 cm (0.62 in)	d_1 = 1.694 cm (0.667 in)
A = 0.413 cm^2 (0.064 in^2)	A = 0.413 cm^2 (0.064 in^2)
σ_u = 1.38×10^8 Pa (20000 psi)	σ_u = 8.96×10^7 Pa (13000 psi)
n_1 = 3	n_1 = 3

c_1 = 0.22

τ_i = 1.38-3.45x10^6 Pa (200-500 psi)

τ_{c_u} = 4.83-10.34x10^6 Pa (700-1500 psi)

c_1 = 0.20

τ_i = 1.38-3.45x10^6 Pa (200-500 psi)

τ_{c_z} = 4.83-15.86x10^7 Pa (700-2300 psi)

Longitudinal Rod Pull-Out, $l_{h_{min}}$, cm (in)				Head Shear-Off, $l_{h_{min}}$, cm (in)			
Z		U,V or W		Z		U,V or W	
τ_i=500	τ_i=200	τ_i=500	τ_i=200	τ_c=1500	τ_c=700	τ_c=2300	τ_c=700
9.86 (3.88)	24.64 (9.7)	7.036 (2.77)	17.60 (6.93)	1.12 (0.44)	2.41 (0.95)	0.66 (0.26)	2.18 (0.86)

There appears to be no problem with the head shear-off mode of failure. However, longitudinal rod pull-out may be a problem at room temperature which is a typical failure mode for carbon-carbon. The assumption of 3 active rods is highly conservative but the extent to which other rods in the head are effective is impossible to estimate. The interfacial shear strength will increase with temperature as the interfacial cracks close, a factor of three being not unusual. Thus, at elevated temperature, a more realistic tensile failure may result.

APPENDIX B

RING TEST DESCRIPTION

Equipment

Item - # Req'd	Model/Drawing #	Remarks
(1) Test Ring - 1	Figure B-1	4D C-C Composite Specimen
(2) Upper Face Plate - 1	Figure B-1	
(3) Lower Face Plate - 1	Figure B-1	
(4) Tension Bolts and Nuts - 8	Figure B-1	
(5) Spacers - 4	Figure B-1	
(6) Rubber Bladder -1	3.50 - R	
(7) Valve Stems - 2	Figure B-1	
(8) Pressure Gage - 1	Enerpac 15000 psi	
(9) Pump - 1	Enerpac P-39	Oil Filled
(10) Spacer	Figure B-1	

Pre-Test Requirement

(1) Mark specimen every 30° starting work 0° to 330°, the 0° line should be parallel to a U-yarn. This marking should be visible on the specimen but in no way scratch, deface the part, or increase ring thickness above tolerance.

(2) Inspect specimen for visual defects and record observations on ring test data sheet, Table B-1.

(3) Measure inside and outside ring diameters and ring thickness every 30° around the specimen (U+0° to U+330°). Record on ring test data sheet along with any noticeable anomalies.

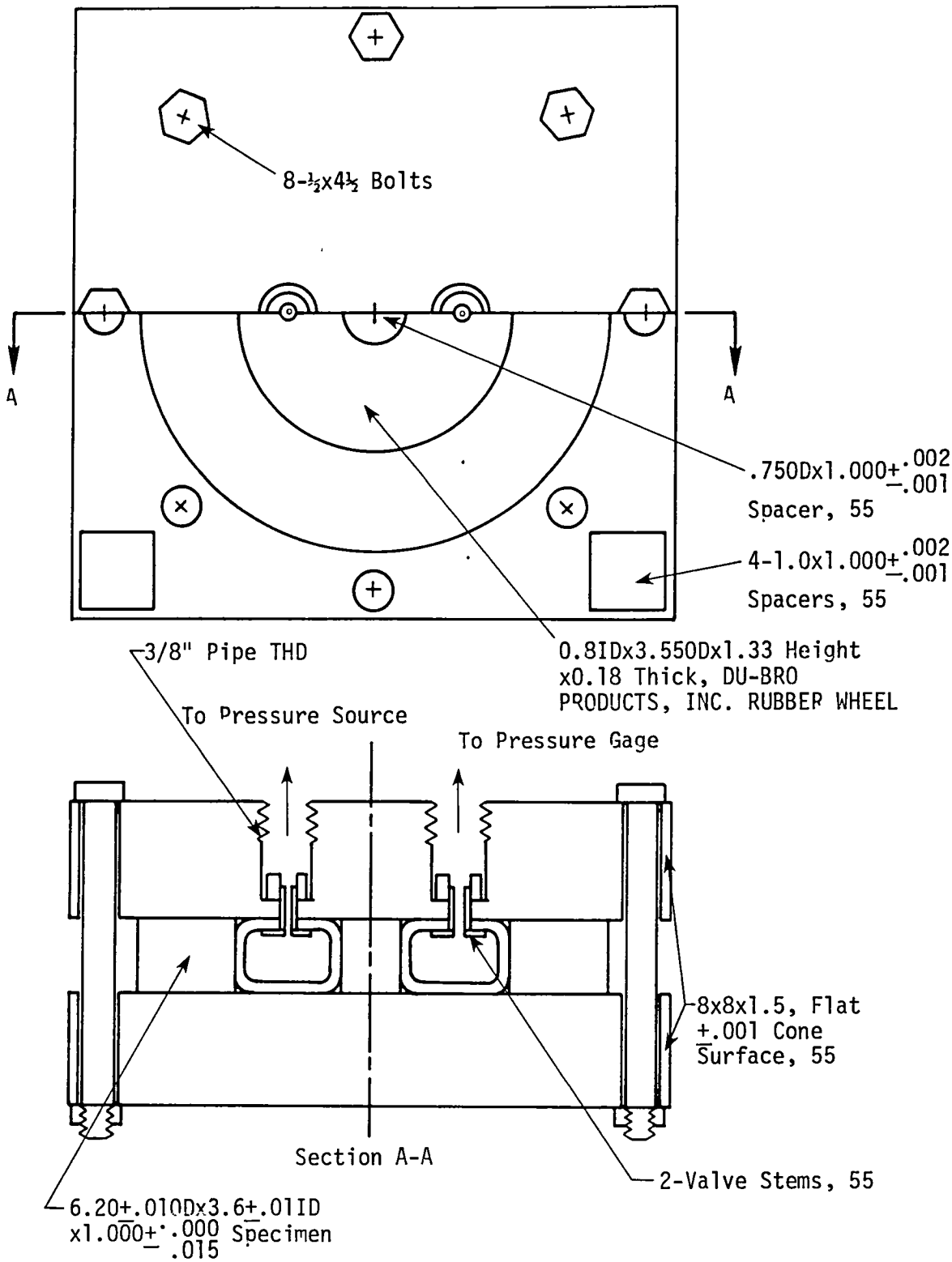

Figure B-1. Ring Test Fixture and Specimen

TABLE B-1. RING TEST DATA SHEET

DATE

SPECIMEN NO.

DENSITY

MAX. PRESSURE

MOD.

DEFLECTION AT MAXIMUM PRESSURE

GENERAL REMARKS

Cir. Deg.	PRE-TEST DIMENSIONS*			POST-TEST DIMENSIONS*		REMARKS
	I.D.	O.D.	Thickness	Wall Thickness	Thickness	
0						
30						
60						
90						
120						
150						
180						
210						
240						
270						
300						
330						

Note: All Dimensions are in cm(in) unless specified otherwise

* Wall Thickness = Radial Thickness Thickness= Axial Thickness

(4) If any place on the ring is greater than 2.54 cm (1.000 in) thick (axial direction) use fine grain sandpaper to grind surface to tolerance. Thickness should be 2.54 + .000 - .005 cm (1.00 + .000 - .002 in). Ring to be checked around total circumference to meet this tolerance. Ring also to be checked using a height gauge to ensure that it is flat. If the height gauge measurements do not fall within the above tolerance, the ring is to be sanded until the tolerance is met.

Assembly Procedure

(1) Fabricate pressure bladder ⑥*; valve stems ⑦ should be diametrically opposed (180° ± 1° apart).

(2) Place rubber bladder on upper face plate ② with valve stems ⑦ inserted into face plate center holes and secured into place. Bladder should have spacer ⑩ in center.

(3) Place ring specimen ① on upper face plate.

(4) Insert tension bolts ④ into upper face plate and bolt lower face plate ③ to upper face plate; bolts to be torqued to 2.25 N-m (200 in-lbs) after the spacers ⑤ are in place.

(5) Attach pump ⑨, and pressure gauge to the test fixture.

(6) Verify clearance at 30° intervals around circumference between ring and top plate by use of feeler gauge (.1 mm).

---

* Number enclosed with a circle indicates items number in equipment list

Test Procedure

(1) Entire test to be conducted at room temperature, 20 $\pm$ 8°C.

(2) Begin test by slowly, 1.38×10^7 Pa/min (2000 psi/min) increasing bladder pressure and holding at each 3.45×10^6 Pa (500 psi) increment for no more than 10 sec.

(3) Continue to increase pressure till burst. After failure has been obtained, re-zero and determined max. pressure specimen can withstand.

(4) Minimum Data Required

(a) Pre-test ring dimensions, see Pre-Test Requirements (3)
(b) Max. pressure at failure
(c) Pre and post test pictures

Post Test Requirements

(1) Record required data on ring test data sheet with any comments which are required to clarify test results.

(2) Reduce and record date required for the data sheets, Table B-1.

(3) Take specimen picture - at least one overall shot and one closeup of fracture.

1 Report No	2 Government Accession No	3 Recipient's Catalog No
NASA CR-165838		

4 Title and Subtitle	5 Report Date
INTEGRAL THROAT ENTRANCE DEVELOPMENT, QUALIFICATION AND PRODUCTION FOR THE ANTARES III NOZZLE	January 1982
	6 Performing Organization Code

7 Author(s)	8 Performing Organization Report No
F. I. Clayton, R. B. Dirling, D. A. Eitman, and W. C. Loomis	
	10 Work Unit No

9 Performing Organization Name and Address	11 Contract or Grant No
Science Applications Incorporated Materials Sciences Operation 18872 Bardeen Irvine, CA 92715	NAS1-15650, Task 6

12 Sponsoring Agency Name and Address	13 Type of Report and Period Covered
National Aeronautics and Space Administration Washington, DC 20546	Contractor Report Feb. 1977-Oct. 1980
	14 Sponsoring Agency Code 490-02-02-77

15 Supplementary Notes

Langley Technical Monitor: J. David Dearing

Use of commercial products or names of manufacturers in this report does not constitute official endorsement of such products or manufacturers, either expressed or implied, by the National Aeronautics and Space Administration.

16 Abstract

This report documents the work performed to develop, qualify and produce an integral throat entrance for the Antares III solid rocket motor nozzle. The initial work consisted of design analyses of a G-90 graphite design that had evolved from past experience. While the analyses indicated acceptable margins of safety, the nozzle throat insert suffered a thermostructural failure during the first development firing. Subsequent re-analysis using properties measured on material from the same billet as the nozzle throat insert showed negative margins. Several design modifications were investigated showing only limited improvement. Carbon-carbon was investigated and found to result in large positive margins of safety.

The SAI Fast Processed 4-D material was selected to replace the G-90 graphite. This material uses Hercules HM 10000 fiber as the reinforcement. Its unique construction allows powder filling of the interstices after preform fabrication which accelerates the densification process. Allied 15V coal tar pitch is then used to complete densification. The properties were extensively characterized on this material and six nozzles were subjected to demonstration, development, and qualification firings.

17 Key Words (Suggested by Author(s))	18 Distribution Statement
Antares III nozzle throat Carbon-carbon material	Unclassified- Unlimited Subject Category 15

19 Security Classif (of this report)	20 Security Classif (of this page)	21 No of Pages	22 Price
Unclassified	Unclassified	229	A11

For sale by the National Technical Information Service, Springfield, Virginia 22161

End of Document